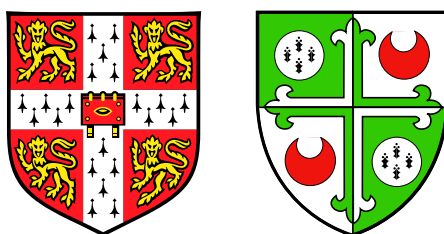# Measuring Anisotropic Interactions Using Solid-State NMR Spectroscopy

A dissertation submitted in part fulfilment of the requirements
for admission to the degree of Doctor of Philosophy at the
University of Cambridge

Robin Macnab Orr

Girton College
University of Cambridge

Declaration

This thesis describes work carried out by the author between October 2003 and September 2006 in the University Chemical Laboratory, University of Cambridge, under the supervision of Dr Melinda J. Duer. Except where otherwise stated, the contents are the original work of the author and nothing is contained which is the outcome of work done in collaboration. This dissertation has not previously been submitted in whole or part for any degree or diploma at this or any other university. The number of words does not exceed 60,000.

<div align="right">

R. M. Orr

October 2006

</div>

Acknowledgements

Abstract

Solid-state nuclear magnetic resonance (NMR) spectroscopy measurements of anisotropic nuclear spin interactions, such as the dipolar coupling and chemical shift anisotropy interactions, are useful for structure elucidation of solids. The focus of this dissertation is the development of new solid-state NMR methods that can assist the measurement of these interactions. In Chapters 1 and 2, the standard theoretical and experimental techniques used in this work are outlined. In Chapter 3, current methods for structural studies using solid-state NMR are reviewed.

For powder samples, the chemical shift anisotropy interaction can be measured using either static powder pattern spectra or spinning sideband intensities in magic-angle spinning (MAS) experiments. Standard one-dimensional experiments are frequently complicated by overlapping lineshapes. Instead, multiple-pulse two-dimensional NMR methods with MAS are used to separate these overlapping spinning sidebands or powder patterns in a second dimension. In Chapter 4, a robust two-dimensional experiment is developed that allows the measurement of small chemical shift anisotropies by correlating chemical shift anisotropy spinning sidebands at the true spinning frequency with those at a lower frequency. In Chapter 5, new implementations are described of two existing multiple-pulse experiments to separate quasi-static powder patterns in a two-dimensional spectrum. The original experiments are sensitive to pulse imperfections and the spectra they generate frequently contain serious artefacts and distortions which prevent accurate determination of chemical shift anisotropy parameters. The new approaches are shown to be robust and avoid the distortions and artefacts seen in the spectra recorded using their original versions. The experiments in Chapters 4 and 5 allow the CSA to be measured sufficiently accurately for the resulting values to be used in structural studies.

In the one-dimensional ^{13}C MAS spectra of ^{13}C–^{14}N spin pairs, an asymmetric splitting is seen in the ^{13}C signal, owing to the large quadrupole coupling often experienced by the ^{14}N nucleus. This causes an undesirable reduction in the signal-to-noise ratio of ^{14}N coupled ^{13}C sites, and complicates the lineshapes obtained in two-dimensional spectra. Chapter 6 describes a new method for decoupling ^{14}N and removing the residual splitting seen in the ^{13}C MAS spectrum. In addition, experiments are investigated for determining the relative orientations of the ^{13}C–^{14}N dipolar coupling and ^{13}C chemical shift interaction tensors, and the relative orientation of the ^{13}C chemical shift anisotropy and ^{14}N quadrupolar interaction tensors in ^{13}C–^{14}N spin pairs.

Contents

1

A quantum mechanical description of nuclear spin and NMR

Nuclear magnetic resonance (NMR) experiments exploit the property of nuclear spin angular momentum, and its associated magnetic moment, possessed by 'spin-active' nuclei. Conventionally, a sample is located in a static magnetic field, and the response of the nuclei to interactions with this field, and other time dependent magnetic fields, is recorded as an electromagnetically-induced current in a coil surrounding the sample. The quantum mechanical description of NMR and the notation used in later chapters to understand and explain the results of NMR experiments is outlined in this chapter. In addition to the references cited throughout this chapter, references [1–12] were used in its preparation.

1.1   A quantum mechanical description of a single spin

The intrinsic spin angular momentum possessed by a nucleus is characterised by its spin quantum number I, which is a constant for a particular nucleus (in a particular nuclear state). For example, $I = \frac{1}{2}$ for ^{13}C, ^{1}H and ^{15}N, and $I = 1$ for ^{14}N; a nucleus is said to be spin-active if $I > 0$. The magnetic moment of a nucleus, with its quantum mechanical operator expressed as $\hat{\boldsymbol{\mu}}$, is proportional to the spin angular momentum operator $\hat{\boldsymbol{I}}$

$$\hat{\boldsymbol{\mu}} = \gamma \hat{\boldsymbol{I}}, \tag{1.1}$$

where the constant of proportionality γ is the magnetogyric ratio, and is different for each nuclear isotope. Here, the units of angular momenta are $\hbar$. Both $\hat{\boldsymbol{\mu}}$ and $\hat{\boldsymbol{I}}$ are vector operators, and if $\boldsymbol{i}$, $\boldsymbol{j}$ and $\boldsymbol{k}$ are unit vectors along the Cartesian directions of an (as yet unspecified) axis frame, Equation (1.1) can be written using the three Cartesian components of $\hat{\boldsymbol{\mu}}$ and $\hat{\boldsymbol{I}}$:

$$\hat{\mu}_x \boldsymbol{i} + \hat{\mu}_y \boldsymbol{j} + \hat{\mu}_z \boldsymbol{k} = \gamma \left(\hat{I}_x \boldsymbol{i} + \hat{I}_y \boldsymbol{j} + \hat{I}_z \boldsymbol{k} \right). \tag{1.2}$$

In Appendix A the quantum mechanical notation used here is presented, and relationships between angular momentum operators, rotation operators and Euler angles are summarised.

1.1.1 A nucleus in a uniform and static magnetic field

Classically, the energy of a magnetic moment $\boldsymbol{\mu}$ in a magnetic field $\mathbf{B}_0$ is given by $E = -\boldsymbol{\mu} \cdot \mathbf{B_0}$. Applying the correspondence principle, it follows from Equation (1.1) that the Hamiltonian ($\hat{\mathcal{H}}$) for a nuclear spin in a magnetic field is

$$\hat{\mathcal{H}} = -\gamma \hat{\boldsymbol{I}} \cdot \mathbf{B}_0, \tag{1.3}$$

where energies have been chosen to be in angular frequency units. If the static magnetic field of the NMR experiment is chosen to lie along the z-axis of the laboratory frame of reference, and has a field strength B_0, then the Hamiltonian for the spin is

$$\hat{\mathcal{H}}_Z = -\gamma B_0 \hat{I}_z = \omega_0 \hat{I}_z, \tag{1.4}$$

where the quantity $\omega_0 = -\gamma B_0$ is the Larmor frequency. A nucleus with spin I has $2I + 1$ different eigenfunctions of $\hat{I}_z$, denoted $|I, m\rangle$ where m is the eigenvalue and takes the values $m = -I, -I + 1, \ldots, I - 1, I$. Therefore, in a magnetic field, the $2I + 1$ eigenstates are non-degenerate, with adjacent energy levels separated by $|\gamma B_0|$, although the ordering in energy of the eigenstates depends on the sign of γ. $\hat{\mathcal{H}}_Z$ is the called the Zeeman Hamiltonian, and the eigenfunctions of $\hat{I}_z$ are the Zeeman states.

1.1.2 Superposition states

A wavefunction $|\psi\rangle$ can be expressed as a linear combination, or superposition, of a set of linearly independent functions $|\phi_n\rangle$, which are referred to as a basis set

$$|\psi\rangle = \sum_n a_n |\phi_n\rangle, \tag{1.5}$$

where the a_n coefficients may be complex. The basis functions will also be assumed here to be orthonormal ($\langle \phi_i | \phi_j \rangle = \delta_{i,j}$ for all i and j). The basis set is used to represent an

operator $\hat{Q}$ in a matrix form, with elements Q_{ij} given by

$$Q_{ij} = \langle \phi_i | \hat{Q} | \phi_j \rangle. \tag{1.6}$$

The eigenfunctions of $\hat{I}_z$ form a complete and finite basis set of $2I + 1$ orthonormal functions, called the Zeeman basis. For a single spin-1/2 nucleus, its spin wavefunction is described by

$$|\psi\rangle = \sum_{m=-I}^{+I} a_m |I, m\rangle = a_\alpha |\alpha\rangle + a_\beta |\beta\rangle, \tag{1.7}$$

where for convenience the two eigenfunctions of $\hat{I}_z$ (Zeeman states) have been written as $\left|\frac{1}{2}, +\frac{1}{2}\right\rangle \equiv |\alpha\rangle$ and $\left|\frac{1}{2}, -\frac{1}{2}\right\rangle \equiv |\beta\rangle$. The matrix representations of the spin angular momentum operators in the spin-1/2 Zeeman basis, ordered as $|\alpha\rangle$, $|\beta\rangle$, are

$$I_x = \tfrac{1}{2} \begin{pmatrix} 0 & 1 \\ 1 & 0 \end{pmatrix} \quad I_y = \tfrac{1}{2} \begin{pmatrix} 0 & -i \\ i & 0 \end{pmatrix} \quad I_z = \tfrac{1}{2} \begin{pmatrix} 1 & 0 \\ 0 & -1 \end{pmatrix} \tag{1.8}$$

$$I_+ = \begin{pmatrix} 0 & 1 \\ 0 & 0 \end{pmatrix} \qquad I_- = \begin{pmatrix} 0 & 0 \\ 1 & 0 \end{pmatrix}, \tag{1.9}$$

where the elements of the matrix representations of $\hat{I}_x$ and $\hat{I}_y$ are evaluated using the raising and lowering operators defined in Equation (A.11).

Operators may also be represented by the basis functions. From the definition of the matrix elements in Equation (1.6), the operator $\hat{Q}$ is expressed as

$$\hat{Q} = \sum_{i,j} |\phi_i\rangle Q_{ij} \langle \phi_j| = \sum_{i,j} Q_{ij} |\phi_i\rangle\langle \phi_j|. \tag{1.10}$$

Using the single spin-1/2 Zeeman basis, the angular momentum operators are written as

$$\hat{I}_x = \tfrac{1}{2} \{ |\alpha\rangle\langle\beta| + |\beta\rangle\langle\alpha| \}, \ \hat{I}_y = \tfrac{1}{2} i \{ |\beta\rangle\langle\alpha| - |\alpha\rangle\langle\beta| \}, \ \hat{I}_z = \tfrac{1}{2} \{ |\alpha\rangle\langle\alpha| - |\beta\rangle\langle\beta| \}. \tag{1.11}$$

1.1.3 Time evolution of the spin wavefunction

The eigenfunctions of $\hat{I}_z$ are solutions to the time-independent Schrödinger equation ($\hat{\mathcal{H}}|\phi_n\rangle = E_n|\phi_n\rangle$, Equation (A.5)) for an isolated spin in a static magnetic field. Consequently, the solution to the time-dependent Schrödinger equation in this case is

simply constructed using $|\phi_n(t)\rangle = |\phi_n\rangle \exp(-iE_nt)$ (Equation (A.4) on page 221) to give

$$|\psi(t)\rangle = a_\alpha(0) \exp\left(-i\tfrac{1}{2}\omega_0 t\right) |\alpha\rangle + a_\beta(0) \exp\left(+i\tfrac{1}{2}\omega_0 t\right) |\beta\rangle, \tag{1.12}$$

where $a_\alpha(0)$ and $a_\beta(0)$ are the expansion coefficients in Equation (1.7) at time $t = 0$. Using the time-dependent wavefunction expressed in Equation (1.12), the expectations values of the three components of the magnetic moment can be evaluated. For example, the $\hat{\mu}_z$ component is

$$\begin{aligned}
\langle\hat{\mu}_z\rangle(t) &= \gamma\langle\psi(t)|\hat{I}_z|\psi(t)\rangle \\
&= \gamma\tfrac{1}{2}\left[a_\alpha(0)\exp(-i\tfrac{1}{2}\omega_0 t)\right]^*\left[a_\alpha(0)\exp(-i\tfrac{1}{2}\omega_0 t)\right] \\
&\quad - \gamma\tfrac{1}{2}\left[a_\beta(0)\exp(+i\tfrac{1}{2}\omega_0 t)\right]^*\left[a_\beta(0)\exp(+i\tfrac{1}{2}\omega_0 t)\right] \\
&= \tfrac{1}{2}\gamma|a_\alpha(0)|^2 - \tfrac{1}{2}\gamma|a_\beta(0)|^2.
\end{aligned} \tag{1.13}$$

Consequently the expectation value of the magnetic moment parallel to the z-axis of the laboratory frame is independent of time. The quantities $|a_\alpha(0)|^2$ and $|a_\beta(0)|^2$ represent the probability that a measurement of $\hat{I}_z$ will yield a value of $m = \tfrac{1}{2}$ and $m = -\tfrac{1}{2}$ respectively. The μ_x component is

$$\begin{aligned}
\langle\hat{\mu}_x\rangle(t) &= \gamma\langle\psi(t)|\hat{I}_x|\psi(t)\rangle = \tfrac{1}{2}\gamma\langle\psi(t)|\hat{I}_+ + \hat{I}_-|\psi(t)\rangle \\
&= \gamma\tfrac{1}{2}\left[a_\alpha(0)\exp\left(-i\tfrac{1}{2}\omega_0 t\right)\right]^*\left[a_\beta(0)\exp\left(+i\tfrac{1}{2}\omega_0 t\right)\right] \\
&\quad + \gamma\tfrac{1}{2}\left[a_\beta(0)\exp\left(+i\tfrac{1}{2}\omega_0 t\right)\right]^*\left[a_\alpha(0)\exp\left(-i\tfrac{1}{2}\omega_0 t\right)\right] \\
&= \gamma\tfrac{1}{2}a_\alpha^*(0)a_\beta(0)\exp\left(+i\omega_0 t\right) + \gamma\tfrac{1}{2}a_\beta^*(0)a_\alpha(0)\exp\left(-i\omega_0 t\right),
\end{aligned} \tag{1.14}$$

and similarly the μ_y component is

$$\begin{aligned}
\langle\hat{\mu}_y\rangle(t) &= \gamma\langle\psi(t)|\hat{I}_y|\psi(t)\rangle = -i\gamma\tfrac{1}{2}\langle\psi(t)|\hat{I}_+ - \hat{I}_-|\psi(t)\rangle \\
&= -i\tfrac{1}{2}\gamma a_\alpha^*(0)a_\beta(0)\exp\left(+i\omega_0 t\right) + i\tfrac{1}{2}\gamma a_\beta^*(0)a_\alpha(0)\exp\left(-i\omega_0 t\right).
\end{aligned} \tag{1.15}$$

Equations (1.14) and (1.15) are combined into a more informative format by expanding the complex exponentials, and identifying the expectation value of $\hat{\mu}_x$ and $\hat{\mu}_y$ at $t = 0$, to

give

$$
\begin{aligned}
\langle\hat{\mu}_x\rangle(t) &= \tfrac{1}{2}\gamma a_\alpha^*(0)a_\beta(0)\exp(+\mathrm{i}\omega_0 t) + \tfrac{1}{2}\gamma a_\beta^*(0)a_\alpha(0)\exp(-\mathrm{i}\omega_0 t)\\
&= \tfrac{1}{2}\gamma a_\alpha^*(0)a_\beta(0)[\cos(\omega_0 t) + \mathrm{i}\sin(\omega_0 t)] + \tfrac{1}{2}\gamma a_\beta^*(0)a_\alpha(0)[\cos(\omega_0 t) - \mathrm{i}\sin(\omega_0 t)]\\
&= \gamma\cos(\omega_0 t)[\tfrac{1}{2}a_\alpha^*(0)a_\beta(0) + \tfrac{1}{2}a_\beta^*(0)a_\alpha(0)] - \gamma\sin(\omega_0 t)[\mathrm{i}\tfrac{1}{2}a_\alpha^*(0)a_\beta(0) - \mathrm{i}\tfrac{1}{2}a_\beta^*(0)a_\alpha(0)]\\
&= \cos(\omega_0 t)\langle\hat{\mu}_x\rangle(0) - \sin(\omega_0 t)\langle\hat{\mu}_y\rangle(0),
\end{aligned}
\tag{1.16}
$$

and for $\langle\hat{\mu}_y\rangle(t)$

$$
\langle\hat{\mu}_y\rangle(t) = \sin(\omega_0 t)\langle\hat{\mu}_x\rangle(0) + \cos(\omega_0 t)\langle\hat{\mu}_y\rangle(0).
\tag{1.17}
$$

Equations (1.16) and (1.17) show that if a nucleus has an initial magnetic moment in the *xy*-plane of the laboratory frame, then over time its magnitude remains constant (if the effects of relaxation are ignored, see Section 1.6), but it precesses about the *z*-axis at the Larmor frequency ω_0. The direction of precession depends on the sign of γ, through the dependence of ω_0 upon γ.

1.1.4   Total magnetization of a sample: ensemble averaging

In the previous section, the time evolution of the wavefunction describing a single spin-1/2 nucleus was described. In practice, a real sample contains many nuclei, and any physical measurement has a contribution from each of the N_{bulk} nuclei in the sample. For example, the magnetic moment of a bulk sample, which is referred to as the magnetization **M**, has the component M_z along the *z*-axis (the *z*-magnetization) given by

$$
M_z = \sum_{i=1}^{N_{\text{bulk}}}\langle\psi^{(i)}|\hat{\mu}_z|\psi^{(i)}\rangle,
\tag{1.18}
$$

where $|\psi^{(i)}\rangle$ is the wavefunction of the ith spin. A bulk sample can be treated as a Gibbs ensemble of spins. Within this ensemble there is a distribution of the spins over the accessible states. If the probability of a spin being in the spin state $|\psi_k\rangle$ is P_k, the ensemble average of an observable represented by an operator $\hat{Q}$ is defined by

$$
\overline{\langle\hat{Q}\rangle} = \sum_k P_k\langle\psi_k|\hat{Q}|\psi_k\rangle,
\tag{1.19}
$$

where the 'bar' over $\langle\hat{Q}\rangle$ indicates the ensemble average, and the summation is over all possible states of the spins. In the limit of a large number of nuclear spins (large N_{bulk}), then measurement of $\hat{Q}$ is accurately described by

$$\langle\hat{Q}\rangle_{\text{bulk}} = N_{\text{bulk}}\overline{\langle\hat{Q}\rangle}. \tag{1.20}$$

For example the z-magnetization is $M_z = N_{\text{bulk}}\overline{\langle\hat{\mu}_z\rangle} = N_{\text{bulk}}\gamma\overline{\langle\hat{I}_z\rangle}$.

1.2   The density operator

The ensemble averaged expectation value of $\hat{Q}$ in Equation (1.19) may be rewritten using the closure theorem ($\sum_n |\phi_n\rangle\langle\phi_n| = \hat{\mathbf{1}}$, where $\hat{\mathbf{1}}$ is the identity operator) as

$$\begin{aligned}
\overline{\langle\hat{Q}\rangle} &= \sum_{i,j}\sum_k P_k\langle\psi_k|\phi_i\rangle\langle\phi_i|\hat{Q}|\phi_j\rangle\langle\phi_j|\psi_k\rangle \\
&= \sum_{i,j}\langle\phi_i|\hat{Q}|\phi_j\rangle\sum_k P_k\langle\phi_j|\psi_k\rangle\langle\psi_k|\phi_i\rangle.
\end{aligned} \tag{1.21}$$

This leads to the definition of a new operator

$$\hat{\rho} = \sum_k P_k|\psi_k\rangle\langle\psi_k| = \overline{|\psi\rangle\langle\psi|}, \tag{1.22}$$

where $\hat{\rho}$ is the density operator. With this definition, the ensemble average of an observable is evaluated by

$$\begin{aligned}
\overline{\langle\hat{Q}\rangle} &= \sum_{i,j}\langle\phi_i|\hat{Q}|\phi_j\rangle\langle\phi_j|\hat{\rho}|\phi_i\rangle \\
&= \sum_i\langle\phi_i|\hat{Q}\hat{\rho}|\phi_i\rangle \\
&= \text{Tr}\left[\hat{Q}\hat{\rho}\right],
\end{aligned} \tag{1.23}$$

where the trace $\text{Tr}[\hat{Q}']$ means the sum of the diagonal elements of the matrix representation of $\hat{Q}'$. The result in Equation (1.23) means that once the density operator has been determined, *any* bulk spin-property of the sample can be evaluated without further detailed calculation.

1.2.1 Operator expansion of the density operator

In an analogous manner to the expansion of the wavefunction as a linear combination of basis functions, the density operator may also by expanded, but as a linear combination of operators. For the matrix representation of the density operator in a basis of n functions, a set of n^2 independent operators are needed for the expansion of $\hat{\rho}$. The simplest basis set is the single element operators $\hat{I}_{ij} = |\phi_i\rangle\langle\phi_j|$, expressed using the representation defined in Equation (1.10), although other convenient choices may be more appropriate. For example, using the spin-1/2 Zeeman basis, a suitable set of operators is the Cartesian components of angular momentum, or the shift operators, in addition to the identity operator $\hat{\mathbf{1}}$ giving

$$\hat{\rho} = c_1\hat{\mathbf{1}} + c_x\hat{I}_x + c_y\hat{I}_y + c_z\hat{I}_z = c_1\hat{\mathbf{1}} + c_+\hat{I}_+ + c_-\hat{I}_- + c_z\hat{I}_z. \tag{1.24}$$

The coefficients c_1, c_x, c_y, c_z, $c_+ = \frac{1}{2}(c_x - \mathrm{i}c_y)$, and $c_- = \frac{1}{2}(c_x + \mathrm{i}c_y)$ may be complex and time dependent.

1.2.2 Populations and coherences

For an ensemble of isolated spins in a static magnetic field, the matrix representation of the density operator expressed in the Zeeman basis has diagonal elements, $\rho_{mm} = \overline{|a_m|^2}$, where a_m is an expansion coefficient from $|\psi\rangle = \sum_{m=-I}^{+I} a_m|I, m\rangle$. The diagonal element ρ_{mm} may be interpreted as the population of the state $|I, m\rangle$. At thermal equilibrium, the populations of the Zeeman states are determined by the Boltzmann distribution:[*]

$$\overline{|a_m|^2} = \frac{1}{Z}\exp\left(-E_m/kT\right) = \frac{\exp(-E_m/kT)}{\sum_i \exp(-E_i/kT)}, \quad E_i = \omega_0\hbar\langle\phi_i|\hat{I}_z|\phi_i\rangle. \tag{1.25}$$

Where Z is the partition function. Off-diagonal elements are $\rho_{nm} = \overline{a_n{}^*a_m} = \overline{|a_n||a_m|\mathrm{e}^{\mathrm{i}(\alpha_m - \alpha_n)}}$, where α_i is the complex argument of the coefficient a_i. Under the assumption that at thermal equilibrium the phase α_i of the coefficients are random among the spins in the ensemble, and that the phase is independent of the magnitude of a_n, the ensemble average $\overline{a_n{}^*a_m}$ will be zero.

A non-zero off-diagonal element ρ_{nm} indicates that there is a correlation of the α_i phases among different spins in the ensemble. This means there is a coherent superposition of

---

[*]The factor of $\hbar$ has been included in the expression for E_i to ensure that $\hbar\omega_0/kT$ is unitless.

eigenstates within the ensemble, or more simply, a coherence between states $|\phi_n\rangle$ and $|\phi_m\rangle$. The order of the coherence ρ_{nm} between two states $|\phi_m\rangle \rightarrow |\phi_n\rangle$ is defined as

$$p_{nm} = \frac{\langle\phi_n|\hat{I}_z|\phi_n\rangle}{\langle\phi_n|\phi_n\rangle} - \frac{\langle\phi_m|\hat{I}_z|\phi_m\rangle}{\langle\phi_m|\phi_m\rangle}. \tag{1.26}$$

In an operator expansion of the density operator, the $\hat{I}_+$ and $\hat{I}_-$ operators represent $(+1)$- and (-1)-quantum coherences respectively, which can be seen by considering the raising and lowering properties of the shift operators. The $\hat{I}_z$ operator represents zero-quantum coherences in the density operator.

At thermal equilibrium, the matrix form of the density operator in the Zeeman basis is diagonal, with elements given by Equation (1.25). Consequently, the density operator can be written as

$$\hat{\rho}_{eq} = \frac{\exp\left(-\hbar\omega_0\hat{I}_z/kT\right)}{\text{Tr}\left[\exp\left(-\hbar\omega_0\hat{I}_z/kT\right)\right]} = \frac{\hat{\mathbf{1}} - \hbar\omega_0\hat{I}_z/kT + \frac{1}{2!}(\hbar\omega_0\hat{I}_z/kT)^2 - \ldots}{\text{Tr}\left[\hat{\mathbf{1}} - \hbar\omega_0\hat{I}_z/kT + \frac{1}{2!}(\hbar\omega_0\hat{I}_z/kT)^2 - \ldots\right]}, \tag{1.27}$$

where the exponential terms have been expanded as power series. With the high temperature approximation, $kT \gg |\hbar\omega_0|$, the series can be truncated at the second term:

$$\hat{\rho}_{eq} = \frac{1}{Z}\left(\hat{\mathbf{1}} - \frac{\hbar\omega_0}{kT}\hat{I}_z\right), \quad Z = (2I + 1). \tag{1.28}$$

The identity operator $\hat{\mathbf{1}}$ commutes with all spin operators, and remains unchanged under the effect of any Hamiltonian. Further, the Boltzmann factor $(\hbar\omega_0)/(kT)$ in Equation (1.28) only scales the $\hat{I}_z$ term. For these reasons, it is usual to write the equilibrium density operator as

$$\hat{\rho}_{eq} = \hat{I}_z, \tag{1.29}$$

and to omit the identity operator and Boltzmann factor.

Most NMR experiments start with the spin system at thermal equilibrium, so the future state of the spin system can be predicted by computing the evolution of the equilibrium density operator under the effect of the Hamiltonian that governs the spin system. How this is evaluated is the subject of the next section.

1.3   Time evolution of the density operator

The density operator evolves over time in a manner dependent upon the Hamiltonian governing the spin system. Taking the time derivative of $|\psi\rangle\langle\psi|$ gives

$$\frac{\partial|\psi\rangle\langle\psi|}{\partial t} = \frac{\partial|\psi\rangle}{\partial t}\langle\psi| + |\psi\rangle\frac{\partial\langle\psi|}{\partial t}$$

$$= -\,\mathrm{i}\hat{\mathcal{H}}|\psi\rangle\langle\psi| + \mathrm{i}|\psi\rangle\langle\psi|\hat{\mathcal{H}} \tag{1.30}$$

$$= -\,\mathrm{i}\left[\hat{\mathcal{H}}, |\psi\rangle\langle\psi|\right], \tag{1.31}$$

where the time-dependent Schrödinger equation (Equation (A.3)) has been used to obtain Equation (1.30). The ensemble average of Equation (1.31) gives the equation of motion that describes the evolution of the density operator

$$\frac{\partial}{\partial t}\hat{\rho}(t) = -\mathrm{i}\left[\hat{\mathcal{H}}, \hat{\rho}(t)\right]. \tag{1.32}$$

This is the Liouville–von Neumann equation, and has the formal solution

$$\hat{\rho}(t) = \hat{U}(t)\hat{\rho}(0)\hat{U}^{-1}(t), \;\; \text{where} \; \frac{\partial}{\partial t}\hat{U}(t) = -\mathrm{i}\hat{\mathcal{H}}(t)\hat{U}(t). \tag{1.33}$$

The operator $\hat{U}(t)$ is termed the propagator. Three classes of Hamiltonian can be distinguished. First, if $\hat{\mathcal{H}}(t)$ is time independent, the propagator is

$$\hat{U}(t) = \exp\left\{-\mathrm{i}\hat{\mathcal{H}}t\right\}. \tag{1.34}$$

Second, if the Hamiltonian is time dependent, but commutes with itself at different times, $\left[\hat{\mathcal{H}}(t'), \hat{\mathcal{H}}(t'')\right] = 0$, it is said to be dynamically-inhomogeneous in the terminology of Maricq and Waugh.[13] With this condition fulfilled, the propagator is

$$\hat{U}(t) = \exp\left\{-\mathrm{i}\int_0^t \hat{\mathcal{H}}(t')\mathrm{d}t'\right\}. \tag{1.35}$$

The final class occurs when the Hamiltonian is time dependent but does not commute with itself at different times, and is termed homogeneous. In this case, the propagator is

evaluated according to

$$\hat{U}(t) = \hat{\mathcal{T}} \exp\left\{-\mathrm{i} \int_0^t \hat{\mathcal{H}}(t')dt'\right\} \tag{1.36}$$

$$= \prod_{n=0,\ \lim \Delta t \to 0}^{n=t/\Delta t} \exp\left\{\mathrm{i}\hat{\mathcal{H}}(n\Delta t)\Delta t\right\} \tag{1.37}$$

$$\overset{n=t/\Delta t}{\underset{\lim \Delta t \to 0}{=}} \exp\left\{\mathrm{i}\hat{\mathcal{H}}(n\Delta t)\Delta t\right\} \ldots \exp\left\{\mathrm{i}\hat{\mathcal{H}}(2\Delta t)\Delta t\right\} \exp\left\{\mathrm{i}\hat{\mathcal{H}}(\Delta t)\Delta t\right\} \exp\left\{\mathrm{i}\hat{\mathcal{H}}(0)\Delta t\right\}. \tag{1.38}$$

In Equation (1.36), $\hat{\mathcal{T}}$ is the Dyson time ordering operator that ensures Equation (1.36) is evaluated according to the time-ordered product in Equations (1.37) and (1.38). Equations (1.33) to (1.37) provide a strategy for computing the evolution the density operator over time, from which any property of the ensemble of spins can be calculated using Equation (1.23).

For a time-independent Hamiltonian $\hat{\mathcal{H}}$, if the density operator is represented using the eigenfunctions of $\hat{\mathcal{H}}$, a coherence between the nth and m^{th} eigenstates ($|n\rangle$ and $|m\rangle$) is represented by the element ρ_{nm} of the matrix representation of the density operator. Over time, the ρ_{nm} coherence evolves and simply acquires a phase since

$$\begin{aligned}
\rho_{nm}(t) &= \langle n| \exp\left(-\mathrm{i}\hat{\mathcal{H}}t\right) \hat{\rho}(0) \exp\left(\mathrm{i}\hat{\mathcal{H}}t\right) |m\rangle \\
&= \sum_j \sum_k \langle n| \exp\left(-\mathrm{i}\hat{\mathcal{H}}t\right) |j\rangle\langle j|\hat{\rho}(0)|k\rangle\langle k| \exp\left(\mathrm{i}\hat{\mathcal{H}}t\right) |m\rangle \\
&= \exp\left(-\mathrm{i}\langle \phi_n|\hat{\mathcal{H}}|\phi_n\rangle t\right) \rho_{nm}(0) \exp\left(\mathrm{i}\langle \phi_m|\hat{\mathcal{H}}|\phi_m\rangle t\right) \\
&= \rho_{nm}(0) \exp\left(\mathrm{i}\left(\langle \phi_m|\hat{\mathcal{H}}|\phi_m\rangle - \langle \phi_n|\hat{\mathcal{H}}|\phi_n\rangle\right)t\right),
\end{aligned} \tag{1.39}$$

and the coherence is phase-modulated at a frequency equal to the separation in energy of the eigenstates. If the Hamiltonian is time dependent, but heterogeneous, then the phase acquired by a coherence between the nth and m^{th} eigenstate is evaluated by the integral over time of the energy separation of the eigenstates $\int_0^t \left(\langle \phi_m|\hat{\mathcal{H}}(t')|\phi_m\rangle - \langle \phi_n|\hat{\mathcal{H}}(t')|\phi_n\rangle\right) \mathrm{d}t'$.

1.3.1 Average Hamiltonian theory

The propagator for a homogeneous Hamiltonian cannot be calculated analytically. In this case, an approach for approximating the propagator $\hat{U}(t)$, that often gives useful insight into the time evolution of the spin system, assumes that over a short time period from

$t = 0$ to $t = t_a$, $\hat{U}(t_a)$ can be written in the form

$$\hat{U}(t_a) = \exp\left\{-\mathrm{i}\overline{\hat{\mathcal{H}}}t_a\right\} \tag{1.40}$$

$$\overline{\hat{\mathcal{H}}} = \overline{\hat{\mathcal{H}}^{(1)}} + \overline{\hat{\mathcal{H}}^{(2)}} + \overline{\hat{\mathcal{H}}^{(3)}} + \dots , \tag{1.41}$$

where $\overline{\hat{\mathcal{H}}}$ is the average Hamiltonian over the time period t_a. Equation (1.41) is the Magnus expansion of the average Hamiltonian, and the terms $\overline{\hat{\mathcal{H}}^{(i)}}$ are referred to as the ith-order average Hamiltonian. The first three terms in the Magnus expansion are evaluated by[14]

$$\overline{\hat{\mathcal{H}}^{(1)}} = \frac{1}{t_a} \int_0^{t_a} \mathrm{d}t \, \hat{\mathcal{H}}(t), \tag{1.42}$$

$$\overline{\hat{\mathcal{H}}^{(2)}} = -\frac{\mathrm{i}}{2t_a} \int_0^{t_a} \mathrm{d}t_2 \int_0^{t_2} \mathrm{d}t_1 \left[\hat{\mathcal{H}}(t_2), \hat{\mathcal{H}}(t_1)\right], \tag{1.43}$$

$$\overline{\hat{\mathcal{H}}^{(3)}} = -\frac{1}{6t_a} \int_0^{t_a} \mathrm{d}t_3 \int_0^{t_3} \mathrm{d}t_2 \int_0^{t_2} \mathrm{d}t_1 \left\{\left[\hat{\mathcal{H}}(t_3), \left[\hat{\mathcal{H}}(t_2), \mathcal{H}(t_1)\right]\right] + \left[\left[\hat{\mathcal{H}}(t_3), \hat{\mathcal{H}}(t_2)\right], \hat{\mathcal{H}}(t_1)\right]\right\}. \tag{1.44}$$

The first-order term is the time-averaged Hamiltonian, whereas the higher-order terms involve more complicated commutators of the Hamiltonian at different times.

The propagator $\hat{U}(t_a)$ is approximated using the first few terms of the Magnus expansion in the exponential of Equation (1.40). However, the Magnus expansion is only useful if the series converges rapidly, ideally at the first or second term. To ensure that this occurs, the Hamiltonian is divided into a dominant part $\hat{\mathcal{H}}_0$, for which the corresponding propagator $\hat{U}_0(t)$ is determined analytically using Equation (1.34) or (1.35), and a smaller perturbing Hamiltonian $\hat{\mathcal{H}}_1$: $\hat{\mathcal{H}} = \hat{\mathcal{H}}_0 + \hat{\mathcal{H}}_1$.[†] The total propagator $\hat{U}(t)$ is factored into the product of two individual operators

$$\hat{U}(t) = \hat{U}_0(t)\hat{\mathcal{L}}(t). \tag{1.45}$$

The form of $\hat{\mathcal{L}}(t)$ is derived as follows,[16] using Equation (1.33) with $\hat{\mathcal{H}} = \hat{\mathcal{H}}_0 + \hat{\mathcal{H}}_1$

$$-\mathrm{i}\left[\hat{\mathcal{H}}_0(t) + \hat{\mathcal{H}}_1(t)\right]\hat{U}(t) = \frac{\partial \hat{U}(t)}{\partial t}$$

$$-\mathrm{i}\hat{\mathcal{H}}_0(t)\hat{U}(t) - \mathrm{i}\hat{\mathcal{H}}_1(t)\hat{U}(t) = \frac{\partial U_0(t)}{\partial t}\hat{\mathcal{L}}(t) + \hat{U}_0(t)\frac{\partial \hat{\mathcal{L}}(t)}{\partial t}. \tag{1.46}$$

[†]Small is usually taken to mean $\|\hat{\mathcal{H}}_1\|t \ll 1$, where $\|\hat{\mathcal{H}}_1\| = \left\{\mathrm{Tr}\left[\hat{\mathcal{H}}_1^2\right]\right\}^{1/2}$.[2] A detailed discussion of the convergence of the Magnus expansion has been given by Maricq.[15]

But from Equation (1.33), $\partial \hat{U}_0(t)/\partial t = -i\hat{\mathcal{H}}_0(t)\hat{U}_0(t)$, and so

$$-i\hat{\mathcal{H}}_1(t)\hat{U}_0(t)\hat{\mathcal{L}}(t) = \hat{U}_0(t)\frac{\partial \hat{\mathcal{L}}(t)}{\partial t}$$

$$-i\hat{U}_0^{-1}(t)\hat{\mathcal{H}}_1(t)\hat{U}_0(t)\hat{\mathcal{L}}(t) = \frac{\partial \hat{\mathcal{L}}(t)}{\partial t}$$

$$-i\hat{\mathcal{H}}_1^*(t)\hat{\mathcal{L}}(t) = \frac{\partial \hat{\mathcal{L}}(t)}{\partial t} . \tag{1.47}$$

The formal integral of Equation (1.47) is

$$\hat{\mathcal{L}}(t) = \hat{\mathcal{T}} \exp\left\{ -i \int_0^t \hat{\mathcal{H}}^*(t')\mathrm{d}t' \right\}. \tag{1.48}$$

The Hamiltonian $\hat{\mathcal{H}}_1^*$ is called the interaction-frame Hamiltonian, and corresponds to $\hat{\mathcal{H}}_1$ as viewed in the frame of reference that moves with the evolution of the system due to $\hat{\mathcal{H}}_0$. The interaction-frame Hamiltonian $\hat{\mathcal{H}}_1^*$ is written as an average Hamiltonian $\overline{\hat{\mathcal{H}}_1^*}$, and its Magnus expansion evaluated using Equations (1.42) to (1.44) (with $\hat{\mathcal{H}}_1^*(t)$ rather than $\hat{\mathcal{H}}(t)$). Only the smaller part of the total Hamiltonian is used in this average, so the Magnus expansion converges much more rapidly than the Magnus expansion for $\hat{\mathcal{H}}_0(t) + \hat{\mathcal{H}}_1(t)$ over the same time period.

Calculation of the propagator $\hat{U}(t)$ is simplified if (*i*) $\hat{\mathcal{H}}_0(t)$ is periodic over a time t_c ($\hat{\mathcal{H}}_0(t) = \hat{\mathcal{H}}_0(t + Nt_c)$) and (*ii*) cyclic over the same time period so that $\hat{U}_0(t_c) = \hat{\mathbf{1}}$. When these conditions are fulfilled, the propagator is reduced to $\hat{U}(Nt_c) = \hat{\mathbf{1}}\mathcal{L}(Nt_c) = \left[\hat{U}^*(t_c)\right]^N$, where $\mathcal{L}(t_c)$ has been relabelled as $\hat{U}^*(t_c)$. It follows that if measurements are made stroboscopically at time intervals of t_c, the evolution of the system only depends on the interaction-frame average Hamiltonian $\overline{\hat{\mathcal{H}}_1^*}$.[16]

An interaction-frame density operator $\hat{\rho}^*(t)$ can also be defined as

$$\hat{\rho}^*(t) = \hat{U}_0^{-1}(t)\hat{\rho}(t)\hat{U}_0(t). \tag{1.49}$$

The Liouville–von Neumann equation, Equation (1.32), can be written in terms of $\hat{\rho}^*$ to give

$$-i\left[\left(\hat{\mathcal{H}}_0 + \hat{\mathcal{H}}_1\right), \hat{U}_0\hat{\rho}^*\hat{U}_0^{-1}\right] = \frac{\partial}{\partial t}\hat{U}_0\hat{\rho}^*\hat{U}_0^{-1}$$

$$-i\left[\hat{\mathcal{H}}_0, \hat{U}_0\hat{\rho}^*\hat{U}_0^{-1}\right] - i\left[\hat{\mathcal{H}}_1, \hat{U}_0\hat{\rho}^*\hat{U}_0^{-1}\right] = \frac{\partial}{\partial t}\hat{U}_0\hat{\rho}^*\hat{U}_0^{-1}. \tag{1.50}$$

The product rule is used to evaluate the derivative of the right hand side of Equation (1.50)

to obtain

$$-\mathrm{i}\left[\hat{\mathcal{H}}_0, \hat{U}_0 \hat{\rho}^* \hat{U}_0^{-1}\right] - \mathrm{i}\left[\hat{\mathcal{H}}_1, \hat{U}_0 \hat{\rho}^* \hat{U}_0^{-1}\right] = \frac{\partial \hat{U}_0}{\partial t} \hat{\rho}^* \hat{U}_0^{-1} + \hat{U}_0 \frac{\partial \hat{\rho}^*}{\partial t} \hat{U}_0^{-1} + \hat{U}_0 \hat{\rho}^* \frac{\partial \hat{U}_0^{-1}}{\partial t}$$

$$= -\mathrm{i}\hat{\mathcal{H}}_0 \hat{U}_0 \hat{\rho}^* \hat{U}_0^{-1} + \hat{U}_0 \frac{\partial \hat{\rho}^*}{\partial t} \hat{U}_0^{-1} + \mathrm{i}\hat{U}_0 \hat{\rho}^* \hat{U}_0^{-1} \hat{\mathcal{H}}_0$$

$$-\mathrm{i}\left[\hat{\mathcal{H}}_1^*, \hat{\rho}^*\right] = \frac{\partial \hat{\rho}^*}{\partial t}. \tag{1.51}$$

This demonstrates that, as viewed within this interaction frame, $\hat{\rho}^*$ evolves due to $\hat{\mathcal{H}}_1^*$ as prescribed by the Liouville-von Neumann equation.

Both the transformation into the interaction frame and the evaluation of the average Hamiltonian is used several times in this dissertation to simplify the analysis of NMR experiments.

1.4   Multiple-spin systems

Often a group of coupled nuclei is of interest. The methods of the earlier sections are applied to multiple-spin systems by using a Zeeman product basis. This is generated by the direct product (represented by $\otimes$) of the Zeeman states of the constituent nuclei in the spin system. For an N-spin system, this gives the states

$$|m_1 m_2 \cdots m_N\rangle = |I_1, m_1\rangle \otimes |I_2, m_2\rangle \otimes \cdots \otimes |I_N, m_N\rangle. \tag{1.52}$$

There will be a total of $\prod_{i=1}^{N}(2I_i + 1)$ product states. Each product state is an eigenfunction of the z-component of the angular momentum operator of the ith spin $\hat{I}_{z,i}$

$$\hat{I}_{z,i}|m_1 m_2 \cdots m_N\rangle = m_i |m_1 m_2 \cdots m_N\rangle, \tag{1.53}$$

and also of the z-component of the total spin angular momentum operator $\hat{I}_z = \sum_i \hat{I}_{z,i}$

$$\hat{I}_z|m_1 m_2 \cdots m_N\rangle = (m_1 + m_2 + \cdots + m_N)|m_1 m_2 \cdots m_N\rangle. \tag{1.54}$$

The product Zeeman basis is used to represent operators, and the evolution of the density operator is determined using the same method as for a single-spin.
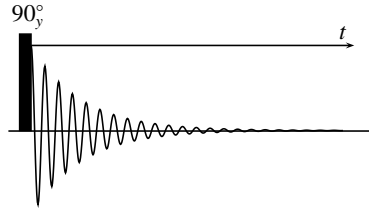
Figure 1.1: Representation of the one-pulse experiment. The black rectangle represents a pulse of RF irradiation. The duration of the pulse is indicated above in terms of the rotation of the magnetization caused by it, and the phase (φ) of the RF irradiation is shown as a subscript to this number. The oscillating line indicates that the NMR signal is detected immediately after the pulse, as a function of time t.

Under the high temperature approximation, the density operator at thermal equilibrium is

$$\hat{\rho}_{\text{eq}} = \frac{1}{Z}\left(\hat{\mathbf{1}} + \beta_1\hat{I}_{z,1} + \beta_2\hat{I}_{z,2} + \cdots + \beta_N\hat{I}_{z,N}\right), \quad \text{where,} \quad \beta_i = \frac{-\hbar\omega_0^i}{kT} \tag{1.55}$$

and ω_0^i is the Larmor frequency of the ith spin. Usually the identity operator and Boltzmann factors β_i are omitted from Equation (1.55).

1.5 A radio-frequency pulse

The simplest NMR experiment starts with the spin system at thermal equilibrium and a 'pulse' of radio-frequency (RF) radiation is applied to the sample. Once the irradiation has ended, the current induced in a coil surrounding the sample is recorded as the NMR signal. This experiment is illustrated by the pulse sequence in Figure 1.1.

The sample is located inside a small cylindrical coil, assumed here to have its cylindrical axis parallel to the x-axis of the laboratory frame, which is defined by the unit vectors $\boldsymbol{i}$, $\boldsymbol{j}$ and $\boldsymbol{k}$ parallel to the $x-$, $y-$ and $z-$directions respectively.

1.5.1 The radio-frequency field Hamiltonian

When an oscillating electric current is passed through the coil, an oscillating magnetic field $\mathbf{B}_1(t)$ is generated along the laboratory-frame x-axis, with maximum field strength B_1, that is described by

$$\mathbf{B}_1(t) = \boldsymbol{i}B_1 \cos\left(|\omega_{\text{RF}}|t + \varphi_{\text{RF}}\right), \tag{1.56}$$

where φ_{RF} is the initial RF phase (at $t = 0$) of the field oscillating with angular frequency $|\omega_{\text{RF}}|$. The RF Hamiltonian is $\hat{\mathcal{H}}_{\text{RF}} = -\gamma\hat{\boldsymbol{I}} \cdot \mathbf{B}_1$, and the $\mathbf{B}_1$ field may be decomposed into

two counter-rotating components

$$\mathbf{B}_{1,\mathrm{A}}(t) = \tfrac{1}{2} B_1 \left\{ \boldsymbol{i} \cos(|\omega_{\mathrm{RF}}|t + \varphi_{\mathrm{RF}}) + \boldsymbol{j} \sin(|\omega_{\mathrm{RF}}|t + \varphi_{\mathrm{RF}}) \right\}, \tag{1.57}$$

$$\mathbf{B}_{1,\mathrm{B}}(t) = \tfrac{1}{2} B_1 \left\{ \boldsymbol{i} \cos(|\omega_{\mathrm{RF}}|t + \varphi_{\mathrm{RF}}) - \boldsymbol{j} \sin(|\omega_{\mathrm{RF}}|t + \varphi_{\mathrm{RF}}) \right\}. \tag{1.58}$$

Using rotation operators, the total Hamiltonian $\hat{\mathcal{H}}_{\mathrm{total}}$ of the spin system consists of the Zeeman Hamiltonian $\hat{\mathcal{H}}_{\mathrm{Z}}$ and an RF Hamiltonian $\hat{\mathcal{H}}_{\mathrm{RF}}$

$$\hat{\mathcal{H}}_{\mathrm{total}} = \hat{\mathcal{H}}_{\mathrm{Z}} + \hat{\mathcal{H}}_{\mathrm{RF}}(t) \tag{1.59}$$

$$= \omega_0 \hat{I}_z - \tfrac{1}{2}\gamma B_1 \hat{R}_z(|\omega_{\mathrm{RF}}|t + \varphi_{\mathrm{RF}})\hat{I}_x \hat{R}_z^{-1}(|\omega_{\mathrm{RF}}|t + \varphi_{\mathrm{RF}})$$

$$- \tfrac{1}{2}\gamma B_1 \hat{R}_z^{-1}(|\omega_{\mathrm{RF}}|t + \varphi_{\mathrm{RF}})\hat{I}_x \hat{R}_z(|\omega_{\mathrm{RF}}|t + \varphi_{\mathrm{RF}}). \tag{1.60}$$

1.5.2 The rotating frame

Interpretation of the effect of an RF pulse is simplified by transforming the laboratory frame Hamiltonian into to a new frame of reference that is rotating about the laboratory frame z-axis at a frequency ω_{ref} - this is the rotating frame.

The transformation to the rotating frame is equivalent to dividing the Hamiltonian into two parts ($\hat{\mathcal{H}}_{\mathrm{total}} = \hat{\mathcal{H}}_0 + \hat{\mathcal{H}}_1$): a dominant part $\hat{\mathcal{H}}_0 = \omega_{\mathrm{ref}}\hat{I}_z$ and smaller component $\hat{\mathcal{H}}_1 = (\omega_0 - \omega_{\mathrm{ref}})\hat{I}_z + \hat{\mathcal{H}}_{\mathrm{RF}}$, and transforming into the interaction frame of the dominant Hamiltonian as described in the Section 1.3.1. The value of ω_{ref} is chosen to have the same *magnitude* as $|\omega_{\mathrm{RF}}|$, and the opposite *sign* as the gyromagnetic ratio γ, to ensure that that $\hat{\mathcal{H}}_1$ is small compared with $\hat{\mathcal{H}}_0$.[17] The propagator due to the dominant $\hat{\mathcal{H}}_0 = \omega_{\mathrm{ref}}\hat{I}_z$ term is $\hat{U}_0(t) = \hat{R}_z(\omega_{\mathrm{ref}}t + \phi_{\mathrm{ref}})$, where ϕ_{ref} accounts for an initial phase of the rotating frame at $t = 0$.

The rotating-frame Hamiltonian $\hat{\tilde{\mathcal{H}}}$ is defined by $\hat{\tilde{\mathcal{H}}} = \hat{U}_0^{-1}(t)\hat{\mathcal{H}}_1\hat{U}_0(t)$. This gives

$$\hat{\tilde{\mathcal{H}}} = \Omega\hat{I}_z - \tfrac{1}{2}\gamma B_1 \hat{R}_z \left(|\omega_{\mathrm{RF}}|t - \omega_{\mathrm{ref}}t + \varphi_{\mathrm{RF}} - \phi_{\mathrm{ref}}\right) \hat{I}_x \hat{R}_z^{-1} \left(|\omega_{\mathrm{RF}}|t - \omega_{\mathrm{ref}}t + \varphi_{\mathrm{RF}} - \phi_{\mathrm{ref}}\right)$$

$$- \tfrac{1}{2}\gamma B_1 \hat{R}_z^{-1} \left(|\omega_{\mathrm{RF}}|t + \omega_{\mathrm{ref}}t + \varphi_{\mathrm{RF}} + \phi_{\mathrm{ref}}\right) \hat{I}_x \hat{R}_z \left(|\omega_{\mathrm{RF}}|t + \omega_{\mathrm{ref}}t + \varphi_{\mathrm{RF}} + \phi_{\mathrm{ref}}\right), \tag{1.61}$$

where $\Omega = \omega_0 - \omega_{\mathrm{ref}}$ is the offset frequency. With $\omega_{\mathrm{ref}} = -(\gamma/|\gamma|)|\omega_{\mathrm{RF}}|$, the rotating-frame Hamiltonian is accurately approximated by the first-order average Hamiltonian (Equation (1.42)) calculated over the one period $t_{\mathrm{c}} = 2\pi/|\omega_{\mathrm{RF}}|$, where $\hat{\mathcal{H}}(t + t_{\mathrm{c}}) = \hat{\mathcal{H}}(t)$. The time-dependent term in Equation (1.61) (the second term for $\gamma > 0$, and the third term for $\gamma < 0$) will not contribute to the first-order average Hamiltonian, and by

defining $\phi_{\mathrm{p}} = -(\gamma/|\gamma|)\varphi_{\mathrm{RF}}$, the first-order average Hamiltonian can be written in a form independent of the sign of γ as[17]

$$\overline{\tilde{\hat{\mathcal{H}}}^{(1)}} = \Omega\hat{I}_z - \tfrac{1}{2}\gamma B_1 \hat{R}_z(\phi_{\mathrm{p}} - \phi_{\mathrm{ref}})\hat{I}_x\hat{R}_z^{-1}(\phi_{\mathrm{p}} - \phi_{\mathrm{ref}}), \tag{1.62}$$

For this reason, the rotating-frame RF Hamiltonian is usually written with only the term that affects the spin system to first-order:

$$\tilde{\hat{\mathcal{H}}}_{\mathrm{RF}} = -\tfrac{1}{2}\gamma B_1 \hat{R}_z(\phi_{\mathrm{p}} - \phi_{\mathrm{ref}})\hat{I}_x\hat{R}_z^{-1}(\phi_{\mathrm{p}} - \phi_{\mathrm{ref}}). \tag{1.63}$$

Hereafter, the convention that $\phi_{\mathrm{ref}} = \pi$ if $\gamma > 0$ and $\phi_{\mathrm{ref}} = 0$ if $\gamma < 0$ is applied, and the quantity $\omega_1 = |\tfrac{1}{2}\gamma B_1|$ is defined as the RF field strength. The rotating-frame Hamiltonian is given by

$$\tilde{\hat{\mathcal{H}}} = \Omega\hat{I}_z + \omega_1 \hat{R}_z(\phi_{\mathrm{p}})\hat{I}_x\hat{R}_z^{-1}(\phi_{\mathrm{p}}), \tag{1.64}$$

where the bar and superscript (1) of $\overline{\tilde{\hat{\mathcal{H}}}^{(1)}}$ has been omitted for convenience.

The rotating-frame density operator is $\tilde{\rho} = \hat{U}_0^{-1}(t)\hat{\rho}\hat{U}_0(t)$, which at thermal equilibrium gives $\tilde{\rho}_{\mathrm{eq}} = \hat{I}_z$. As noted Section 1.3.1, as viewed in the rotating frame, the rotating-frame density operator evolves according to the Liouville–von Neumann equation with the rotating-frame Hamiltonian, and this is used to evaluate the effect of RF pulse on $\tilde{\rho}$.

If the pulse is 'on resonance' ($\Omega = 0$), or if the pulse is 'hard' in the sense that $\omega_1 \gg |\Omega|$, the first term in Equation (1.64) is zero, or has a negligible effect on the evolution of the spin system in comparison to the second term. In this case, the rotating-frame density operator at time t is calculated using Equation (1.33), and is

$$\tilde{\rho}(t) = \exp\left[-\mathrm{i}\omega_1 \hat{R}_z(\phi_{\mathrm{p}})\hat{I}_x\hat{R}_z^{-1}(\phi_{\mathrm{p}})t\right]\hat{I}_z\exp\left[+\mathrm{i}\omega_1 \hat{R}_z(\phi_{\mathrm{p}})\hat{I}_x\hat{R}_z^{-1}(\phi_{\mathrm{p}})t\right]. \tag{1.65}$$

This is interpreted geometrically as a rotation of the $\hat{I}_z$ term of $\tilde{\rho}$ about an axis at an angle ϕ_{p} from the x-axis in the xy-plane of the rotating frame. The angle ϕ_{p} is (loosely) referred to as the 'phase of the pulse'; for $\phi_{\mathrm{p}} = 0$ the pulse is called a x-pulse because the rotation is about the x-axis in the rotating frame, and if $\phi_{\mathrm{p}} = 90°$ it is a y-pulse. The angular frequency of the rotation, or nutation, about this axis is ω_1. This is illustrated in Figure 1.2 on the next page.

The magnetic moment operator is $\hat{\boldsymbol{\mu}} = -\gamma\hat{\boldsymbol{I}}$, and the magnetization of sample is calculated by $\boldsymbol{M} = \gamma N_{\mathrm{bulk}}\mathrm{Tr}\left[\hat{\boldsymbol{I}}\hat{\rho}\right]$. If the density operator is expanded in the Cartesian components of the angular momentum operator, the coefficients of the $\hat{I}_x$, $\hat{I}_y$ and $\hat{I}_z$ terms are proportional
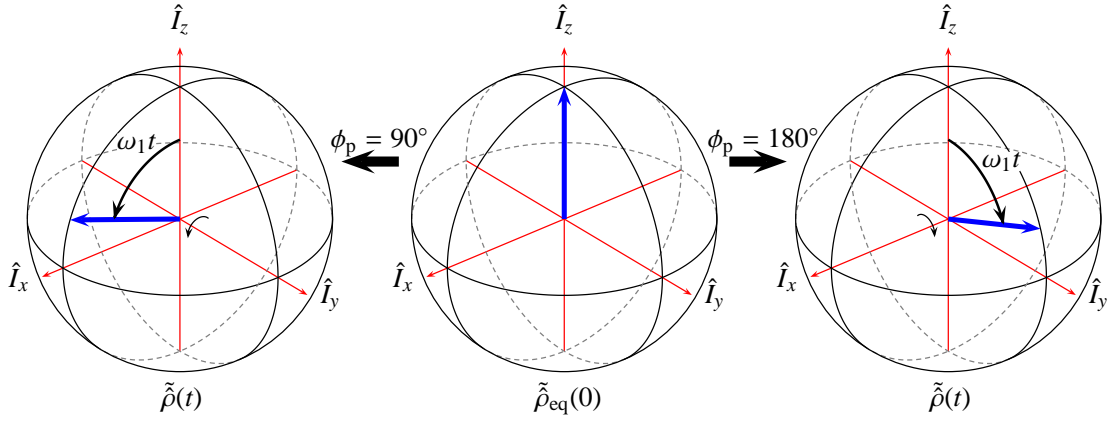
Figure 1.2: Evolution of the density operator due to irradiation by a pulse of duration t and RF field strength ω_1. In the centre, the equilibrium density operator ($\tilde{\hat{\rho}}(0) = \hat{I}_z$) is represented by the vector parallel to the $\hat{I}_z$-direction, the effect of a pulse of RF irradiation with phase $\phi_p = 90°$ and $\phi_p = 180°$ is shown on the left and right hand side respectively.

to the x, y and z components of the magnetization respectively. Therefore the effect of the pulse is to rotate the thermal equilibrium z-magnetization in the same sense as the $\hat{I}_z$ operator.

The angle of rotation caused by a pulse of length τ_p is $\theta_p = \omega_1 \tau_p$. The convention chosen for the value of ϕ_{ref} means that the sense of rotation by RF irradiation is always positive, regardless of the sign of γ (although this choice is arbitrary).

The second-order average Hamiltonian of Equation (1.61) can be evaluated, and this contribution to the rotating-frame Hamiltonian causes the Bloch-Siegert shift.[14,18] For the on-resonance ($\Omega = 0$) case, the second-order average Hamiltonian is $\overline{\tilde{\hat{\mathcal{H}}}^{(2)}} = \left[\omega_1^2 / (2\omega_0) \right] \hat{I}_z$, which has a negligible effect on the spin system under the usual conditions, since ω_1 is usually of the order of kHz whilst ω_0 is many MHz. If the pulse is far off-resonance ($|\Omega| \gg \omega_1$), then the second-order average Hamiltonian is $\overline{\tilde{\hat{\mathcal{H}}}^{(2)}} = \omega_0 \left[\omega_1^2 / \left(\omega_{ref}^2 - \omega_0^2 \right) \right] \hat{I}_z$. In this latter scenario, the effect also tends to be rather small under typical experimental conditions, although the it can become noticeable when irradiation occurs continuously during signal detection.

Hereafter, the ~ symbol is dropped from rotating-frame Hamiltonian $\tilde{\hat{\mathcal{H}}}$ and rotating-frame density operator $\tilde{\hat{\rho}}$, and the rotating frame will be assumed unless otherwise stated.

1.5.3   Free precession in the rotating frame

Once the pulse has ended, the only term in the rotating-frame Hamiltonian is due to the static field $\hat{\mathcal{H}} = \Omega \hat{I}_z$. Assuming that the pulse length is calibrated to give a rotation angle of $\omega_1 \tau_p = 90°$ about the y-axis of the rotating frame, as indicated in Figure 1.1, the density operator at the end of the pulse is $\hat{\rho}(\tau_p) = \hat{I}_x$. If $t = 0$ at the start of the pulse, then following the pulse, the density operator evolves in the rotating frame according to

$$\hat{\rho}(t) = \exp\left[-i\Omega(t - \tau_p)\hat{I}_z\right]\hat{I}_x \exp\left[+i\Omega(t - \tau_p)\hat{I}_z\right] = \hat{I}_x \cos\left(\Omega(t - \tau_p)\right) + \hat{I}_y \sin\left(\Omega(t - \tau_p)\right);$$
(1.66)

that is, the density operator is rotated about the z-axis at the offset frequency Ω; equivalently, this can be viewed as the magnetization precessing about the z-axis at this frequency.

At the end of the $90°_y$-pulse $\hat{\rho}(\tau_p) = \hat{I}_x$, and because $\hat{I}_x = \frac{1}{2}\left(\hat{I}_+ + \hat{I}_-\right)$, the matrix representation of density operator contains $(+1)$- and (-1)-quantum coherences. Under evolution due to $\hat{\mathcal{H}} = \Omega \hat{I}_z$, the $(+1)$- and (-1)-quantum coherences acquire phases $-\Omega(t - \tau_p)$ and $\Omega(t - \tau_p)$ respectively

$$\hat{\rho}(t) = \frac{1}{2}\exp\left[-i\Omega(t - \tau_p)\hat{I}_z\right]\left(\hat{I}_+ + \hat{I}_-\right)\exp\left[+i\Omega(t - \tau_p)\hat{I}_z\right] = \frac{1}{2}\left(\hat{I}_+ e^{-i\Omega(t-\tau_p)} + \hat{I}_- e^{+i\Omega(t-\tau_p)}\right)$$
(1.67)

Thus, evolution of the (-1)-quantum coherences in the complex plane parallels the evolution of the magnetization in the rotating frame.

1.6   Relaxation

In practice, free precession of the coherences does not continue indefinitely. Following any disturbance of the spin system from equilibrium by RF-irradiation, the density operator will, over time, return to thermal equilibrium through the process of relaxation. The two most important forms of relaxation are spin-lattice and spin-spin relaxation. First, spin-lattice (longitudinal) relaxation is the return of the spin populations back to their thermal equilibrium values, determined by the Boltzmann distribution. Second, spin-spin (transverse) relaxation is the process by which coherences decay to zero over time.

For isolated spin-1/2 nuclei, each process can often be characterised by a single time constant: T_1 for spin-lattice relaxation and T_2 for spin-spin relaxation, with the populations and coherences both decaying exponentially back to their thermal equilibrium

values. A detailed treatment of relaxation requires the use of time-dependent perturbation theory, first introduced by Bloembergen, Purcell and Pound,[19] but this is not described here, as relaxation effects are not explicitly dealt with in this work.

For proper operation of a pulse sequence, the spin system needs to be in the same equilibrium state at the start of each experiment. The spin-lattice relaxation behaviour determines the time that must be inserted between repeating an experiment. As will be discussed in the following section, the NMR signal is generated by coherences, so the spin-spin relaxation determines how rapidly the signal will decay. The spin-spin relaxation also limits the duration of delays that can be inserted between the initial excitation of coherences and signal detection.

1.7 Signal detection and Fourier transform NMR

The response of the spin system to the RF pulse is recorded by the current induced in a coil surrounding the sample. Assuming the cylindrical axis of the coil is parallel to the x-axis of the laboratory frame, the current (which is the signal measured in the experiment) is proportional to the time derivative of the magnetization parallel to the x-axis, in accordance with the Faraday-Lenz law of electromagnetic induction. Since the magnetization parallel to the x-axis is calculated by

$$M_x(t) = \gamma N_{\text{bulk}} \text{Tr} \left[\hat{I}_x \hat{\rho}_{\text{lab}}(t) \right] = \frac{\gamma}{2} N_{\text{bulk}} \text{Tr} \left[\left(\hat{I}_+ + \hat{I}_- \right) \hat{\rho}_{\text{lab}} \right], \tag{1.68}$$

where $\hat{\rho}_{\text{lab}}$ is the laboratory frame density operator, only coherence orders of $p_{nm} = \pm 1$ (single-quantum coherences) are detectable, regardless of whether higher-order coherences have been generated by the point of signal detection.

All modern spectrometers perform Fourier transform NMR[20] and use quadrature receivers. This can be *thought of* as having two orthogonal detectors in the rotating frame, with the x_{rec}-axis oriented at an angle ϕ_{rec} with respect to the rotating frame x-axis as illustrated in Figure 1.3.[17] For example, if $\phi_{\text{rec}} = 0$ the detectors are oriented along the rotating frame x- and y-axes.

A complex signal is recorded with the real part corresponding to the magnetization along the x_{rec}-axis and the imaginary part to the magnetization along the y_{rec}-axis: $s(t) \propto M_{x_{\text{rec}}} + i M_{y_{\text{rec}}}$. Since the raising operator $\hat{I}_+ = \hat{I}_x + i\hat{I}_y$, the detected signal is proportional to $\langle \hat{R}_z(\phi_{\text{rec}}) \hat{I}_+ \hat{R}_z^{-1}(\phi_{\text{rec}}) \rangle(t)$, where rotation operators have been used to
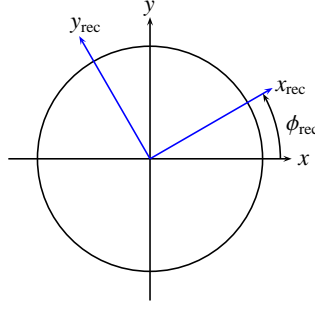
Figure 1.3: Orientation of the quadrature detector with respect to the rotating-frame axes, labelled x and y. The receiver orientation is specified by the angle ϕ_{rec}.

account for the receiver phase. The signal is evaluated from the rotating-frame density operator by

$$s(t) = \text{Tr}\left[e^{-i\phi_{\text{rec}}\hat{I}_z}\hat{I}_+e^{i\phi_{\text{rec}}\hat{I}_z}\hat{\rho}(t)\right] = \text{Tr}\left[\hat{I}_+e^{-i\phi_{\text{rec}}}\hat{\rho}(t)\right]. \tag{1.69}$$

For simplicity, proportionality constants have been neglected. The signal is digitized for storage on the spectrometer computer, and an additional phase shift, called the post-digitizer phase shift $-\phi_{\text{dig}}$, is applied to the digitized signal. Provided the quadrature receiver behaves ideally, the ϕ_{rec} and ϕ_{dig} phases have exactly the same effect. In the following calculations ϕ_{dig} is set to zero.

Using the example of an ensemble of isolated spins, following a 90°_y-pulse the rotating-frame density operator is $\hat{\rho}(0) = \hat{I}_x$. With $t = 0$ at the end of the pulse, the resulting signal is

$$\begin{aligned}
s(t) &= \text{Tr}\left[\hat{I}_+\left(e^{-i\Omega t\hat{I}_z}\hat{I}_xe^{+i\Omega t\hat{I}_z}\right)\right]e^{-i\phi_{\text{rec}}} \\
&= \tfrac{1}{2}\text{Tr}\left[\hat{I}_+e^{-i\Omega t\hat{I}_z}\left(\hat{I}_+ + \hat{I}_-\right)e^{+i\Omega t\hat{I}_z}\right]e^{-i\phi_{\text{rec}}} \\
&= \tfrac{1}{2}\text{Tr}\left[\hat{I}_+\hat{I}_-\right]e^{i\Omega t}e^{-i\phi_{\text{rec}}} \\
s(t) &= ce^{i\Omega t}e^{-i\phi_{\text{rec}}},
\end{aligned} \tag{1.70}$$

where $\text{Tr}\left[\hat{I}_+\hat{I}_+\right] = 0$ has been used and the constant c has been included to account for the various factors that affect the signal intensity. Thus, it is the (-1)-quantum coherences that are detected and the signal, often referred to as the free induction decay (FID), oscillates at the offset frequency Ω. In addition, account must be taken for the effects of relaxation of the coherences, which usually occurs as an exponential decay characterised by the time constant T_2, to give

$$s(t) = e^{-i\phi_{\text{rec}}}\sum_j c_j \exp\left(i\Omega^{(j)}t\right)\exp(-t/T_2^{(j)}). \tag{1.71}$$
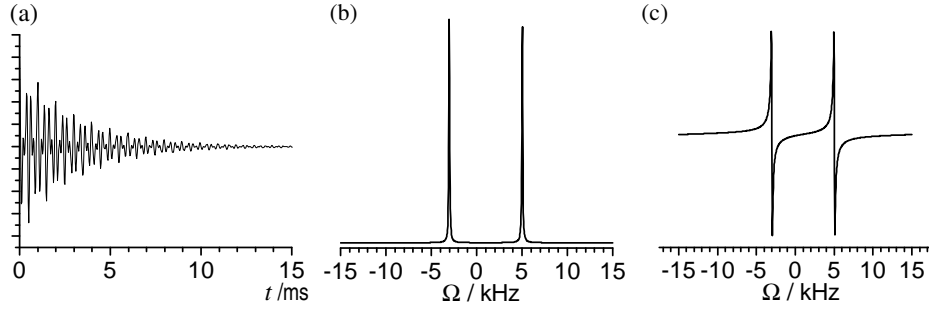
Figure 1.4: (a) The real part of a simulated FID and (b) the corresponding absorption and (c) dispersion Lorentzian lineshapes following Fourier transformation of the time-domain signal.

In Equation (1.71), allowance has been made for the presence of more than one spin environment in the sample by summing over these sites (the cause of the different environments is described in Section 1.9). Each site has a different offset frequency $\Omega^{(j)}$, spin-spin relaxation time constant $T_2^{(j)}$ and weighting c_j. The FID is not in a convenient form for presentation and analysis. Instead, Fourier transformation of the signal is performed and produces a spectrum containing peaks at the rotating-frame offset frequencies $\Omega^{(j)}$ of each different spin environments in the sample. The form of this spectrum $S(\omega)$ is

$$
\begin{aligned}
S(\omega) &= e^{-i\phi_{rec}} \int_0^\infty \sum_j c_j \exp\left(i\Omega^{(j)}t\right) \exp\left(-t/T_2^{(j)}\right) \exp\left(-i\omega t\right) dt \\
&= e^{-i\phi_{rec}} \sum_j c_j \left(\mathcal{A}_j(\omega) + i\mathcal{D}_i(\omega)\right),
\end{aligned} \tag{1.72}
$$

where $\mathcal{A}_j(\omega)$ and $\mathcal{D}_j(\omega)$ are the absoption and dispersion Lorentzian lineshapes defined as

$$
\mathcal{A}_j(\omega) = \frac{T_2^{(j)}}{1 + \left(\omega - \Omega^{(j)}\right)^2 T_2^{(j)2}} \qquad \mathcal{D}_j(\omega) = \frac{-\left(\omega - \Omega^{(j)}\right) T_2^{(j)2}}{1 + \left(\omega - \Omega^{(j)}\right)^2 T_2^{(j)2}}. \tag{1.73}
$$

It is usual to plot the absorption lineshapes in the spectrum, because the dispersion lineshape has a broad base that obscures other peaks in the spectrum. Figure 1.4 compares the FID and the absorption and dispersion mode spectra from Fourier transformation of the FID.

1.8   Signal processing

1.8.1   Discrete sampling of the NMR signal

Experimentally, the signal is sampled at discrete time points during digitization of the signal. The time points for detection are separated by the dwell time τ_{dwell}. The signal is processed using a discrete Fourier transform, defined as[21]

$$S(\omega_n) = \frac{1}{N} \sum_{k=0}^{N-1} s(k\tau_{\text{dwell}}) \exp\left(-\mathrm{i}2\pi kn/N\right); \qquad \omega_n = \frac{n}{N\tau_{\text{dwell}}} \text{ where } \tfrac{-N}{2} \leq n \leq \tfrac{N}{2} - 1.$$

(1.74)

In the resulting spectrum, frequency data points are spaced at intervals of $1/(N\tau_{\text{dwell}})$ and cover the frequency range $-1/(2\tau_{\text{dwell}})$ to $(N/2 - 1)/(N\tau_{\text{dwell}})$. The frequency span of the spectrum is referred to as the spectral width. According to the Nyquist theorem, frequencies that differ by multiples of $1/\tau_{\text{dwell}}$ are indistinguishable from one another. Consequently, signals (and noise components) that lie outside the spectral window are aliased, or 'folded', into the spectrum and appear at an erroneous frequency. A combination of analogue and digital filtering is used to prevent aliasing of high frequency components and to reduce the noise recorded.[22]

1.8.2   Signal averaging

The signal-to-noise ratio is defined as the ratio of the maximum peak height to the root mean square value of the noise in the spectrum, where the noise in the FID is caused mainly by thermal noise from the coil and spectrometer hardware. The NMR signal from a single acquisition often has a low intensity, and the signal-to-noise ratio of the spectrum may be undesirably low. For this reason, experiments are repeated several times and the resulting FIDs are summed. The NMR signal in each FID adds together constructively, so repetition of the experiment N times gives an N-fold increase in the signal intensity. In contrast, the (root mean square) noise (assuming that it is random) increases as $\sqrt{N}$. Overall this gives a $\sqrt{N}$-fold increase in the signal-to-noise ratio.

1.8.3   Phasing the spectrum

In practice, the real part of the Fourier transformed signal usually contains a mixture of absorptive and dispersive lineshapes, owing to the $\mathrm{e}^{-\mathrm{i}\phi_{\text{rec}}}$ factor in the signal and other

hardware factors such as filters and ampifiers. Rather than adjusting the receiver phase to ensure $e^{-i\phi_{rec}} = 1$, it is simpler to multiply each data point (usually) in the frequency domain spectrum by $\exp\{i\phi_0\}$, where ϕ_0 is chosen so that pure absorption lineshapes are achieved in the real part of the spectrum. This process is referred to as phasing the spectrum and ϕ_0 is termed the zero-order phase correction.

Often is is not possible to make all the peaks in the spectrum have absorption lineshapes by adjusting only ϕ_0. This can be caused by a delay between the end of the excitation pulse and starting detection, and by off-resonance effects of the pulses used in the experiment. To remove this effect (to a good approximation), a further phase correction is performed, where the phase shift applied to the data points varies linearly with their frequency. This is the first-order phase correction.

1.8.4 Weighting the signal

Often the recorded signal, $s(t_k)$, is multiplied by a weighting function, $f(t_k)$, prior to Fourier transform of the modified signal $s'(t_k)$:

$$s'(t_k) = s(t_k)f(t_k). \tag{1.75}$$

This process is equivalent to convolution of the frequency domain spectrum with the Fourier transform of $f(t_k)$:[21]

$$\mathrm{FT}\left[s(t_k)f(t_k)\right] = \mathrm{FT}\left[s(t_k)\right] \otimes \mathrm{FT}\left[f(t_k)\right], \tag{1.76}$$

using $\otimes$ to indicate the convolution.

Typical forms of the weighting functions are exponential functions, Gaussian decays and sine functions.[12, 23] Weighting is performed for a number of reasons. First, if the signal has not fully decayed to zero at the end of acquisition, the spectrum will contain truncation artefacts, typically appearing as ripples at the base of peaks in the spectrum. By weighting the signal with a function that decays to zero at the end of the signal, these artefacts are removed; this application is called apodization. Weighting the FID by a decaying function also has the effect of increasing the width of the peaks in the spectrum, and is also referred to as line broadening. For an exponential weighting function, the line broadening is described by the additional linewidth added to the peaks in the spectrum.

Line broadening weighting functions are also used to enhance the signal-to-noise ratio of

the spectrum.[24] The enhancement is obtained by reducing the weighting of the noise at the end of the FID. In contrast, a weighting function that counteracts the relaxation decay of the signal narrows the lines, but at the expense of a reduced signal-to-noise ratio.[24]

1.9 Internal nuclear spin interactions

In the previous sections it was assumed that nuclei were isolated in a magnetic field, and so all nuclei of the same isotope would appear at the same frequency in an NMR spectrum. Of course, in real chemical systems this is not the case: the nuclei interact with the surrounding electrons and other nuclear spins. Consequently, the frequency at which the signal from a nucleus appears in an NMR spectrum is dependent upon its local environment.[25]

The total spin Hamiltonian, defined in the laboratory frame, can be divided into two parts: one $\hat{\mathcal{H}}_{\text{ext}}$ arising from external interactions (with respect to the sample) with the static magnetic field and RF pulses, and the other $\hat{\mathcal{H}}_{\text{int}}$ from internal nuclear spin interactions.

The principal internal interactions of interest in solid-state NMR are of the nuclear spin with the local magnetic field generated by the surrounding electrons, called chemical shielding, and the magnetic moment of other nearby nuclear spins, known as dipole-dipole coupling. In addition, nuclei with $I > 1/2$ have a non-zero electric quadrupole moment that interacts with the electric field gradient at the nucleus.

Each nuclear spin interaction present in a spin system contributes a term to the internal Hamiltonian $\hat{\mathcal{H}}_{\text{int}}$. The form of the Hamiltonian for each interaction is summarised in Table 1.1.[1] In each case, a second-rank tensor relates two vector quantities, using the notation $\boldsymbol{\sigma}$, $\boldsymbol{D}$ and $\boldsymbol{V}$ for chemical shielding, dipolar coupling and quadrupolar coupling tensors respectively.

1.9.1 Truncation of the nuclear spin interactions

The internal Hamiltonian $\hat{\mathcal{H}}_{\text{int}}$ is homogeneous. To evaluate the effect of the nuclear spin interactions in the presence of the larger Zeeman interaction, average Hamiltonian theory can be used. Transformation into the Zeeman interaction frame, which was described in Sections 1.3.1 and 1.5.2, gives the interaction-frame Hamiltonian

$$\hat{\mathcal{H}}_{\text{int}}^* = \hat{U}_0^{-1}\hat{\mathcal{H}}_{\text{int}}\hat{U}_0 \ \text{ where } \ \hat{U}_0 = \hat{R}_z(\omega_0 t). \tag{1.77}$$

Interaction	Hamiltonian
Chemical shielding	$\hat{\mathcal{H}}_{\mathrm{CS}}^{\mathrm{full}} = \gamma \hat{\boldsymbol{I}} \cdot \boldsymbol{\sigma} \cdot \mathbf{B}_0$
Dipole-dipole coupling	$\hat{\mathcal{H}}_{IS}^{\mathrm{full}} = -\frac{\mu_0 \hbar}{4\pi} \gamma_I \gamma_S \left(\frac{\boldsymbol{I} \cdot \boldsymbol{S}}{r^3} - 3 \frac{(\boldsymbol{I} \cdot \boldsymbol{r})(\boldsymbol{S} \cdot \boldsymbol{r})}{r^5} \right)$
	$\phantom{\hat{\mathcal{H}}_{IS}^{\mathrm{full}}} = \sum_{\alpha,\beta=x,y,z} D_{\alpha\beta} \left[\frac{1}{2}(\hat{I}_\alpha \hat{S}_\beta + \hat{I}_\beta \hat{S}_\alpha) - \frac{1}{3}\delta_{\alpha\beta} \hat{\boldsymbol{I}} \cdot \hat{\boldsymbol{S}} \right]$
	$\phantom{\hat{\mathcal{H}}_{IS}^{\mathrm{full}}} = \hat{\boldsymbol{I}} \cdot \boldsymbol{D} \cdot \hat{\boldsymbol{S}}$
	$D_{\alpha\beta} = b_{IS}\left\{ 3(\boldsymbol{e}_\alpha \cdot \boldsymbol{r})(\boldsymbol{e}_\beta \cdot \boldsymbol{r})/r^2 - \delta_{\alpha\beta} \right\}, \; b_{IS} = -\frac{\mu_0 \hbar}{4\pi} \frac{\gamma_I \gamma_S}{r^3}$
Quadrupolar coupling	$\hat{\mathcal{H}}_Q^{\mathrm{full}} = \sum_{\alpha,\beta=x,y,z} \frac{eQ}{2I(2I-1)\hbar} V_{\alpha\beta} \left[\frac{1}{2}(\hat{I}_\alpha \hat{I}_\beta + \hat{I}_\beta \hat{I}_\alpha) - \frac{1}{3}\delta_{\alpha\beta} \hat{\boldsymbol{I}} \cdot \hat{\boldsymbol{I}} \right]$
	$\phantom{\hat{\mathcal{H}}_Q^{\mathrm{full}}} = \frac{eQ}{2I(2I-1)\hbar} \hat{\boldsymbol{I}} \cdot \boldsymbol{V} \cdot \hat{\boldsymbol{I}}$
	$V_{\alpha\beta} = \left. \dfrac{\partial^2 E}{\partial x_\alpha \partial x_\beta} \right|_{\text{at the nucleus}}$

Table 1.1: Internal nuclear spin Hamiltonians for the chemical shielding, dipole-dipole coupling and quadrupole interaction.[1] The quantity b_{IS} is the dipolar coupling constant, $\boldsymbol{r}$ is the internuclear vector between dipolar coupled spins I and S, with magnitude r, and $\boldsymbol{e}_\alpha$ are unit vectors in the α-direction. For the quadrupolar coupling Hamiltonian Q is the nuclear quadrupole moment and E is the electric field. The symbols $\boldsymbol{\sigma}$, $\boldsymbol{D}$ and $\boldsymbol{V}$ represent second-rank tensors. Further details are given in the text.

Many of the terms in the interaction-frame Hamiltonian are time dependent. In most cases $\hat{\mathcal{H}}_{\mathrm{Z}}$ is much larger than $\hat{\mathcal{H}}_{\mathrm{int}}$, so the interaction-frame Hamiltonian is approximated by the first-order average Hamiltonian, calculated over one Larmor period $t_{\mathrm{c}} = 2\pi/\omega_0$. In practice, the condition of stroboscopic observation of the spin system at the cycle time t_{c} can be lifted, as t_{c} is very short compared with the interval between measurements. The same approach was used to evaluate the effect of an RF pulse in the Section 1.5.2

The first-order average Hamiltonian gives a 'truncated Hamiltonian' that is much simpler than the full Hamiltonians given in Table 1.1, but still accurately describes the effect of the internal interactions on the spin system, as viewed in the rotating frame.

1.10   Chemical shielding

Chemical shielding arises from the presence of electrons surrounding the nuclei. When an atom or molecule is located in a static magnetic field, two contributions affect the local magnetic field at the nucleus. First, the external static field induces currents in the electron cloud, which circulate about the static field generating a secondary magnetic field; this is the diamagnetic contribution to the shielding. Second, the external static field
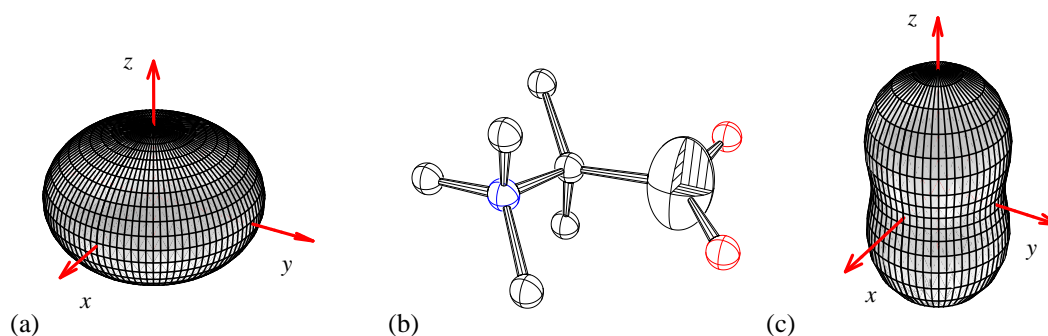
Figure 1.5: (a) Ellipsoid representation of a shielding tensor with principal values $\sigma_{xx}^{\mathrm{PAF}} : \sigma_{yy}^{\mathrm{PAF}} : \sigma_{zz}^{\mathrm{PAF}} = 1 : 1 : 2$. (b) Schematic illustration of the glycine carbonyl carbon shielding tensor PAF orientation fixed with respect to the molecular structure (PAF indicated by the shaded octant of the ORTEP[29] style ellipsoid). (c) Ovaloid representation of the ellipsoid in (a).

distorts and polarizes the unperturbed electronic ground state, again generating a local magnetic field; this is termed the paramagnetic contribution. A perturbation treatment leads to the perturbed electronic ground state being written as a superposition of the unperturbed ground and excited electronic states, and the paramagnetic contribution can then be viewed as a mixing of paramagnetic excited states with the electronic ground state.[26] Both contributions are proportional to the external static field strength.

The chemical shielding interaction tensor $\boldsymbol{\sigma}$, and in general any second-rank tensor, can be represented by a 3×3 matrix, with elements σ_{ij}, where $i, j = x, y, z$ and x, y and z correspond to the Cartesian directions in a specified frame of reference.

The local magnetic field generated by the electrons is $-\boldsymbol{\sigma} \cdot \mathbf{B}_0$: $-\sigma_{ij} B_{0,j}$ is the magnetic field generated by the electrons along the i-axis due to the component of the external field along the j-axis ($B_{0,j}$). In general $\boldsymbol{\sigma}$ has an antisymmetric component, however in practice only the symmetric part has an effect on NMR spectra to first order.[27,28] The antisymmetric part of the shielding tensor is neglected and $\boldsymbol{\sigma}$ is taken to be symmetric.

It is possible to choose the axis frame in which the interaction tensor is defined such that only the diagonal elements of the matrix are non-zero; this frame is termed the principal axis frame (PAF), and the diagonal elements are the principal components/values. The PAF of a tensor has a fixed orientation with respect to the molecule or crystal structure, since the interaction that the tensor describes is determined by the local structure about the nucleus. It is sometimes useful to visualise the shielding tensor as an ellipsoid with semi-axes $1/\sqrt{\sigma_{xx}^{\mathrm{PAF}}}$, $1/\sqrt{\sigma_{yy}^{\mathrm{PAF}}}$ and $1/\sqrt{\sigma_{zz}^{\mathrm{PAF}}}$, where the superscript indicates that the tensor is defined in the PAF. The form of the ellipsoid is shown in Figure 1.5(a) and the visualisation of the PAF and tensor with respect to a molecule is shown schematically in Figure 1.5(b).
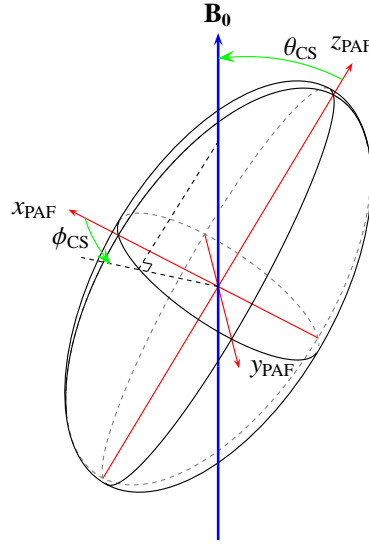
Figure 1.6: Orientation of the external field in the chemical shielding principal axis frame, defined by the two polar angles θ_{CS} and ϕ_{CS}. The chemical shielding tensor has been represented by an ellipsoid.

Expressing the chemical shielding tensor in the laboratory frame, denoted $\boldsymbol{\sigma}^{lab}$, and assuming that the static field lies parallel to the z-direction, the truncated chemical shielding Hamiltonian is

$$\hat{\mathcal{H}}_{CS} = \gamma \hat{I}_z \sigma_{zz}^{lab} B_0. \tag{1.78}$$

The value of σ_{zz}^{lab} depends on the orientation of the molecule with respect to the magnetic field. The orientation of the chemical shield tensor PAF with respect to the laboratory frame is defined by a set of Euler angles $\Omega_{PL} = \{\phi_{CS}, \theta_{CS}, 0\}$, where θ_{CS} and ϕ_{CS} are the polar angles describing the orientation of the static external field in the PAF, as shown in Figure 1.6. The shielding tensor expressed in laboratory frame is related to the shielding tensor defined in the PAF by the rotation $\boldsymbol{\sigma}^{lab} = \hat{R}^{-1}(\phi_{CS}, \theta_{CS}, 0)\boldsymbol{\sigma}^{PAF}\hat{R}(\phi_{CS}, \theta_{CS}, 0)$. The third Euler angle is redundant, as its value has no effect on the value of σ_{zz}^{lab}, and is arbitrarily set to zero. This gives

$$\sigma_{zz}^{lab} = \overline{\sigma} + \frac{1}{2}\Delta_{CS}\left(3\cos^2\theta_{CS} - 1 + \eta_{CS}\sin^2\theta_{CS}\cos 2\phi_{CS}\right), \tag{1.79}$$

where

$$\overline{\sigma} = \frac{1}{3}(\sigma_{xx}^{PAF} + \sigma_{yy}^{PAF} + \sigma_{zz}^{PAF}) \tag{1.80}$$

$$\Delta_{CS} = \sigma_{zz}^{PAF} - \overline{\sigma} \tag{1.81}$$

$$\eta_{CS} = (\sigma_{yy}^{PAF} - \sigma_{xx}^{PAF})/(\sigma_{zz}^{PAF} - \overline{\sigma}). \tag{1.82}$$

Equations (1.80)-(1.82) are the isotropic shielding, chemical shielding anisotropy and

asymmetry parameters respectively.

Returning to the ellipsoid representation of the shielding tensor, it may be easily shown that the radius of the ellipsoid in any direction corresponds to $1/\sqrt{\sigma_{zz}^{\mathrm{lab}}}$ when the external field is aligned along the same direction. An alternative representation is the ovaloid,[30] which is a shape that has a radius in any direction equal to $\sigma_{zz}^{\mathrm{lab}}$, when the field is aligned along the same direction. The equivalent ovaloid representation of the ellipsoid in Figure 1.5(a) is shown in Figure 1.5(c) on page 26.

Chemical shielding causes a change the energy of the Zeeman state $|I, m\rangle$ by $m\gamma\sigma_{zz}^{\mathrm{lab}}B_0$. Therefore the effect on the NMR spectrum is a frequency shift of the signal, equal to $\gamma\sigma_{zz}^{\mathrm{lab}}B_0$, from that of an unshielded nucleus. Chemical shielding depends on the electron distribution about the nucleus, and thus measurement of this interaction can provide information about the local structure and bonding at the observed nucleus.

1.10.1 Frequency references and the chemical shift

It is not possible to measure chemical shielding directly, as this would require knowledge of the Larmor frequency of a bare nucleus. Instead, the chemical shift scale is used, where frequencies are measured relative to the frequency $\omega_{\mathrm{standard}}$ of the signal from a reference sample. A parts per million (ppm) scale is used, defined as

$$\delta = 10^6 \times \frac{\omega - \omega_{\mathrm{standard}}}{\omega_{\mathrm{standard}}}, \tag{1.83}$$

where δ is the chemical shift of the corresponding frequency ω. For example, the standard reference for $^{13}\mathrm{C}$ and $^{1}\mathrm{H}$ NMR are the respective signals from tetramethylsilane.

The chemical shift is a deshielding scale (the absolute offset frequency $|\Omega|$ increases with δ) and spectra are always plotted with the chemical shift increasing from right to left. The frequency scale in Hertz is related to the ppm scale by $10^{-6}\delta\omega_{\mathrm{standard}}/2\pi$, thus the direction in which the Hertz scale increases depends upon the sign of γ for the nucleus studied.

From the definition of the chemical shift in Equation (1.83), the chemical shift tensor is defined with elements

$$\delta_{ij} = 10^6 \frac{\sigma_{\mathrm{standard}} - \sigma_{ij}^{\mathrm{lab}}}{1 - \sigma_{\mathrm{standard}}}. \tag{1.84}$$

The isotropic chemical shift, chemical shift anisotropy and asymmetry parameters are

$$\delta_{\text{iso}} = \frac{1}{3}\left(\delta_{xx}^{\text{PAF}} + \delta_{yy}^{\text{PAF}} + \delta_{zz}^{\text{PAF}}\right) \tag{1.85}$$

$$\delta_{\text{aniso}} = \delta_{zz}^{\text{PAF}} - \delta_{\text{iso}} \tag{1.86}$$

$$\eta_{\text{CS}} = \left(\delta_{yy}^{\text{PAF}} - \delta_{xx}^{\text{PAF}}\right)/\delta_{\text{aniso}}. \tag{1.87}$$

The dependence of the chemical shift on the tensor orientation with respect to the static field, specified by the polar angle θ_{CS} and ϕ_{CS}, is given by

$$\delta_{zz}^{\text{lab}} = \delta_{\text{iso}} + \frac{1}{2}\delta_{\text{aniso}}\left(3\cos^2\theta_{\text{CS}} - 1 + \eta_{\text{CS}}\sin^2\theta\cos 2\phi_{\text{CS}}\right). \tag{1.88}$$

1.10.2   Liquid-state and solid-state samples

The spectrum obtained from an NMR experiment depends upon the form of the sample used. If the sample is in solution, then rapid isotropic molecular motion averages to zero the anisotropic components of the chemical shift (and other anisotropic interactions present). Only the effect of the isotropic chemical shielding is seen (neglecting J-coupling), and the spectra contain sharp peaks.

By contrast, within a solid sample there is no molecular motion, or at least motion is restricted, and the anisotropy of the nuclear spin interactions is not averaged to zero. Two types of solid sample can be identified: single crystal and powder samples.

For a single crystal sample, the number of different nuclear spin environments for a general orientation of the single crystal is equal to the number of species in the unit cell of the crystal structure; however, sites that are related by a centre of inversion appear equivalent. Single crystal spectra contain sharp lines (neglecting any effects of dipolar coupling) for each different nuclear environment, although their frequencies depend on the crystal orientation with respect to external static field.

Powder samples consist of many small crystallites, each with a different orientation with respect to the external static field. Therefore the NMR spectrum of a powder sample corresponds to the superimposition of the single-crystal spectra from each crystallite orientation. If the sample is a uniform powder (crystallites are randomly oriented) a characteristic lineshape called a powder pattern[31] is seen in the spectrum for each nuclear
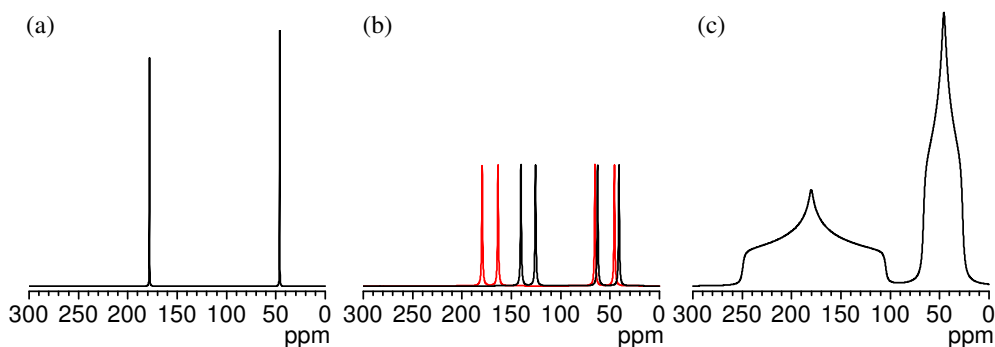
Figure 1.7: Simulated ^{13}C NMR spectra for α-glycine. (a) A solution sample, sharp peaks are seen at the isotropic chemical shift. (b) A single crystal sample gives rise to four peaks. Two different crystal orientations have been plotted, one in black and the other in red. (c) The expected spectrum for a powder sample. In each spectrum, the peak heights have been arbitrarily scaled. Exponential line broadening of (a) 20 Hz, (b) 100 Hz and (c) 2000 Hz was used. The effects of dipolar coupling are neglected here.

site in the asymmetric unit (nuclear sites related by symmetry elements will contribute to the same power pattern).

As an example, Figure 1.7 compares calculated ^{13}C NMR spectra for α-glycine. In solution only the two isotropic peaks are seen (Figure 1.7(a)), while for a single crystal there are four peaks owing to four magnetically different ^{13}C sites in the unit cell (Figure 1.7(b)).[‡§] For a powder sample, two powder patterns are seen for the two ^{13}C sites in the asymmetric unit (Figure 1.7(c)).

The ideal powder pattern lineshape is shown by the dotted line in Figure 1.8(a). Asymptotic behaviour occurs at three frequency values in the lineshape. The solid line in Figure 1.8(a) is more representative of experimentally observed lineshapes, as the effects of an intrinsic signal linewidth have been included, by convolution of the dotted line with a Lorentzian lineshape of full width at half-height of 300 Hz.

The frequencies at which the two edges and peak occur in the powder patterns are related to the principal components of the chemical shift tensor. Two common conventions are used to define the PAF components of the chemical shift tensor. The Haeberlen convention uses principal components $(\delta_{xx}^{\text{PAF}}, \delta_{yy}^{\text{PAF}}, \delta_{zz}^{\text{PAF}})$ ordered as

$$|\delta_{zz}^{\text{PAF}} - \delta_{\text{iso}}| \geq |\delta_{xx}^{\text{PAF}} - \delta_{\text{iso}}| \geq |\delta_{yy}^{\text{PAF}} - \delta_{\text{iso}}|,$$

thus the asymmetry parameter lies in the range $0 \leq \eta_{\text{CS}} \leq 1$.[14] The IUPAC con-

---

[‡]α-glycine has the space group P2$_1$/n, so that there are four equivalent positions in the unit cell, with pairs of sites related by a centre of inversion. There is one molecule in the asymmetric unit.[32]

[§]The effects of dipolar coupling are neglected here.
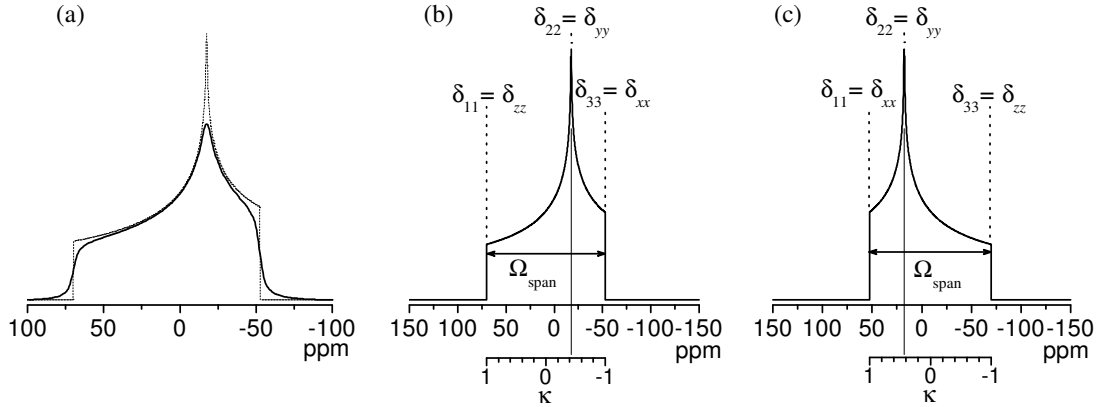
Figure 1.8: (a) A typical powder pattern line shape (solid line). Overlaid is the ideal powder pattern lineshape (dotted line). (b) and (c) Comparison of the IUPAC and Haeberlen conventions for characterising the powder pattern and ordering the principal components of the chemical shift tensor. In each case $\delta_{\text{iso}} = 0$ ppm. (a) and (b) $\Omega_{\text{span}} = 122.5$ ppm, $\kappa = -0.429$, $\delta_{\text{aniso}} = 70$ ppm and $\eta_{\text{CS}} = 0.5$. (c) $\Omega_{\text{span}} = 122.5$ ppm $\kappa = 0.429$, $\delta_{\text{aniso}} = -70$ ppm and $\eta_{\text{CS}} = 0.5$.

vention uses principal components components $(\delta_{11}, \delta_{22}, \delta_{33})$, with $\delta_{11} \geq \delta_{22} \geq \delta_{33}$ and $\delta_{\text{iso}} = \frac{1}{3}(\delta_{11} + \delta_{22} + \delta_{33})$.[33] The notation of span (Ω_{span}) and skew (κ) can also be used to describe the powder pattern,[34] with these parameters defined as

$$\Omega_{\text{span}} = \delta_{11} - \delta_{33}, \quad \kappa = 3\left(\delta_{22} - \delta_{\text{iso}}\right)/\Omega_{\text{span}} \ \ (-1 \leq \kappa \leq 1). \tag{1.89}$$

For $\delta_{\text{aniso}} > 0$ the Haeberlen convention is related to the IUPAC convention through $\delta_{zz} = \delta_{11}$, and if $\delta_{\text{aniso}} < 0$, then $\delta_{zz} = \delta_{33}$. These two conventions are illustrated in Figure 1.8.

1.11 Dipole-dipole coupling

Dipole-dipole coupling arises from a direct, through space, interaction between the magnetic moments of a pair of nuclei. The truncated Hamiltonian is evaluated by transforming $\hat{\mathcal{H}}_{IS}^{\text{full}}$ into a doubly-rotating frame (the interaction frame of $\omega_0^I \hat{I}_z + \omega_0^S \hat{S}_z$, where ω_0^I and ω_0^S are the Larmor frequencies of the I and S spin respectively). The truncated Hamiltonians for the homonuclear ($\hat{\mathcal{H}}_{IS}^{\text{Homo}}$) and heteronuclear ($\hat{\mathcal{H}}_{IS}^{\text{Het}}$) spin pair

cases are

$$\hat{\mathcal{H}}_{IS}^{\text{Homo}} = D_{zz}^{\text{lab}} \left[\hat{I}_z \hat{S}_z - \frac{1}{2} \left(\hat{I}_x \hat{S}_x + \hat{I}_y \hat{S}_y \right) \right]$$

$$= \frac{1}{2} D_{zz}^{\text{lab}} \left[3\hat{I}_z \hat{S}_z - \hat{\mathbf{I}} \cdot \hat{\mathbf{S}} \right], \tag{1.90}$$

$$\hat{\mathcal{H}}_{IS}^{\text{Het}} = D_{zz}^{\text{lab}} \hat{I}_z \hat{S}_z. \tag{1.91}$$

The components of the dipolar coupling tensor are

$$D_{ij}^{\text{lab}} = b_{IS} \left\{ 3(\boldsymbol{e}_i \cdot \boldsymbol{r})(\boldsymbol{e}_j \cdot \boldsymbol{r})/r^2 - \delta_{ij} \right\} \text{ where } b_{IS} = -\frac{\mu_0 \hbar}{4\pi} \frac{\gamma_I \gamma_S}{r^3}. \tag{1.92}$$

In Equation (1.92) $\boldsymbol{e}_i$ is a unit vector along the i-axis of the laboratory frame. From Equation (1.92), $\boldsymbol{D}$ is a symmetric and traceless tensor, and there is no isotropic component to dipolar coupling. The PAF has its z-direction parallel to the $I - S$ internuclear vector, and has components $D_{xx}^{\text{PAF}} = D_{yy}^{\text{PAF}} = -b_{IS}$ and $D_{zz}^{\text{PAF}} = 2b_{IS}$.

To the dipolar coupling tensor in the laboratory frame is related to the dipolar coupling tensor in the PAF by $\boldsymbol{D}^{\text{lab}} = \hat{R}^{-1}(0, \theta_{\text{D}}, 0) \boldsymbol{D}^{\text{PAF}} \hat{R}(0, \theta_{\text{D}}, 0)$. As for the chemical shielding interaction, the third Euler angle has no effect on D_{zz}^{lab}, and similarly the first Euler angle has no effect because $D_{xx}^{\text{PAF}} = D_{yy}^{\text{PAF}}$, so both angles are set to zero. The angle θ_{D} corresponds to the angle between the PAF z-axis (the internuclear axis) and the laboratory frame z-axis. This gives

$$D_{zz}^{\text{lab}} = D_{zz}^{\text{PAF}} \frac{1}{2} (3\cos^2 \theta_{\text{D}} - 1) = b_{IS} (3\cos^2 \theta_{\text{D}} - 1). \tag{1.93}$$

The dipolar coupling interaction depends on the internuclear separation of the coupled spins as r^{-3}. This makes it a useful probe of internuclear distances, if the strength of the coupling can be measured.

Heteronuclear dipolar coupling between a spin pair I–S splits the I spin signal into $2S + 1$ signals of equal weighting, separated in frequency by D_{zz}^{lab}. This is shown for a spin-1/2 pair in Figure 1.9(a) on the next page. If the sample is a powder, a characteristic powder pattern is observed with the 'horns' separated by $|b_{IS}|$.

The effects of homonuclear dipolar coupling on the NMR spectrum are quite different. This arises from there being degenerate Zeeman states. The effect of the dipole-dipole coupling perturbation is to remove the degeneracy of these states. For an isolated homonuclear spin-1/2 pair, the eigenfunctions of $\hat{\mathcal{H}}_{\text{total}} = \hat{\mathcal{H}}_{\text{Z}} + \hat{\mathcal{H}}_{IS}^{\text{Homo}}$ are $|\alpha\alpha\rangle$,
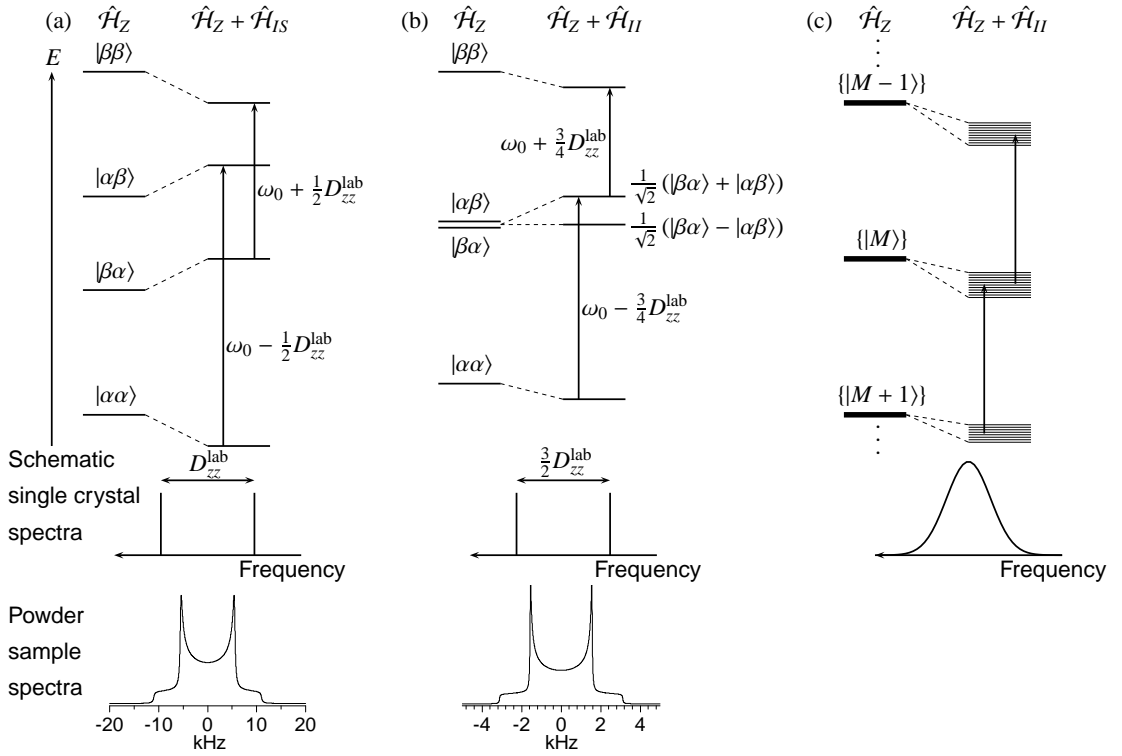
Figure 1.9: Comparison of the effects of (a) heteronuclear dipolar coupling between a heteronuclear spin pair ($b_{IS}/2\pi = -11$ kHz), (b) homonuclear dipolar coupling between an isolated spin pair ($b_{IS}/2\pi = -2.08$ kHz) and (c) homonuclear dipolar coupling between abundant spins. In each case, the Zeeman states are shown, and adjacent to them the energies of the eigenstates with dipolar coupling taken into account are shown. It has been assumed that $\gamma > 0$. Schematic spectra for single crystal samples, and for powder samples are also given. In (a), only the S spin transitions and spectra are shown.

$\frac{1}{\sqrt{2}}(|\alpha\beta\rangle + |\alpha\beta\rangle)$, $|\beta\beta\rangle$, (triplet states) and $\frac{1}{\sqrt{2}}(|\alpha\beta\rangle - |\alpha\beta\rangle)$ (singlet state), where a Zeeman product basis has been used. Only coherences between the triplet states are allowed, which means that their are two peaks of equal weighting in the spectrum with separation $\frac{3}{2}D_{zz}^{\text{lab}}$. For powder samples, a powder pattern also forms, as presented in Figure 1.9(b) on this page.

For homonuclear dipolar coupling between a small number of spins, the powder pattern is characteristic of the geometry and number of spins involved.[35] However, if the spin involved is abundant, and many nuclei are dipolar coupled, there are many degenerate Zeeman states (in the absence of the dipolar coupling term in the Hamiltonian). Using a Zeeman product basis for N coupled spins, the degenerate Zeeman states are characterised by the quantum number $M = m_1 + m_2 + \cdots + m_N$, and the set of states $\{|M\rangle\}$ contains $n_M = N!/[(N/2 - M)!(M + N/2)!]$ members. The degeneracy of the $\{|M\rangle\}$ states is lifted by the homonuclear coupling, which causes a very broad range of single quantum transition energies, illustrated in Figure 1.9(c) on the current page. The overall effect on

the spectrum is to cause very broad lineshapes, approximating to a Gaussian in the limit of many coupled spins, even for single crystals.[1,36] For example, the ^{1}H NMR linewidth for organic solids is often several kilohertz wide.

1.12 Quadrupolar coupling

As stated earlier, quadrupolar coupling occurs for nuclei with spin $I > 1/2$. The magnitude of the quadrupolar coupling depends upon the quadrupole moment eQ of the nucleus (Q is the quadrupole moment and e is the elementary charge), and the electric field gradient at the nucleus, which is expressed by the quadrupole coupling tensor $\boldsymbol{V}$. The components of this tensor $V_{\alpha\beta}$ are the second partial derivatives of the electric field with respect to the α and β directions, evaluated at the nucleus. The electric field gradient depends upon the electron distribution about the nucleus and so the quadrupole interaction can provide information about local bonding and structure.

The truncated Hamiltonian is evaluated in the same manner as for the other interactions. However, the quadrupole coupling is often sufficiently large compared to the Zeeman interaction that the second-order term of the Magnus expansion is required. The first-order ($\hat{\mathcal{H}}_Q^{(1)}$) and second-order ($\hat{\mathcal{H}}_Q^{(2)}$) quadrupole Hamiltonians are

$$\hat{\mathcal{H}}_Q^{(1)} = \frac{eQ}{4I(2I-1)\hbar} V_{zz}^{\text{lab}} \left(3\hat{I}_z\hat{I}_z - \hat{\boldsymbol{I}} \cdot \hat{\boldsymbol{I}} \right) \tag{1.94}$$

$$\hat{\mathcal{H}}_Q^{(2)} = \left(\frac{eQ}{4I(2I-1)\hbar} \right)^2 \frac{1}{2\omega_0} \left[\left(V_{xz}^{\text{lab}\,2} + V_{yz}^{\text{lab}\,2} \right) \left\{ 4\hat{\boldsymbol{I}} \cdot \hat{\boldsymbol{I}} - 8\hat{I}_z^2 - 1 \right\} \right.$$
$$\left. - \left(\tfrac{1}{4} \left(V_{xx}^{\text{lab}} - V_{yy}^{\text{lab}} \right)^2 + V_{xy}^{\text{lab}\,2} \right) \left\{ 2\hat{\boldsymbol{I}} \cdot \hat{\boldsymbol{I}} - 2\hat{I}_z^2 - 1 \right\} \right] \hat{I}_z, \tag{1.95}$$

where only those parts of the second-order average Hamiltonian that commute with the Zeeman Hamiltonian have been kept in the truncated form.[37,38]

The PAF component V_{zz}^{PAF} is written as eq, and the magnitude of the quadrupole coupling is characterised by the quadrupole coupling constant $C_Q = e^2qQ/h$. The value of V_{zz}^{lab} is related to the principal components by

$$V_{zz}^{\text{lab}} = \frac{1}{2}eq \left(3\cos^2\theta_Q - 1 + \eta_Q \sin^2\theta_Q \cos 2\phi_Q \right), \tag{1.96}$$

where $\eta_Q = (V_{yy}^{\text{PAF}} - V_{xx}^{\text{PAF}})/eq$, and the polar angles θ_Q (colatitude) and ϕ_Q (longitude) specify the orientation of the external static magnetic field within the PAF of $\boldsymbol{V}$, in analogy
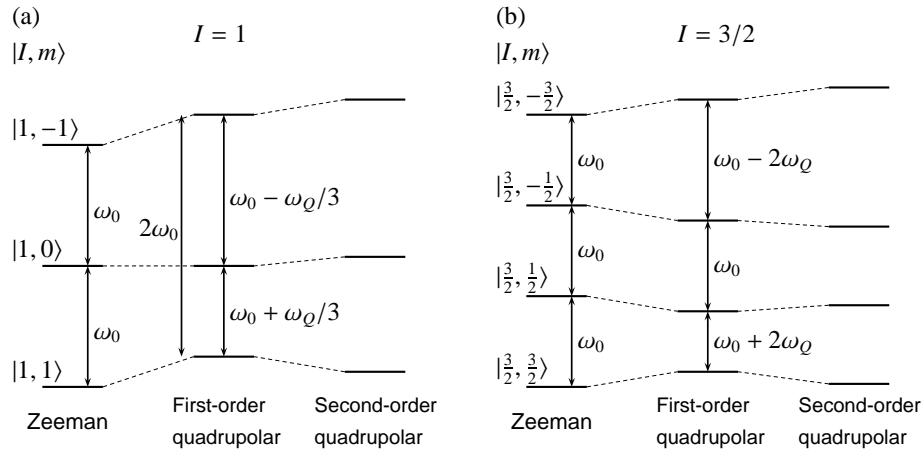
Figure 1.10: The change in energy of the Zeeman states due to the first-order quadrupole coupling Hamiltonian and the further shift due to the second-order quadrupole coupling Hamiltonian. In (a) $I = 1$ and (b) $I = 3/2$. It has been assumed that $\gamma > 0$.

with those used for the chemical shielding tensor. The quadrupolar coupling tensor V is traceless and so there is no isotropic component to the first-order quadrupole coupling, which is often written in the form

$$\hat{\mathcal{H}}_Q^{(1)} = \frac{\omega_Q}{3}\left(3\hat{I}_z^2 - I(I+1)\right) \text{ where } \omega_Q = \frac{\omega_Q^{\text{PAF}}}{2}\left(3\cos^2\theta_Q - 1 - \eta_Q\sin^2\theta_Q\cos 2\phi_Q\right),$$
(1.97)

using the quadrupole splitting parameter $\omega_Q^{\text{PAF}} = (3\pi C_Q)/(2I(2I-1))$.

Quadrupole coupling causes a shift in the energies of Zeeman states. The first- and second-order shifts are shown schematically for the spin-1 and spin-3/2 cases in Figure 1.10. For spin-1, both single-quantum transition energies are affected by the first-order coupling. In contrast, in the spin-3/2 case the splitting between the $|I, +1/2\rangle$ and $|I, -1/2\rangle$ states (the central transition) is unaffected to first-order. To second order, all the transition energies are affected for both spin-1 and spin-3/2. The second-order Hamiltonian is proportional to the inverse Larmor frequency (ω_0^{-1}), so its effect decreases with higher static field strengths.

The magnitude of quadrupolar coupling constant C_Q is often of the order of several MHz, causing the range of single-quantum transition frequencies within a powder sample to be so large that they occur well beyond the range that can be excited by the RF pulses, or be detected by the spectrometer in a standard experiment. For integer spin nuclei, this is particularly problematic because both single-quantum transitions are affected to first order. However, deuterium usually experiences quadrupole coupling of the order of a few 100 kHz and a powder pattern of the form simulated in Figure 1.11(a) can be recorded. For
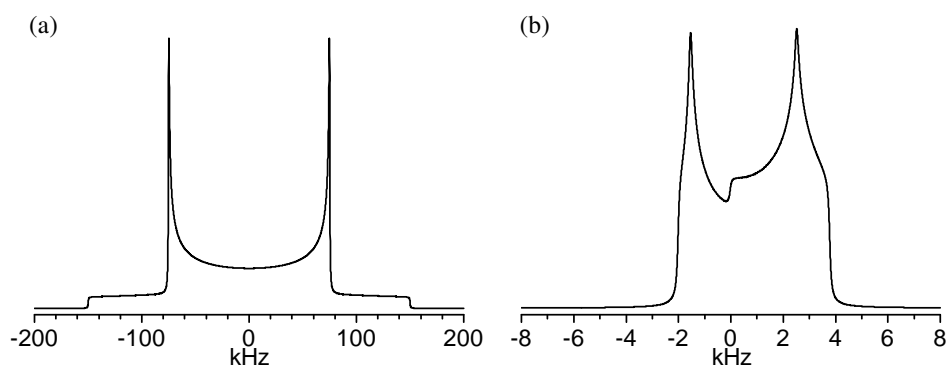
Figure 1.11: (a) Quadrupolar powder pattern for $I = 1$ and $C_Q/2\pi = 200$ kHz, $\eta_Q = 0$. (b) The central transition powder pattern for an $I = \frac{3}{2}$ spin. Only the central transition is seen for a large quadrupole coupling, and the powder pattern arises from the second-order quadrupole interaction, $C_Q/2\pi = 2$ MHz, $\eta_Q = 0.2$ and $\omega_0/2\pi = 105.9$ MHz. The SIMPSON package[39] was used to calculate the lineshapes.

half-integer spins, the central transition is only affected to second order by the quadrupole interaction and is readily observed. In this case, a characteristic lineshape is recorded for powder samples (for example see Figure 1.11(b)) that is somewhat more complicated than seen for chemical shielding; nevertheless, it is readily simulated and can be used to determine C_Q and η_Q.

2

Basic techniques in solid-state NMR

In this chapter, methodology that has become an established part of the NMR field is described. First, techniques specifically used in solid-state NMR are discussed; second, the principle of two-dimensional experiments is presented along with methods to select only desired contributions to the signal. Finally, the process of computer simulation of NMR experiments is outlined.

2.1   Experimental methods in solid-state NMR

2.1.1   Magic-angle spinning

Static powder samples generally give rise to broad lineshapes that, in the case of more than a few different nuclear environments, give highly overlapped lineshapes in the spectra.

The pioneering experiments of Lowe[40] and Andrew[41] demonstrated that rotating samples about an axis, whilst performing the NMR experiment, could lead to line-narrowing in the NMR spectra of solids. Sample spinning is now a routine technique with standard laboratory hardware allowing rotation frequencies up to 35 kHz, and sample spinning at 70 kHz has been reported.[42]

Sample rotation introduces a time dependent, but periodic, modulation of the internal spin interactions. As this methodology is used extensively in this work, a detailed analysis is presented here. To analyse the effect of spinning, it is useful to introduce axis frames associated with the crystallite and the rotor. Transformation from axis system X to Y is described by a set of three Euler angles $\Omega_{XY} = \{\alpha_{XY}, \beta_{XY}, \gamma_{XY}\}$, as detailed in Section A.4. The connection between these frames is illustrated in Figure 2.1 on the next page. For the case of chemical shielding, the shielding tensor as defined in the rotor frame is labelled σ^{R}, and in the laboratory frame σ^{lab}. The tensor σ^{lab} is related to the shielding tensor expressed in the rotor frame by $\sigma^{lab} = \hat{R}^{-1}(\omega_{r}t, \beta_{RL}, 0)\sigma^{R}\hat{R}(\omega_{r}t, \beta_{RL}, 0)$, where ω_{r} is the spinning frequency in angular frequency units. Evaluating this expression gives, after
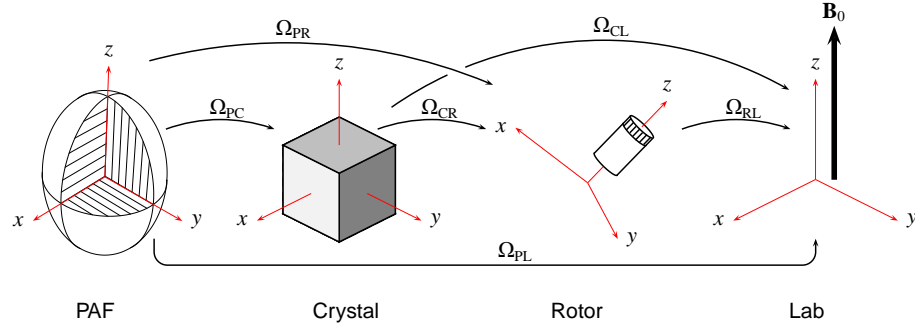
Figure 2.1: Relationship between the principal axis frame (PAF), crystal frame, rotor frame and laboratory frame.

using various trigonometric identities, the zz component of σ^{lab}

$$\sigma_{zz}^{\text{lab}}(t) = \overline{\sigma} + \tfrac{1}{2}\left(3\cos^2\beta_{\text{RL}} - 1\right)\left[\sigma_{zz}^{\text{R}} - \overline{\sigma}\right] + \sin(2\beta_{\text{RL}})\left[\sigma_{xz}^{\text{R}}\cos(\omega_{\text{r}}t) + \sigma_{yz}^{\text{R}}\sin(\omega_{\text{r}}t)\right]$$
$$+ \sin^2\beta_{\text{RL}}\left[\tfrac{1}{2}(\sigma_{xx}^{\text{R}} - \sigma_{yy}^{\text{R}})\cos(2\omega_{\text{r}}t) + \sigma_{xy}^{\text{R}}\sin(2\omega_{\text{r}}t)\right]. \tag{2.1}$$

The shielding tensor defined in the rotor frame is related to the chemical shielding tensor specified in the PAF by $\sigma^{\text{R}} = \hat{R}^{-1}(\alpha_{\text{PR}}, \beta_{\text{PR}}, \gamma_{\text{PR}})\sigma^{\text{PAF}}\hat{R}(\alpha_{\text{PR}}, \beta_{\text{PR}}, \gamma_{\text{PR}})$, so one obtains[34]

$$\sigma_{zz}^{\text{lab}}(t) = \overline{\sigma} + \tfrac{1}{2}\left(3\cos^2\beta_{\text{RL}} - 1\right)\left[\sigma_{zz}^{\text{R}} - \overline{\sigma}\right] + \left[c_1\cos(\omega_{\text{r}}t + \gamma) + c_2\cos(2\omega_{\text{r}}t + 2\gamma)\right.$$
$$\left. + s_1\sin(\omega_{\text{r}}t + \gamma) + s_2\sin(2\omega_{\text{r}}t + 2\gamma)\right] \tag{2.2}$$

where,

$$c_1 = \sin(2\beta_{\text{RL}})\left[-\tfrac{3}{4}\Delta_{\text{CS}}\sin(2\beta)\left(1 + \tfrac{1}{3}\eta_{\text{CS}}\cos(2\alpha)\right)\right] \tag{2.3}$$

$$c_2 = \sin^2(\beta_{\text{RL}})\tfrac{3}{4}\Delta_{\text{CS}}\left[\sin^2\beta - \tfrac{1}{3}\eta_{\text{CS}}\cos(2\alpha)\left(1 + \cos^2\beta\right)\right] \tag{2.4}$$

$$s_1 = \frac{1}{2}\sin(2\beta_{\text{RL}})\left[\Delta_{\text{CS}}\eta_{\text{CS}}\sin(2\alpha)\sin\beta\right] \tag{2.5}$$

$$s_2 = \frac{1}{2}\sin^2(\beta_{\text{RL}})\left[\Delta_{\text{CS}}\eta_{\text{CS}}\sin(2\alpha)\cos\beta\right], \tag{2.6}$$

and the subscript has been omitted for the Euler angles $\{\alpha_{\text{PR}}, \beta_{\text{PR}}, \gamma_{\text{PR}}\}$ relating the PAF frame to rotor frame.

Considering only the chemical shielding interaction, the rotating-frame Hamiltonian is defined to be

$$\hat{\mathcal{H}}(t; \Omega_{\text{PR}}) = \omega(t; \Omega_{\text{PR}})\hat{I}_z, \tag{2.7}$$

where $\omega(t; \Omega_{\text{PR}})$ describes the precession frequency of the magnetization in the rotating frame for a crystallite with orientation Ω_{PR}. Equation (2.7) will be referred to as the chemical shift Hamiltonian. The $\omega(t; \Omega_{\text{PR}})$ factor is related to the expressions in

Equation (2.2) by

$$\omega(t; \Omega_{PR}) = \omega_{iso} + \omega'(\Omega_{PR}) + \left[C_1 \cos(\omega_r t + \gamma) + C_2 \cos(2\omega_r t + 2\gamma) \right.$$
$$\left. + S_1 \sin(\omega_r t + \gamma) + S_2 \sin(2\omega_r t + 2\gamma) \right], \tag{2.8}$$

where

$$C_1 = -\omega_0 c_1, \ C_2 = -\omega_0 c_2, \ S_1 = -\omega_0 s_1, \ S_2 = -\omega_0 s_2 \tag{2.9}$$

$$\omega_{iso} = \omega_0 \left[1 - \overline{\sigma} \right] - \omega_{ref}, \quad \omega'(\Omega_{PR}) = -\tfrac{1}{2}\omega_0 \left(3\cos^2 \beta_{RL} - 1 \right) \left[\sigma_{zz}^R - \overline{\sigma} \right]. \tag{2.10}$$

Unlike the first term in Equation (2.8), the second and third terms in Equation (2.8) depend on the orientation of the crystallite. For this reason, the part of the chemical shift Hamiltonian $\hat{\mathcal{H}}(t; \Omega_{PR})$ that contains these two terms is referred to as the chemical shift anisotropy (CSA).

The internal Hamiltonian is dynamically heterogeneous if the internal Hamiltonian only has contributions from chemical shielding, heteronuclear dipolar coupling or quadrupolar coupling. The propagator of the rotating-frame density operator in this case is given by Equation (1.35) on page 9. Continuing with the example of chemical shielding, this propagator will be

$$\hat{U}_{MAS}(t) = \exp\left\{ -i \int_0^t \omega(t'; \Omega_{PR}) \hat{I}_z dt' \right\}. \tag{2.11}$$

The detected signal is proportional to the ensemble-averaged expectation value of $\hat{I}_+$, so for an initial density operator following excitation by a 90°_y-pulse $\hat{\rho}(0) = \tfrac{1}{2} \left(\hat{I}_+ + \hat{I}_- \right)$, one obtains for a crystallite orientation Ω_{PR}:

$$\begin{aligned} s(t; \Omega_{PR}) &= \overline{\langle \hat{I}_+ \rangle} \\ &= \text{Tr}\left[\hat{U}_{MAS}(t) \hat{\rho}(0) \hat{U}_{MAS}^{-1}(t) \hat{I}_+ \right] \\ &= \frac{1}{2} \exp\left\{ i \int_0^t \omega(t'; \Omega_{PR}) dt' \right\}. \end{aligned} \tag{2.12}$$

The first term in Equation (2.8) is independent of both time and crystallite orientation, so only causes a uniform frequency shift of the signal from every crystallite; this is the isotropic frequency. The third term in brackets in Equation (2.8) contains terms oscillating with frequency ω_r and $2\omega_r$. This causes the signal from each crystallite to break up into a series of peaks at multiples of the spinning frequency, centred about the isotropic frequency; these are the spinning sidebands. As the sample spinning frequency is increased, the intensity of the spinning sidebands diminishes, and if sufficiently fast spinning is used, only the isotropic peak is observed. This is shown by the example of a
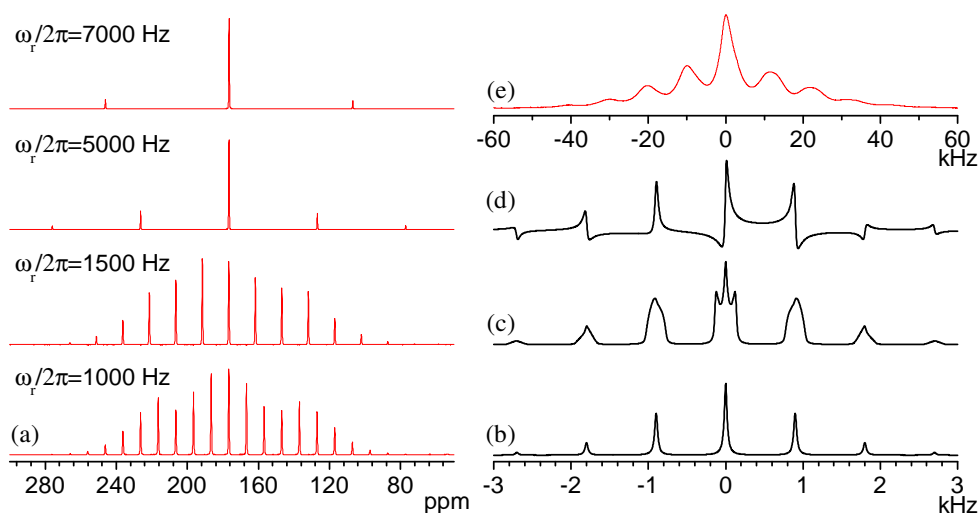
Figure 2.2: (a) Experimental MAS ^{13}C NMR spectrum of ^{13}C-1-α-glycine (powder sample) showing spinning sidebands at four different spinning frequencies. (b) Simulated MAS spinning sideband spectrum for a powder sample using $-\Delta_{CS}\omega_0/2\pi$ = 2000 Hz, η_{CS} = 1, $\omega_r/2\pi$ = 900 Hz. (c) As in (b) but with β_{RL} = 52°. (d) As in (b) but for a single crystal sample with arbitrary orientation Ω_{PR} = $\{-30, -20, -40\}$. (e) Experimental ^{1}H NMR spectrum of α-glycine, showing the broad spinning sidebands due to homonuclear dipolar coupling.

powder sample of α-glycine in Figure 2.2(a), where $\beta_{RL} = \tan^{-1}\sqrt{2}$ was used.

The second term in Equation (2.2) is time independent and causes a shift in the frequency of all the spinning sidebands; however, the frequency shift depends on the crystallite orientation and the rotor orientation. If $\beta_{RL} = \tan^{-1}\sqrt{2}$, dubbed the *magic angle*, then the second term is zero and the spinning sidebands are sharp, and the technique is referred to as magic-angle spinning (MAS). Away from this angle, a powder pattern will result at each spinning sideband if a powder sample is used, as shown in Figure 2.2(c). If a single crystal is used, then for a general orientation, not all the spinning sidebands in the spectrum are absorption lineshapes; for example see Figure 2.2(d). Only when there is a uniform distribution of crystallites over all possible values of γ, for each crystallite orientation $\{\alpha, \beta\}$, do absorption lineshapes occur for each spinning sideband.[43]

If the internal Hamiltonian is dynamically homogeneous, rather different behaviour occurs. This situation generally occurs when homonuclear dipolar coupling interactions are present. The propagator cannot be evaluated by integrating the rotating-frame Hamiltonian, but must be determined (numerically) according to Equation (1.37) on page 10. The overall result is that the static powder pattern does not break up into sharp spinning sidebands, and even at moderate spinning frequencies broad spinning sidebands occur. An example of the proton spectrum from a powder sample of α-glycine using MAS at 10 kHz is shown in Figure 2.2(e). Very fast spinning is usually required to achieve a
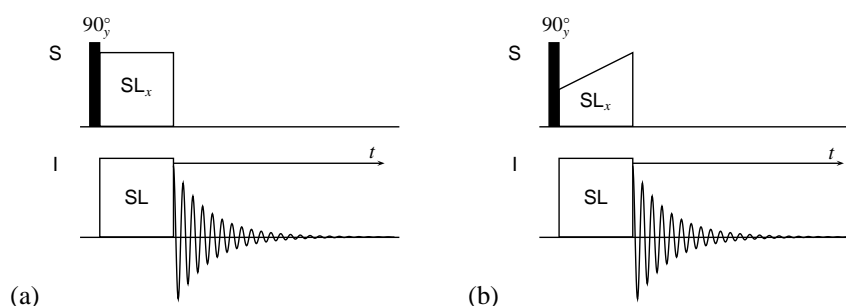
Figure 2.3: The cross polarization pulse sequence with (a) a constant amplitude spin-lock field and (b) a ramped amplitude spin-lock field applied to the S spin.

significant improvement in resolution.[13]

There are a number of practical considerations when implementing MAS, as it can cause undesirable effects on the sample. Friction leads to sample heating that may affect the structure of the sample, either through a phase change in the material or denaturing of a biological sample, or can cause dehydration. Moreover, the forces exerted on the sample may be significant and induce a structure or phase change. This is especially important for biological samples.

2.1.2 Cross polarization

A common problem encountered when studying a rare spin nucleus is the weak NMR signals obtained by direct excitation of the nuclei using a 90° pulse. If an abundant nucleus with large magnetogyric ratio is present in the sample, then the rare spin signal intensity can be enhanced using cross polarization (CP),[44,45] whereby magnetization is transferred from the abundant spins to the rare spin. This method is ubiquitous in ^{13}C and ^{15}N NMR of organic solids, where magnetization is transferred from the abundant ^{1}H spins to the observed nucleus.

The pulse sequence for this experiment is illustrated in Figure 2.3(a). Following initial direct excitation of the abundant S spin by a 90°_y pulse that rotates the S spin magnetization parallel to the x-axis of the S spin rotating frame, a spin-lock field is applied along the x-axis of this rotating frame and simultaneously in the transverse plane of the rare I spin rotating frame. The term 'spin lock' arises from the precession in the rotating frame due to resonance offsets being effectively suppressed if the RF field strength associated with the spin lock is sufficiently strong, and the magnetization is aligned (locked) along this field.

During the application of the spin-lock field, magnetization is transferred from the S spin to the I spin provided that the Hartmann-Hahn match $\omega_1^I = \omega_1^S$ is fulfilled,[46] where ω_1^I and ω_1^S are the RF field strengths of the I and S spin-lock fields. This transfer is mediated by the dipolar coupling between the two spins. This can be verified by analysis of a heteronuclear spin pair using average Hamiltonian theory. The rotating-frame Hamiltonian in the presence of the spin-lock field is

$$\hat{\mathcal{H}} = b_{IS} \left(3 \cos^2 \theta_D - 1 \right) \hat{I}_z \hat{S}_z + \omega_1^I \hat{I}_x + \omega_1^S \hat{S}_x, \tag{2.13}$$

where b_{IS} and θ_D were defined in Section 1.11. Transforming into the interaction frame of the $\omega_1^I \hat{I}_x + \omega_1^S \hat{S}_x$ part of this Hamiltonian, the interaction frame Hamiltonian is

$$\hat{\mathcal{H}}^*(t) = b_{IS} \left(3 \cos^2 \theta_D - 1 \right) \left[\hat{I}_z \cos(\omega_1^I t) + \hat{I}_y \sin(\omega_1^I t) \right] \left[\hat{S}_z \cos(\omega_1^S t) + \hat{S}_y \sin(\omega_1^S t) \right]. \tag{2.14}$$

Imposing the Hartmann-Hahn condition and calculating the first-order average Hamiltonian over $t_c = 1/2\pi\omega_1^I$ (where $\hat{\mathcal{H}}^*(t + t_c) = \hat{\mathcal{H}}^*(t)$) gives

$$\overline{\hat{\mathcal{H}}^{*(1)}} = \frac{b_{IS}}{2} \left(3 \cos^2 \theta_D - 1 \right) \left[\hat{I}_z \hat{S}_z + \hat{I}_y \hat{S}_y \right] = B_{IS} \left[\hat{I}_z \hat{S}_z + \hat{I}_y \hat{S}_y \right], \tag{2.15}$$

where $B_{IS} = \frac{b_{IS}}{2}(3 \cos^2 \theta_D - 1)$. Equation (2.15) shows that there is a non-zero first-order average Hamiltonian governing the spin system during the spin-lock field. The propagator of the rotating-frame density operator is

$$\hat{U}(t) = \exp\left[-iB_{IS} \left(\hat{I}_z \hat{S}_z + \hat{I}_y \hat{S}_y \right) t \right] = \exp\left[-i\hat{I}_z \hat{S}_z B_{IS} t \right] \exp\left[-i\hat{I}_y \hat{S}_y B_{IS} t \right], \tag{2.16}$$

where the commutator $\left[\hat{I}_z \hat{S}_z, \hat{I}_y \hat{S}_y \right] = 0$ (which is valid for spin-1/2 I and S) allows the exponential operator in Equation (2.16) to be written as the product of two separate exponential operators. After the 90_y°-pulse, the rotating-frame density operator is given by $\hat{\rho}(0) = \hat{S}_x$, omitting the $\hat{I}_z$ term. The density operator at a later time is given by

$$\hat{\rho}(t) = e^{\left(-i\hat{I}_z \hat{S}_z B_{IS} t \right)} e^{\left(-i\hat{I}_y \hat{S}_y B_{IS} t \right)} \hat{S}_x e^{\left(i\hat{I}_y \hat{S}_y B_{IS} t \right)} e^{\left(i\hat{I}_z \hat{S}_z B_{IS} t \right)}. \tag{2.17}$$

Equation (2.17) is evaluated using $\exp\left[-i\theta\hat{A} \right] \hat{B} \exp\left[+i\theta\hat{A} \right] = \hat{B} \cos \kappa\theta + \hat{C} \sin \kappa\theta$ which applies for operators $\hat{A}$, $\hat{B}$, $\hat{C}$ that obey cyclic commutators of the form $\left[\hat{A}, \hat{B} \right] = i\kappa\hat{C}$, together with the specific cyclic commutators (for spin-1/2 I and S) $\left[2\hat{I}_y \hat{S}_y, \hat{S}_x \right] = -i2\hat{I}_y \hat{S}_z$,

$\left[2\hat{I}_z\hat{S}_z, \hat{S}_x\right] = \mathrm{i}2\hat{I}_z\hat{S}_y$ and $\left[2\hat{I}_z\hat{S}_z, 2\hat{I}_y\hat{S}_z\right] = -\mathrm{i}\hat{I}_x$. This gives

$$
\begin{aligned}
\hat{\rho}(t) &= \mathrm{e}^{\left(-\mathrm{i}\hat{I}_z\hat{S}_z B_{IS} t\right)} \left[\hat{S}_x \cos\left(\tfrac{B_{IS}}{2}t\right) - \hat{I}_y\hat{S}_z \sin\left(\tfrac{B_{IS}}{2}t\right)\right] \mathrm{e}^{\left(\mathrm{i}\hat{I}_z\hat{S}_z B_{IS} t\right)} \\
&= \hat{S}_x \cos^2\left(\tfrac{B_{IS}}{2}t\right) + \hat{I}_z\hat{S}_y \cos\left(\tfrac{B_{IS}}{2}t\right)\sin\left(\tfrac{B_{IS}}{2}t\right) - \hat{I}_y\hat{S}_z \sin\left(\tfrac{B_{IS}}{2}t\right)\cos\left(\tfrac{B_{IS}}{2}t\right) + \hat{I}_x \sin^2\left(\tfrac{B_{IS}}{2}t\right) \\
&= \frac{1}{2}\left(1 + \cos(B_{IS}t)\right)\hat{S}_x + \frac{1}{2}\left(1 - \cos(B_{IS}t)\right)\hat{I}_x + \frac{1}{2}\sin(B_{IS}t)\left[\hat{I}_z\hat{S}_y - \hat{I}_y\hat{S}_z\right]. \qquad (2.18)
\end{aligned}
$$

Equation (2.18) predicts an oscillation of the initial transverse S-spin magnetization between the two spins. The maximum signal intensity of the I spin is determined by the Boltzmann factor of the S spin and, relative to direct excitation, there is a maximum enhancement of the I spin signal by a factor of γ_S/γ_I (the ratio of their magnetogyric ratios). The predicted oscillatory behaviour is not seen for the typical experimental situation where the abundant S spins are part of a homonuclear dipolar coupled network, partly because there is interference from multiple heteronuclear dipolar couplings, but more importantly the coupling between the homonuclear spins causes damping of these oscillations. Typically, the build up of magnetization approaches its final value approximately exponentially over time. A thermodynamic treatment leads to the same conclusion of a maximum enhancement in the I spin signal by γ_S/γ_I.[47]

Under static conditions, a plot of the I spin signal intensity following CP as a function of ω_1^I (the matching profile) gives a peak centred at the Hartmann-Hahn match that has a width of the order of the strength of the $I - S$ heteronuclear dipolar coupling. When MAS is used with CP, the matching profile breaks up into a series of relatively sharp peaks separated by the spinning frequency. This arises because the $(3\cos^2\theta_D - 1)$ factor in Equation (2.14) is time dependent under MAS and the first-order average Hamiltonian (evaluated over one rotor period) is zero unless the modified Hartmann-Hahn condition $\omega_1^I - \omega_1^S = \pm n\omega_r$ is fulfilled, where ω_r is the spinning frequency and $n = 1$ or 2. In this case the time dependence of the spatial part of the heteronuclear dipolar coupling is cancelled by the time dependence of the spin operator part of the Hamiltonian,[48] leading to a non-zero first-order average Hamiltonian over one rotor period. In addition, MAS averaging of the homonuclear dipolar coupling of the S spins contributes to this effect.[49]

The narrower matching condition with increasing spinning frequency is undesirable, because it proves difficult to optimise CP for samples with a low sensitivity. The matching profile can be restored to a broad shape by modulating the spin-lock field strength[50] or the RF phase[51] during the CP process. A commonly used method is a linear ramp of the RF field strength for one nucleus during the spin locking, as presented in Figure 2.3(b) on page 41.

The gain in intensity is a great advantage for rare spins, as an n-fold increase in signal intensity by using cross-polarization reduces the number of acquisitions required to achieve the desired signal-to-noise ratio by a factor of $1/n^2$. A second advantage is that the spin-lattice relaxation time of protons is often much shorter than that of the observed rare spin. The delay between acquisitions in a cross-polarisation experiment is determined by the spin-lattice relaxation time of the protons, and so the time required to obtain a specific signal-to-noise ratio is further reduced.

2.1.3 Heteronuclear dipolar decoupling

In the NMR spectra of rare spins in organic solids, such as ^{13}C or ^{15}N, broad peaks are generally observed, even when using magic-angle spinning. The dominant contribution to the line-width is from dipolar coupling to the abundant ^{1}H nuclei, which are themselves homonuclear dipolar coupled to each other. Line narrowing is achieved by heteronuclear decoupling.

The simplest method of heteronuclear decoupling is contiuous irradiation of the S spin with a fixed RF phase during the experiment. This is referred to as continuous-wave (CW) decoupling. A simple analysis can be made using an average Hamiltonian approach, similar to that used for analysis of CP in Section 2.1.2. The rotating-frame Hamiltonian during irradation of the S spin, including only the heteronuclear dipolar coupling internal interaction, is

$$\hat{\mathcal{H}} = b_{IS}(3\cos^2\theta_D - 1)\hat{I}_z\hat{S}_z + \omega_1^S\hat{I}_x \tag{2.19}$$

After transformation into the interaction representation of the RF Hamiltonian $\omega_1^S\hat{I}_x$, the interaction-frame Hamiltonian is

$$\hat{\mathcal{H}}_{IS}^*(t) = b_{IS}(3\cos^2\theta_D - 1)\hat{I}_z\left(\hat{S}_z\cos(\omega_1^S t) + \hat{S}_y\sin(\omega_1^S t)\right). \tag{2.20}$$

Calculating the average Hamiltonian over $t_c = 2\pi/\omega_1^S$, (since the $\hat{\mathcal{H}}_{IS}^*(t)$ is periodic with period t_c), the heteronuclear dipolar coupling term in the first-order average Hamiltonian is zero, indicating that decoupling is achieved. This simple analysis, of course, neglects the effects of resonance offsets, homonuclear dipolar coupling of the abundant spin and MAS, which can all reduce the efficiency of CW decoupling.

Experimentally, it is usually found that CW decoupling gives reduced linewidths with increasing RF field strengths, but becomes less effective with increasing spinning
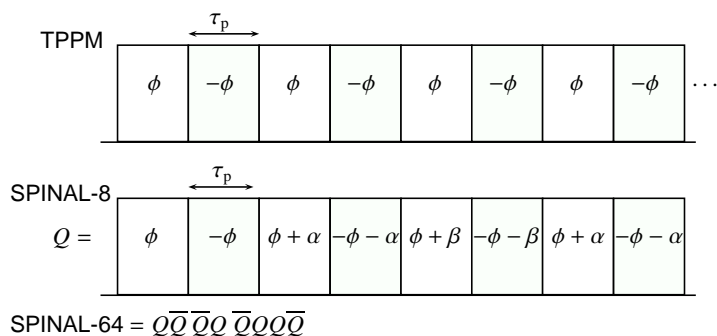
Figure 2.4: The Two Pulse Phase Modulation (TPPM) and Small Phase INcremental ALternation (SPINAL) heteronuclear decoupling sequences. SPINAL-64 is constructed as a super-cycle of SPINAL-8, where $\overline{Q}$ indicates that all the pulse phases are opposite in sign to those of SPINAL-8. For optimal performance, $\omega_1\tau_p \approx (10/12)\pi$ and $\phi \approx 10°$ for TPPM; for SPINAL-64 $\omega_1\tau_p \approx (11/12)\pi$, $\phi = 10°$, $\alpha = 5°$ and $\beta = 10°$.[54]

frequencies. Probe hardware imposes a practical limit on the RF field strength that can be used for decoupling, and has driven the development of more robust decoupling schemes that use a phase modulation of the decoupling RF field to give superior line-narrowing than CW decoupling under sample spinning conditions. Two examples include two-pulse phase modulation (TPPM)[52] and small phase incremental alternation (SPINAL),[53,54] which have both been used in this thesis and are detailed in Figure 2.4. The caption of Figure 2.4 includes details of the optimum pulse durations and phase modulations that are used for these sequences,[54] although in practice they are optimised for each sample. Two recent reviews have compared different heteronuclear decoupling schemes, both experimentally and theoretically.[55,56]

2.2   Two-dimensional NMR experiments

One-dimensional spectra often suffer from the overlap of different peaks, and are also limited in the information that can be extracted. Two-dimensional experiments can be used to resolve overlapping signals, by separating the signals over a second dimension. Also, two-dimensional experiments can be utilised to correlate different signals present in the one-dimensional spectrum, or even in the one-dimensional spectra of different nuclei, according to some property such as close spatial proximity. Other multi-dimensional experiments can probe molecular motion and chemical exchange.

For example, an experiment of particular interest in this dissertation involves separation of chemical shift powder patterns in a two-dimensional experiment, with the spectra correlating a high resolution MAS spectrum in one dimension with powder pattern
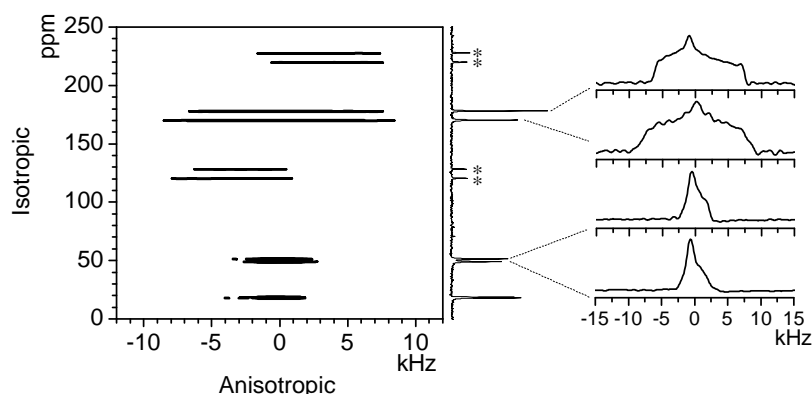
Figure 2.5: An example of a ^{13}C two-dimensional chemical shift powder pattern separation experiment for the dipeptide Ala-Ala. Cross-sections through four peaks in the high resolution dimension are shown. Asterisks indicate spinning sidebands.

lineshapes in the other. This is illustrated in Figure 2.5.

In a one-dimensional experiment, the evolution of the spin system is recorded as a function of a single time variable. In a two-dimensional experiment, the evolution of the spin system is (effectively) recorded as a function of two separate time periods. The general form of a two-dimensional experiment is shown in Figure 2.6. The preparation pulses create coherences that evolve during the t_1 evolution period. This is followed by a mixing period that converts the coherences present at the end of the t_1 period to those of interest during the signal detection. The pulses used during the mixing period determine the type of correlations seen between different signals. A mixing period may not be required for two-dimensional experiments designed to resolve overlapping peaks, but a different effective Hamiltonian must govern the spin system during the t_1 and t_2 periods. It is worth noting that two-dimensional experiments are not limited to recording the evolution of only single-quantum coherences in the indirectly-detected evolution dimension.

During a two-dimensional experiment, a series of one-dimensional experiments are
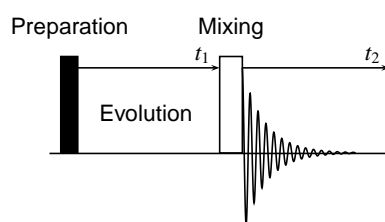

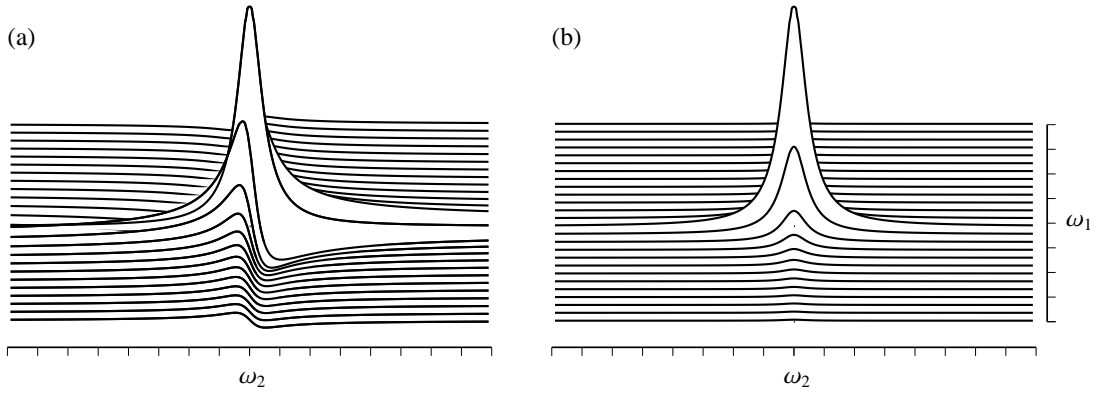Figure 2.6: General scheme for a two-dimensional NMR experiment.

Figure 2.7: The real part of (a) the phase twist lineshape and (b) the double absorption lineshape.

performed with the t_1 period is incremented (or effectively incremented) and the resulting FID measured during the t_2 period is stored. These separate experiments are combined to form a two-dimensional dataset. The FID for each t_1 value is the same as in a simple one-dimension experiment, except that each point in the FID is phase-modulated or amplitude-modulated[*] by the evolution that occurred during the t_1 time period. The two-dimensional dataset is Fourier transformed in both time dimensions to produce a two-dimensional frequency spectrum. The details of this process are described in the following section.

2.2.1 Lineshapes in two-dimensional NMR

As in one-dimensional NMR, the lineshapes in a two-dimensional spectrum can contain absorptive and dispersive contributions to the lineshapes. It is desirable to plot spectra that have pure absorption lineshapes in both dimensions, owing to the broad base of the lineshapes of the phase-twisted lineshape that occurs when there are mixed absorption and dispersion contributions; the two lineshapes are compared in Figure 2.7. If a single (cosine) amplitude-modulated two-dimensional dataset is recorded, then the signal is[57]

$$s_{\cos}(t_1, t_2) = \cos(\Omega_1 t_1) \exp(\mathrm{i}\Omega_2 t_2) \exp(-t_1/T_{2,1}) \exp(-t_2/T_{2,2}), \qquad (2.21)$$

where Ω_1 and Ω_2 are the evolution frequencies of the spins during the two time periods, and $T_{2,1}$ and $T_{2,2}$ their corresponding transverse relaxation time constants. After Fourier transformation in the second time dimension (t_2), one obtains

$$S'_{\cos}(t_1, \omega_2) = \tfrac{1}{2}\{\exp(\mathrm{i}\Omega_1 t_1) + \exp(-\mathrm{i}\Omega_1 t_1)\} \exp(-t_1/T_{2,1})\{\mathcal{A}_2 + \mathrm{i}\mathcal{D}_2\}, \qquad (2.22)$$

---

[*]Whether the signal is phase- or amplitude-modulated is determined by the precise pulse sequence used.

where $\mathcal{A}_2$ and $\mathcal{D}_2$ are absorption and dispersion Lorentzian lineshapes defined in Equation (1.73) on page 21, and the subscript 2 indicates they are function of the F_2 frequency. Fourier transformation of the first time dimension (t_1) gives

$$S_{\cos}(\omega_1, \omega_2) = \tfrac{1}{2}\{\mathcal{A}_1^+ + i\mathcal{D}_1^+ + \mathcal{A}_1^- + i\mathcal{D}_1^-\}\{\mathcal{A}_2 + i\mathcal{D}_2\}, \qquad (2.23)$$

where the superscript + and − refer to Lorentzian lineshapes located at $+\Omega_1$ and $-\Omega_1$ in the first frequency dimension (F_1) respectively. The real part of $S_{\cos}(\omega_1, \omega_2)$ contains both absorptive and dispersive components that cannot be separated by phasing the spectrum:

$$\mathrm{Re}[S_{\cos}(\omega_1, \omega_2)] = \tfrac{1}{2}\{(\mathcal{A}_1^+\mathcal{A}_2 - \mathcal{D}_1^+\mathcal{D}_2) + (\mathcal{A}_1^-\mathcal{A}_2 - \mathcal{D}_1^-\mathcal{D}_2)\}. \qquad (2.24)$$

In addition, discrimination of the sign of Ω_1 is not possible, so this form of spectrum is highly undesirable. In order to obtain double-absorption lineshapes, two datasets must be recorded and combined during the data processing. Methods are described here for amplitude-modulated signals and phase-modulated signals; that is, signals recorded in the t_2 period which are modulated according to the amplitude, or phase, of the desired coherences at the end of the t_1 period.

(i) Amplitude-modulated signals

If amplitude-modulated signals are detected in an experiment, then both sine- and cosine-modulated datasets must be recorded. Following Fourier transform of the two-dimensional FID with respect to t_2, one has

$$S'_{\cos}(t_1, \omega_2) = \cos(\Omega_1 t_1)\exp(-t_1/T_{2,1})\{\mathcal{A}_2 + i\mathcal{D}_2\} \qquad (2.25)$$

$$S'_{\sin}(t_1, \omega_2) = \sin(\Omega_1 t_1)\exp(-t_1/T_{2,1})\{\mathcal{A}_2 + i\mathcal{D}_2\}. \qquad (2.26)$$

The real parts of these two datasets are used to form a new complex data set $S'_{\text{States}}(t, \omega_2)$, which is Fourier transformed in the t_1 dimension to give the spectrum $S_{\text{States}}(\omega_1, \omega_2)$

$$S'_{\text{States}}(t_1, \omega_2) = \mathrm{Re}[S'_{\cos}(t_1, \omega_2)] + i\mathrm{Re}[S'_{\sin}(t_1, \omega_2)]$$

$$= \exp(i\Omega_1 t_1)\exp(-t_1/T_{2,1})\mathcal{A}_2$$

$$S_{\text{States}}(\omega_1, \omega_2) = \{\mathcal{A}_1^+ + i\mathcal{D}_1^+\}\mathcal{A}_2. \qquad (2.27)$$

The real part of $S_{\text{States}}(\omega_1, \omega_2)$ is in double-absorption mode (it contains no dispersive component in either frequency dimension), and frequency discrimination is achieved.

This is referred to as the States method.[58] An alternative approach is the Time Proportional Phase Incrementation (TPPI) method of Marion and Würtrich.[59] TPPI was not used in this dissertation and so is not discussed further.

(ii) Phase-modulated signals

If phase-modulated signals are detected in a two-dimensional experiment, two separate datasets are also recorded. The phase modulation of one dataset is in the opposite sense to that of the other during the t_1 period, and they are processed according to the echo anti-echo method.[60] Distinguishing the echo and anti-echo phase-modulated signals by the subscripts $-$ and $+$ respectively, after Fourier transformation of the t_2 dimension the two datasets are

$$S'_+(t_1, \omega_2) = \exp(+i\Omega_1 t_1)\exp(-t_1/T_{2,1})\{\mathcal{A}_2 + i\mathcal{D}_2\} \qquad (2.28)$$

$$S'_-(t_1, \omega_2) = \exp(-i\Omega_1 t_1)\exp(-t_1/T_{2,1})\{\mathcal{A}_2 + i\mathcal{D}_2\}. \qquad (2.29)$$

A new dataset, $S'_{\text{E-AE}}(t_1, \omega_2)$, is constructed by summing the S'_+ dataset with the complex conjugate of the S'_- dataset. Following this, Fourier transformation of $S'_{\text{E-AE}}(t_1, \omega_2)$ in the t_1 dimension is performed to give the spectrum $S_{\text{E-AE}}(\omega_1, \omega_2)$

$$S'_{\text{E-AE}}(t_1, \omega_2) = S'_+(t_1, \omega_2) + [S'_-(t_1, \omega_2)]^*$$

$$= 2\exp(i\Omega_1 t)\exp(-t_1/T_{2,1})\mathcal{A}_2$$

$$S_{\text{E-AE}}(\omega_1, \omega_2) = 2\{\mathcal{A}_1^+ + i\mathcal{D}_1^+\}\mathcal{A}_2. \qquad (2.30)$$

As for the States method, frequency sign discrimination and pure absorption lineshapes are obtained.

2.3   Phase cycling

The effect of an RF pulse is to convert coherences of one order to another:

$$\rho_{nm} \overset{\text{Pulse}}{\to} \rho_{qp} + \text{other coherences,}$$

where ρ_{nm} and ρ_{qp} are elements of the matrix representation of the density operator. In a multiple-pulse experiment, coherence-transfer pathways (CTPs) describe the sequence of coherence orders that finally lead a (-1)-quantum coherence giving rise to the detected
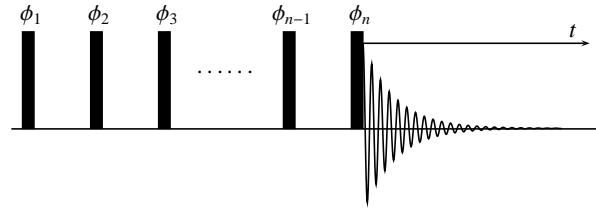
Figure 2.8: A generic pulse sequence. The angle above each pulse represents the RF phase of the pulse.

signal. Generally, a number of different CTPs will contribute to the detected signal, but usually only a small set of these are of interest while the other CTPs contribute unwanted signal to the FID.

The different CTPs may be distinguished by the effect that the RF phase ϕ has upon the coherences generated by a pulse. It may be shown that the coherences generated by a pulse with RF phase ϕ acquire an additional phase $-\phi\Delta p$,[61] relative to when an x-pulse ($\phi = 0$) is used, where Δp is the change in coherence order caused by the pulse. That is,

$$\rho_{nm} \xrightarrow{\text{Pulse } \phi=0} \rho_{qp} + \rho_{sr} + \dots$$
$$\rho_{nm} \xrightarrow{\text{Pulse } \phi\neq0} \rho_{qp} \exp\left[-i\phi(p_{qp} - p_{nm})\right] + \rho_{sr} \exp\left[-i\phi(p_{sr} - p_{nm})\right] + \dots,$$

where p_{nm} is the coherence order of the coherence represented by the element ρ_{nm} of the matrix representation of the density operator. The additional phase shift generated by the pulse will be carried forward to the (-1)-quantum coherence that eventually contributes to the detected signal.

Considering the generic pulse sequence in Figure 2.8, with pulses labelled $1, 2, 3, \dots, n$, a CTP can be concisely described by a vector $\boldsymbol{p} = [p_{0,1}, p_{1,2}, p_{2,3}, \dots, p_{(n-1),n}]$, where $p_{i,j}$ is the coherence order in the pathway between the ith and j^{th} pulses. In the case that all the pulse phases and receiver phase ϕ_{rec} (see Section 1.7) are set to zero, the signal contains contributions from all possible CTPs and can be represented as

$$S(t; 0, 0, 0, \dots) = \sum_{\boldsymbol{p}=\text{all possible}} S_{\boldsymbol{p}}(t; 0, 0, 0, \dots), \tag{2.31}$$

where the summation is over all the possible CTPs. For a set of pulses with phases $\phi_1, \phi_2, \phi_3 \dots \phi_n$, the signal detected has a phase shift relative to the signal detected with all

phases set to zero. The two signal are related by

$$S_{\boldsymbol{p}}(t; \phi_1^{(m)}, \phi_2^{(m)}, \phi_3^{(m)}, \dots) = S_{\boldsymbol{p}}(t; 0, 0, 0, \dots) \exp\left[-i\Phi^{(m)}(\boldsymbol{p})\right] \tag{2.32}$$

$$\Phi^{(m)}(\boldsymbol{p}) = \phi_1^{(m)}\Delta p_1 + \phi_2^{(m)}\Delta p_2 + \phi_3^{(m)}\Delta p_3 + \cdots + \phi_n^{(m)}\Delta p_n + \phi_{\text{rec}}^{(m)}, \tag{2.33}$$

where $\Delta p_i = (p_{i,i+1} - p_{i-1,i})$ is the change in coherence order at the ith pulse and, for coherence-transfer pathway $\boldsymbol{p}$, $\Phi^{(m)}(\boldsymbol{p})$ is called the coherence pathway phase. The superscript (m) has been introduced to indicate a particular set of pulse phases.

Phase cycling involves repeating the acquisition of the FID N times with some, or all, of the pulse and receiver phases changed between each scan in such a way that the contributions to the signal from the desired CTPs add constructively, whilst the signals from unwanted CTPs average to zero. If the phase cycle has N steps, with the set of phases for the mth step indicated by the superscript (m), the phase cycle must fulfil the the condition:

$$\frac{1}{N}\sum_{m=0}^{N-1} S_{\boldsymbol{p}}(t; \phi_1^{(m)}, \phi_2^{(m)}, \phi_3^{(m)}, \dots) = \frac{1}{N}\sum_{m=0}^{N-1} S_{\boldsymbol{p}}(t; 0, 0, 0, \dots) \exp\left[-i\Phi^{(m)}(\boldsymbol{p})\right] \tag{2.34}$$

$$= \begin{cases} S_{\boldsymbol{p}}(t; 0, 0, 0, \dots) \text{ if } \boldsymbol{p} \in \{\boldsymbol{p}^0, \boldsymbol{p}^{0'}, \boldsymbol{p}^{0''}, \dots\} \\ 0 \text{ otherwise} \end{cases} ;$$

$$\tag{2.35}$$

or more concisely, it is required that

$$\frac{1}{N}\sum_{m=0}^{N-1} \exp\left[-i\Phi^{(m)}(\boldsymbol{p})\right] = \begin{cases} 1 \text{ if } \boldsymbol{p} \in \{\boldsymbol{p}^0, \boldsymbol{p}^{0'}, \boldsymbol{p}^{0''}, \dots\} \\ 0 \text{ otherwise} \end{cases}, \tag{2.36}$$

where $\{\boldsymbol{p}^0, \boldsymbol{p}^{0'}, \boldsymbol{p}^{0''}, \dots\}$ is the set of desired CTPs, and m is the phase cycle step with pulse phases $\phi_i^{(m)}$. Two approaches to achieved this are used: nested phase cycling and cogwheel phase cycling, both of which are used in this work.

2.3.1   Nested phase cycling

In the nested phase cycling scheme, the phase of each pulse is incremented independently following the scheme for the ith pulse: $\phi_i = 2\pi k_i/N_i$, with k_i incremented from 0 to $(N_i - 1)$. Each pulse has its phase cycled independently of all others in the pulse sequence, so the

total number of steps is $N = \prod_{i=1}^{n} N_i$.[61] The coherence pathway phase is

$$\Phi^{(m)}(\boldsymbol{p}) = + \frac{2\pi k_1^{(m)}}{N_1} \Delta p_1 + \frac{2\pi k_2^{(m)}}{N_2} \Delta p_2 + \frac{2\pi k_3^{(m)}}{N_3} \Delta p_3 \cdots + \frac{2\pi k_n^{(m)}}{N_n} \Delta p_n + \phi_{\text{rec}}^{(m)}, \tag{2.37}$$

with

$$k_1^{(m)} = m, \ k_2^{(m)} = \text{Floor}\,[m/N_1]\,, \ k_3^{(m)} = \text{Floor}\left[\frac{\text{Floor}\,[m/N_1]}{N_2}\right], \ldots, \ k_i^{(m)} = \text{Floor}\,[k_{i-1}/N_{i-1}]\,, \tag{2.38}$$

where Floor[x] is a function that returns the highest integer not greater than x, and m is the phase cycle step.

To ensure that the signal from the desired CTP $\boldsymbol{p}^0$ accumulates constructively, the receiver phase must be adjusted so that $\Phi^{(m)}(\boldsymbol{p}^0) = 0$ for all m:

$$\phi_{\text{rec}}^{(m)} = -\frac{2\pi k_1^{(m)}}{N_1} \Delta p_1^0 - \frac{2\pi k_2^{(m)}}{N_2} \Delta p_2^0 - \frac{2\pi k_3^{(m)}}{N_3} \Delta p_3^0 \cdots - \frac{2\pi k_n^{(m)}}{N_n} \Delta p_n^0, \tag{2.39}$$

where $\Delta p_i^0 = (p_{i,i+1}^0 - p_{i-1,i}^0)$ is the desired change in coherence order at the ith pulse.

Substituting Equation (2.39) into Equation (2.37), the summation in Equation (2.36) takes the form:

$$\frac{1}{N} \sum_{k_1=0}^{N_1-1} \sum_{k_2=0}^{N_2-1} \sum_{k_2=0}^{N_3-3} \cdots \sum_{k_n=0}^{N_n-1} \exp\left[-\mathrm{i}\frac{2\pi k_1(\Delta p_1 - \Delta p_1^0)}{N_1}\right] \exp\left[-\mathrm{i}\frac{2\pi k_2(\Delta p_2 - \Delta p_2^0)}{N_2}\right]$$
$$\times \exp\left[-\mathrm{i}\frac{2\pi k_3(\Delta p_3 - \Delta p_3^0)}{N_3}\right] \cdots \exp\left[-\mathrm{i}\frac{2\pi k_n(\Delta p_n - \Delta p_n^0)}{N_n}\right]. \tag{2.40}$$

Equation (2.40) is readily evaluated by considering each summation

$$\sum_{k_i=0}^{N_i-1} \exp\left[-\mathrm{i}\frac{2\pi k_i(\Delta p_i - \Delta p_i^0)}{N_i}\right] = \sum_{k_i=0}^{N_i-1} \exp\left[-\mathrm{i}\frac{2\pi k_i \Xi_i}{N_i}\right], \tag{2.41}$$

where $\Xi_i = (\Delta p_i - \Delta p_i^0)$, as the sum of a geometric series. Using the summation formula for a geometric series gives

$$\sum_{k_i=0}^{N_i-1} \exp\left[-\mathrm{i}\frac{2\pi \Xi_i}{N_i}\right]^{k_i} = \frac{1 - \left\{e^{-\mathrm{i}2\pi\Xi_i/N_i}\right\}^{N_i}}{1 - e^{-\mathrm{i}2\pi\Xi_i/N_i}}. \tag{2.42}$$

The summation in Equation (2.41) is clearly equal to N_i if $\Xi = Z_i N_i$ (where Z_i is any integer), or equivalently $\Delta p_i = \Delta p_i^0 + Z_i N_i$, as each term in the geometric series is one.

From Equation (2.42), the summation is zero for $\Xi_i \neq Z_i N_i$. Thus, at the ith pulse, the nested phase cycle selects CTPs with the desired coherence order change Δp_i^0, and all other CTPs that differ in the change in coherence order at the ith pulse by a multiple of N_i. By choosing appropriate values of N_i for each pulse, a single pathway (or set of desired pathways) can be selected for an entire pulse sequence.

2.3.2   Cogwheel phase cycling

The recently reported cogwheel phase cycling scheme[62] is slightly different to nested phase cycling: the phases of *all* pulses may be incremented on consecutive acquisitions, with the phase of the ith pulse determined by

$$\phi_i^{(m)} = \frac{2\pi m \nu_i}{N},\tag{2.43}$$

where N is the total number of steps in the phase cycle, m is the phase cycle step number and ν_i is dubbed the winding number of the ith pulse.[62] The coherence pathway phase in terms of the winding numbers is

$$\Phi^{(m)}(\boldsymbol{p}) = \frac{2\pi m}{N}\left(\nu_1 \Delta p_1 + \nu_2 \Delta p_2 + \nu_3 \Delta p_3 + \cdots + \nu_n \Delta p_n + \nu_{\text{rec}}\right).\tag{2.44}$$

Defining $\Delta \nu_{q,q+q} = \nu_{q+1} - \nu_q$, and expanding the $\Delta p_k = (p_{k,k+1} - p_{k-1,k})$ terms allows Equation (2.44) to be rewritten as

$$\Phi^{(m)}(\boldsymbol{p}) = -\frac{2\pi m}{N}\left(\nu_1 p_{0,1} + \Delta \nu_{1,2} p_{1,2} + \Delta \nu_{2,3} p_{2,3} + \cdots + \Delta \nu_{n-1,n} p_{n-1,n} - \nu_n p_{n,\text{rec}} - \nu_{\text{rec}}\right).\tag{2.45}$$

The initial coherence order is zero for a spin system at thermal equilibrium, so $p_{0,1} = 0$ for all CTPs. The receiver phase must be cycled to ensure that the desired CTP $\boldsymbol{p}^0$ is selected. This requires that

$$\nu_{\text{rec}} = \Delta \nu_{1,2} p_{1,2}^0 + \Delta \nu_{2,3} p_{2,3}^0 + \cdots + \Delta \nu_{n-1,n} p_{n-1,n}^0 - \nu_n p_{n,\text{rec}}^0.\tag{2.46}$$

So the coherence pathway phase $\Phi^{(m)}(\boldsymbol{p})$ is written as

$$
\Phi^{(m)}(\boldsymbol{p}) = -\frac{2\pi m}{N}\Big(\Delta\nu_{1,2}(p_{1,2} - p_{1,2}^0) + \Delta\nu_{2,3}(p_{2,3} - p_{2,3}^0) + \ldots
$$

$$
+\Delta\nu_{n-1,n}(p_{n-1,n} - p_{n-1,n}^0) - \nu_n(p_{n,\mathrm{rec}} - p_{n,\mathrm{rec}}^0)\Big) \tag{2.47}
$$

$$
= \frac{2\pi m}{N}\Lambda \tag{2.48}
$$

$$
\text{where } \Lambda = -\Big(\Delta\nu_{1,2}(p_{1,2} - p_{1,2}^0) + \Delta\nu_{2,3}(p_{2,3} - p_{2,3}^0) + \ldots
$$

$$
+\Delta\nu_{n-1,n}(p_{n-1,n} - p_{n-1,n}^0) - \nu_n(p_{n,\mathrm{rec}} - p_{n,\mathrm{rec}}^0)\Big). \tag{2.49}
$$

Evaluation of Equation (2.36) for the cogwheel phase cycling scheme leads to

$$
\frac{1}{N}\sum_{m=0}^{N-1}\exp\left[-\mathrm{i}\Phi^{(m)}(\boldsymbol{p})\right] = \frac{1}{N}\sum_{m=0}^{N-1}\exp\left[-\mathrm{i}\frac{2\pi m}{N}\Lambda\right] = \frac{1}{N}\sum_{m=0}^{N-1}\exp\left[-\mathrm{i}\frac{2\pi}{N}\Lambda\right]^m \tag{2.50}
$$

$$
= \begin{cases} 1 & \text{if } \Lambda = NZ \\ 0 & \text{otherwise} \end{cases}, \tag{2.51}
$$

where Z is any integer number. Equation (2.50) is evaluated using the standard summation formula for a geometric series. Consequently, the phase cycle selects CTPs ($\boldsymbol{p}$) that satisfy the condition

$$
NZ = \Delta\nu_{1,2}(p_{1,2} - p_{1,2}^0) + \Delta\nu_{2,3}(p_{2,3} - p_{2,3}^0) + \cdots + \Delta\nu_{n-1,n}(p_{n-1,n} - p_{n-1,n}^0) - \nu_n(p_{n,\mathrm{rec}} - p_{n,\mathrm{rec}}^0),
$$
$$\tag{2.52}$$

where Z is any integer. A convenient way to express the selection rules of the phase cycle is to define the pathway signature as the quantity:

$$
\sum_{q=1}^{n-1}\Delta\nu_{q,q+1}p_{q,q+1} - \nu_n p_{n,\mathrm{rec}}. \tag{2.53}
$$

To select only the desired CTP, the values of $\Delta\nu_{q,q+1}$ must be chosen so that its pathway signature is (*i*) different from the pathway signatures associated with any undesired CTPs, and (*ii*) does not differ by a multiple of N (the total number of steps in the phase cycle) from any undesired phase signature value.

Comparing cogwheel phase cycling with the nested scheme, the former selects absolute coherence order between pulses, while the latter selects according to changes in coherence order at each pulse. The total number of steps required in the nested phase cycle scheme can increase rapidly with the number of pulses in the sequence, and it is frequently found that phase cycling (with the same selectivity) can be achieved in fewer steps by

the cogwheel method.[63] However, it is generally easier to determine the necessary phase cycle for the nested scheme, as the systematic algorithm described in Section 2.3.1 can be used. For cogwheel phase cycling, numerical searches may be needed to identify the required winding numbers,[64] although some conjectures for determining the shortest cogwheel phase cycle have been reported.[65] In all cases, however, it must be assumed that the phases of the pulses and receiver are accurately generated by the spectrometer throughout the phase cycling procedure.

The cogwheel phase cycling approach is important in this dissertation, because of its ability, in some cases, to dramatically reduce the number of phase cycle steps required when many pulses are applied in the experiment.

2.3.3 Multiplex phase cycling

A third class of phase cycling, called multiplex phase cycling, has been recently introduced by Levitt and co-workers.[66] Muliplex phase cycling can offer time savings when performing two-dimensional experiments. This scheme involves separate storage of the N signal transients $(S(t; \phi_1^{(m)}, \phi_2^{(m)}, \phi_3^{(m)}, \dots) = \sum_p S_p(t; 0, 0, 0, \dots) \exp\left[-\Phi^{(m)}(p)\right]$, $m = 0 \dots N - 1)$ acquired for each t_1 increment of the experiment. The set of N transients are processed by applying a numerical phase shift $\Phi_{\text{num}}^{(m)}$, using complex multiplication, and averaged to give the phase-cycled signal

$$S(t) = \frac{1}{N} \sum_{p=\text{all possible}} \sum_{m=0}^{N-1} S_p(t; 0, 0, 0, \dots) \exp\left[-\Phi^{(m)}(p)\right] \exp\left[-i\Phi_{\text{num}}^{(m)}\right] \qquad (2.54)$$

This procedure allows for the selection of different CTPs from the same set of experimental data, by simply adjusting the values of the numerical phase shift such that

$$\frac{1}{N} \sum_{m=0}^{N-1} \exp\left[-i\left(\Phi^{(m)}(p) + \Phi_{\text{num}}^{(m)}(M)\right)\right] = \begin{cases} 1 \text{ if } p \in \{p_M^0, p_M^{0'}, p_M^{0''}, \dots\} \\ 0 \text{ otherwise} \end{cases},$$

$$\frac{1}{N} \sum_{m=0}^{N-1} \exp\left[-i\left(\Phi^{(m)}(p) + \Phi_{\text{num}}^{(m)}(M')\right)\right] = \begin{cases} 1 \text{ if } p \in \{p_{M'}^0, p_{M'}^{0'}, p_{M'}^{0''}, \dots\} \\ 0 \text{ otherwise} \end{cases},$$

$$\vdots \qquad\qquad \vdots$$

where $\{p_M^0, p_M^{0'}, p_M^{0''}, \dots\}$ is the set of desired CTPs for the numerical phase shifts $\Phi_{\text{num}}^{(m)}(M)$. Thus, multiplex phase cycling allows filtering of the signals from the pathway sets

$\{\boldsymbol{p}_M^0, \boldsymbol{p}_M^{0'}, \boldsymbol{p}_M^{0''}, \dots\}$ and $\{\boldsymbol{p}_{M'}^0, \boldsymbol{p}_{M'}^{0'}, \boldsymbol{p}_{M'}^{0''}, \dots\}$ from the same set of experimental data.

Multiplex phase cycling can be particularly useful for two-dimensional experiments, where two separate phase- or amplitude-modulated datasets are required to achieve pure absorption lineshapes. In this case, multiplex phase cycling may allow the two phase-modulated signals needed for pure absorption lineshapes to be extracted from a single experimental dataset; this achieves up to a halving of the minimum experiment time if the signal-to-noise ratio is not a limiting factor.

The multiplex scheme may be combined with both nested and cogwheel phase-cycling schemes and an application of the multiplex method is given in Chapter 5.

2.4   NMR simulations

Computer simulation of NMR experiments is frequently used to develop new experimental methods and, more often, to extract information from experimental results by fitting the recorded spectrum with a simulated spectrum.

Simulations are usually implemented by numerical evaluation of the Liouville–von Neumann equation (1.33).[67–70] The usual approach is to represent operators in a product Zeeman basis and to evaluate the propagator numerically using the time-ordered product defined in Equation (1.37) on page 10, or analytically for a heterogeneous Hamiltonian. The Hamiltonian can be treated as constant over the time step Δt, if this time step is made sufficiently short. To ensure rapid convergence to this limit, simulations are usually performed in the rotating frame, which accurately parallels experimental measurements.

A number of computer programs are available to perform numerical simulations and to allow for magic-angle spinning in the simulation. The SIMPSON package (*SIM*ulation *P*rogram for *S*olid-state *N*MR spectroscopy) of Bak *et al.*[39] is a simulation program that is capable of calculating the expected results of most solid-state NMR experiments, and is particularly convenient because of its simple input file format and built-in processing and optimisation routines. It has been used extensively in this dissertation.

SIMPSON, and most other NMR simulation programs, evaluate the propagator of the density operator using a method that involves diagonalisation of the matrix representation of the Hamiltonian. This is computationally inefficient and an alternative approach, based on the Chebyshev expansion, has recently been developed and implemented in the SPINEVOLUTION program by Veshtort and Griffin.[71] SPINEVOLUTION has
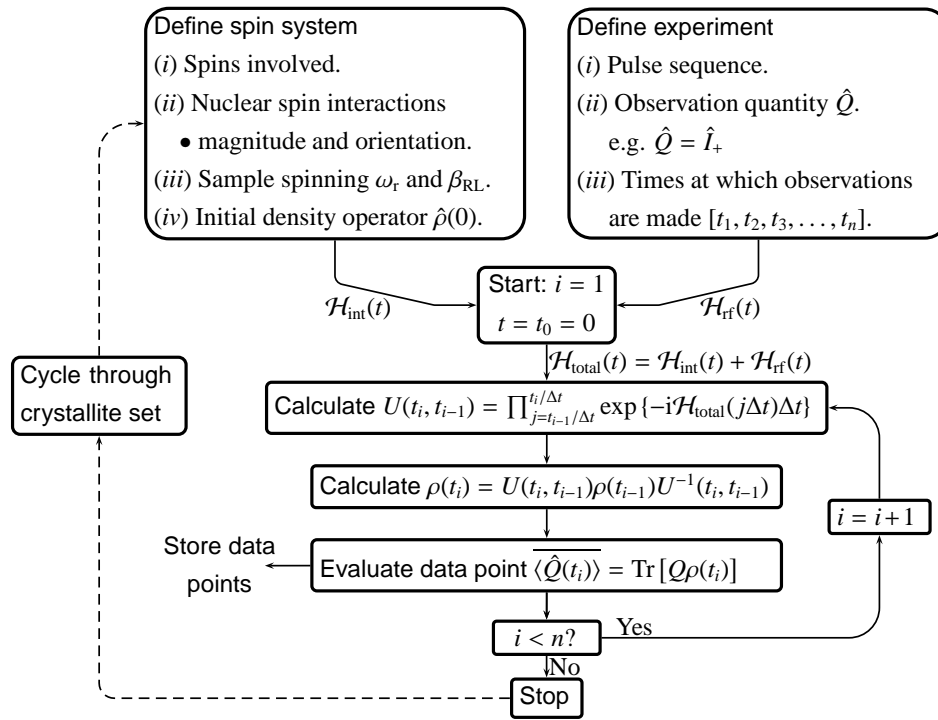
Figure 2.9: General scheme for time-domain simulations based on numerical evaluation of the Liouville–von Neumann equation. Matrix representations of the operators are used in the calculations.

been shown to be particularly useful for simulations involving multiple-spin systems,[71] however SIMPSON has the distinct advantage of an intuitive input file format.[39] SPINEVOLUTION only became available in 2006, and was not used in the work presented here.

The simulation process can be broken down into a series of steps, and is represented in Figure 2.9. First, the spin system involved in the calculation must be defined. This is used to construct the product Zeeman basis in which all spin operators are represented. Also, the internal spin Hamiltonian is specified, including both the magnitude and orientation of the interaction tensor PAF, experienced by each spin. Usually the Euler angles relating the PAF of the interaction λ to the crystallite frame (Ω_{PC}^{λ}) are used. If sample spinning is used, the rotation frequency and orientation of the rotation axis with respect to the static field must be specified. In addition, the initial rotating-frame density operator $\hat{\rho}(0)$ must be defined. A crystallite orientation is chosen, and then the matrix representation ($\mathcal{H}_{int}(t)$) of the internal nuclear spin Hamiltonian ($\hat{\mathcal{H}}_{int}(t)$) can be constructed.

Second, the pulse sequence must be defined. This is used to generate the matrix representation of the RF Hamiltonian $\hat{\mathcal{H}}_{RF}(t)$. In addition, the time points at which 'data points' are to be acquired must be detailed. The 'observed' quantity is represented by an

operator $\hat{Q}$ and its ensemble averaged value evaluated as specified by Equation (1.23) on page 6. $\hat{Q}$ may be chosen to be $\hat{I}_+$, as detected experimentally, but can of course be chosen to be any operator (or set of operators) corresponding to coherences of interest.

Once all the input parameters have been specified, the simulation is initiated and the propagator between observation times is calculated. The density operator at the observation times is determined and the observation quantity evaluated until all data points have been calculated. Since most of time performing a simulation is spent calculating the propagators, the efficiency of the simulation can be significantly improved by reusing a previously calculated propagator, if the Hamiltonian is the same over two or more time periods.

A simulation is performed for a particular crystallite orientation Ω_{CR} for spinning samples and Ω_{CL} for static samples. For a powder sample, it is necessary to repeat the simulation for a number of different crystallite orientations and to calculate the weighted average (the 'powder average') of the results as an approximation to the integral over all possible crystallite orientations, which represents the case for a powder sample. The powder averaged signal $\overline{s(t)}$ is

$$\overline{s(t)} = \frac{1}{8\pi^2} \int_0^{2\pi} \int_0^{\pi} \int_0^{2\pi} s(\alpha, \beta, \gamma; t) \sin\beta \, d\alpha \, d\beta \, d\gamma \approx \frac{1}{8\pi^2} \sum_i^N \sum_j^{N_\gamma} w(\alpha_i, \beta_i) s(\alpha_i, \beta_i, \gamma_j; t),$$

(2.55)

where $w(\alpha_i, \beta_i)$ is the weighting for the crystallite orientation (α_i, β_i) and the average over γ has been assumed to be performed using N_γ uniform steps over the range 0 to 2π. For convenience, the subscripts of $\{\alpha_{CR}, \beta_{CR}, \gamma_{CR}\}$ or $\{\alpha_{CL}, \beta_{CL}, \gamma_{CL}\}$ for rotating or static samples have been dropped. For static samples, the average over γ is unnecessary.

In practice, powder averaging must be repeated with an increasing number of of crystallite orientations until no further change in the averaged result is observed. The approximation in Equation (2.55) is then valid, and the powder average is said to have converged. Repetition of the entire calculation for each crystallite orientation is time consuming, and efficient powder averaging schemes must be chosen. Uniform steps over the ranges of α and β are relatively inefficient, in the sense that many orientations are required to reach convergence. A number of more efficient schemes are available such as the popular REPULSION,[72] ZCW[73] and Lebedev schemes,[74,75] which were all used in this dissertation. Depending on the orientational dependence of the Hamiltonian, only a fraction of the range of α and β may need to be sampled in the powder average. This is described in detail by Edén and Levitt,[70,74] and summarised in Table 2.1.

Case	Required orientational average for α and β
1. General case, e.g. multiple pulse experiments	$0 \leq \alpha \leq 2\pi$, $0 \leq \beta \leq \pi$ (Full sphere)
2. Several interactions with different PAFs	$0 \leq \alpha \leq 2\pi$, $0 \leq \beta \leq \pi/2$ (Hemisphere)
3. Several interactions with the same PAF, $\eta_{CS}, \eta_Q \neq 0$	$0 \leq \alpha \leq \pi/2$, $0 \leq \beta \leq \pi/2$ (Octant)
4. Several interactions with the same PAF, $\eta_{CS}, \eta_Q = 0$	$0 \leq \beta \leq \pi/2$

Table 2.1: Ranges of the required orientational averages for α and β angles for particular combinations of interactions.[70,74] In cases 2-4 it is assumed that only one-dimensional spectra are simulated, with the initial magnetization being prepared such that it is independent of crystallite orientation.

3 Structural information from solid-state NMR experiments

One of the principal challenges of materials research is to develop an understanding of the relationship between a material's structure and its properties. Diffraction techniques and NMR methods have contributed much to this field by allowing the structures of bulk material to be determined at atomic resolution.

Neutron and X-ray diffraction crystallography methods can frequently be used to determine the complete three-dimensional structure of solids and are often considered the ultimate techniques for structure elucidation. There are, however, limitations on diffraction methods, caused by the technique relying on the long range periodicity of the structure. In particular, they require sufficiently large, high quality crystals which may be difficult to grow for single-crystal analysis. Powder diffraction methods only require microcrystalline samples, which are usually much easier to prepare than large single crystals, but it may not be possible to determine a structure unambiguously from the powder diffraction pattern alone. The need for crystalline samples also precludes the use of diffraction methods to study amorphous or composite materials, or other substances where the crystalline form is not its functional state. Moreover, diffraction techniques are not easily able to probe molecular motion within a solid.

In contrast, solid-state NMR does not directly give information about the long-range order of a structure, but instead is sensitive to the local structure about the spin-active nucleus being studied. It is not necessary to use crystalline samples, so amorphous or composite materials can be investigated, and NMR may be used to investigate the dynamics and motion within a sample.[76] Therefore, solid-state NMR is, in many ways, complementary to diffraction methods. Indeed, the literature contains a growing number of examples where powder X-ray diffraction and solid-state NMR measurements have been combined to assist structure elucidation.[77–81]

For these reasons, there have been applications of solid-state NMR to a multitude of diverse areas such as biological materials,[82] solid polymers,[5,83] minerals[84,85] and glasses.[86]

The vast volume of literature on solid-state NMR methods to assist structure elucidation makes a comprehensive review of this field impossible. Instead, only a brief overview of the basic principles by which structural information is gathered from solid-state NMR experiments is given here, with emphasis placed on techniques and examples using spin-1/2 nuclei, which are of most interest in this dissertation. The many techniques that are used for quadrupolar nuclei are not dealt with here; this diverse area of research has recently been reviewed by Duer and Ashbrook.[87] The main subject of this dissertation is the development of robust methods for measurement of the chemical shift tensors, so the current methods for doing this are discussed in the final section.

3.1 Structural information from solid-state NMR experiments

NMR methods to determine structural information rely on the effects upon the observed nuclei of the various nuclear spin interactions, which in turn depend upon the local structure.

A typical NMR strategy to determine a structure first involves measuring several nuclear spin interactions; a fitting process is then used to determine a structure that is constrained to have a geometry consistent with all the NMR measurements (and possibly X-ray diffraction results, or any other known information). Structural constraints may, for example, be in the form of distance measurements between pairs of nuclei in the structure, or chemical shift tensor measurements that restrict the possible local bonding geometry.

The methods used in solid-state NMR differ markedly from those applied in solution-state NMR studies.[88] This arises from the anisotropic components of the interactions not being averaged by rapid molecular tumbling in the solid state. For example, this means that the dipolar coupling between pairs of nuclei can be directly measured in the solid state, whereas solution-state NMR can only measure the dipolar coupling indirectly through the nuclear Overhauser effect, or its effect on relaxation behaviour. The presence of anisotropic interactions is a mixed blessing. Unless single crystal samples are available, powder samples must generally be used and, as Section 1.9 showed, the spectra from static samples will contain broad powder pattern lineshapes. Resolution is therefore a ubiquitous problem for static experiments. Magic-angle spinning is the standard tool for achieving resolution, but this averages the internal nuclear spin interactions to an isotropic value and the anisotropic information (including the dipolar coupling) is lost.

Nonetheless, the MAS spectrum contains significant information. As used in solution-state NMR, the isotropic chemical shift is characteristic of the functional group containing the observed nucleus, and these values are tabulated for the most frequently studied nuclei.[89] Higher level structural information may also be inferred from the isotropic chemical shift; for example, empirical[90] and computational[91] studies show that the isotropic shifts of the C_α carbon sites in peptides adopting an α-helix structure are about 3 ppm higher than in random coil structures, while those in β-sheet structures are typically 2 ppm lower. These features may be used to assign the secondary structure of proteins.

Differing from solution-state NMR, the total number of peaks present in the MAS spectrum depends on the number of different environments in the asymmetric unit of a crystal structure, which may be used to identify the number of molecules in the asymmetric unit[92] and to restrict the number of possible space groups for the structure.[81,93] This information can then be used to reduce the range of possible structures considered when solving the corresponding X-ray powder diffraction data. Although the linewidths in an MAS spectrum depend on many factors, such as proton decoupling efficiency, further information about the crystallinity *versus* amorphicity of the sample can sometimes be inferred from the linewidths. Crystalline samples typically give rise to ^{13}C linewidths of 10s of Hz, while amorphous samples frequently suffer severe line broadening from a distribution in chemical shift, owing to structural inhomogeneity.[94]

In order to exploit the information contained in the anisotropic components of the nuclear spin interactions while using MAS, it is necessary to selectively reintroduce ('recouple') the specific combination of nuclear spin interactions of interest.

The most frequently used technique to prevent the sample spinning from averaging a nuclear spin interaction involves applying a series of rotor-synchronised pulses to the sample, referred to as a recoupling sequence. The recoupling sequence manipulates the spin-operator part of the Hamiltonian, so that the time modulation of spatial- and spin-parts of the Hamiltonian interfere, and the interaction is not averaged to zero. Most recoupling sequences have been developed to recouple a specific interaction. The recently discovered C and R symmetry based pulse sequences of Levitt and co-workers are an exception.[95–97] These ingenious pulse sequences consist of rotor synchronised phase- (and possibly amplitude-) modulated RF irradiation; by following a simple set of rules, the sequences can be adjusted to recouple particular combinations of interactions of interest, based on their symmetry properties. As outlined in Section 2.2, the usual strategy to resolve and measure anisotropic nuclear spin interactions is to perform a two-dimensional experiment, where at least one dimension corresponds to a MAS spectrum

and has high resolution. The other dimension contains the anisotropic information as a broad lineshape, or is also a high-resolution dimension with cross-peak intensities in the spectrum containing information about the magnitude of the anisotropic interaction.

Structural constraints from measurement of anisotropic interactions in solid-state NMR can broadly be grouped into those based on dipolar coupling measurements, those from chemical shift tensors, and those correlating pairs of interaction tensors. These are discussed in turn below.

3.1.1 Dipolar-coupling measurements

Dipolar recoupling has become a highly popular technique to measure distances in a variety of systems. In the simplest approach, a two-dimensional experiment is performed using dipolar recoupling during the t_1 period, prior to signal detection. The modulation of the peak intensities in the F_2 dimension as the recoupling period is increased is analysed to extract dipolar coupling constants. Different techniques are used to recouple the homonuclear and heteronuclear dipolar interactions. For heteronuclear dipolar coupling measurements, the multiple-pulse REDOR experiment in its various forms[98–100] is most widely used, perhaps due to its simplicity and relative robustness. To a lesser extent, applications of rotary resonance recoupling,[101] which involves irradiation of a nucleus using an RF field strength equal to the spinning frequency, and symmetry based C and R sequences have also been reported in the literature.[102–104] For homonuclear dipolar recoupling, a wider variety of recoupling experiments is commonly used, such as rotational resonance,[105] RFDR,[106] BABA[107] and C7,[108] among many other variants. Dusold and Sebald have written a detailed review of the most popular homonuclear and heteronuclear dipolar recoupling sequences.[109]

The value of dipolar coupling measurements arises from the simplicity of their interpretation, because the dipolar coupling constant ($b_{ij}=-\mu_0\hbar\gamma_I\gamma_S/4\pi r_{ij}^3$) for a spin pair is directly related to the internuclear separation r_{ij}. This provides a conceptually simple distance constraint that is easily incorporated into structure refinement programs.

There are a wide variety of dipolar recoupling applications in the literature. For instance, dipolar coupling measurements to obtain both ^{13}C–^{13}C and ^{13}C–^{15}N distance constraints between selectively isotopically labelled sites were used in the recent structure determination of the 14-residue peptide mastoparan-X.[110] These distances were combined with torsion angle predictions, based on the isotropic chemical shifts, to give a complete

structure of the peptide backbone. Applications to native biological samples include a ^{13}C–^{31}P REDOR study of bone,[111] which used dipolar coupling measurements to propose a model for the binding of glutamate carboxylate groups in the protein component of bone to the surface of the mineral component. Non-biological applications are also common, such as the demonstration of vanadium imido bonds between surface bound species and supported catalysts by ^{51}V–^{15}N REDOR.[112]

Problems arise if a nucleus is coupled to more that one other nucleus, as a strong dependence on both the relative orientation and strength of each dipolar interaction is observed for the detected signal, and severely complicates accurate determination of the dipolar coupling constants. For heteronuclear dipolar coupling measurements, the θ-REDOR experiment overcomes this problem to a good approximation.[113] However, if there is also homonuclear dipolar coupling between abundant nuclei, the analysis is further complicated. This has been neatly illustrated recently by Drobny and co-workers with ^{15}N–^{31}P REDOR measurements using diammonium hydrogen phosphate,[114] in which there is heteronuclear dipolar coupling between ^{15}N and the abundant ^{31}P nuclei, and homonuclear dipolar coupling among the latter. At least the nearest five ^{31}P nuclei needed to be included in simulations, as well as the homonuclear coupling between the ^{31}P nuclei, to obtain a good fit between calculated ^{15}N REDOR curves and their experimental data.[114] A number of two-dimensional and three-dimensional experiments have been reported for measuring multiple ^{13}C–^{15}N dipolar couplings in uniformly ^{13}C and ^{15}N enriched peptides;[115–118] although applications have been largely restricted to model peptides, the structure determination of an amyloid fibril has been demonstrated.[119] Methods for analysing multiple homonuclear dipolar couplings have also been reported.[120, 121]

The chemical shift of either homonuclear or heteronuclear dipolar-coupled spins pairs can also be correlated in a two-dimensional spectrum, by including a dipolar recoupling sequence during the mixing period of a two-dimensional experiment.[106] Correlations appear as cross-peaks between signals from spins that are close in space, with the duration of the recoupling sequence determining the distances over which correlations are seen. From these correlations, structural constraints may be inferred. For example, a recent application of this type of experiment by Emsley *et al.* uses the effect of spin diffusion, brought about by strong homonuclear dipolar coupling between ^{1}H spins during the mixing time.[122, 123] By measuring the cross-peak intensities as a function of the spin-diffusion mixing time, several ^{1}H–^{1}H distances were determined from a phenomenological model for the spin diffusion dynamics. These distances were then
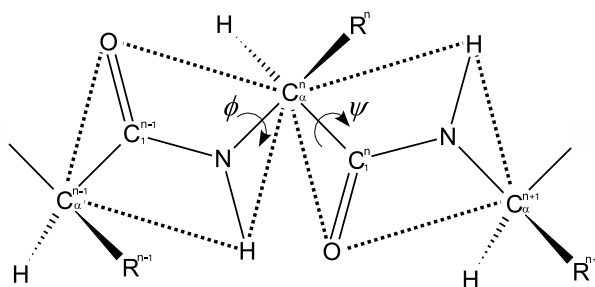
Figure 3.1: For a stretch of bonded atoms A–B–C–D, the torsion angle about B–C is defined as the angle subtended by A–B and C–D when veiwed along B–C; it is zero when AB and CD are coincident (eclipsed), and positive when C–D rotates clockwise relative to A–B. For the case of a peptide, ϕ is the torsion angle for the C^{n-1}–N–C_α–C^n moiety and ψ is the torsion angle for the N–C_α–C^n–N group. Dotted lines indicate peptide planes.

used to assess the best structural model from a set of trial structures. This approach is very much in its infancy, but a more common application of dipolar correlation is in protein studies, where correlation spectra of labelled peptides allow assignment of the signals to specific amino acids residues. For example, near complete assignment of the uniformly $^{13}C,^{15}N$-labelled 140-residue protein α-synuclein has been achieved by this approach.[124] Once assignment of the signals has been made, the isotropic chemical shifts can be analysed, according to known empirical correlations with the secondary structure, to generate torsion angle constraints (see Figure 3.1) that can be used to calculate plausible models for the peptide backbone structure.[125]

Double quantum-single quantum correlation experiments are also used for structure elucidation in homonuclear spin systems. Double-quantum coherences are initially generated between pairs of (usually) spin-1/2 nuclei by recoupling of the dipolar coupling between them. These evolve during the t_1 period before being converted to single-quantum coherences for detection. Correlations between pairs of signals occur at the sum of their isotropic shifts in the F_1 dimension, and the spectra benefit from improved resolution in F_1 compared with the single-quantum correlation experiments. Furthermore, correlations with symmetry related signals are clearly resolved while the signals from isolated spins do not appear. This type of experiment has recently been used by Levitt and co-workers to investigate the framework structure of zeolites.[79, 80]

For structural studies, an intrinsic limitation of dipolar coupling measurements is the need for the two dipolar-coupled nuclei to be separated by a conformation-dependent distance, which places a useful restriction on the three-dimensional structure. For example, distance measurements between nuclei within a rigid region of a molecule will not provide useful information. In addition, it worth noting that many dipolar coupling measurements require

isotopic enrichment of specific nuclear sites to ensure that spin pairs are present in the sample. Unfortunately this can be prohibitively costly and time consuming for many samples. These two factors, perhaps ironically, make structural studies of small and moderately sized molecular solids by dipolar coupling measurements more difficult than those of large peptides, since the isotopic labelling possibilities are limited and isotopic enrichment is often much more difficult (or impossible) and less routine than for peptides.

3.1.2 Chemical shift tensor measurements

Chemical shift tensor (CST) measurements provide additional information to that obtained from the isotropic component of the chemical shift alone. Different functional groups tend to possess characteristic CST principal values; for example, Veeman has compiled a review of ^{13}C chemical shift tensors for several molecular species and discussed trends in their values.[126] The chemical shift interaction depends on the electronic structure, therefore the CST is strongly influenced by local symmetry and bonding geometry about the observed nucleus, and this information may be lost when measuring only the isotropic shift. Indeed, this has been nicely illustrated by Smith *et al.*, who showed that the CST of the thiophene carbon in the three polymorphs of 5-methyl-2-[(2-nitophenyl)amino]-3-thiophenecarbonitrile is sensitive to molecular conformation, even though the isotropic shift for this site in all three polymorphs is similar.[127] This effect can be used to assist the assignment of peaks with similar isotropic chemical shifts,[128, 129] using either calculated values or empirical data to distinguish the different sites based on δ_{aniso}. The difference in the chemical shift tensors of signals with the similar isotropic shifts has also been exploited by Schmidt-Rohr in the CSA-filtered experiment,[130] which differentiates di-oxygenated alkyl (O-C-O) ^{13}C sites from aromatic carbons by the larger δ_{aniso} of the latter.

The main difficulty associated with using CST measurements as a detailed probe of molecular structure is the problem of interpretation of experimentally-obtained tensor principal values. This is in contrast to dipolar coupling measurements, which give directly interpretable distance constraints. Fortunately, recent developments in theoretical methods for *ab initio* calculation of chemical shift tensors, and technological advances in computing that facilitate these calculations in a practical length of time, are starting to make CST predictions for trial structures a routine procedure.

Quantum-mechanical calculation of the CST of any site in a structure is complicated by the need to account for the surrounding lattice; that is, a molecule in a solid is not

isolated and the CST is influenced by the electrons of other nearby species in the crystal structure. The commonly used computational methods for predicting CSTs have recently been reviewed.[131–133] In brief, the problem of accounting for the surrounding crystal structure is often overcome by performing calculations that are based on a cluster of molecules that approximate an extended structure,[134,135] or by the embedded ion method, where an array of point charges are used to approximate the surrounding lattice.[136,137] Most recently, however, there has been much interest in the CASTEP code[138,139] that implements a period boundary condition, and thus calculates the CSTs based on the full three-dimensional crystal structure. This latter approach has given highly promising results.[140–142] In addition to accounting for the crystal lattice, it may be necessary to include the effects of dynamics within the structure, in order to obtain results that are consistent with experimental observations.[143–145]

The two principal areas that have seen application of CST measurements for structure determination are biological materials and crystal polymorphism,[146] the latter driven by its relevance to the pharmaceutical industry where a drug's pharmacological activity and stability can be strongly affected by its crystal structure.

For biological samples, there has been a particular focus on correlating the CST principal values with the torsion angles (ϕ, ψ) of the peptide backbone structure (Figure 3.1 on page 65). Tjandra and Bax were the first so show a significant difference in the C_α chemical shift anisotropy parameter* for α-helix and β-sheet conformations[147] in solution-state NMR. Since then, *ab initio* methods have been used to calculate CST principal values as a function of torsion angles.[148,149] These predict that β-branched amino acids are expected to have C_α sites with Ω_{span} values that are strongly characteristic of the torsion angles, whilst the CSA tensor PAF orientations of *all* amino acids are strongly dependent on the torsion angles. Experimental CST measurements have been found to be consistent with these quantum-mechanical calculations for a variety of model peptides.[137,150–152]

A number of 'real' biological systems have been investigated using CST measurements. For example, the recent work by Witter and co-workers showed their CST measurements of silk fibroin II were consistent with principal values calculated for a proposed structure from the literature,[145] although it would have been interesting if a comparison had also been made with calculated CST principal values for alternative structures. Cellulose

---

*The definition of the chemical shift anisotropy parameter used in reference [147] differs from that used in solid-state NMR, and is defined as $\delta_{\mathrm{orth}} - \delta_{\mathrm{par}}$, where δ_{orth} is the average shift when the static field is aligned perpendicular to the C–H bond, and δ_{par} is the chemical shift when the static field is aligned parallel to the C–H bond.

has also been investigated, both theoretically[143] and experimentally,[153,154] and use of the isotropic chemical shifts as a basis for crystal structure refinement has very recently been reported, where CST measurements were compared with calculated values as further evidence for the refined structure.[155]

In the polymorphism field, there has been considerable work by Grant and co-workers on combining CST measurements with powder X-ray diffraction results in a single structure refinement process, with particular emphasis on utilising embedded ion method for rapid calculations of CST values.[156,157] This may become an established technique, but in the mean time, most studies of polymorphism have compared calculated CST values for proposed crystal structures with those determined experimentally.[158,159] Nonetheless, these studies demonstrate the potential of CST measurements for assisting structural studies.

3.1.3   Correlation of multiple interaction tensors

Knowledge of the relative orientation of the principal axis frames of two interaction tensors can provide further useful structural information. For instance, it is possible to determine the relative orientation of a dipolar coupling tensor PAF with respect to that of chemical shift tensor. A dipolar coupling tensor principal axis frame is known to be oriented with its z-axis along the internuclear vector, therefore the orientation of the CST with respect to the molecular frame can be partially determined. For powder samples, the static two-dimensional separated local field experiment[160] gives an X-Y (X is typically ^{13}C or ^{15}N and Y is ^{1}H) heteronuclear dipolar coupling powder pattern in the F_1 dimension, correlated with the X-spin CSA powder pattern in the F_2 dimension; the ridges seen in the spectrum allow the relative orientation and magnitude of two tensors to be determined. Of course, this experiment suffers from poor resolution when there are multiple sites within the sample, unless selective enrichment of the site of interest is used. Alternative methods analyse the spinning sideband intensities,[161] or powder patterns,[162,163] obtained when both the dipolar coupling and chemical shift interactions govern the evolution of the spin system. For these experiments, two-dimensional methods are use to separate the anisotropic information by a high-resolution dimension.[164–167] Other experiments to correlate pairs of interactions have focused upon direct measurement of torsion angles, either by correlation of two chemical shift tensors,[168] or two dipolar coupling tensors.[169]

3.2 Experimental measurement of chemical shift tensors

There are numerous methods to measure the CST principal values in solids. The simplest is, of course, from the powder pattern lineshapes of static samples (provided heteronuclear dipolar couplings have been removed). Unfortunately, this is usually not possible because overlap of the powder patterns from different nuclear environments rapidly complicates the spectrum.

The use of single crystal samples avoids this problem, because only one peak occurs in the spectrum for each magnetically inequivalent (observed) nucleus in the unit cell. The components of the CST are determined by recording the chemical shift as a function of sample orientation as it is rotated sequentially about three orthogonal axes.[126, 170] Both the principal values and orientation of the PAF with respect to the crystal frame it determined by this method. Further, if the crystal structure is know (from X-ray crystallography), the CST orientations in the molecular frame is also determined. However, this technique is experimentally demanding and requires considerable data analysis. Some significant improvements to automation of both the hardware and analysis software have recently been made,[171] together with techniques to reduce the number of orthogonal axes about which the crystal must be rotated.[172] Few laboratories possess these facilities, and the need for high quality single crystals and their corresponding low sensitivity have perhaps prevented single crystal NMR becoming commonplace. Moreover, if high quality, large single crystals can be grown, then diffraction methods may provide a more direct and useful route to structural information.

Magic-angle spinning gives a series of sharp spinning sidebands arising from the CSA of each site in the structure (Section 2.1.1), mitigating the problems of resolution in the spectra of static sample. The intensity of the spinning sidebands are related to the CST (assuming it is the only interaction present), although analysis of the MAS spectrum is less straightforward than for powder patterns. Herzfeld and Berger evaluated the spinning sideband intensities using a Bessel function expansion and proposed a graphical method, based on the analysis of the relative intensity of spinning sidebands, to determine CST principal values.[34] This is usually no longer used, as the wide availability of computers has made it preferable to use programs that rapidly generate and fit simulated spectra to experimental results by varying the values of δ_{aniso} and η_{CS}. Simulated spectra can be generated using either the Herzfeld-Berger method[34, 173] or using time domain simulations[13, 174, 175] outlined in Section 2.4.

Disregarding for the present the often limited resolution in the spectra of static samples,

Hodgkinson and Emsley have compared the accuracy and reliability of chemical shielding principal values derived from spinning sidebands and powder patterns.[176] They concluded that if spectra were recorded under the same experimental conditions (the integrated signal intensity and noise level are the same for all spectra) then δ_{aniso} is most reliably determined from spinning sideband spectra. This can be rationalised by the higher sensitivity achieved by concentrating the signal intensity into sharp spinning sidebands. They recommended that for $0.1 < \eta_{\text{CS}} \leq 1$, the spinning frequency should be chosen so that $|\omega_{\text{r}}/(\omega_0 \Delta_{\text{CS}})| \approx 0.39$, and slower spinning should for used for $0 \leq \eta_{\text{CS}} \leq 0.1$, to obtain optimum accuracy for the fitted δ_{aniso} values. In contrast, the asymmetry parameter is most accurately determined from static powder patterns.

A further consideration when choosing between powder pattern and spinning sideband measurements is that partial orientational ordering within the sample (a non-uniform distribution of crystallite orientations), is readily seen in the lineshape of powder patterns,[177] whereas it is much less easily identified from the intensities of a few spinning sidebands. This is not a common problem, except for coarsely ground samples, but the effect has been used to study aligned polymer samples.[178] Similarly, if more that one site has the same isotropic shift, or if there is structural disorder, it is much harder to identify this from the overlap of two (or more) sets of spinning sideband intensities than the overlap of static powder patterns.

Separation of the signal from different nuclear sites is achieved using two-dimensional experiments, where one dimension is a high-resolution spectrum, and contains a series of sharp peaks at the isotropic chemical shifts (and possibly spinning sidebands). Each of these peaks is correlated with its anisotropic component, represented by either a quasi-static powder pattern or spinning sidebands in the other dimension. The comparison by Hodgkinson and Emsley of the accuracy of sideband and powder pattern analysis[176] does not directly apply when comparing different two-dimensional experiments that recouple quasi-static powder patterns and spinning sidebands. However, it is fair to say that sideband patterns in the F_1 dimension will generally benefit from a higher signal-to-noise ratio than quasi-static powder patterns, owing to the signal intensity being distilled into discrete sidebands, rather than spread across the full frequency range of the powder pattern. Despite this, the simplicity and intuitive interpretation of the powder pattern lineshape is often appealing.

The techniques used to obtain the anisotropic-isotropic correlation spectra can be roughly categorised into methods using multiple pulses with MAS, and methods that incorporate a mechanical strategy, in the sense that the physical motion of the bulk sample is adjusted
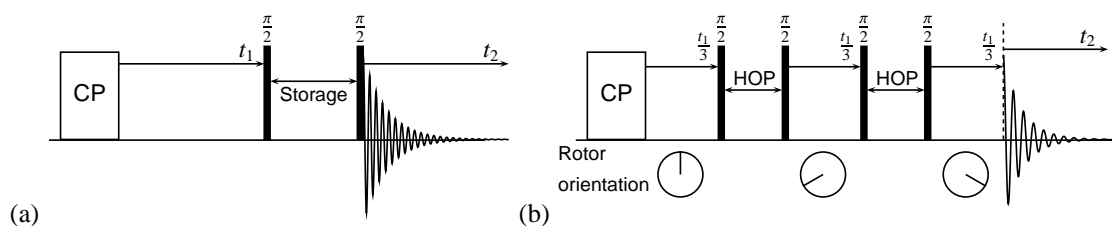
Figure 3.2: (a) Pulse sequence used for the stop-and-go,[179] switched-speed spinning,[180] and flipped-angle spinning[181] experiments. Changes to the spinning frequency or angle occur during the storage period. (b) Magic-angle hopping pulse sequence.[182] The rotor is hopped between three orientations indicated below the pulse sequence. Only the observed channel is shown, assuming an initial CP step.

during the experiment, rather than simply using constant frequency MAS.

3.2.1 Mechanical approaches to reintroduce the CSA

Two methods that might be considered a 'brute force' solution to generating anisotropic-isotropic spectra, in the sense that the averaging of the chemical shift anisotropy is prevented by means of changing the MAS frequency, are the stop-and-go method[179] and switched-speed spinning experiment.[180] These experiments are very similar (see Figure 3.2(a)) and involve either a static sample or slow MAS throughout the t_1 evolution period. During the mixing period, the magnetization is 'stored' parallel to the rotating-frame z-axis, where it does not evolve under the chemical shift interaction. During this time, magic-angle spinning is started, or the spinning frequency is increased. Once a stable MAS has been established, the magnetization is rotated back into the rotating-frame xy-plane where it evolves during the t_2 period. These experiments therefore correlate the high-frequency MAS spectrum with static powder patterns in the stop-and-go method, or spinning sidebands at two different spinning frequencies in the switched-speed spinning experiment. The demands on the spectrometer hardware is substantial and probably compromises the longevity of the MAS unit, probe head and rotor. With alternative methods available, these two approaches are not recommended. Furthermore, during the mixing period, spin-lattice relaxation occurs and substantial loss of signal will occur if the storage time is long (compared to T_1).

An alternative approach uses sample spinning away from the magic angle. In this case the spinning sidebands due to the CSA are no longer sharp, but are powder patterns as illustrated in Figure 2.2(c) on page 40. If the spinning frequency is sufficiently large that only the centre-band has significant intensity, the spectrum contains quasi-static powder patterns scaled from their true frequency span by a factor of $\frac{1}{2}(\cos\beta_{RL} - 1)$. This can be

incorporated into a two-dimensional experiment using the pulse sequence in Figure 3.2(a) on the preceding page. Sample spinning about an axis oriented away from the magic-angle occurs during t_1, typically $\beta_{RL} = 90°$ to give $\frac{1}{2}(\cos\beta_{RL} - 1) = -1/2$. During the mixing period, the magnetization is stored parallel to the rotating-frame z-axis and the spinner axis is changed to the magic-angle so that during detection the usual MAS signal is recorded.[181] This gives a spectrum correlating a quasi-static powder pattern with the high-resolution MAS spectrum. Flipping of the rotor axis can be accomplished much faster that changing the spinning frequency, so the signal loss from spin-lattice relaxation during the mixing period is less than for the stop-and-go or switched-speed-spinning experiments. Recently a switched-angle high spinning frequency probe ($\approx$ 20 kHz) has been reported,[183] although the technique is not common in the literature.

In the magic-angle hopping experiment (Figure 3.2(b) on the previous page), instead of MAS the sample hops between three orientations about the rotor axis, separated by rotations of 120°.[182] The t_1 period is divided equally between the three orientation and during the hopping the magnetization is stored parallel to the z-axis. Evolution in the three orientations may easily be shown to average the evolution due to the anisotropic part of the chemical shift to zero. Thus, the isotropic dimension results from the evolution during the t_1 period (in which the hopping occurs) and requires many t_1 increments to obtain good frequency resolution in this dimension, due to the sharpness of the signals expected. Because a one-dimensional spectrum must be recorded for each t_1 increment, this experiment can be very time consuming for low sensitivity samples.

Finally, the variable-angle correlation experiment (VACSY)[184] is a rather different and ingenious experiment. Unlike a conventional two-dimensional experiment, there is only one evolution period. Instead, a two-dimensional dataset is generated by incrementing the rotor axis orientation (with respect to the static magnetic field) and recording a one-dimensional experiment at each orientation. By using appropriate sampling of the rotor axis orientation and data processing, quasi-static lineshapes correlated with their isotropic peaks are obtained. The important advantage of this approach is its high signal-to-noise ratio, which is achieved because no signal is discarded by using a storage period. This, however, is at the expense of complex experimental requirements and data analysis.

While these mechanical approaches are robust and give reliable results, they suffer from the need for specialist hardware that is not widely available, perhaps owing to the low cost benefit for groups that do not wish to perform CST measurements frequently. Consequently, they are not in common use and most research groups are limited to multiple-pulse recoupling techniques for these measurements.

3.2.2 Multiple-pulse CSA recoupling

The spatial averaging of the MAS process can be interrupted by RF pulses synchronised with the orientation of the sample as it is rotated. This approach was first identified by Alla and co-workers,[185] who devised an experiment where two π-pulses were applied per complete rotation of the sample (at 1/4 and 3/4 of a rotor period) with the signal detected at the end of each rotor period. This gives a characteristic powder pattern, different from the static lineshape, but can nevertheless be used to determine δ_{aniso} and η_{CS}. Yarim-Agaev et al. developed the theoretical scheme of Alla and co-workers and introduced an experiment that uses six π-pulses per rotor period and possesses the beneficial property of being able to control the width of the powder patterns obtained in the F_1 dimension.[186] As in the two π-pulse experiment of Alla et al., the quasi-static powder patterns do not, in general, have the same form as the static case. More seriously, the asymmetry parameter must be extracted from slight variations in the edge of the powder pattern lineshape, making the accuracy of the determined values rather poor.

Bax et al. developed a scheme that utilised a $(2\pi_x 2\pi_{-x})$-pulse per rotor period.[187] The $(2\pi_x 2\pi_{-x})$-pulses compensate for pulse imperfections (see Section 4.5.1). The powder patterns obtained by this experiment do not, in general, have exactly the same lineshape as static spectra, but are more similar to them than those achieved by the experiment of Yarim-Agaev and co-workers.[186] The recoupling experiment of Tycko, Dabbagh and Mirau[188] was the first multiple-pulse technique to allow the normal static powder pattern to be obtained in the F_1 dimension. This has the advantage that the CSA tensor values can be simply read from the spectrum. The experiment uses four or six π-pulses per rotor period; the pulse sequence is shown in Figure 5.2 on page 116. Unfortunately, pulse sequences using several π-pulses are generally rather sensitive to pulse imperfections, which cause large artefacts in the F_1 dimension of the resulting spectra and unwanted distortions in the powder pattern lineshape. This has certainly been shown for this pulse sequence.[153,188] It is also found that heteronuclear dipolar coupling between ^{13}C and ^{1}H can be a particular problem and causes the quasi-static powder patterns to appear strongly line broadened. This arises from the heteronuclear dipolar recoupling effect of the π-pulse in the pulse sequence when there is simultaneous ^{1}H irradiation, and a very high power ^{1}H RF field strength is required to overcome this effect ($\omega_1^{\mathrm{H}} = 3\omega_1^{\mathrm{C}}$, where ω_1^{H} and ω_1^{C} are the ^{1}H and ^{13}C RF field strengths respectively).[189] Both the effects of pulse imperfections and heteronuclear dipolar coupling prevent accurate measurement of the CST.

Schmidt-Rohr and co-workers have combined the powder pattern recoupling experiments

of Bax and Tycko to produce the Separation of Undistorted Powder patterns by Effortless Recoupling (SUPER) experiment,[190] which is shown in Figure 5.4 on page 121. This experiment achieves partial compensation for pulse imperfections with the $(2\pi_x 2\pi_{-x})$-pulses used in the Bax pulse sequence,[187] but still gives quasi-static powder patterns that are identical to those of static solids. Although the artefacts seen in the spectra recorded using the method of Tycko and co-workers do not occur when using the SUPER experiment, the powder patterns are still often distorted from the ideal lineshape due to the effects of pulse imperfections.[190–192] This hinders accurate measurement of the CST.

In another strategy to generate quasi-static powder patterns in a two-dimensional experiment, Ishii and Terao have investigated using amplitude-modulated continuous irradiation during the evolution period to recouple the chemical shift anisotropy.[193] Although they demonstrated the technique for a range of compounds, the very high sensitivity to resonance offsets and complicated experimental setup have meant that this method has not been widely adopted.

As an alternative to fast MAS techniques, the magic-angle turning (MAT) experiment,[194, 195] which is based on the magic-angle hopping experiment,[187] uses very slow sample spinning ($\lesssim$100 Hz). Slow spinning is much easier to implement than hopping, but the same pulse sequence shown in Figure 3.2(b) on page 71 is used. MAT was, itself, further improved in the PHORMAT[196] and related FIREMAT[197, 198] experiments. A problem arising from very slow MAS is that heteronuclear ^{1}H decoupling can be less effective than at higher spinning frequencies, which reduces the resolution in the isotropic dimension.[199] The MAT experiments involving two or more storage periods generally have low sensitivity and require many t_1 increments to obtain high resolution in the F_1 dimension. Further, they require specialist spinning hardware to achieve stable slow sample spinning and accurate synchronisation of the pulses with the sample rotation, which is not widely available.

Multiple-pulse experiments can also be used to extract the CST from spinning sideband intensities. A very useful approach is to use moderately slow MAS and to separate the spinning sidebands in the indirectly observed dimension of the experiment. This removes the problem of overlapping spinning sidebands in a one-dimensional spectrum. The schemes devised to perform this are based on the initial work of Dixon.[200] The first two-dimensional experiment to perform sideband separation used the 2D-TOSS sequence,[201] shown in Figure 3.3(a) on the next page. 2D-TOSS has the disadvantage of involving a period during which the magnetization is stored parallel to the z-axis, which causes a loss of signal intensity from only one orthogonal component of the transverse magnetization
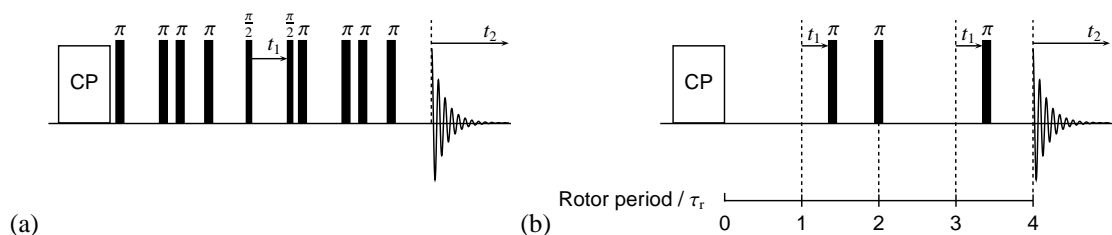
Figure 3.3: (a) The 2D-TOSS[201]/CSA amplification[203,204] pulse sequence. Only the observed channel is shown, assuming an initial CP step. (b) The XCS/SPEED pulse sequence.[205,206] In both (a) and (b), t_1 is incremented from zero to one rotor period during the experiment.

being stored. In addition, 2D-TOSS is sensitive to imperfections in the π-pulses used in the pulse sequence. A more robust approach is the 2D-PASS experiment,[202] shown on page 83 in Figure 4.2. 2D-PASS involves only five π-pulses and no storage period, and therefore benefits from a higher signal-to-noise ratio that 2D-TOSS. Moreover, phase cycling can be implemented to remove most of the effects of pulse imperfections. In both 2D-TOSS and 2D-PASS, there is no net isotropic chemical shift evolution during the t_1 period, a feature which turns out to be very efficient in terms of the number and range of t_1 values that must be acquired (see Section 4.1).

2D-TOSS and 2D-PASS require slow sample spinning if a sufficient number of spinning sidebands are to be recorded for analysis. The slow sample spinning required to measure small values of δ_{aniso} can be unstable and difficult to maintain without specialised hardware. In addition, homonuclear dipolar coupling (if present) may dominate the spectrum when using slow spinning frequencies. It may therefore desirable to be able to record spectra where the chemical shift anisotropy (or equivalently the spinning frequency) is effectively scaled by a multiple-pulse technique, so that many more spinning sidebands are recorded in F_1 than in the directly observed F_2 dimension. This gives a spectrum that correlates of spinning sidebands at two different spinning frequencies, from which the spinning sideband intensities at the slower (effective) spinning frequency can be extracted. A number of experiments have been developed to achieve this.

Kolbert *et al.* demonstrated an experiment that used a t_1 evolution time in the indirect dimension of a two-dimensional experiment that contained a single π-pulse at it's mid-point ($t_1/2$). During the two-dimensional experiment, t_1 is increased from zero. This was shown to give the effect of doubling the chemical shift anisotropy (or effectively halving the spinning frequency) in the indirectly observed dimension.[180] The Extended Chemical-Shift modulation (XCS) experiment of Gullion[205] developed an approach using a fixed evolution time in the indirect dimension of a two-dimensional experiment, this experiment allows a scaling effect larger than two of the CSA. The pulse sequence for a

scaling down of the spinning frequency by a factor of four is shown in Figure 3.3(b) on the previous page. Because there is net evolution of the magnetization due to the isotropic chemical shift during the t_1 period of XCS, an unconventional data processing routine is required to generate the sideband patterns at the scaled spinning frequency, which is inconvenient. This pulse sequence has reappeared as the *S*troboscopic *P*hase *E*ncoding in the *E*volution *D*imension (SPEED) experiment,[206] but in this case the experimental data is processed using the non-standard replication and TIGER methods.[207]

The recent CSA-amplification method of Titman an co-workers[203, 204] is closely related to the 2D-TOSS and 2D-PASS experiments, and has the same pulse sequence as the 2D-TOSS experiment shown in Figure 3.3(a) on the preceding page, although the number of pulses used may be greater. The CSA-amplification experiment does not involve net evolution of the magnetization due to the isotropic shift during the t_1 period, and therefore benefits from an efficient t_1 sampling range (see Section 4.1). Furthermore, it requires only the usual data processing routines. For these reasons, it is probably the most useful of the current techniques for correlating spinning sidebands at two spinning frequencies, although scaling of the CSA is limited to less that a factor of 12. As for the 2D-TOSS experiments, the pulse sequence includes a storage period, which discards half the signal intensity, and the experiment is rather sensitive to pulse imperfections.[204]

Finally, the ROSES experiment (Results in the Observation of Slower Effective Spinning) has been proposed by the Emsley group.[208] ROSES involves sampling the t_1 period at intervals of $\tau + \tau_r$, where τ_r is one rotor period; between these sample times in the t_1 dimension, π-pulses are applied at $\tau + \tau_r/2$ and $\tau + \tau_r$ of each t_1 increment. A scaling down of the spinning frequency by a factor of $(\tau_r + \tau)/\tau$ is achieved by this experiment. ROSES has the disadvantage of only scaling, and not suppressing, the isotropic shift evolution during the t_1 period. This means that it is necessary to record many t_1 increments in order to obtain sufficient frequency resolution in the F_1 dimension of the spectrum. Also, with the many π-pulses used, the experiment is sensitive to resonance offsets unless high-power ^{13}C pulses ($\omega_1 \approx 120$ kHz) are used. Nonetheless, very large scaling effects were demonstrated using ROSES[208] ($N \approx 30$).

3.3   Summary

The recent advances in *ab initio* calculations of CSTs and the emerging methodology for incorporating experimental measurements into structure refinement programs demonstrate that the use of CST measurements is a useful approach in structure elucidation.

This may be especially useful for organic, solids if isotopic labelling of the sample, which may be required for dipolar coupling measurements, is either prohibitively expensive or difficult to perform. However, for this approach to be viable, it is necessary that accurate CST measurements can be made. For convenience and practical application in general NMR laboratories not specialising in CST measurements, it is desirable that a recoupling experiment be (*i*) simple to perform, process and analyse; (*ii*) robust and reliable; and (*iii*) require no specialised hardware, such as slow spinning control units, variable-angle or single crystal probes. As discussed earlier, there is value in being able to record both spinning sideband intensities and quasi-static powder patterns: quasi-static powder patterns are intuitive to interpret and it is easier to identify the overlap of multiple powder patterns from signals with the same isotropic shift. Also, powder patterns allow accurate determination of the chemical-shift asymmetry parameter η_{CS}, whilst spinning sideband intensity measurements benefit from higher sensitivity.

The 2D-PASS experiment is a very robust method for separating spinning sidebands and has found wide application. However, the techniques to correlate spinning sidebands at two different spinning frequencies currently suffer from requiring either unconventional data processing techniques or data analysis, such as the XCS,[205] SPEED[166] and ROSES,[208] or have been found to be sensitive to pulse imperfections, including the CSA-amplification[203,204] and the ROSES experiments. In Chapter 4, development of a robust experiment for correlating spinning sidebands at two different spinning frequencies, that requires only simple data processing and analysis, is presented. The approach is based on extending the 2D-PASS[202] and CSA-amplification experiments.[204,209]

Of the multiple-pulse experiments to resolve quasi-static powder patterns, the MAT[194,195,197] experiments currently give the most accurate experimental results. This is because the powder patterns are unscaled and recorded in the directly-observed dimension. However, MAT requires specialist hardware and can be time consuming, owing to the high-resolution spectrum being in the indirectly-observed dimension. Unfortunately, all the current multiple-pulse techniques using MAS, and recording the high resolution spectrum in the F_2 dimension, are sensitivity to pulse imperfections which cause distorted powder pattern lineshapes. This, in part, explains why these experiments have not found widespread use. Thus, there is a need for more robust techniques of this type. The SUPER[190] experiment and the recoupling experiment of Tycko and co-workers[188] are simple to perform, since they require only standard hardware and processing routines. For this reason, they were chosen as 'starting points' to develop improved methods for recoupling CSA powder patterns. This work is described in Chapter 5.

4

Two-dimensional correlation of CSA spinning sidebands

This chapter describes a new two-dimensional experiment that correlates CSA spinning sidebands at two different spinning frequencies: at an effective spinning frequency ω_r/N in the indirectly observed dimension and the true spinning frequency ω_r in the directly observed dimension, where N is referred to as the scaling factor.

This type of experiment is useful for measuring the chemical shift tensor principal values of sites that have small δ_{aniso}, where 2D-PASS would require slow MAS that is prone to instability. The particular aim of the work presented here was to develop an experiment that gives spinning sideband intensities that are identical to those obtained from a simple one-dimensional experiment at the effective spinning frequency, but does not require non-standard data processing routines and is robust with respect to pulse imperfections.

Before detailing the experiment, the description of the signal from rotating samples in Section 2.1.1 is extended for the purposes of outlining the notation used in the following sections.

4.1   CSA MAS spinning sidebands

Under MAS conditions, the propagator $\hat{U}_{\text{MAS}}(t)$, which describes the time-evolution of the rotating-frame density operator for a single spin governed by the chemical shift Hamiltonian $\hat{\mathcal{H}}_{\text{CS}} = \omega(t'; \Omega_{\text{PR}})\hat{I}_z$, is

$$\hat{U}_{\text{MAS}}(t) = \exp\left\{-\mathrm{i}\int_0^t \omega(t'; \Omega_{\text{PR}})\hat{I}_z \mathrm{d}t'\right\},\qquad(4.1)$$

where $\omega(t'; \Omega_{\text{PR}})$ was defined in Equation (2.8) on page 39 and Ω_{PR} is the set of Euler angles $\{\alpha, \beta, \gamma\}$ relating the principal axis frame of the CSA tensor to the rotor axis frame (for convenience, the subscript has been omitted from $\alpha_{\text{PR}}, \beta_{\text{PR}}$ and γ_{PR}). The expression for $\omega(t'; \Omega_{\text{PR}})$ was given in Equation (2.8) for a general spinning axis orientation β_{RL} with

respect to the static field, under MAS this expression can be written in the form

$$\omega(t; \Omega_{PR}) = \omega_{iso} + \left[C_1' \cos(\omega_r t) + C_2' \cos(2\omega_r t) + S_1' \sin(\omega_r t) + S_2' \sin(2\omega_r t) \right], \quad (4.2)$$

$$C_1' = C_1 \cos(\gamma) + S_1 \sin(\gamma) \quad (4.3)$$

$$S_1' = S_1 \cos(\gamma) - C_1 \sin(\gamma) \quad (4.4)$$

$$C_2' = C_2 \cos(2\gamma) + S_2 \sin(2\gamma) \quad (4.5)$$

$$S_2' = S_2 \cos(2\gamma) - C_2 \sin(2\gamma), \quad (4.6)$$

where C_1, S_1, C_2, S_2 were defined on page 39. Using Equation (4.2), one obtains

$$\int_{t_a}^{t_b} \omega(t'; \Omega_{PR}) \mathrm{d}t' = \omega_{iso}(t_b - t_a) + \Phi(t_b; \Omega_{PR}) - \Phi(t_a; \Omega_{PR}), \quad (4.7)$$

with $\Phi(t, \Omega_{PR})$ defined as

$$\Phi(t; \Omega_{PR}) = \frac{1}{\omega_r} \left[C_1' \sin(\omega_r t) + \frac{1}{2} C_2' \sin(2\omega_r t) - S_1' \cos(\omega_r t) - \frac{1}{2} S_2' \cos(2\omega_r t) \right] \quad (4.8)$$

$$= \frac{1}{\omega_r} \left[C_1 \sin(\gamma + \omega_r t) + \frac{1}{2} C_2 \sin(2\gamma + 2\omega_r t) \right.$$

$$\left. - S_1 \cos(\gamma + \omega_r t) - \frac{1}{2} S_2 \cos(2\gamma + 2\omega_r t) \right]. \quad (4.9)$$

Therefore, the propagator under MAS between time t_a and t_b is

$$\hat{U}_{MAS}(t_b, t_a) = \exp \left\{ -\mathrm{i} \left[\omega_{iso}(t_b - t_a) + \Phi(t_b; \Omega_{PR}) - \Phi(t_a; \Omega_{PR}) \right] \hat{I}_z \right\} \quad (4.10)$$

The detected signal is proportional to the ensemble averaged expectation value of $\hat{I}_+$. For an initial density operator following CP $\hat{\rho}(0) = \frac{1}{2} \left(\hat{I}_+ + \hat{I}_- \right)$, the signal from a crystallite with orientation Ω_{PR} is

$$s(t; \Omega_{PR}) = \overline{\langle \hat{I}_+ \rangle}$$

$$= \mathrm{Tr} \left[\hat{U}_{MAS}(t, 0) \hat{\rho}(0) \hat{U}_{MAS}^{-1}(t, 0) \hat{I}_+ \right]$$

$$= \frac{1}{2} \exp \left\{ \mathrm{i} \int_0^t \omega(t'; \Omega_{PR}) \mathrm{d}t' \right\}$$

$$= \frac{1}{2} \mathrm{e}^{\mathrm{i}\omega_{iso} t} \mathrm{e}^{\mathrm{i}\Phi(t; \Omega_{PR})} \mathrm{e}^{-\mathrm{i}\Phi(0; \Omega_{PR})}, \quad (4.11)$$

where the effects of relaxation have been neglected. When transforming from the PAF frame to the rotor frame, the γ Euler angle corresponds to a rotation about the rotor axis,

which gives the relation

$$\Phi(t; \alpha, \beta, \gamma) = \Phi(t + \gamma/\omega_r; \alpha, \beta, 0). \tag{4.12}$$

In addition, $\Phi(t, \Omega_{PR})$ is periodic with frequency ω_r, so the function $\exp[i\Phi(t; \alpha, \beta, \gamma)]$ can be expanded as a Fourier series

$$\exp[i\Phi(t; \alpha, \beta, \gamma)] = \exp[i\Phi(t + \gamma/\omega_r; \alpha, \beta, 0)] = \sum_{k=-\infty}^{+\infty} F_k(\alpha, \beta) e^{ik\gamma} e^{ik\omega_r t}, \tag{4.13}$$

where $F_k(\alpha, \beta)$ are Fourier coefficients which are evaluated by

$$F_k(\alpha, \beta) = \frac{1}{2\pi} \int_0^{\tau_r} \exp(i\Phi(t + \gamma/\omega_r; \alpha, \beta, 0)) \exp(-ik(\omega_r t + \gamma)) d(\omega_r t + \gamma)$$

$$= \frac{1}{2\pi} \int_0^{2\pi} \exp(i\Phi(\gamma'/\omega_r; \alpha, \beta, 0)) \exp(-ik\gamma') d\gamma', \quad (\gamma' = \omega_r t + \gamma). \tag{4.14}$$

Thus, the detected signal can be expressed as

$$s(t; \Omega_{PR}) = \frac{1}{2} e^{i\omega_{iso}t} e^{-i\Phi(0;\Omega_{PR})} \sum_{k=-\infty}^{+\infty} F_k(\alpha, \beta) e^{ik\gamma} e^{ik\omega_r t}$$

$$= \frac{1}{2} e^{i\omega_{iso}t} \sum_{k'=-\infty}^{+\infty} \sum_{k=-\infty}^{+\infty} F_{k'}^*(\alpha, \beta) F_k(\alpha, \beta) e^{i(k-k')\gamma} e^{ik\omega_r t}. \tag{4.15}$$

Equation (4.15) emphasises that the spectrum will contain a peak at the isotropic frequency, flanked spinning sidebands at integer multiples of the rotor frequency.

The intensity of the kth order spinning sideband (the sideband that occurs at a frequency $k\omega_r$ away from the isotropic peak) is $I_k(\Omega_{PR}) = \frac{1}{2} e^{-i\Phi(0;\Omega_{PR})} F_k(\alpha, \beta) e^{ik\gamma}$.

Referring back to the definitions of C_1, C_2, S_1 and S_2 on page 38, each of these terms is proportional to the chemical shielding anisotropy (Δ_{CS}), therefore $\Phi(t + \gamma/\omega_r; \alpha, \beta, 0)$ is proportional to the ratio Δ_{CS}/ω_r. Consequently, the sideband intensities, $I_k(\Omega_{PR})$, depend only upon this ratio (Δ_{CS}/ω_r) and also the asymmetry parameter η_{CS}.

It will prove useful in the following discussions to consider the special case when the isotropic shift (ω_{iso}) is zero. Under this condition, the spinning sidebands are centred about the zero frequency in the spectrum and the signal has the form

$$s(t; \Omega_{PR}) = \frac{1}{2} e^{i\Phi(t;\Omega_{PR})} e^{-i\Phi(0;\Omega_{PR})} = \frac{1}{2} \sum_{k=-\infty}^{+\infty} \sum_{k'=-\infty}^{+\infty} F_{k'}^* F_k e^{i(k-k')\gamma} e^{ik\omega_r t}. \tag{4.16}$$
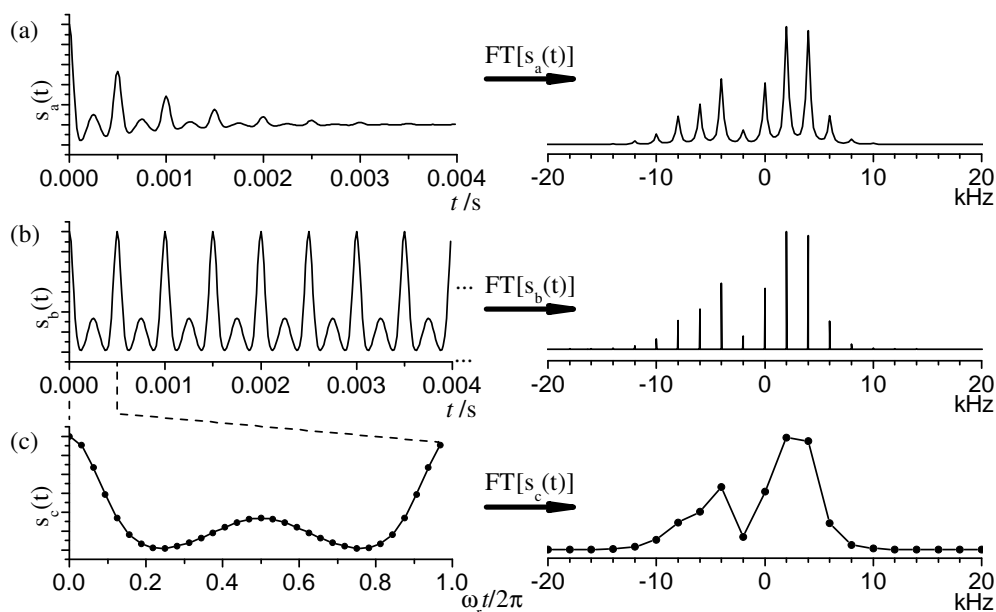
Figure 4.1: Simulated signal and corresponding Fourier transformation for (a) many rotor periods with relaxation, (b) many rotor periods without relaxation and (c) a single rotor echo without relaxation. Simulation parameters: $-\omega_0\Delta_{CS}/2\pi = -10$ kHz, $\eta_{CS} = 0$, $\omega_r/2\pi = 2$ kHz. A powder average using 2000 REPULSION[72] (α,β) orientations was used.

In a real one-pulse experiment, relaxation will cause the signal to decay over time and the spinning sidebands have a finite width, as shown in Figure 4.1(a) for a powder sample. If there were no relaxation, however, the spectrum would contain infinitesimally narrow spinning sideband peaks, which is illustrated in Figure 4.1(b). The integrated peak intensities are the same in the two spectra in Figure 4.1(a) and (b) (although the spectra have not been plotted with the same vertical scale in Figure 4.1).

The discrete Fourier transform implicitly assumes that the input function is periodic. For this reason, the signal without relaxation must be recorded for an integer number of rotor periods, otherwise the spectrum will contain artefacts. Provided this is done, all data points in the spectrum are zero except those at exact multiples of the MAS frequency.

Finally, discrete Fourier transformation of the signal (without relaxation) sampled discretely over one rotor period gives a spectrum where each data point is separated in frequency by ω_r and represents a sideband intensity. This latter case is illustrated in Figure 4.1(c), where the line joining the data points in the frequency spectrum is the envelope to the sidebands in Figure 4.1(b). All three spectra in Figure 4.1 contain exactly the same information about the chemical shift tensor.

The sampling of the signal in the last case is particularly efficient, requiring only as many

data points as there are significant spinning sidebands in the frequency dimension to avoid aliasing. This is neither useful nor practical for direct detection of an NMR signal, because there is no difficulty in recording many data points. In addition, nearly all samples of interest contain multiple nuclear spin environments, each with a different isotropic shift, so it is not possible for the isotropic shift to be zero in each case. However, this method of detecting the signal can be used in the indirectly observed dimension of a two-dimensional experiment, where it can give significant time savings. In this case, the isotropic shift can be suppressed while maintaining the evolution due to the CSA by using an appropriate multiple pulse sequence. The efficient sampling of t_1 values is now important and highly desirable, since each t_1 data point requires a one-dimensional spectrum to be recorded. Using this method, it is only necessary to record as many t_1 points as there are significant spinning sidebands in the frequency domain, with t_1 values spaced evenly over the range $0 \le t_1 < \tau_r$.

4.2   A CSA spinning sideband correlation experiment

To obtain a spectrum correlating spinning sidebands at two different spinning frequencies, the pulse sequence must cause the spin system to evolve during the t_1 period as if the sample were spinning at a fraction $1/N$ of the true sample spinning frequency. Equation (4.14) of the previous section showed that the sideband intensities only depend upon the ratio of Δ_{CS} to ω_r, rather than their absolute values, so the scaling of the spinning frequency by $1/N$ is equivalent to Δ_{CS} being scaled by a factor N. The frequency axis scale must be adjusted for the chosen interpretation of the scaling effect, but this is unimportant if spinning sidebands are identified by their order. In addition, to take advantage of efficient sampling of t_1 data points, which was explained at the end of the previous section, the pulse sequence must also suppress evolution of the spin system due to the isotropic chemical shift during the t_1 period. In the t_2 period of the experiment, the magnetization evolves under normal MAS conditions.

In fact, the two-dimensional phase-adjusted spinning sideband (2D-PASS)[202] and 2D-TOSS experiments,[201] briefly introduced in Section 3.2, both perform the desired experiment for the special case of $N = 1$, suggesting these might be useful starting points for the experiment of interest here. The CSA-amplification experiment developed by the Titman group[203, 204, 209] is based on the 2D-TOSS form of experiment, so here the possibility of extending the 2D-PASS method is investigated. A close parallel with the approach used in the development of the CSA-amplification experiment is acknowledged.
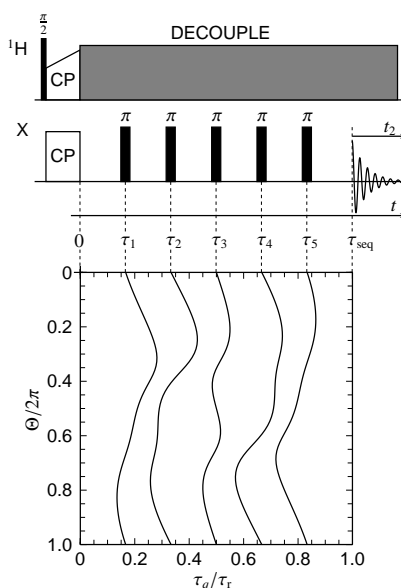
Figure 4.2: The 2D-PASS experiment using five π-pulses. The π-pulses are applied over a fixed t_1 period. During the two-dimensional experiment the pitch, Θ, is incremented from 0 to 2π and the pulse times are adjusted, following the timings in the plot shown below the pulse sequence.

The 2D-PASS experiment uses a sequence of π-pulses applied during the t_1 period of the two-dimensional experiment, shown in Figure 4.2. In contrast to most two-dimensional experiments, the t_1 evolution period is fixed throughout the experiment and instead the delays between the pulses are varied. A new variable called the pitch, Θ, is introduced, which is incremented instead of t_1 during the two-dimensional experiment. Associated with any value of Θ is a timing for each π-pulse in the sequence; pulse timings for $0 \leq \Theta \leq 2\pi$ are shown in the lower part of Figure 4.2. The overall effect of each set of pulse timings is to cause the magnetization from each crystallite to have evolved as if the sample had rotated an angle Θ during the t_1 period.[*] Therefore, to obtain the t_1 signal for (effective) rotation through one rotor period, Θ must be varied from 0 to 2π during the experiment.

The effect of a sequence of n π-pulses at times $\tau_1, \tau_2, \ldots, \tau_n$ and a total evolution period τ_{seq}, shown in Figure 4.3 on the following page, is concisely analysed using average Hamiltonian theory. It will be assumed that the only internal interaction is the chemical shift. The Hamiltonian governing the spin system has two terms $\hat{\mathcal{H}} = \hat{\mathcal{H}}_{\text{RF}} + \hat{\mathcal{H}}_{\text{CS}}$, where $\hat{\mathcal{H}}_{\text{RF}}$ is the RF pulse Hamiltonian, and $\hat{\mathcal{H}}_{\text{CS}} = \omega(t; \Omega_{\text{PR}})\hat{I}_z$ is the chemical shift Hamiltonian with $\omega(t; \Omega_{\text{PR}})$ defined in Equation (4.2). The propagator of the rotating-frame density

---

[*]An alternative description of the pitch is that the kth order spinning sideband in F_2 acquires an additional phase shift $k\Theta$ during the pulse sequence.[200, 202]
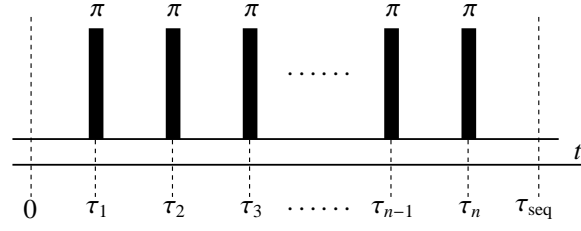
Figure 4.3: A general multiple π-pulse recoupling sequence consisting of n pulses, and a total evolution period τ_{seq}.

operator is

$$\hat{U}(t) = \hat{\mathcal{T}} \exp\left\{-\mathrm{i} \int_0^t \hat{\mathcal{H}}(t')\mathrm{d}t'\right\}, \quad \text{where } \hat{\mathcal{H}} = \hat{\mathcal{H}}_{\text{RF}} + \hat{\mathcal{H}}_{\text{CS}}, \tag{4.17}$$

where $\hat{\mathcal{T}}$ is the Dyson time ordering operator. This propagator can be factored into two parts, $\hat{U}(t) = \hat{U}_{\text{RF}}(t)\hat{U}^*(t)$, following the method outlined in Section 1.3.1 on page 10. The propagator due to the RF pulses is $U_{\text{RF}}(t)$, and $\hat{U}^*(t)$ describes the evolution of the spin system due to the chemical shift Hamiltonian, as viewed in the interaction frame of the RF pulses.

The RF propagator is

$$\hat{U}_{\text{RF}}(t) = \exp\left\{- \int_0^t \hat{\mathcal{H}}_{\text{RF}}(t')\mathrm{d}t'\right\} \tag{4.18}$$

where $\hat{\mathcal{H}}_{\text{RF}} = \omega_1 \hat{I}_x$ during a pulse, assuming an x-pulse with RF field strength ω_1, and otherwise is zero. Treating all the π-pulses as x-pulses, and making the approximation that the π-pulses are infinitely short, the RF propagator after the qth pulse and at τ_{seq} is

$$\hat{U}_{\text{RF}}(t) = \exp\left\{-\mathrm{i}q\pi\hat{I}_x\right\} \quad \tau_q < t < \tau_{q+1} \tag{4.19}$$

$$\hat{U}_{\text{RF}}(\tau_{\text{seq}}) = \exp\left\{-\mathrm{i}n\pi\hat{I}_x\right\}. \tag{4.20}$$

Evaluation of $\hat{U}^*(\tau_{\text{seq}})$ is deferred until the next section, but it is noted that it depends on the pulse timings used in the pulse sequence. To indicate this $\hat{U}^*(\tau_{\text{seq}})$ is written as $\hat{U}^*(\Theta)$.

The new spinning sideband correlation experiment requires the spin system to evolve over the course of the recoupling sequence as if under MAS with the anisotropic part of the chemical shift scaled by a factor of N, and the isotropic chemical shift being zero. Therefore, the aim is to find pulse times that cause the spin system to evolve during the pulse sequence *as if* it were effectively governed by the Hamiltonian

$$\hat{\mathcal{H}}_{\text{eff}}(t) = -N\left[C_1' \cos(\omega_{\text{r}}t) + C_2' \cos(2\omega_{\text{r}}t) + S_1' \sin(\omega_{\text{r}}t) + S_2' \sin(2\omega_{\text{r}}t)\right] \hat{I}_z, \tag{4.21}$$

from $t = 0$ to $t = \Theta/2\pi$, where Θ is the pitch that describes the *effective* rotation angle of the sample during the t_1 period, as described earlier. It turns out that the pulse sequence must also effectively reverse the sign of Δ_{CS}, which is why a minus sign is included in the right-hand side of Equation (4.21).[†]

Evolution of the density operator $\hat{\rho}$ when the spin system is governed by the Hamilton in Equation (4.21) is described by the propagator $\hat{U}_{eff}(\tau_{seq})$

$$\hat{U}_{eff}(\tau_{seq}) = \exp\left(-i \int_0^{\Theta/\omega_r} \hat{\mathcal{H}}_{eff}(t)dt\right) = \exp\left\{iN\left(\Phi(\Theta/\omega_r; \Omega_{PR}) - \Phi(0; \Omega_{PR})\right)\hat{I}_z\right\}. \quad (4.22)$$

Following CP, the density operator at start of the CSA-amplified PASS pulse sequence is $\hat{\rho}(0) = \frac{1}{2}\left(\hat{I}_+ + \hat{I}_-\right)$. The propagator in Equation (4.22) would lead to the density operator at the end of the pulse sequence

$$\begin{aligned}\hat{\rho}(\tau_{seq}, \Theta) &= \frac{1}{2}\hat{U}_{eff}(\tau_{seq})\left(\hat{I}_+ + \hat{I}_-\right)\hat{U}_{eff}^{-1}(\tau_{seq}) \\ &= \frac{1}{2}\left(\hat{I}_+ e^{-i\phi} + \hat{I}_- e^{+i\phi}\right),\end{aligned} \quad (4.23)$$

where $\phi = -N\left[\Phi(\Theta/\omega_r; \Omega_{PR}) - \Phi(0; \Omega_{PR})\right]$, and the density operator has been written as a function of the pitch. It follows that the pulse times must be chosen for each value of Θ so that the propagator $\hat{U}(\tau_{seq}, \Theta)$ for the pulse sequence, which is now written as a function of Θ, causes the same evolution of the initial density operator $\hat{\rho}(0)$ as the propagator $\hat{U}_{eff}(\tau_{seq})$ in Equation (4.22). Using $\hat{U}(\tau_{seq}, \Theta) = \hat{U}_{RF}(\tau_{seq})\hat{U}^*(\Theta) = e^{-in\pi\hat{I}_x}\hat{U}^*(\Theta)$, the required form of $\hat{U}^*(\Theta)$ can be identified

$$\begin{aligned}e^{-in\pi\hat{I}_x}(\tau_{seq})\hat{U}^*(\Theta)\hat{\rho}(0)\hat{U}^{*-1}(\Theta)e^{+in\pi\hat{I}_x} &= \frac{1}{2}\left(\hat{I}_+ e^{-i\phi} + \hat{I}_- e^{+i\phi}\right) \\ \hat{U}^*(\Theta)\hat{\rho}(0)\hat{U}^{*-1}(\Theta) &= \frac{1}{2}\left(\hat{I}_+ e^{-i(-1)^n\phi} + \hat{I}_- e^{+i(-1)^n\phi}\right) \quad (4.24) \\ &= \frac{1}{2}R_z((-1)^n\phi)\left(\hat{I}_+ + \hat{I}_-\right)R_z^{-1}((-1)^n\phi), \quad (4.25)\end{aligned}$$

where the relations $e^{i\pi\hat{I}_x}\hat{I}_+ e^{-i\pi\hat{I}_x} = \hat{I}_-$ and $e^{i\pi\hat{I}_x}\hat{I}_- e^{-i\pi\hat{I}_x} = \hat{I}_+$ have been used to obtain Equation (4.24). Thus, $\hat{U}^*(\Theta)$ is required to take the form

$$\hat{U}^*(\Theta) = \exp\left\{i(-1)^n N\left[\Phi(\Theta/\omega_r; \Omega_{PR}) - \Phi(0; \Omega_{PR})\right]\hat{I}_z\right\}. \quad (4.26)$$

The subsequent evolution of the density operator during the t_2 period can be evaluated

---

[†]The minus sign is introduced here so that the values of the scaling factors for which pulse timings can actually be calculated are positive.

using

$$\hat{\rho}(\tau_{\text{seq}}, \Theta, t_2) = \hat{U}_{\text{MAS}}(t_2 + \tau_{\text{seq}}, \tau_{\text{seq}})\hat{\rho}(\tau_{\text{seq}}, \Theta)\hat{U}_{\text{MAS}}^{-1}(t_2 + \tau_{\text{seq}}, \tau_{\text{seq}}), \qquad (4.27)$$

where, from Equation (4.10),

$$\hat{U}_{\text{MAS}}(t_2 + \tau_{\text{seq}}, \tau_{\text{seq}}) = \exp\left\{-i\left[\omega_{\text{iso}}t_2 + \Phi(t_2 + \tau_{\text{seq}}; \Omega_{\text{PR}}) - \Phi(\tau_{\text{seq}}; \Omega_{\text{PR}})\right]\hat{I}_z\right\}. \qquad (4.28)$$

The detected signal is proportional to $\overline{\langle \hat{I}_+ \rangle}$, which is evaluated using the using the expression for $\hat{\rho}(\tau_{\text{seq}}, \Theta, t_2)$, and has the form

$$s(\Theta/\omega_{\text{r}}, t_2) = \frac{1}{2}\overbrace{e^{iN\Phi(0)}e^{-iN\Phi(\Theta/\omega_{\text{r}})}}^{t_1 \text{ pulse sequence}}\overbrace{e^{-i\Phi(\tau_{\text{seq}})}e^{i\Phi(t_2+\tau_{\text{seq}})}e^{i\omega_{\text{iso}}t_2}}^{t_2 \text{ MAS}}, \qquad (4.29)$$

where the braces identify the origin of the different terms.

The spectrum $S(\omega_1, \omega_2)$ is generated by Fourier transformation of $s(\Theta/\omega_{\text{r}}, t_2)$ with respect to Θ/ω_{r} and t_2. To interpret this spectrum, the projection onto the F_1 and F_2 axes is calculated by summing over the frequency points in the F_2 and F_1 dimension respectively

$$P_1(\omega_1^{(j)}) = \sum_k S(\omega_1^{(j)}, \omega_2^{(k)}) \qquad\qquad P_2(\omega_2^{(k)}) = \sum_j S(\omega_1^{(j)}, \omega_2^{(k)}),$$

where $P_1(\omega_1)$ is the projection of $S(\omega_1, \omega_2)$ onto the F_1 axis, and $P_2(\omega_2)$ is the projection onto the F_2 axis. The sum relation of the discrete Fourier transform[21] states that if $G(\omega^{(k)})$ is the discrete Fourier transformation of $g(t^{(j)})$ then

$$g(0) = \sum_k G(\omega^{(k)}). \qquad (4.30)$$

It follows that the projections correspond to

$$P_1(\omega_1^{(k)}) = \text{FT}[s(\Theta/\omega_{\text{r}}, 0)]_{\Theta/\omega_{\text{r}}} \qquad P_2(\omega_2^{(j)}) = \text{FT}[s(0, t_2)]_{t_2},$$

where $\quad s(\Theta/\omega_{\text{r}}, 0) = \frac{1}{2}e^{iN\Phi(0)}e^{-iN\Phi(\Theta/\omega_{\text{r}})} \qquad s(0, t_2) = \frac{1}{2}e^{-i\Phi(\tau_{\text{seq}})}e^{i\Phi(t_2+\tau_{\text{seq}})}e^{i\omega_{\text{iso}}t_2},$

using the notation $\text{FT}[g(t)]_t$ to indicate the Fourier transformation of $g(t)$ with respect to t. Comparison of $s(0, t_2)$ with the signal described in Equation (4.11) on page 79, shows that the F_2 projection ($P_2(\omega_2)$) is simply the same as the one-dimensional MAS spectrum, with spinning sidebands separated by the spinning frequency ω_{r}.

By contrast, comparison of the signal $s(\theta/\omega_{\text{r}}, 0)$ with that described in Equation (4.11)

shows that the two signals have the same form, except for a scaling of the $\Phi(t)$ terms in the exponential factor by $-N$ and $t = \Theta/\omega_r$ for $s(\theta/\omega_r, 0)$. As stated before, Θ is sampled over the range 0 to 2π to give the effect of evolution through one complete rotor period, so the F_1 projection ($P_1(\omega_1)$) takes the form a spinning sideband envelope, as shown in Figure 4.1(c) on page 81. The scaling of the $\Phi(t)$ terms gives the desired effect of scaling the CSA by $-N$, or equivalently the spinning frequency by $1/N$ (with a reversal in sign of Δ_{CS}). Therefore, calculation of the F_1 projection is the used to determine the spinning sideband intensities at the effective spinning frequency ω_r/N.

This experiment will be referred to as CSA-amplified PASS, to recognise its close relation to the 2D-PASS and CSA-amplification[203, 204, 209] experiments. Determination of the required π-pulse timings for this experiment is addressed in the next section.

4.2.1   Calculation of pulse timings

The approach proposed by Antzutkin and co-workers for obtaining pulse-timings in the 2D-PASS experiment is followed here.[202]

The interaction-frame chemical shift Hamiltonian is calculated by

$$\hat{\mathcal{H}}_{CS}^*(t) = \hat{U}_{RF}^{-1}(t)\hat{\mathcal{H}}_{CS}(t)\hat{U}_{RF}(t), \tag{4.31}$$

and $\hat{U}^*(\Theta)$ is approximated using the first-order interaction-frame average Hamiltonian, defined in Equation (1.42), to give

$$\hat{U}^*(\Theta) = \exp\left\{-i\overline{\hat{\mathcal{H}}_{CS}^{*(1)}}\tau_{seq}\right\} \tag{4.32}$$

$$\overline{\hat{\mathcal{H}}_{CS}^{*(1)}} = \frac{1}{\tau_{seq}} \int_0^{\tau_{seq}} \hat{\mathcal{H}}_{CS}^*(t)\, dt. \tag{4.33}$$

Using the RF propagator defined in Equation (4.19), the first-order average Hamiltonian of a sequence of n π-pulses is calculated to be

$$\frac{1}{\tau_{seq}} \int_0^{\tau_{seq}} \hat{\mathcal{H}}_{CS}^*(t)dt = \frac{\hat{I}_z}{\tau_{seq}} \left\{ \int_0^{\tau_1} \omega(t; \Omega_{PR})\, dt - \int_{\tau_1}^{\tau_2} \omega(t; \Omega_{PR})\, dt + \ldots \right.$$
$$\left. + (-1)^{n-1} \int_{\tau_{n-2}}^{\tau_n} \omega(t; \Omega_{PR})\, dt + (-1)^n \int_{\tau_n}^{\tau_{seq}} \omega(t; \Omega_{PR})\, dt \right\}, \tag{4.34}$$

which is evaluated using Equation (4.2) for $\omega(t; \Omega_{PR})$, to obtain

$$\frac{1}{\tau_{seq}} \int_0^{\tau_{seq}} \hat{\mathcal{H}}_{CS}^*(t')\mathrm{d}t' = \frac{\hat{I}_z}{\tau_{seq}} \left\{ \omega_{iso}\left((-1)^n \tau_{seq} + 2\sum_{q=1}^n (-1)^{q-1}\tau_q \right) + \frac{(-1)^n}{\omega_r} \left(C_1' \sin(\omega_r \tau_{seq}) \right. \right.$$

$$\left. \frac{1}{2} C_2' \sin(2\omega_r \tau_{seq}) - S_1' \cos(\omega_r \tau_{seq}) - \frac{1}{2} S_2' \cos(2\omega_r \tau_{seq}) \right)$$

$$+ \frac{2}{\omega_r} \sum_{q=1}^n (-1)^{q-1} \left(C_1' \sin(\omega_r \tau_q) + \frac{1}{2} C_2' \sin(2\omega_r \tau_q) \right.$$

$$\left. \left. - S_1' \cos(\omega_r \tau_q) - \frac{1}{2} S_2' \cos(2\omega_r \tau_q) \right) + \frac{1}{\omega_r} \left[S_1' + \frac{1}{2} S_2' \right] \right\}. \quad (4.35)$$

As detailed earlier, the propagator $\hat{U}^*(\Theta)$ is required to have the form

$$\hat{U}^*(\Theta) = \exp\left\{ -\mathrm{i}\overline{\hat{\mathcal{H}}_{CS}^{*(1)}} \tau_{seq} \right\} = \exp\left\{ \mathrm{i}(-1)^n N \left[\Phi(\Theta/\omega_r; \Omega_{PR}) - \Phi(0; \Omega_{PR}) \right] \hat{I}_z \right\}, \quad (4.36)$$

so the first-order average Hamiltonian is required to be equal to

$$\overline{\hat{\mathcal{H}}_{CS}^{*(1)}} = \frac{1}{\tau_{seq}} \int_0^{\tau_{seq}} \hat{\mathcal{H}}_{CS}^*(t)\,\mathrm{d}t = -\frac{(-1)^n}{\tau_{seq}} N \left[\Phi(\Theta/\omega_r; \Omega_{PR}) - \Phi(0; \Omega_{PR}) \right] \hat{I}_z. \quad (4.37)$$

To determine the required pulse times to fulfil Equation (4.37), the $\Phi(\Theta/\omega_r; \Omega_{PR})$ functions in the right-hand-side of Equation (4.37) are written in term of C_1', S_1', C_2' and S_2', using Equation (4.8). The right-hand-side of Equation (4.37) is then equated with the average Hamiltonian in Equation (4.35), and coefficients of ω_{iso}, C_1', S_1', C_2' and S_2' are extract to obtain a set of five simultaneous equations that must be satisfied in order to achieve the desired average Hamiltonian. These are

$$0 = (-1)^n \cos(m\omega_r \tau_{seq}) + 2\sum_{q=1}^n (-1)^{q-1} \cos(m\omega_r \tau_q) -$$

$$(1 + (-1)^n N) + (-1)^n N \cos(m\Theta) \quad (4.38)$$

$$0 = (-1)^n \sin(m\omega_r \tau_{seq}) + 2\sum_{q=1}^n (-1)^{q-1} \sin(m\omega_r \tau_q) + (-1)^n N \sin(m\Theta) \quad (4.39)$$

$$0 = (-1)^n \tau_{seq} + 2\sum_{q=1}^n (-1)^{q-1}\tau_q, \quad (4.40)$$

where $m = 1$ and $m = 2$. Equation (4.40) arises from the requirement that there is no net evolution of the spin system due to the isotropic chemical shift during the t_1 period.

To calculate numerical solutions to these non-linear simultaneous equations, there must
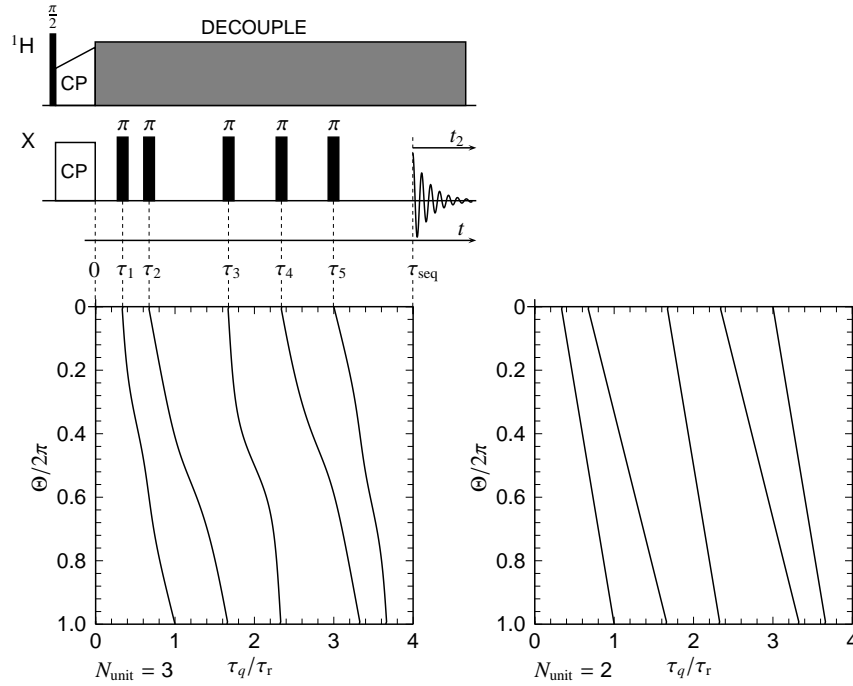
Figure 4.4: The CSA-amplfified PASS pulse sequence. The plots below the pulse sequence show the required pulse timings as a function of Θ for scaling factors $N_{\text{unit}} = 3$ and $N_{\text{unit}} = 2$.

be at least as many unknowns (pulses times) as equations. Thus, there is a minimum of five pulses in the sequence. Solutions to these equations were determined using a routine executed by the MuPAD[210] Computer Algebra System; this routine can be found in Appendix B.

For the minimum possible number of pulses $n = 5$, solutions with $1 \leq N \leq 3.4$ were found. In particular, sequences of a total length $\tau_{\text{seq}} = \tau_{\text{r}}$ can be found with a scaling factor $1 \leq N < 2$. For scaling factors in the range $2 \leq N \leq 3.4$, the shortest sequences that avoid pulses of a finite length overlapping require $\tau_{\text{seq}} = 4\tau_{\text{r}}$. The pulse timings as a function of Θ are plotted for $N = 3$ and $N = 2$ in Figure 4.4. Using more than five π-pulses it was not possible to find solutions to Equations (4.38) to (4.40) using numerical methods, as convergence to valid solutions for an under-determined set of simultaneous non-linear equations is difficult.

Despite not finding five π-pulse sequences that achieve larger scaling factors than $N = 3.4$, sequences that achieve higher scaling factors can be constructed by concatenating the basic five-pulse units. Hereafter, the scaling factor associated with each five-pulse unit is labelled N_{unit}. For a sequence of $(j + 1)$ five-pulse units, the total scaling factor is $N = (j + 1)N_{\text{unit}}$. This scheme is illustrated in Figure 4.5 on the following page. An additional π-pulse is required between adjacent five-pulse units to ensure that the
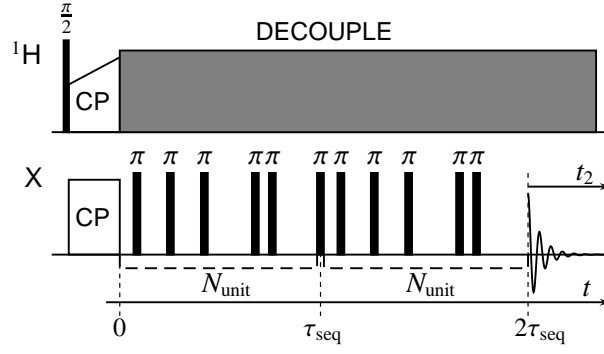
Figure 4.5: Concatenation of two pulse-sequence units with scaling factor N_{unit} achieves a total scaling factor of $2N_{\text{unit}}$. A π-pulse separates the two pulse-sequence units.

evolution of the spin system during the first five-pulse unit is not reversed by evolution during the second. This can be shown to be necessary by considering the case of two five-pulse units without the additional π-pulse, where the propagator over the full sequence $\hat{U}_{\text{total}}(2\tau_{\text{seq}}, \Theta)$ is

$$
\begin{aligned}
\hat{U}_{\text{total}}(2\tau_{\text{seq}}, \Theta) &= \hat{U}(\tau_{\text{seq}}, \Theta)\hat{U}(\tau_{\text{seq}}, \Theta) \\
&= \hat{U}_{\text{RF}}(\tau_{\text{seq}})\hat{U}^*(\Theta)\hat{U}_{\text{RF}}(\tau_{\text{seq}})\hat{U}^*(\Theta) \\
&= e^{-i5\pi\hat{I}_x}\hat{U}^*(\Theta)e^{-i5\pi\hat{I}_x}\hat{U}^*(\Theta) \\
&= e^{-i5\pi\hat{I}_x}e^{-i5\pi\hat{I}_x}e^{+i5\pi\hat{I}_x}\hat{U}^*(\Theta)e^{-i5\pi\hat{I}_x}\hat{U}^*(\Theta) \\
&= e^{-i10\pi\hat{I}_x}\hat{U}^{*-1}(\Theta)\hat{U}^*(\Theta) \\
&= e^{-i10\pi\hat{I}_x},
\end{aligned}
\tag{4.41}
$$

where $\exp(-i5\pi\hat{I}_x)\exp(i5\pi\hat{I}_x) = \hat{\mathbf{1}}$ and

$$
\begin{aligned}
\exp(i5\pi\hat{I}_x)\hat{U}^*(\Theta)\exp(-i5\pi\hat{I}_x) &= \exp(i5\pi\hat{I}_x)e^{\{-iN[\Phi(\Theta/\omega_r;\Omega_{\text{PR}})-\Phi(0;\Omega_{\text{PR}})]\hat{I}_z\}}\exp(-i5\pi\hat{I}_x) \\
&= \exp\{+iN[\Phi(\Theta/\omega_r;\Omega_{\text{PR}}) - \Phi(0;\Omega_{\text{PR}})]\hat{I}_z\} \\
&= \hat{U}^{*-1}(\Theta)
\end{aligned}
\tag{4.42}
$$

have been used. Equation (4.41) shows that there would be no net evolution of the density operator if the additional π-pulse was not used, as $\frac{1}{2}e^{-i10\pi\hat{I}_x}\left(\hat{I}_+ + \hat{I}_-\right)e^{i10\pi\hat{I}_x} = \frac{1}{2}\left(\hat{I}_+ + \hat{I}_-\right)$.

With the additional π-pulse included

$$
\begin{aligned}
\hat{U}_{\text{total}}(2\tau_{\text{seq}}, \Theta) &= \hat{U}(\tau_{\text{seq}}, \Theta)e^{-i\pi\hat{I}_x}\hat{U}(\tau_{\text{seq}}, \Theta) \\
&= \hat{U}_{\text{RF}}(\tau_{\text{seq}})\hat{U}^*(\Theta)e^{-i\pi\hat{I}_x}\hat{U}_{\text{RF}}(\tau_{\text{seq}})\hat{U}^*(\Theta) \\
&= e^{-i5\pi\hat{I}_x}\hat{U}^*(\Theta)e^{-i\pi\hat{I}_x}e^{-i5\pi\hat{I}_x}\hat{U}^*(\Theta) \\
&= e^{-i5\pi\hat{I}_x}e^{-i6\pi\hat{I}_x}e^{i6\pi\hat{I}_x}\hat{U}^*(\Theta)e^{-i6\pi\hat{I}_x}\hat{U}^*(\Theta) \\
&= e^{-i11\pi\hat{I}_x}\hat{U}^*(\Theta)\hat{U}^*(\Theta),
\end{aligned}
\tag{4.43}
$$

and the $\hat{U}^*(\Theta)\hat{U}^*(\Theta)$ part of Equation 4.43 means that the density operator evolves with the scaling factor $N = 2N_{\text{unit}}$.

Concatenation of the five-pulse units gives sequences of 11 and 17 π-pulses, with maximum scaling factors of 6.8 and 10.2 respectively. Larger scaling factors may be obtained using longer pulse sequences.

4.3 Experimental implementation of CSA-amplified PASS

To perform the experiment in a convenient manner, the pulse timings for the various scaling factors and number of Θ values are stored in a series of files on the spectrometer computer. The required file is then chosen as an input variable in the pulse sequence when performing the experiment. This means that several versions of the pulse program are not needed. In addition to optimising the usual CP and ^{1}H decoupling parameters, it is only necessary to specify the π-pulse length, the sample spinning frequency, and the required scaling factor. The necessary phase cycle, which is explained in the following section, is automatically calculated for the chosen number of five π-pulse units used.

4.3.1 Cogwheel phase cycling

The CSA-amplified PASS sequence acts on transverse magnetization generated by CP (or a 90°-pulse). The initial density operator is $\hat{\rho}(0) = \frac{1}{2}\left(\hat{I}_+ + \hat{I}_-\right)$, so initially there are $(+1)$- and (-1)-quantum coherences. The effect of the π-pulses is to change the sign of the coherence order and so the desired coherence-transfer pathway ($\boldsymbol{p}^0$) is as shown by the red line below the CSA-amplified PASS pulse sequence in Figure 4.6 on page 93.

Nested phase cycling and cogwheel phase cycling were outline in Section 2.3. To select the desired coherence-transfer pathway using a nested phase cycling scheme, coherence

order changes of 2 (or -2) need to be selected at each π-pulse, which requires the RF phase of each π-pulse to be cycled independently in steps of $2\pi/3$. This would necessitate a total phase cycle of $3^5 = 243$ steps for the five π-pulse experiment. For the 11 pulse experiment, this becomes $3^{11} = 177147$ steps, which is completely impractical. Instead, a cogwheel phase cycle can be used, as suggested by Ivchencko and co-workers for 2D-PASS.[66]

The selection rules for cogwheel phase cycling are conveniently visualised by cogwheel splitting diagrams.[62] The cogwheel splitting diagram plots the build up of the pathway signature, which is defined as

$$\sum_{q=1}^{n-1} \Delta\nu_{q,q+1} p_{q,q+1} - \nu_n p_{n,\text{rec}} \tag{4.44}$$

where $p_{q,q+1}$ is the coherence order between the qth and $(q+1)^{\text{th}}$ pulse and $\Delta\nu_{q,q+1}$ is the difference in the winding numbers of the same pair of pulses. The selection rules require that the winding numbers of the pulses must be chosen so that the pathway signature of the desired coherence-transfer pathway is (*i*) different from the pathway signature associated with any undesired coherence-transfer pathway, and (*ii*) does not differ by a multiple of N_{PC} (the total number of steps in the phase cycle) from any other undesired pathway signature value. The subscript PC is used in this chapter to differentiate the number of steps in the phase cycle from the scaling factor.

For an isolated spin-1/2 nucleus, the desired coherence order is equal to ± 1 at any interval between pulses in the sequence. The first condition is easily achieved by ensuring that $\Delta\nu_{q,q+1} = p^0_{q,q+1}$ and $\nu_n = -p^0_{n,\text{rec}} = +1$ (or equally $\Delta\nu_{q,q+1} = -p^0_{q,q+1}$ and $\nu_n = p^0_{n,\text{rec}} = -1$). This is shown in the lower part of Figure 4.6, where the cogwheel splitting diagram plots the build up of the pathway signatures for *all* possible coherence-transfer pathways (black lines). The pathway signature for the desired coherence-transfer pathway is plotted in red, and has a unique value at all points throughout the pulse sequence. Only phase signatures that pass through the barrier on the right-hand-side of the cogwheel splitting diagram are selected. The holes in the barrier are spaced at intervals equal to the number of steps in the phase cycle, and the position of the holes is determined by adjusting the receiver phase according to Equation (2.46) on page 53 to ensure selection of the desired coherence-transfer pathway. From this diagram, it is clear that the number of steps in the phase cycle must be $N_{\text{PC}} = 13$ to fulfil condition (*ii*) and avoid selecting any other coherence-transfer pathway. Having determined the necessary values of $\Delta\nu_{q,q+1}$, the absolute values of the winding numbers can be derived from the condition $\nu_n = 1$. This result can easily be extended to the concatenated sequences, as the cogwheel splitting diagram has the same
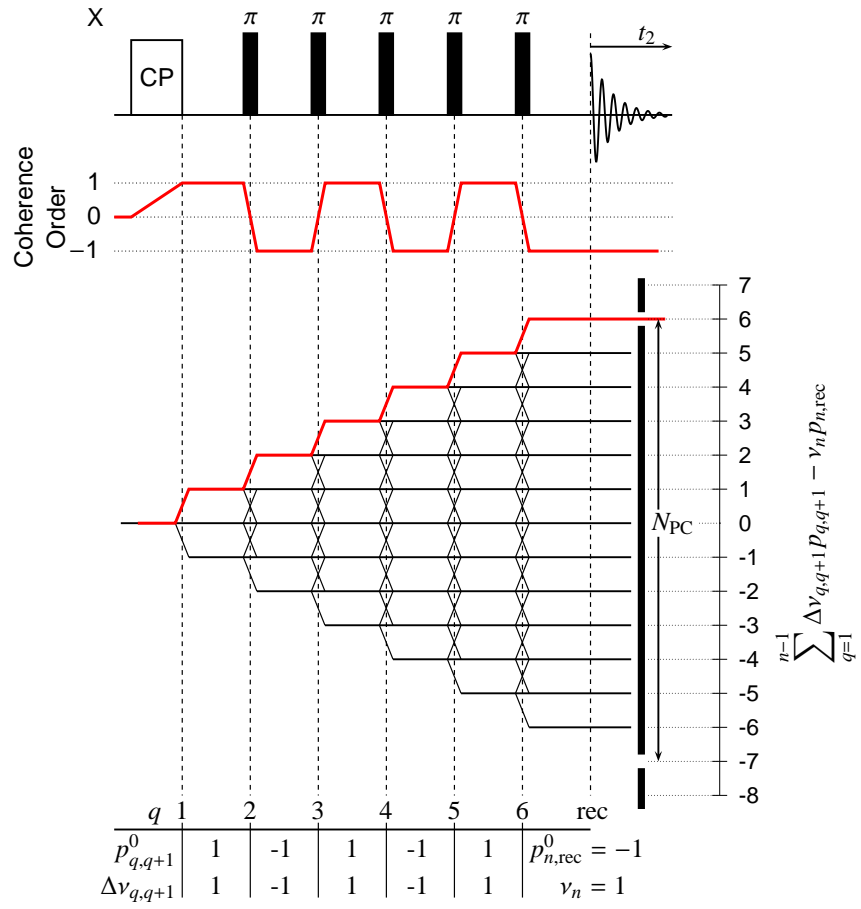
Figure 4.6: (Top) The CSA-amplified PASS pulse sequence and the required coherence-transfer pathway (red). (Bottom) The build up of the pathway signature for all possible coherence-transfer pathways is plotted in black, the desired pathway signature is plotted in red. Figure based on reference [66].
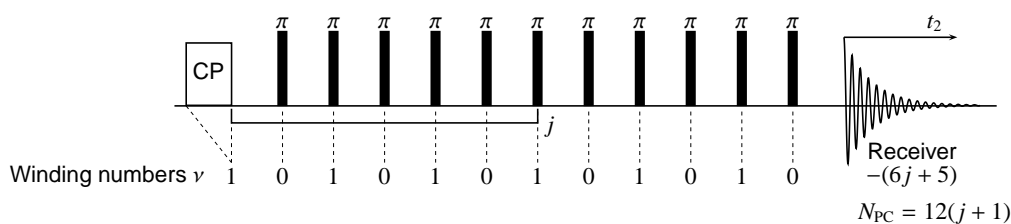
Figure 4.7: The required winding numbers of each pulse in the CSA-amplified PASS sequence. The total number of steps in the cogwheel phase cycle is $N_{PC} = 12(j + 1)$, where j is number of times the five pulse unit is repeated.

form as in Figure 4.6, although the range of phase signature values is larger.

The details of artefacts arising from an incorrectly adjusted quadrature receiver, so-called quadrature images and DC-offsets, are not detailed here (see reference [211], for example). However, it should be noted that for the phase cycle to remove these artefacts, the winding number labelled ν_{rec} above must in fact be adjusted at the post-digitizer phase shift (Section 1.7).[66] If receiver artefacts are sufficiently small that they can neglected, then it can be assumed that only (-1)-quantum coherence are detected by the receiver and ν_n can be chosen to be zero and the number of steps in the phase cycle is reduced by 2.

The spectrometers used to record the spectra shown in this chapter were unable to implement post-digitizer phase shifts in steps smaller that $90°$. For this reason, the receiver phase was adjusted according to ν_{rec} and $\nu_n = 0$ was used. The number of steps in the phase cycle was chosen to be even (by including an additional step in the phase cycle) so that the ^1H $\pi/2$-pulse used before CP could be alternated in phase between on $+x$ and $-x$ on alternate scans an even number of times, the post-digitizer phase being adjusted to account of this. This may be shown to select only carbon signals generated by the CP step and also removes the DC-offset caused by non-ideal behaviour of the quadrature receiver. This means 12 steps in the phase cycle are needed for the five-pulse unit, and for $(j + 1)$ five-pulse units in the sequence a total of $N_{PC} = 12(j + 1)$ steps are needed. The necessary winding numbers and number of steps required for CSA-amplified PASS is summarised in Figure 4.7.

4.4   Experimental demonstration of CSA-amplified PASS

As a first experimental demonstration of the CSA-amplified PASS experiment, the integrated sideband intensities from the one-dimensional MAS spectrum of sodium phosphate spinning at 1666 Hz were compared with the sideband intensities obtained
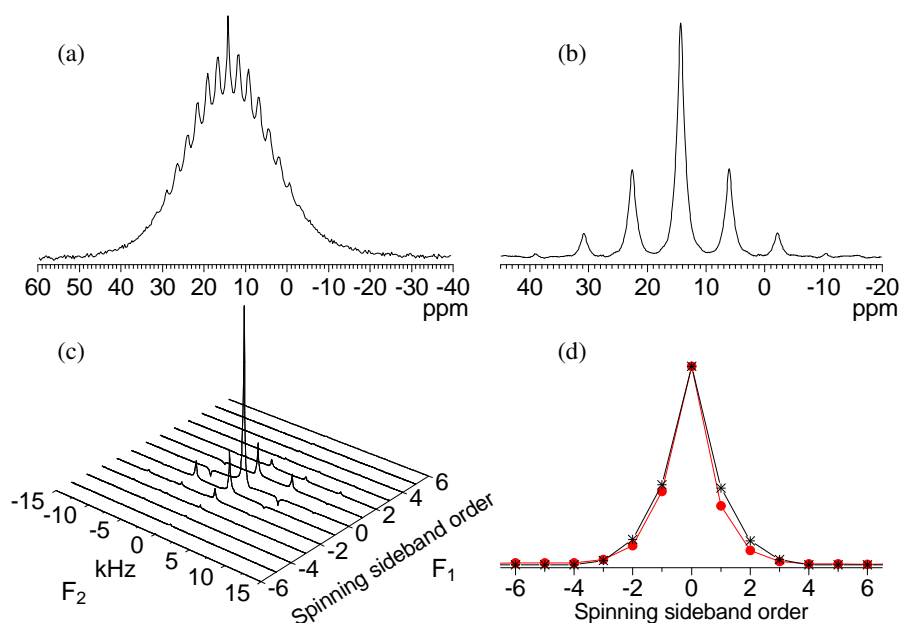
Figure 4.8: Experimental ^{31}P NMR spectra of Na$_3$PO$_4$. (a) MAS spectrum spinning at 500 Hz. (b) MAS spectrum spinning at 1666 Hz. (c) CSA-amplified PASS spectrum at a spinning frequency of 5000 Hz, using a CSA-amplified PASS sequence with scaling factor $N = 3$. (d) Integrated spinning sideband intensities from the one-dimensional spectrum in (b) (black), and the F_1 projection derived from the spectrum in (c) (red).

from a two-dimensional CSA-amplified PASS experiment using scaling factor of $N = 3$ and MAS frequency 5000 Hz. A spinning frequency of 1666 Hz was chosen because at lower frequencies the spectrum is dominated by homonuclear dipolar coupling effects between the abundant ^{31}P nuclei. Figures 4.8(a),(b) show the ^{31}P NMR spectrum of sodium phosphate at MAS frequencies of 500 Hz and 1666 Hz. Following double Fourier transformation of the two-dimensional FID obtained from a CSA-amplified PASS experiment, the spectrum in Figure 4.8(c) is obtained. By summing over the spinning sidebands in the F_2 dimension, the spinning sideband intensities at the effective spinning frequency of 1666 Hz are determined. Figure 4.8(d) compares the F_1 projection with the integrated intensities derived from the one-dimensional spectrum recorded with spinning frequency 1666 Hz in Figure 4.8(b). As expected, the two sets of spinning sideband intensities are consistent with each other. It was not possible to record the complete phase cycle for this sample, owing to its long spin-lattice relaxation time constant. Instead, fixed phases of 0°, 330°, 60°, 330°, 0° for the five π-pulses was used. Consequently, pulse imperfections are probably the main cause of the difference seen between the sideband intensities.

As a second example, the ^{13}C CSA-amplified PASS spectrum of fumaric acid monoethyl

ester was recorded using a scaling factor of $N = 10.2$ and effective spinning frequency $\omega_r/2\pi N = 564$ Hz. The structure and labelling of the ^{13}C sites in fumaric acid monoethyl ester used in this chapter is shown in Figure 4.9. This sample was chosen because it
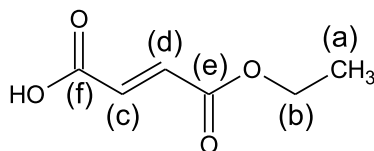

Figure 4.9: Fumaric acid monoethyl ester and the labelling scheme used in this chapter, based on solution-state NMR chemical shift assignments.[212]

contains both sp^2 and sp^3 carbon environments and CH$_2$ and CH$_3$ groups; it is therefore representative of many organic solids. The F_1 projections of the six carbon environments are shown in Figure 4.10 on the next page. While the number of spinning sidebands recorded in the F_1 projection is far more that would normally be necessary to determine the chemical shift anisotropy parameters, it serves as a sensitive test of the pulse sequence.

In order to confirm that the sideband intensities were correctly reproduced by the CSA-amplified PASS experiment, numerical fits to the experimental data were calculated using the SIMPSON[39] program. The simulations involved calculation of one-dimensional spinning sideband spectra, rather than simulating the full two-dimensional experiment. The Simplex method was used to minimise the root mean square deviation between the simulated and experimental sideband intensities by varying δ_{aniso}, η_{CS} and an intensity weighting factor. From the overlay of experimental and simulated F_1 projections in Figure 4.10, it can be seen that the correspondence between the two is excellent for all six ^{13}C sites in the molecule. The fitted values of δ_{aniso} and η_{CS} for each site are shown alongside the projections, although the asymmetry parameter for site (a) is poorly defined by the small number of spinning sidebands recorded and is shown in parenthesis. The fitted CSA parameters are summarised in Table 4.1.

The principal application of the CSA-amplified PASS experiment is the measurement of small chemical shift anisotropies. This may require large scaling factors. To demonstrate that large scaling factors can be implemented, the CSA-amplified PASS experiment was repeated on the fumaric acid monoethyl ester sample using a scaling factor of $N = 20.4$ and effective spinning frequency of $\omega_r/(N2\pi)=147$ Hz to measure the spinning sidebands arising from the CH$_3$ site, and $N = 27.2$ and $\omega_r/(N2\pi)=525$ Hz to measure the spinning sideband intensities of the other five ^{13}C sites. These results are shown in Figure 4.11 on page 99. To confirm the accurate reproduction of the sideband intensities, simulated fits
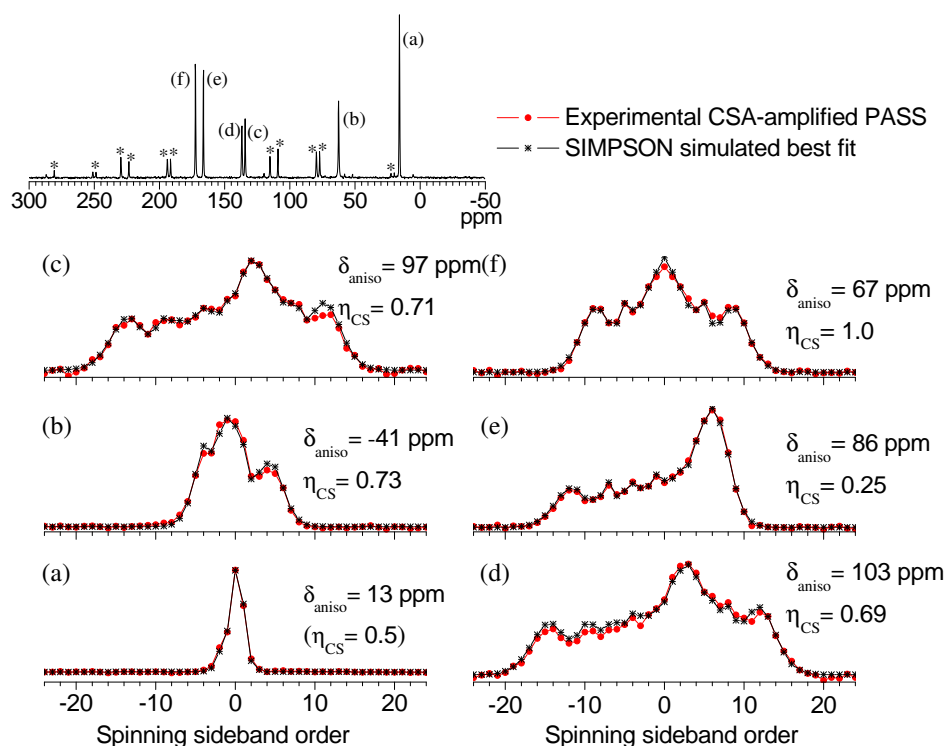
Figure 4.10: Experimental ^{13}C NMR spectra of fumaric acid monoethyl ester at a spinning frequency of 5750 Hz. Asterisks mark spinning sidebands in the one-dimensional spectrum. (a-f) Experimental F_1 projections determined using the CSA-amplified PASS experiment (red circles) for each isotropic peak labelled in the one-dimensional spectrum, an effective spinning frequency of 564 Hz was used ($N = 10.2$). Simulated best fit sideband intensities are illustrated by the overlaid lines and asterisks, together with the δ_{aniso} and η_{CS} values used.

Site	$N = 10.2$	$N = 27.2$
(a)	13±2 ppm	14±1 ppm ($N = 20.4$)
(b)	-41±2 ppm	-40±2 ppm
(c)	97±4 ppm	96±4 ppm
(d)	103±4 ppm	102±4 ppm
(e)	86±3 ppm	85±3 ppm
(f)	67±3 ppm	-66±3 ppm

(a) δ_{aniso} values.

Site	$N = 10.2$	$N = 27.2$
(a)	(0.5±0.4)	0.38±0.07 ($N = 20.4$)
(b)	0.73±0.07	0.78±0.07
(c)	0.71±0.07	0.71±0.07
(d)	0.69±0.07	0.68±0.07
(e)	0.25±0.04	0.25±0.04
(f)	1.0±0.05	0.96±0.07

(b) η_{CS} values.

Table 4.1: Comparison of the fitted (a) δ_{aniso} and (b) η_{CS} values for the six ^{13}C sites of fumaric acid monoethyl ester from the results in Figures 4.10 and 4.11.

were again calculated using the SIMPSON program, and the fitted CSA parameters are shown in Table 4.1.

The correspondence between the experimental and simulated spinning sideband intensities clearly remains good across the full sideband manifold of each ^{13}C site, particularly considering that over 30 spinning sideband intensities are recorded for sites (c) to (f). However, the deviation between the experimental and simulated sideband intensities is noticeably worse for sites (b), (c) and (d) in Figure 4.11, than when using the smaller scaling factor of $N = 10.4$. Nonetheless, this appears to have a negligible effect on the fitted parameters, which are in agreement to within ±1 ppm for the anisotropy and ±0.05 for the asymmetry of those found using the smaller scaling factor in Figure 4.10, which is consistent with the estimated errors in the fitted parameters. The exception is for site (a), where the asymmetry parameter was poorly determined from the result in Figure 4.10.

4.5   Analysis of the robustness of CSA-amplified PASS

To provide a more detailed analyses of the robustness of the CSA-amplified PASS pulse sequence, a series of experiments were performed with an effective spinning frequency in the indirectly observed dimension of $\omega_{\text{r}}/(N2\pi) = 700$ Hz for all experiments, but with a wide range of scaling factors N and actual spinning frequencies. The sample used was ^{13}C-1-glycine. The F_1 projections were compared with the sideband intensities obtained from a one-dimensional spectrum recorded with MAS frequency of 700 Hz. The results are shown in Figure 4.12 on page 100, where it can be seen that the sideband intensities are accurately reproduced in the CSA-amplified PASS experiment, even up to scaling factors of $N = 21$. Only very slight deviation from the spinning sideband intensities measured in the one-dimensional spectrum are seen in the sideband intensity
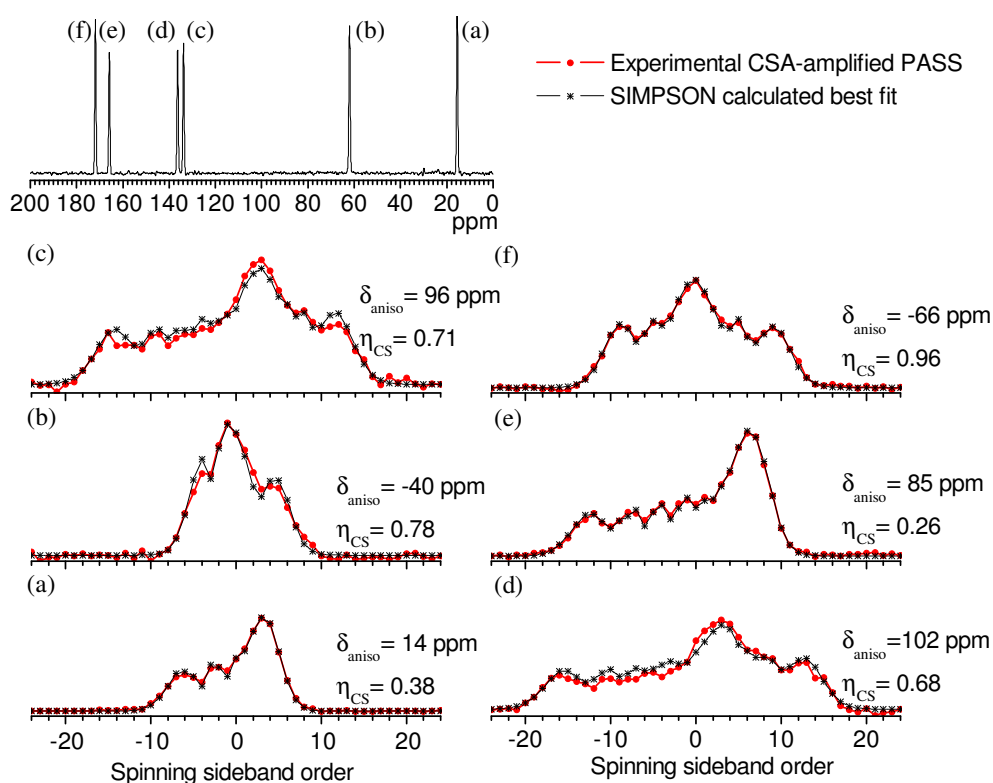
Figure 4.11: (TOP) ^{13}C one-dimensional CPMAS spectrum of fumaric acid monoethyl ester spinning at 14280 Hz indicating sites (a)-(f), and the corresponding F_1 projections for each site recorded using the CSA-amplified PASS experiment. The effective spinning frequency in F_1 was 147 Hz for (a) and 525 Hz for (b)-(f), recorded with scaling factors of $N = 20.4$ and $N = 27.2$ respectively. Best fit simulations are overlaid black.
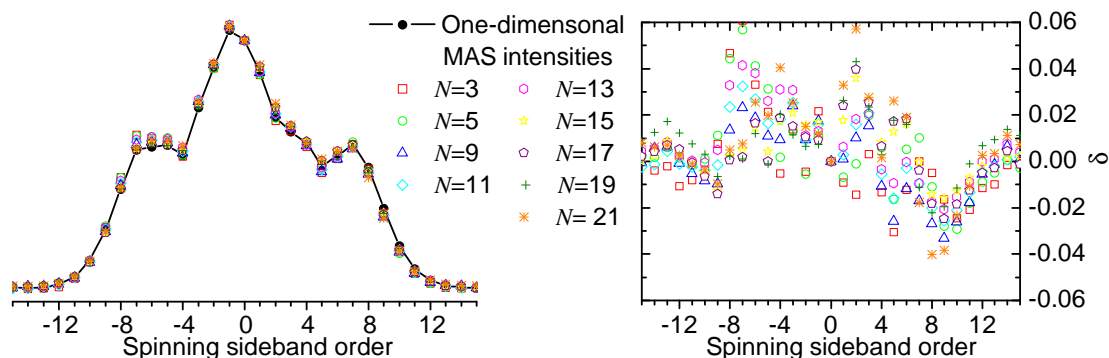
Figure 4.12: Comparison of ^{13}C sideband intensities obtained using the CSA-amplified PASS experiment with the effective spinning frequency $\omega_r/(N2\pi) = 700$ Hz and the sideband intensities derived from a one-dimensional MAS spectrum for ^{13}C-1-glycine. The difference between the one-dimensional MAS sideband intensities and the CSA-amplified PASS derived intensities, normalised to their isotropic peak intensity, is shown on the right.

envelope from CSA-amplified PASS experiments. Although there appears to be some systematic deviation of the F_1 projections from the sideband intensities obtained in the one-dimensional experiment, the deviations are less that 5% of the isotropic peak amplitude, and are unlikely to introduce significant errors into the fitted CSA parameters. The systematic variation is believed to be caused by instability of the spinning frequency whilst recording the one-dimensional spectrum at 700 Hz, as stable spinning was found to be difficult to maintain, rather than from the CSA-amplified PASS experiment.

4.5.1 Pulse imperfections

When several pulses are applied prior to the detection of the signal in an NMR experiment, non-ideal behaviour of the pulses can have a detrimental effect on the resulting spectrum. This is well known for series of π-pulses, where the signal is found to be particularly sensitive to imperfections in the pulses.[213,214] The three most important types of pulse imperfections are (i) off-resonance effects, which cause the rotation of the magnetization to be about an axis that lies out of the transverse plain; (ii) RF field inhomogeneity within the coil of the probe, which cause the rotation angle of the pulse to deviate from an exact π-pulse by an amount that varies throughout the sample volume (this effect is the same as pulse length miscalibration); and (iii) finite RF field strengths, which of course mean that the pulse has a finite duration, which may cause problems if the pulses occupy a significant proportion of a rotor period, and also off-resonance effects are more significant.

To investigate the robustness of the CSA-amplified PASS experiment with respect to each of these possible pulse imperfections, a further series of experiments were performed. A comparison was made between the sideband intensities obtained from a one-dimensional spectrum and those determined from CSA-amplified PASS spectra recorded with experimental parameters intentionally mis-set to simulate the effect of a resonance offset from the isotropic frequency, incorrectly calibrated π-pulse lengths/RF field inhomogeneity and a range of RF field strengths. These experiments employed a scaling factor of $N = 10$ and spinning frequency of $\omega_r = 7000$ Hz using a ^{13}C-1-glycine sample.

The sideband intensity manifolds in Figure 4.13 demonstrate the high tolerance of the experiment to all three pulse imperfections. Systematic deviations from the sideband intensities measured in the one-dimensional experiment are again evident. The difference between the spinning sideband intensities of the CSA-amplified PASS experiment and the one-dimensional spectrum remains less than 4% of the isotropic peak intensity for all sidebands, except for large errors in the pulses length, where the scatter is caused by the low signal-to-noise.

This stability can be attributed to the use of cogwheel phase cycling, since if the phase cycling is omitted, highly unsatisfactory results are obtained for higher scaling factors ($N > 10$). This is readily understood by considering that an ideal π-pulse will cause exact conversion of $(+1)$-quantum coherences to (-1)-quantum coherences, or vice-versa. However, any pulse length error, or resonance offset, will cause other coherence orders to be created. Fortunately, the contribution of these other coherence orders to the detected signal will be averaged to zero by the cogwheel phase cycle, significantly reducing the effect of the pulse imperfections.

For the case of pulse length miscalibration/RF inhomogeneity, it is simple to show that the phase cycle will completely remove the effects of this pulse imperfection. A pulse with RF phase ϕ_p causes a rotation about an axis in the transverse plane at an angle ϕ_p from the rotating-frame x-axis. The propagator that determines the evolution of the density operator during the (on-resonance) pulse can be concisely written using rotation operators as

$$\hat{U}_{\text{pulse}} = \hat{R}_z(\phi_p)\hat{R}_x(\zeta)\hat{R}_z^{-1}(\phi_p), \tag{4.45}$$

were ζ is the rotation angle caused by the pulse. If the density operator before the pulse is $\hat{\rho} = \frac{1}{2}\left(\hat{I}_+ e^{-i\phi} + \hat{I}_- e^{i\phi}\right)$, where ϕ describes the phase acquired by the coherences during
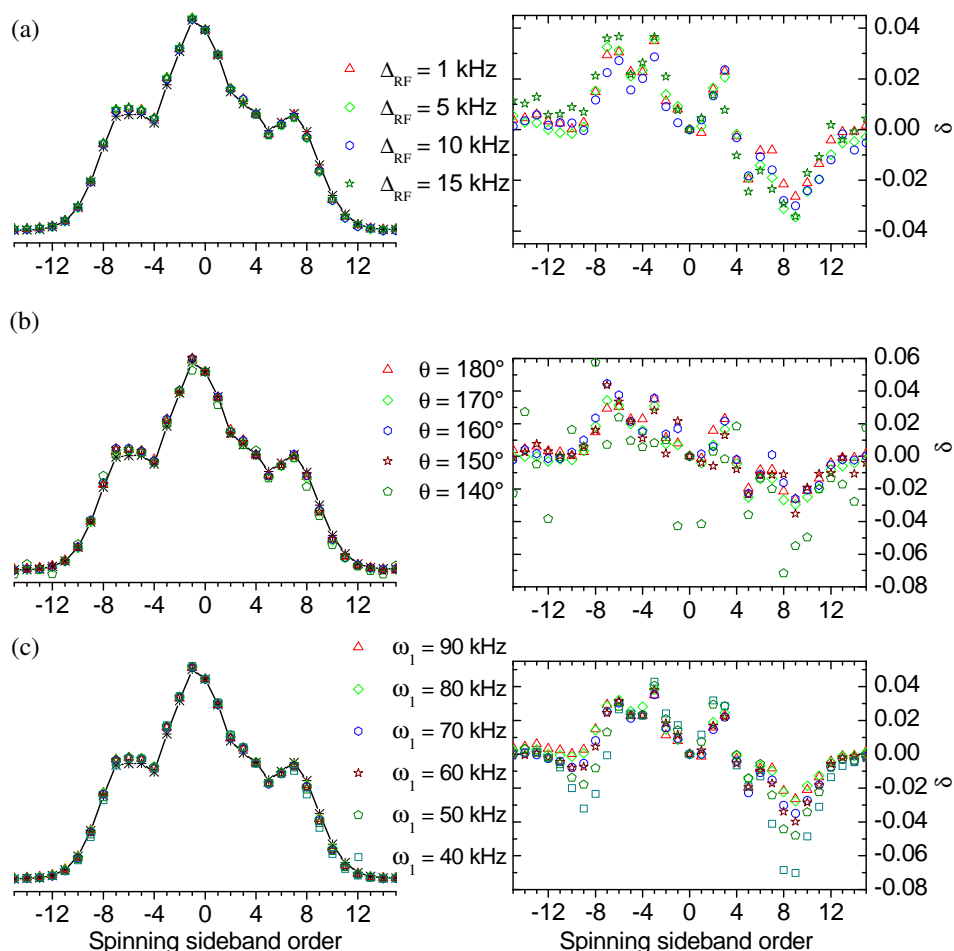
Figure 4.13: Comparison of the F_1 projections of ^{13}C-1-glycine recorded using the CSA-amplified PASS experiment under the conditions of mis-set parameters to simulate the effects of pulse imperfections. The sideband intensities obtained from a conventional one-dimensional MAS spectrum are shown as the solid line. (a) Effects of RF-offsets from the isotropic frequency Δ_{RF}; (b) the effects of incorrect pulse lengths or RF-inhomogeneity leading to a pulse rotation angle of θ (ideal is $\theta = 180°$); and (c) influence of finite RF field strength ω_1. Plots of the difference between the one-dimensional MAS sideband intensities and the CSA-amplified PASS derived intensities, normalised to their isotropic peak intensities, is shown on the right. The experiments employed a scaling factor of $N = 10$ and spinning frequency of $\omega_r/2\pi = 7000$ Hz.

evolution before the pulse, the density operator at the end of the pulse is evaluated to give

$$
\begin{aligned}
\hat{\rho}' &= \hat{U}_{\text{pulse}} \hat{\rho} \hat{U}_{\text{pulse}}^{-1} \\
&= \frac{1}{2} \hat{R}_z(\phi_{\text{p}}) \hat{R}_x(\zeta) \hat{R}_z^{-1}(\phi_{\text{p}}) \left[\hat{I}_+ \text{e}^{-\text{i}\phi} + \hat{I}_- \text{e}^{\text{i}\phi} \right] \hat{R}_z(\phi_{\text{p}}) \hat{R}_x^{-1}(\zeta) \hat{R}_z^{-1}(\phi_{\text{p}}) \\
&= \frac{1}{2} \hat{R}_z(\phi_{\text{p}}) \hat{R}_x(\zeta) \left[\hat{I}_+ \text{e}^{-\text{i}(\phi-\phi_{\text{p}})} + \hat{I}_- \text{e}^{\text{i}(\phi-\phi_{\text{p}})} \right] \hat{R}_x^{-1}(\zeta) \hat{R}_z(\phi_{\text{p}}) \\
&= \frac{1}{2} \hat{R}_z(\phi_{\text{p}}) \left[\frac{1}{2}(1 - \cos\zeta) \left\{ \hat{I}_+ \text{e}^{+\text{i}(\phi-\phi_{\text{p}})} + \hat{I}_- \text{e}^{-\text{i}(\phi-\phi_{\text{p}})} \right\} \right. \\
&\qquad \left. + \frac{1}{2}(1 + \cos\zeta) \left\{ \hat{I}_+ \text{e}^{-\text{i}(\phi-\phi_{\text{p}})} + \hat{I}_- \text{e}^{+\text{i}(\phi-\phi_{\text{p}})} \right\} + \hat{I}_z \sin(\phi - \phi_{\text{p}}) \sin\zeta \right] \hat{R}_z^{-1}(\phi_{\text{p}}) \\
&= \frac{1}{4}(1 - \cos\zeta) \left(\hat{I}_+ \text{e}^{+\text{i}(\phi-2\phi_{\text{p}})} + \hat{I}_- \text{e}^{-\text{i}(\phi-2\phi_{\text{p}})} \right) \\
&\qquad + \frac{1}{4}(1 + \cos\zeta) \left(\hat{I}_+ \text{e}^{-\text{i}\phi} + \hat{I}_- \text{e}^{+\text{i}\phi} \right) - \frac{\text{i}}{4} \hat{I}_z \sin\zeta \left(\text{e}^{\text{i}(\phi-\phi_{\text{p}})} - \text{e}^{-\text{i}(\phi-\phi_{\text{p}})} \right) \qquad (4.46)
\end{aligned}
$$

For a π-puse, the first set of brackets in Equation (4.46) are the desired terms, whilst the second and third brackets arise from the pulse length error.

The three sets of brackets in Equation (4.46) correspond to coherence order changes generated by the pulse of ± 2, 0 and ± 1 respectively. Selection of either the desired $+2$ or -2 coherence order change is, of course, simple using either a nested or cogwheel phase cycle. Consequently, the only effect of the pulse length error will be a loss of signal intensity due to the $1/2(1 - \cos\zeta) \leq 1$ factor in the first term of Equation (4.46).

The knowledge that the CSA-amplified PASS pulse sequence should give accurate results, even under the conditions of gross pulse errors, is important when using samples with an intrinsic low sensitivity, because optimization of pulse lengths is more difficult to perform using these samples. In addition, it should be practical to implement the CSA-amplified PASS experiment using larger coil probes, which allow a greater sample volume to be used, but suffer from higher RF field inhomogeneity and lower achievable RF field strengths than small diameter coils.

In conclusion, these experiments demonstrate that the CSA-amplified PASS experiment is robust with respect to pulse imperfections. This result is significant because previous experiments that achieve the same effect have been sensitive to the accuracy of the pulse settings,[203,204,208] or a detailed analysis has not been presented. In addition, even when large scaling factors are used, the spinning sideband intensities at the effective spinning frequency are reliably reproduced.

4.6   Comparison of CSA-amplified PASS with alternative methods

When comparing the CSA-amplified PASS experiment with the ROSES experiment,[208] two advantages of the CSA-amplified PASS are evident. Firstly, the ROSES experiment does not suppress the isotropic chemical shift over the t_1 period, which requires many data points to be collected in order to obtain sufficient frequency resolution in F_1; secondly, the experiment does not give the usual sideband intensities at the effective spinning frequency, and so conventional fitting routines cannot be used. In contrast, the extended chemical shift (XCS),[205] SPEED[206] and the CSA-amplification[203,204] experiments all reproduce spinning sideband intensities that are identical to those obtained from a one-dimensional spectrum.

The extended chemical shift (XCS) experiment[205] and SPEED experiment[206] both use essentially the same pulse sequence, which, for a scaling factor of N, consists of $(N-1)$ π-pulses applied over N rotor periods (see Figure 3.3 on page 75). From the point of view of recoupling efficiency, in the sense of the ratio of scaling factor to number of π-pulses, these experiments are favourable compared with the CSA-amplified PASS experiment. However, they have the significant disadvantage that the isotropic component of the chemical shift Hamiltonian is not averaged to zero over the course of the recoupling sequence. To correct for this effect, the XCS experiment requires an unconventional data processing routine: a new two-dimensional dataset is generated by combining pairs the t_1 data points in the original two-dimensional FID, followed by Fourier transformation the new dataset with respect to t_2. The projection onto the F_1 axis is calculated by integration over spinning sidebands in the F_2 dimension of this dataset to give a one-dimensional FID. A phase shift that increases linearly with t_1 must then be applied to each data point of the one-dimensional dataset to correct for the isotropic shift. Finally, Fourier transformation of this signal gives the spinning sideband intensities at the effective spinning frequency. This processes is a rather cumbersome to perform using standard spectrometer software and the trivial processing required for CSA-amplified PASS makes it a convenient alternative to XCS.

The SPEED experiment uses a different strategy: stroboscopic sampling at the spinning frequency is performed during signal detection, which reduces the spectral width to the spinning frequency and may cause problems with aliasing of isotropic peaks in the spectrum. A technique called replication allows the signal in the t_1 dimension to be extended beyond the times actually sampled in the experiment, and involves importing

data points from the t_2 dimension into the t_1 dimension. Effects associated with relaxation can introduce artefacts into the spectrum when using replication, but more serious are the phase twist lineshapes in the two-dimensional SPEED spectrum if the FID is processed by double Fourier transformation. To avoid this problem, it was suggested by the developers of this experiment that the TIGER data processing technique[207] should be used instead. The details of the this rather complicated and non-standard method will not be described here. In brief, it involves least-squares fitting of all the peaks in the spectrum obtained from the $t_1 = 0$ increment of the two-dimensional experiment. The frequency, amplitude and lineshape information associated with each fitted peak is used used in a further processing routine that ultimately extracts the F_1 projections associated with each of these peaks. The fitting process is not trivial, and the method is not implemented in standard spectrometer software, making it inconvenient and time consuming when compared with simple double Fourier transformation to process CSA-amplified PASS data.

The CSA-amplification experiments[203, 204] suppress the isotropic component of the chemical shift in the indirect dimension so that minimal t_1 data points are required, and simple double Fourier transformation is used to process the FID. These experiments allow scaling factors of up to $N = 12$, whereas CSA-amplified PASS can achieve much larger scaling factors. Once again, fewer π-pulses are required to obtain the same scaling factor, but the pulse sequence involves a period during which one component of the magnetization is stored parallel to the z-axis; this component corresponds to a zero-quantum coherence. The inclusion of the storage period means that cogwheel phase cycling cannot be implemented easily (or at least no cogwheel phase cycle has been reported), and so the experiments are rather sensitive to pulse imperfections and lack the robust nature of the CSA-amplified PASS experiment. In addition, the selection of only one component of the magnetization for storage means that the signal intensity from this is experiment is halved, compared with the CSA-amplified PASS experiment.

Finally, it noted that since the work presented in this chapter was completed, Titman and co-workers have reported a set of CSA-amplification experiments that can be thought of as special cases of the XCS experiment that *do* suppress the evolution due to the isotropic chemical shift in the indirectly observed dimension.[215] This is achieved by inclusion of an additional rotor period in the evolution period. The allowed scaling factors are restricted to $N = 16$ and $N = 32$, with the number of Θ values restricted to 2^i with $i \leq 3$ and $i \leq 4$ respectively. These sequences will, of course, be useful as they benefit from using comparatively few pulses in the experiment, but they lack the flexibility of the CSA-amplified PASS experiment, for which the scaling factor and number of Θ values can be

varied without restrictions.

4.7   Measuring the CSA of homonuclear dipolar-coupled spins

In this section, application of the CSA-amplified PASS experiment to measure the chemical shift anisotropy of nuclei that experience homonuclear dipolar coupling is investigated. Examples of such systems include uniformly or extensively isotopically-labelled samples, which are common in biomolecular NMR, and, more generally, nuclei that have a high natural abundance such as ^{31}P.

If the Hamiltonian governing the spin system contains multiple dipolar coupling interactions and chemical shift terms, then under MAS conditions it is dynamically homogeneous and numerical simulations are required to evaluate the evolution of the spin system.

Homonuclear-dipolar coupled multiple-spin systems of nuclei with large magnetogyric ratios, such as ^{1}H and ^{19}F, give rise to spectra containing exceedingly broad lineshapes (for example see Figure 2.2(e) on page 40) and can only be studied by specialised techniques.[216] For nuclei with smaller magnetogyric ratios, such as ^{13}C, the homonuclear dipolar coupling is much smaller in magnitude, and the effect on the MAS spectrum is more manageable. In the latter case, comparison of the spectra for ^{13}C enriched and natural abundance samples show that homonuclear dipolar coupling causes the spinning sidebands to have broader linewidths, which can cause problems with resolution at slow spinning frequencies (for example see Figure 4.8(a) on page 95). In addition, the spinning sideband intensities deviate from those that would arise from just the chemical shift anisotropy interaction. To properly analyse these sideband intensities, both the CSA and all the dipolar coupling interactions (and their relative orientations) would need to be included in a numerical simulation. Unfortunately this is computationally demanding and not a realistic practical strategy for determining the CSA of each site in the sample.

In general, increasing the spinning frequency improves the averaging of the homonuclear dipolar interaction, giving narrower linewidths in the spectrum. Care must be taken, however, that the homonuclear dipolar interaction is not recoupled by the rotational resonance effect, which occurs when the frequency difference between two signals in the spectrum is equal to a multiple of the spinning frequency;[217] this can be avoided by a

judicious choice of spinning frequency. In this section, it is shown that the CSA-amplified PASS experiment can be used to recouple the CSA during the evolution period so that many spinning sidebands can be obtained in the indirectly observed dimension, while fast sample spinning attenuates the effects of homonuclear dipolar coupling. It is also demonstrated that under these conditions, spinning sidebands can be fitted using a CSA only sideband intensity model, as used in fitting the experimental results of non-labelled samples in Section 4.4.

Kiihne *et al.* have analysed using the 2D-PASS experiment[202] at high static magnetic field strengths (17.6 T) to study homonuclear dipolar-coupled spin systems.[218] The chemical shift anisotropy scales linearly with the static field strength, while the dipolar coupling does not, so the dipolar coupling has a proportionally smaller effect on the CSA spinning sideband intensities, and faster spinning can be used than at intermediate field strengths to attenuate the line broadening effects of homonuclear dipolar coupling. They showed that this allowed a CSA spinning sideband model to be used to fit experimental results, without including the effects of dipolar coupling. The results of the present study complement those of Kiihne *et al.*, because using CSA-amplified PASS has additional flexibility that the sample spinning need not be sufficiently slow that several spinning sidebands are recorded in the directly observed dimension.

When using rotor synchronised π-pulses, recoupling of the homonuclear dipolar coupling Hamiltonian may occur,[106, 219] although the recoupling effect is very different to that of the CSA. Due to the 2D-PASS format, whereby the pulse timings are adjusted throughout the experiment, detailed analytical treatment using average Hamiltonian theory is difficult. Instead, numerical simulations were used to investigate the typical effects of homonuclear dipolar coupling on the F_1 projections obtained using the CSA-amplified PASS experiment.

4.7.1 Numerical simulations

A series of simulations of a homonuclear dipolar coupled three spin system were performed using the SIMPSON program.[39] Larger spin systems could not be used in the simulations, owing to the computational demands of these calculations. Homonuclear dipolar coupling with the same dipolar coupling constant b_{ij} was included between adjacent spins, with an angle of 120° between the principal z-axes of the two dipolar coupling tensors. The chemical shift anisotropy was included for the central spin, with the

principal z-axis of the chemical shift tensor oriented perpendicular to the plane defined by the two dipolar coupling PAF z-axes. The resulting signal was calculated for the central spin. The complete CSA-amplified PASS pulse sequence was simulated, although π-pulses were treated as infinitely short in the simulations and powder averaging used 320 REPULSION crystallites.[72]

For a chosen geometry of the three-spin simulations, the spinning sideband intensities depend of five parameters: the chemical shift anisotropy to spinning frequency ratio $-\omega_0 \Delta_{CS}/\omega_r$, the dipolar coupling constant to spinning frequency ratio b_{ij}/ω_r, the chemical shift asymmetry parameter η_{CS} and finally the particular recoupling sequence, which is determined by N_{unit} of the five pulse unit, and number of these units used. In the simulations, the actual parameters used for the CSA were $-\omega_0 \Delta_{CS}/2\pi = -5$ kHz and $\eta_{CS} = 0.5$.

To quantify the deviation of the sideband intensities in the calculated F_1 projections using the three spin homonuclear dipolar-coupled system from an isolated single-spin (CSA only) model, the summed absolute difference between the sideband intensities (E) of the two models was calculated:

$$E = \left(\sum_i |I_i^{3-spin} - I_i^{1-spin}| \right) \Big/ \left(\sum_i I_i^{1-spin} \right), \qquad (4.47)$$

where the summations runs over all sideband intensities, and I_i^{3-spin} and I_i^{1-spin} are the sideband intensities for the three-spin model and isolated spin model respectively.

Secondly, the effect of the homonuclear dipolar coupling on parameters derived from fitting the calculate three-spin F_1 projections using an isolated spin model was investigated. The Simplex method was used, varying the parameters δ_{aniso}, η_{CS} and an intensity weighting factor. The difference in the fitted δ_{aniso} and η_{CS} value from the true value used in the three-spin simulations was then determined.

In Figure 4.14 the results of simulation where the dipolar coupling constants, CSA parameters and effective spinning frequency were fixed and the spinning frequency and scaling factor were increased are shown. Figures 4.15 and 4.16 show simulation results where $-\omega_0 \Delta_{CS}/\omega_r = 0.82$ and $\eta_{CS} = 0.5$ were used in both cases but $N = 10.2$ for Figure 4.15 and $N = 3.4$ for Figure 4.16; in both figures the dependence of E on the asymmetry parameter is shown and errors in the parameters fitted to the three-spin simulations are plotted.
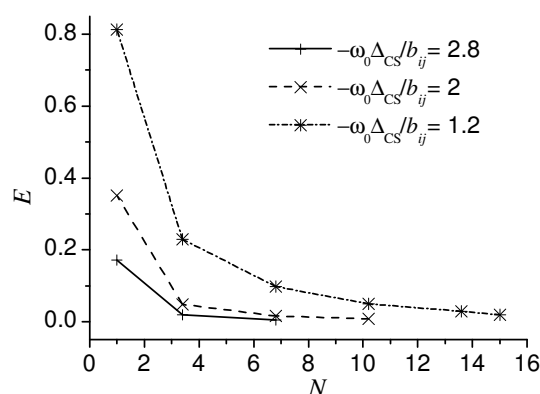
Figure 4.14: The summed difference in sideband intensities between the three-spin simulated intensities and single spin CSA only model (E) for a range of spinning frequency but constant effective spin rate, where $-N\omega_0\Delta_{CS}/\omega_r = 2.77$, and $\eta_{CS} = 0.5$

In summary, the simulations show, as expected, the F_1 projections become increasingly distorted as the strength of the dipolar coupling increases, Figure 4.15(a). For a fixed value of $-\omega_0\Delta_{CS}/\omega_r$, as the scaling factor N is increased, the F_1 projections are affected more by the homonuclear dipolar coupling, which can be seen by comparing the F_1 projections is Figures 4.15(a) and 4.16(a). However, for fixed values of the effective spinning rate ω_r/N, Δ_{CS} and b_{ij}, the deviation of the sideband intensities from the isolated spin model decreases as the spinning frequency is increased; this is illustrated in Figure 4.14. This means that it is advantageous to use higher frequency spinning, despite the greater number of recoupling pulse sequence units needed to achieve the same effective spinning rate.

When homonuclear dipolar coupling is present, there is only a weak dependence of E upon the chemical shift asymmetry parameter (see Figures 4.15(b) and 4.16(b)), but the accuracy of the fitted parameters, assuming an isolated spin model, depend strongly on the true value of η_{CS} (see Figures 4.15(c),(d) and 4.16(c),(d)). This is expected, as the same observation is made when fitting the sideband intensities of sites that do not experience dipolar coupling.[176] In particular, values of the asymmetry parameters near to zero or one require smaller distortions from the CSA sideband intensities for a reliable fitting to be achieved. Finally, the deviation of the sideband intensities from the isolated spin values does not have a strong dependence on the orientation of the chemical shielding tensor in the three spin system (results not shown), which is consistent with the findings of Kiihne et al.[218]

The complicated dependence of the the observed F_1 projection from the CSA-amplified PASS experiment on the nuclear spin interactions, pulse timings and sample spinning frequency means that it is not possible to give general condition under which the
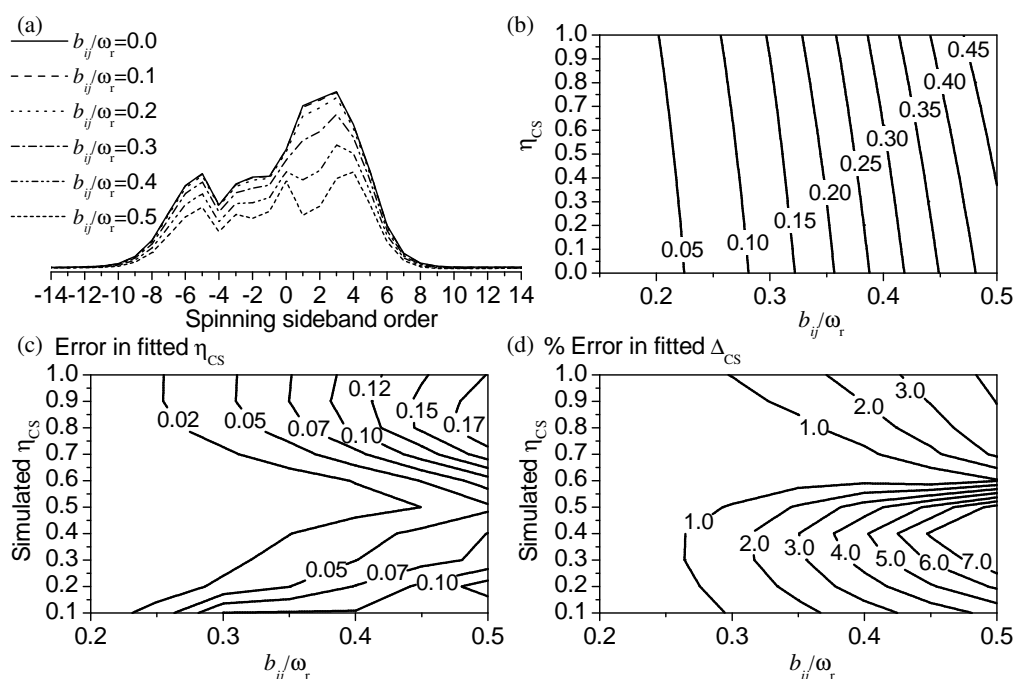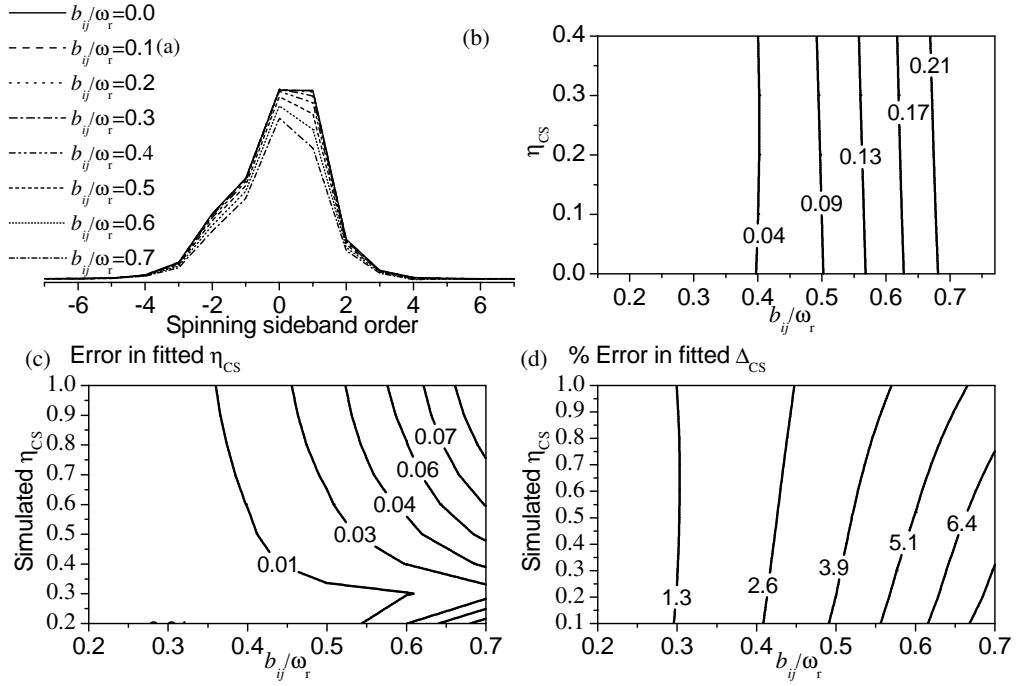
Figure 4.15: Simulations of the effects of homonuclear dipolar coupling on the sideband intensity envelope. (a) The sideband intensity envelope as a function of b_{ij}/ω_r for $\eta_{CS} = 0.5$. (b) The summed difference in sideband intensities between the simulated CSA-Amplified PASS F_1 projection and the isolated spin model sideband intensities E (defined in Equation (4.47)), as a function of b_{ij}/ω_r and η_{CS}. (c),(d) Parameters obtained from the isolated spin model fits to the simulated sideband manifolds under homonuclear dipolar coupling. In all cases $-\omega_0\Delta_{CS}/\omega_r = 0.82$, $N = 10.2$.

approximation of fitting a single spin model is acceptable. In practice, the validity of this approximation is evaluated firstly through the quality of fit achieved with the simulated sideband intensities. Secondly, the experiment may be repeated at several different spinning frequencies and the resulting fitted parameters compared for consistency.

4.7.2 Experimental example

As an example of using the CSA-amplified PASS experiment under conditions where homonuclear dipolar coupling is present, a comparison of the F_1 projections for each of the four sp^2 sites in uniformly ^{13}C enriched L-histidine monohydrochloride monohydrate (Figure 4.17) was made with those obtained from a natural abundance sample of the same material. It was not possible to perform experiments with sufficiently large scaling factors to measure the spinning sideband intensities for the sp^3 ^{13}C sites in histidine.

CSA-amplified PASS spectra were recorded at four different spinning frequencies: 8.4 kHz, 11.2 kHz, 14 kHz and 19.6 kHz; in each case the effective spinning frequency

Figure 4.16: Simulations of the effects of homonuclear dipolar coupling on the sideband intensity envelope. Simulation methods are detailed in the experimental section. (a) The sideband intensity envelope as a function of b_{ij}/ω_r for $\eta_{CS} = 0.5$. (b) The summed difference in sideband intensities between the simulated CSA-Amplified PASS F_1 projection and the isolated spin model sideband intensities E (defined in Equation (4.47)), as a function of b_{ij}/ω_r and the CSA asymmetry parameter. (c),(d) Parameters obtained from the isolated spin model fits to the simulated sideband manifolds under homonuclear dipolar coupling. In all cases $-\omega_0\Delta_{CS}/\omega_r = 0.82$, $N = 3.4$.
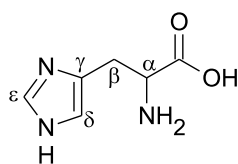
Figure 4.17: The structure of histidine and the labelling used to identify the ^{13}C sites.

in the F_1 projection was 824 Hz. The results are shown in Figure 4.18. At 824 Hz MAS, sideband separation using 2D-PASS was not possible for the uniformly ^{13}C labelled sample because the spinning sidebands were very broad and sample spinning was rather unstable.

The ϵ carbon gives F_1 projections in very good agreement with the natural abundance sample for all spinning frequencies used (see Figure 4.18(a)). This also demonstrates that the experiment can be used at spinning frequencies up to ~20 kHz without finite pulse length effects appearing to affect the spectra. The δ carbon also yields F_1 projections which show good agreement at all the four spinning frequencies (see Figure 4.18(b)). In the case of the carbonyl carbon, a poorer match between the F_1 projections of the non-labelled and the labelled histidine samples was achieved (see Figure 4.18(d)). The deviation of the labelled sample projections from the natural abundance sample sideband intensities is in the central region of the sideband manifold, but the fitted δ_{aniso} is still within 1 ppm of that fitted in the non-labelled case (δ_{aniso} = 67 ppm) for all spinning frequencies used, and the fitted asymmetry parameters for the labelled sample are within ± 0.1 of that for the non-labelled histidine (η_{CS} = 0.97).

The fitted chemical shift anisotropy parameter for the γ carbon in the non-labelled sample was δ_{aniso} = -74 ppm and asymmetry η_{CS} = 0.85. The fitted parameters for the labelled histidine sample using CSA-amplified PASS experiments at 8.4, 11.2 and 14 kHz, were δ_{aniso} = -77 ppm in each case and the asymmetry parameters were 0.81, 0.78 and 0.83, respectively. In addition, a clear improvement in the correspondence between the sideband intensities from the labelled and non-labelled samples is also evident as the spinning frequency is increased, and at 19.6 kHz excellent agreement is obtained (see Figure 4.18(c)).

These experimental results confirm that the CSA-amplified PASS experiment can provide a practical strategy to determine the CSA parameters for homonuclear dipolar-coupled nuclei at intermediate and high static field strengths. Furthermore, the flexibility that the CSA-amplified PASS experiment allows, in terms of the spinning rate used in the experiment, means that the experimenter can avoid rotational resonance effects without
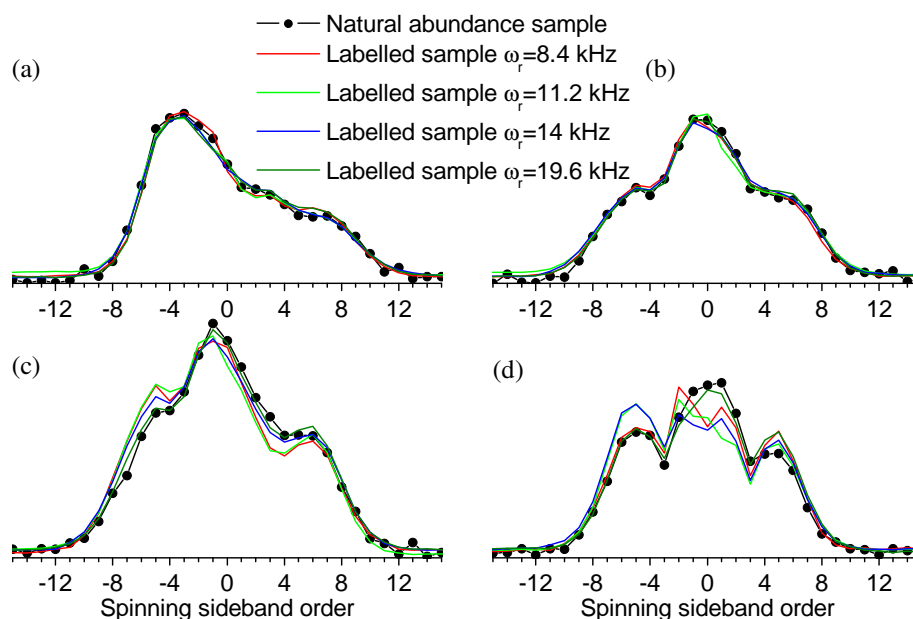
Figure 4.18: F_1 projections obtained from the CSA-amplified PASS experiments using ^{13}C enriched and natural abundance L-histidine monohydrochloride monohydrate samples with an effective spinning frequency of 824 Hz. The projections for the non-labelled sample were obtained using a spinning frequency of 14 kHz. (a) The ϵ carbon site, (b) δ carbon site, (c) γ carbon site and (d) the carbonyl carbon of histidine are shown.

compromising the number of spinning sidebands obtained for subsequent CSA spinning sideband analysis.

4.8   Summary

A new experiment that extends the 2D-PASS experiment to allow correlation of spinning sidebands at two different spinning frequencies has been developed. Experiments with scaling factors up to $N = 27$ have been demonstrated, and the experiment was shown to be robust with respect to pulse imperfections. The CSA-amplified PASS experiment has the advantage of reproducing sideband intensities that are identical to those obtained in a usual one-dimensional experiment, and does not require special data processing routines. Furthermore, it benefits from the 2D-PASS format: no storage period is involved, so signal intensity is not deliberately discarded, and cogwheel phase cycling is easily implemented to reduce the effects of pulse imperfections.[66, 202]

4.9   Experimental details

All ^{13}C NMR spectra were recorded using a Bruker Avance spectrometer operating at 100.56 MHz for ^{13}C with a standard 4 mm Bruker probe, except for the experiments using 19.6 kHz MAS, for which a standard Bruker 2.5 mm probe was used. TPPM[52] or SPINAL-64[54] [1]H decoupling was used with an RF field strength of ~ 95 kHz for the 4 mm probe and ~ 120 kHz for the 2.5 mm probe, and the ^{13}C RF field strength was ~ 90 kHz for the π-pulses. Cross polarization[47] was performed using a ramped amplitude[50] spin-lock field on the ^{1}H channel. Magic angle spinning was stabilised to within ±3 Hz. Recycle delays were between 5 and 9 seconds.

The ^{31}P experiments were performed on a Varian Infinityplus spectrometer, operating at 202.341 MHz for ^{31}P, using a 4 mm rotor. Direct excitation by a 90° pulse was used rather than CP, and ^{1}H decoupling was not required. The [31]P π-pulse length was 12 μs. The delay between scans was 600 s. The slow relaxation rate prevented even the proposed cogwheel phase cycling being implemented and instead fixed phases of the π-pulses of 0°, 330°, 60°, 330°, 0° were used for the five pulses, which have been reported to reduce the effects of pulse imperfections.[220]

Samples of ^{13}C-1-glycine, glycine, sodium phosphate and fumaric acid monoethyl ester and L-histidine monohydrochloride monohydrate were obtained from Sigma-Aldrich. The uniformly [13]C L-histidine monohydrochloride monohydrate sample was purchased from Cambridge Isotope Laboratories. All samples were used without further purification or re-crystallisation. Samples were packed into 2.5/4 mm zirconia rotors. The uniformly ^{13}C labelled histidine sample was restricted to the central third of the 4 mm rotor (owing to the small sample volume), but all other samples filled the entire rotor.

5 | Resolving CSA powder patterns

In comparison with spinning sideband patterns, static powder patterns are easier to interpret and readily reveal overlapping powder patterns with the same isotropic shift, or orientational order within the sample. Overlapping powder patterns in a one-dimensional spectrum are resolved using two-dimensional anisotropic-isotropic experiments, from which quasi-static spectra are obtained from cross-sections through the anisotropic dimension of a two-dimensional spectrum. In this chapter, multiple-pulse methods for recoupling CSA powder patterns under MAS conditions are investigated. The principal aim of the work presented here was to develop methods that allow undistorted and artefact free powder patterns to be resolved, without the need for specialised hardware.

The current experiments to record quasi-static powder patterns were reviewed in Section 3.2.2. The two most simple and convenient methods to perform are the recoupling experiments of Tycko and co-workers,[188] which is referred to here as 2DCSA, and the SUPER experiment.[190] It is well documented that the 2DCSA experiment is highly sensitive to pulse imperfections, which cause severe artefacts at the edge of the spectra and distortions in the powder pattern lineshapes. The SUPER experiment is less sensitive to pulse imperfections, but the experimental lineshapes are also often significantly distorted from an ideal powder pattern.[190–192] For example, Figure 5.1 shows typical experimental
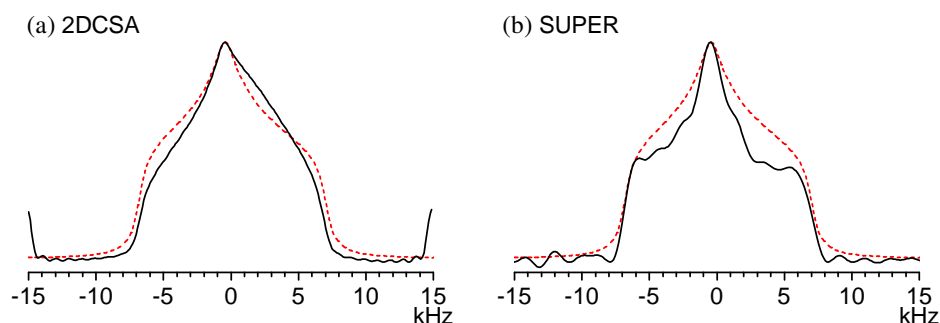
Figure 5.1: Typical (a) 2DCSA and (b) SUPER experimental results. Cross-sections were take though the isotropic carbonyl peak in the F_2 dimension. The sample used in (a) was ^{13}C-1-α-glycine, and in (b) natural abundance α-glycine was used. In both experiments, 32 t_1 values were collected. The dashed red lines show simulated lineshapes using the parameters $\delta_{\mathrm{aniso}} = -71$ ppm and $\eta_{\mathrm{CS}} = 0.91$, which were determined from static sample powder pattern measurements.
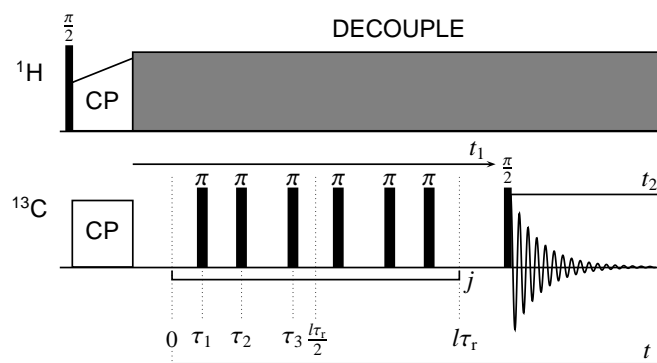
Figure 5.2: The 2DCSA experiment for the six π-pulse unit.[188] The six π-pulses occur symmetrically about $l\tau_r/2$.

results for the cross-sections through the indirectly observed dimension of 2DCSA and SUPER spectra of α-glycine. For accurate measurement of the chemical shift tensor, the distortions in the powder pattern lineshapes must be as small as possible. Moreover, if the effects of partial orientational order within the sample is investigated by analysis of the lineshape, or if two powder patterns with the same isotropic chemical shift overlap, then it is critical that the experiment does not introduce artefacts.

In this chapter, the 2DCSA and SUPER experiments are described in detail, and developed to make them less sensitive to experimental imperfections and lead to artefact free spectra. This is achieved by introducing cogwheel phase cycling[62] into both experiments. In addition, new constant-time and optimised implementations of the 2DCSA experiment are described. A comparison is made between these experiments and practical aspects are discussed.

5.1   The 2DCSA experiment

The 2DCSA pulse sequence is shown in Figure 5.2; it consists of an even number (n) of π-pulses applied symmetrically about the centre of an odd number (l) of rotor periods (τ_r).[188] The n π-pulses form one 'pulse-sequence unit', and usually the number of π-pulses used is $n = 4$ or $n = 6$. Originally, the number of rotor periods was assumed to be one, but Witter and co-workers have recently used sequences with $l = 3$ and $l = 5$ to allow the experiment to be performed at higher MAS frequencies (>10 kHz). This is possible because the π-pulses occupy a smaller proportion of the pulse-sequence unit when $l > 1$.[145,153] During the two-dimensional experiment, the t_1 period is incremented by increasing the number (j) of pulse-sequence units, so that $t_1 = jl\tau_r$.

Analysis of this experiment is performed by calculating the average Hamiltonian over one pulse-sequence unit. The same approach was used in Section 4.2 to analyse the CSA-amplified PASS experiment.

First, for a rotating sample, the rotating-frame chemical shift Hamiltonian can be written as

$$\hat{\mathcal{H}}_{CS}(t) = \{\omega_{iso} + [C_1' \cos(\omega_r t) + C_2' \cos(2\omega_r t) + S_1' \sin(\omega_r t) + S_2' \sin(2\omega_r t)]\}\,\hat{I}_z, \quad (5.1)$$

where C_1', C_2', S_1' and S_2' were defined in Equation (4.2) on page 79. Thus, for a static sample, the chemical shift Hamiltonian can be written as

$$\hat{\mathcal{H}}_{CS} = \{\omega_{iso} + C_1' + C_2'\}\,\hat{I}_z, \quad (5.2)$$

where C_1' and C_2' determine the form of the powder pattern, and ω_{iso} causes a shift of this powder pattern in the frequency domain.

The 2DCSA pulse-sequence unit consists of an even number of π-pulses, which means that the average Hamiltonian treatment for a generic sequence of π-pulses that was outlined in Section 4.2 can be used without further analysis. The π-pulses in the 2DCSA pulse-sequence unit occur symmetrically about the centre of an odd number of rotor periods. Consequently, in Equation (4.35) on page 88 for the first-order interaction-frame Hamiltonian, the cosine terms sum to zero and leave

$$\frac{1}{l\tau_r}\int_0^{l\tau_r}\hat{\mathcal{H}}_{CS}^*(t')\mathrm{d}t' = \left\{\omega_{iso}\frac{1}{l\tau_r}\left(\tau_{seq} + 2\sum_{q=1}^n(-1)^{q-1}\tau_q\right)\right.$$
$$\left. + \frac{1}{l\pi}\sum_{q=1}^n(-1)^{q-1}\left(C_1'\sin(\omega_r\tau_q) + \frac{1}{2}C_2'\sin(2\omega_r\tau_q)\right)\right\}\hat{I}_z. \quad (5.3)$$

For the recoupling sequence to generate quasi-static powder patterns, the pulse timings in Equation (5.3) must give an average Hamiltonian that has the form:

$$\frac{1}{l\tau_r}\int_0^{l\tau_r}\hat{\mathcal{H}}_{CS}^*(t')\mathrm{d}t' = \{\xi\omega_{iso} + \chi(C_1' + C_2')\}\,\hat{I}_z, \quad (5.4)$$

which is related the Hamiltonian in Equation (5.2) by the isotropic scaling factor ξ and anisotropic scaling factor χ. Evolution under this average Hamiltonian gives a powder pattern at the scaled isotropic frequency $\xi\omega_{iso}$ with its span scaled by χ.

By equating the right-hand sides of Equations (5.3) and (5.4), and extracting coefficients of C'_1, C'_2 and ω_{iso}, a set of conditions on the pulse timings is obtained:

$$\xi = \frac{1}{l\tau_{\mathrm{r}}} \left(l\tau_{\mathrm{r}} + 2 \sum_{q=1}^{n} (-1)^{q-1} \tau_q \right) \tag{5.5}$$

$$\chi = \frac{1}{\pi l} \sum_{q=1}^{n} (-1)^{q-1} \sin(\omega_{\mathrm{r}}\tau_q) \tag{5.6}$$

$$\chi = \frac{1}{2\pi l} \sum_{q=1}^{n} (-1)^{q-1} \sin(2\omega_{\mathrm{r}}\tau_q). \tag{5.7}$$

Equation (5.5) is fulfilled for any set of pulse times (τ_q), but the conditions expressed in Equations (5.6) and (5.7) dictate the pulse timings that must be used in order to obtain static powder patterns in the F_1 dimension. In previous work,[153,188] the pulse timings were determined from solutions to

$$\frac{1}{\pi l} \sum_{q=1}^{n} (-1)^{q-1} \sin(\omega_{\mathrm{r}}\tau_q) = \frac{1}{2\pi l} \sum_{q=1}^{n} (-1)^{q-1} \sin(2\omega_{\mathrm{r}}\tau_q), \tag{5.8}$$

for a chosen value of τ_1; the corresponding scaling factors were then calculated. An alternative approach was adopted in this work: Equations (5.6) and (5.7) were treated as simultaneous equations and solved numerically for the desired value of χ. This was performed using the MuPAD computer algebra system.[210] This approach is necessary for developing improved variants of the 2DCSA experiment (Section 5.4).

For the four π-pulse sequence ($n = 4$) over one rotor period ($l = 1$), pulse times are found that give anisotropic scaling factors over the continuous range $\chi = 0 \ldots 0.412$, with each value of χ having a non-zero isotropic scaling factor, except for the special case $\chi = 0.3934$. For the pulse-sequence unit over three rotor periods ($l = 3$), the anisotropic scaling factor can be $\chi = -0.1372 \ldots 0.1372$, with non-zero isotropic scaling factors except for $\chi = -0.13115$. These pulse timings are plotted in Figure 5.3(a) and (b) on the next page.

If the six π-pulse sequence ($n = 6$) is used, the condition that the isotropic scaling factor, ξ, be zero is imposed when finding the pulse times. Under these conditions, the pulse-sequence unit applied over one rotor period allows the anisotropic scaling factor to be varied in the range $\chi = -0.4 \ldots 0.395$, whilst for the pulse-sequence unit applied over three rotor periods $\chi = -0.13 \ldots 0.242$. The pulse timings are plotted in Figure 5.3(c) and (d).
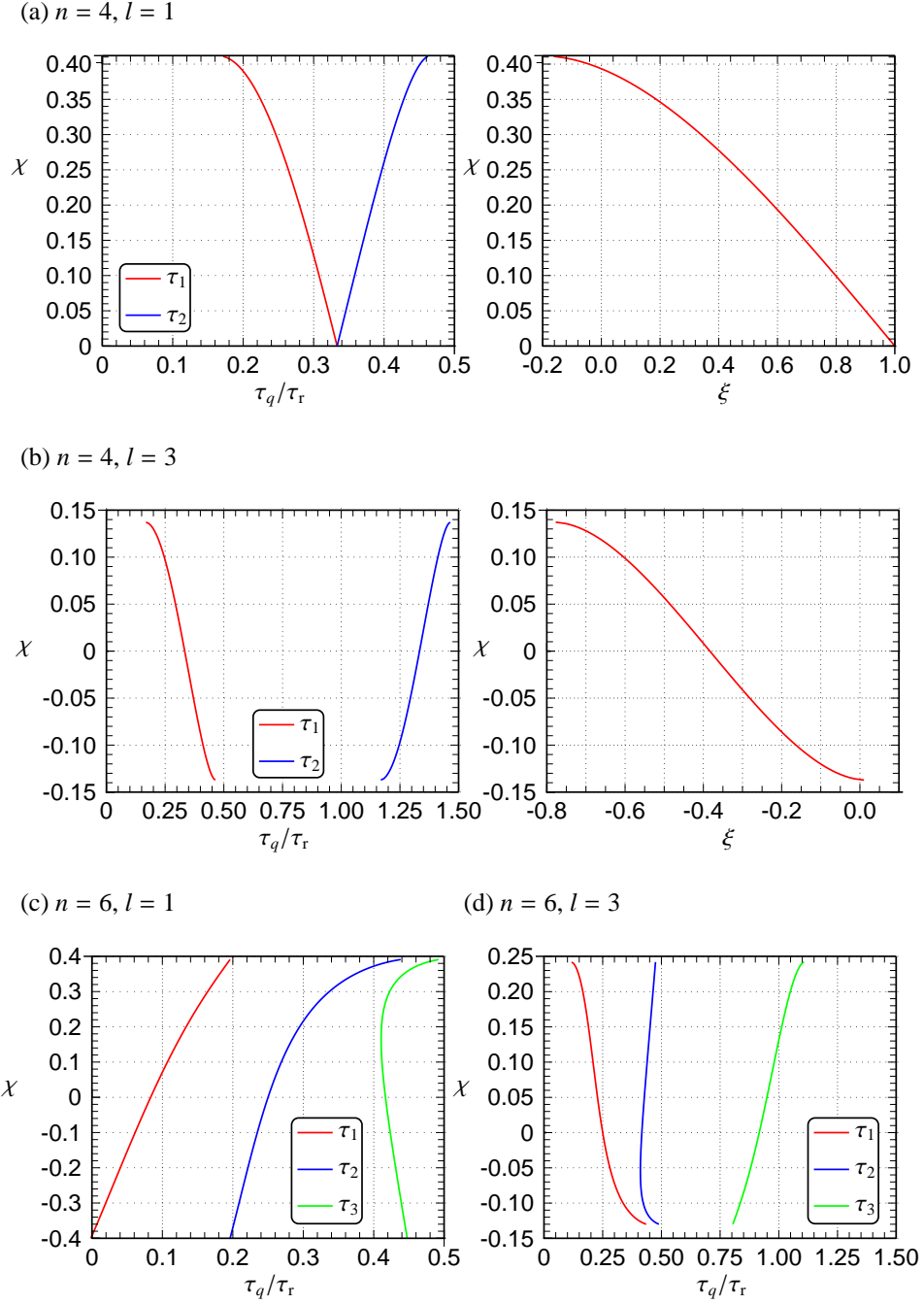
(a) $n = 4$, $l = 1$

(b) $n = 4$, $l = 3$

(c) $n = 6$, $l = 1$

(d) $n = 6$, $l = 3$

Figure 5.3: Pulse timings for the 2DCSA pulse-sequence unit for various numbers of rotor periods (l) and numbers of π-pulses (n). (a) $n = 4$, $l = 1$ and (b) $n = 4$, $l = 3$: the left hand plot shows the pulse timings for the achievable range of the anisotropic scaling factor χ and the right hand plot shows the corresponding isotropic scaling factor. (c) $n = 6$, $l = 1$ and (d) $n = 6$, $l = 3$ with $\xi = 0$ for all values of χ.

For the pulse-sequence units lasting three rotor periods, there are more solutions to Equations (5.6) and (5.7) than are plotted in Figure 5.3(b) and (d). Those that are plotted were chosen for having well-separated pulses that avoid pulse overlap.

Quadrature detection in the indirectly observed dimension is achieved using the States method,[58] outlined in Section 2.2.1. This requires two datasets to be recorded, one with the detected signal cosine amplitude modulated by the evolution during the t_1 period, and the other sine amplitude modulated. Which dataset is recorded is selected by the phase of the $\pi/2$-pulse prior to detection, as shown below. After CP, the density operator is $\hat{\rho}(0) = \hat{I}_x = \frac{1}{2}\left(\hat{I}_+ + \hat{I}_-\right)$. At the end of the recoupling recoupling sequence, and immediately prior to the $\pi/2$ pulse, the density operator has evolved to be

$$\hat{\rho}(t_1) = \frac{1}{2}\left(\hat{I}_+ \mathrm{e}^{-\phi} + \hat{I}_- \mathrm{e}^{+\phi}\right),\tag{5.9}$$

where $\mp\phi$ is the phase acquired by the (± 1)-quantum coherences during the t_1 period. Following the subsequent 90°_x-pulse, the density operator is

$$\hat{\rho}'(t_1) = \frac{1}{2}\cos(\phi)\hat{I}_+ + \frac{1}{2}\cos(\phi)\hat{I}_- + \sin(\phi)\hat{I}_z,\tag{5.10}$$

and so the detected signal, which derives from the $\hat{I}_-$ term in the density operator, is cosine amplitude modulated by the evolution during the t_1 period. The sine-modulated signal is obtained using a 90°_y-pulse.

5.2 The SUPER experiment

The SUPER experiment uses two 4π-pulses located symmetrically about the centre of a rotor period, as shown in Figure 5.4 on the following page.[190] The first 4π-pulse occupies the period τ_a to τ_b.

As in the 2DCSA experiment, the effect of the pulse sequence is analysed by calculating the first-order average Hamiltonian over one pulse-sequence unit. The rotating-frame Hamiltonian has two terms, $\hat{\mathcal{H}} = \hat{\mathcal{H}}_{\mathrm{RF}} + \hat{\mathcal{H}}_{\mathrm{CS}}$, with the first term due to the RF pulses and the second is the chemical shift Hamiltonian. The propagator of the rotating-frame density operator factors into two parts $\hat{U} = \hat{U}_{\mathrm{RF}}\hat{U}^*$; $\hat{U}_{\mathrm{RF}}$ and $\hat{U}^*$ are respectively due to the RF pulse Hamiltonian and chemical shift Hamiltonian as viewed in the interaction frame
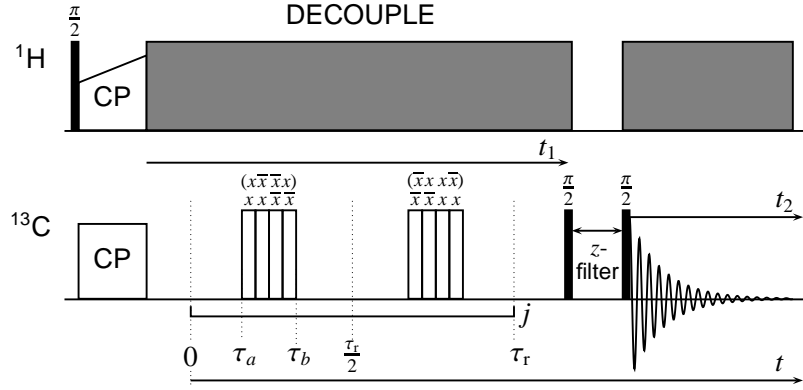
Figure 5.4: The SUPER experiment. The 4π-pulses are divided into π-pulses, and the phase of each π-pulse is indicated above each pulse. On alternate pulse-sequence units in the recoupling sequence the phases shown in parentheses are used. Further details are given in the main text.

of $\hat{\mathcal{H}}_{\mathrm{RF}}$. The RF propagator during the first $(2\pi_x 2\pi_{-x})$-pulse is

$$\hat{U}_{\mathrm{RF}}(t) = \begin{cases} \exp\left\{-\mathrm{i}2\pi\left(\frac{2(t-\tau_{\mathrm{a}})}{\tau_{\mathrm{b}}-\tau_{\mathrm{a}}}\right)\hat{I}_x\right\}, & \tau_{\mathrm{a}} \leq t \leq (\tau_{\mathrm{a}}+\tau_{\mathrm{b}})/2 \\ \exp\left\{-\mathrm{i}2\pi\left(\frac{2(t_{\mathrm{b}}-t)}{\tau_{\mathrm{b}}-\tau_{\mathrm{a}}}\right)\hat{I}_x\right\}, & (\tau_{\mathrm{a}}+\tau_{\mathrm{b}})/2 \leq t \leq \tau_{\mathrm{b}} \end{cases}. \tag{5.11}$$

Over the complete pulse-sequence unit $\hat{U}_{\mathrm{RF}}(\tau_{\mathrm{r}}) = \hat{\mathbf{1}}$, so it is cyclic and $\hat{U}(\tau_{\mathrm{r}}) = \hat{U}^*(\tau_{\mathrm{r}})$. The interaction-frame (chemical shift) Hamiltonian is calculated according to

$$\hat{\mathcal{H}}_{\mathrm{CS}}^*(t) = \hat{U}_{\mathrm{RF}}^{-1}(t)\hat{\mathcal{H}}_{\mathrm{CS}}(t)\hat{U}_{\mathrm{RF}}(t) = \hat{U}_{\mathrm{RF}}^{-1}(t)\omega(t;\Omega_{\mathrm{PR}})\hat{I}_z\hat{U}_{\mathrm{RF}}(t). \tag{5.12}$$

It is assumed here that the mechanical rotation of the sample *during* the pulses is negligible. With this approximation, the first-order iteraction-frame average Hamiltonian over the duration of each 2π-pulse is zero because

$$\begin{aligned}\int_{\tau_{\mathrm{a}}}^{\frac{\tau_a+\tau_b}{2}} \hat{\mathcal{H}}_{\mathrm{CS}}^*(t';\Omega_{\mathrm{PR}})\mathrm{d}t' &= \int_{\tau_{\mathrm{a}}}^{\frac{\tau_a+\tau_b}{2}} \omega(\tau_{\mathrm{a}};\Omega_{\mathrm{PR}})\exp\left[\mathrm{i}2\pi\left(\frac{2(t-\tau_{\mathrm{a}})}{\tau_{\mathrm{b}}-\tau_{\mathrm{a}}}\right)\hat{I}_x\right]\hat{I}_z\exp\left[-\mathrm{i}2\pi\left(\frac{2(t-\tau_{\mathrm{a}})}{\tau_{\mathrm{b}}-\tau_{\mathrm{a}}}\right)\hat{I}_x\right]\mathrm{d}t' \\ &= \int_{\tau_{\mathrm{a}}}^{\frac{\tau_a+\tau_b}{2}} \omega(\tau_{\mathrm{a}};\Omega_{\mathrm{PR}})\left\{\hat{I}_z\cos\left[2\pi\left(\frac{2(t-\tau_{\mathrm{a}})}{\tau_{\mathrm{b}}-\tau_{\mathrm{a}}}\right)\right]+\hat{I}_y\sin\left[2\pi\left(\frac{2(t-\tau_{\mathrm{a}})}{\tau_{\mathrm{b}}-\tau_{\mathrm{a}}}\right)\right]\right\}\mathrm{d}t' \\ &= \int_0^{2\pi} \omega(\tau_{\mathrm{a}};\Omega_{\mathrm{PR}})\left(\hat{I}_z\cos(x)+\hat{I}_y\sin(x)\right)\mathrm{d}x, \quad \text{where } x = 2\pi\left(\frac{2(t-\tau_{\mathrm{a}})}{\tau_{\mathrm{b}}-\tau_{\mathrm{a}}}\right) \\ &= 0.\end{aligned}$$

Using this approximation, the first-order iteraction-frame average Hamiltonian is calculated over one rotor period, using Equation (5.1) for the chemical shift Hamiltonian, to

be

$$\frac{1}{\tau_r} \int_0^{\tau_r} \hat{\mathcal{H}}_{CS}^*(t')dt' = \frac{\hat{I}_z}{\tau_r} \left\{ \int_0^{\tau_a} \omega(t';\Omega_{PR})dt' + \int_{\tau_b}^{\tau_r-\tau_b} \omega(t';\Omega_{PR})dt' + \int_{\tau_r-\tau_a}^{\tau_r} \omega(t';\Omega_{PR})dt' \right\}$$

$$= \frac{\hat{I}_z}{\tau_r} \left\{ \int_0^{\tau_r} \omega(t';\Omega_{PR})dt' - \int_{\tau_a}^{\tau_b} \omega(t';\Omega_{PR})dt' - \int_{\tau_r-\tau_b}^{\tau_r-\tau_a} \omega(t';\Omega_{PR})dt' \right\}$$

$$= \frac{\hat{I}_z}{\tau_r} \left\{ \omega_{iso}\tau_r - \int_{\tau_a}^{\tau_b} \omega(t';\Omega_{PR})dt' - \int_{\tau_r-\tau_b}^{\tau_r-\tau_a} \omega(t';\Omega_{PR})dt' \right\}$$

$$= \frac{\hat{I}_z}{\tau_r} \left\{ \omega_{iso}[\tau_r - 2(\tau_b - \tau_a)] - 2\int_{\tau_a}^{\tau_b} [C_1' \cos(\omega_r t') + C_2' \cos(2\omega_r t')]\, dt' \right\}$$

$$= \frac{\hat{I}_z}{\pi} \left\{ \omega_{iso}[\pi - \omega_r(\tau_b - \tau_a)] + C_1'[\sin(\omega_r\tau_a) - \sin(\omega_r\tau_b)] \right.$$

$$\left. + \frac{1}{2}C_2'[\sin(2\omega_r\tau_a) - \sin(2\omega_r\tau_b)] \right\}. \qquad (5.13)$$

For the same reason as in the 2DCSA experiment, the pulse timings in Equation (5.13) must give an average Hamiltonian that has the form

$$\frac{1}{\tau_r} \int_0^{\tau_r} \hat{\mathcal{H}}_{CS}^*(t')dt' = \{\xi'\omega_{iso} + \chi'(C_1' + C_2')\}\, \hat{I}_z, \qquad (5.14)$$

where ξ' and χ' are the isotropic and anisotropic scaling factors respectively. A prime has been used to differentiate these scaling factors from those of the 2DCSA experiment.

This gives the set of conditions that the pulse timings must fulfil:

$$\xi' = 1 - 2\frac{\tau_b - \tau_a}{\tau_r} \qquad (5.15)$$

$$\chi' = \frac{1}{\pi}[\sin(\omega_r\tau_a) - \sin(\omega_r\tau_b)] \qquad (5.16)$$

$$\chi' = \frac{1}{2\pi}[\sin(2\omega_r\tau_a) - \sin(2\omega_r\tau_b)]. \qquad (5.17)$$

To determine the required pulse timings, simultaneous Equations (5.16) and (5.17) were solved for the desired value of the anisotropic scaling factor. Pulse timings exist that achieve anisotropic scaling factors in the range $\chi' = 0\ldots0.206$ and are plotted in Figure 5.5 on the next page. The effects of sample rotation during the 4π-pulses becomes significant with scaling factors greater than 0.17, and a scaling factor of 0.155 is recommended.[190] To obtain the required spectral width in the F_1 dimension for ^{13}C NMR at intermediate static field strengths, spinning frequencies in the range 2.5-5 kHz are used.
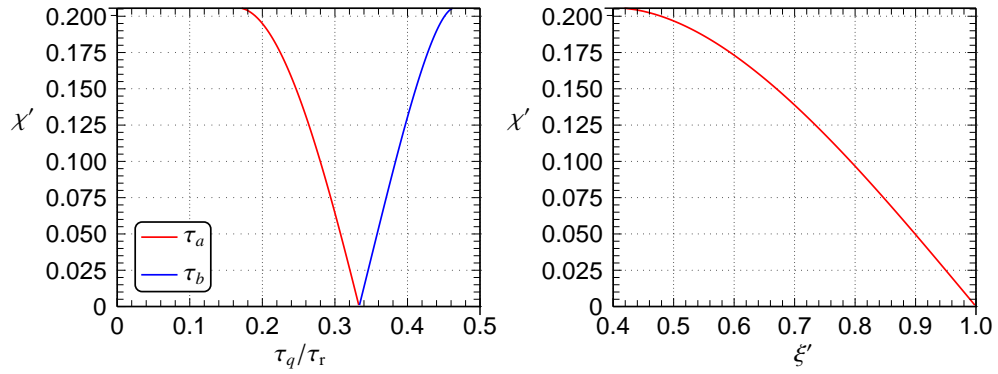
Figure 5.5: The pulse timings for the SUPER experiment. The left hand plot shows the pulse timings and the right hand plot the corresponding isotropic scaling factor.

The phase modulation within the 4π-pulse blocks is intended to reduce the effects of pulse length imperfections. For the $2\pi_x 2\pi_{-x}$ block, if the rotation angle deviates from 2π during the first pulse, this is corrected by the same deviation in the opposite sense by the second pulse, as illustrated in Figure 5.6.

The States[58] method of quadrature detection in the indirectly observed dimension is used in SUPER experiments. To select the sine and cosine amplitude-modulated signals, a $\pi/2$-pulse is applied immediately prior to detection. Assuming this is a 90°_x-pulse, the density operator after this pulse is

$$\hat{\rho}(t_1) = \frac{1}{2}\cos(\phi)\hat{I}_+ + \frac{1}{2}\cos(\phi)\hat{I}_- + \sin(\phi)\hat{I}_z, \tag{5.18}$$

where $\mp\phi$ is the phase acquired by the (± 1)-quantum coherences during the recoupling sequence. At this point in the pulse sequence, the ^{1}H decoupling is turned off. Single-quantum coherences, represented by the $\hat{I}_+$ and $\hat{I}_-$ terms in Equation (5.18), dephase
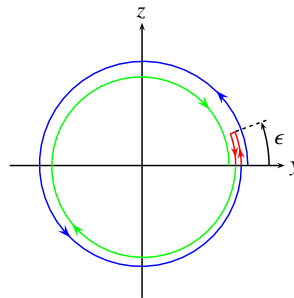
Figure 5.6: The compensation achieved by the $2\pi_x 2\pi_{-x}$ pulses for a pulse length error ϵ. The path of a component of magnetization initially aligned along the y-axis is shown. The rotation caused by the first pulse is illustrated by the blue line and the rotation caused by the second pulse by the green line. The deviation ϵ from the 2π rotations is shown in red for each pulse. The magnetization returns to the initial position, even when pulse length errors are present.

rapidly, owing to the ^{13}C–^{1}H dipolar coupling, while the $\hat{I}_z$ term in the density operator (Equation (5.18)) is unaffected. A second $\pi/2$-pulse converts the $\hat{I}_z$ term in the density operator to single-quantum coherences that give the amplitude-modulated signal; it is cosine modulated if the first $\pi/2$-pulse is a y-pulse, and sine modulated for an x-pulse. This step is labelled the 'z-filter' in Figure 5.4, and typically lasts ≈ 1 ms.

5.3 Cogwheel phase cycled implementations of 2DCSA and SUPER

Artefacts and distortions in the 2DCSA and SUPER spectra are caused by the effects of imperfections in the recoupling sequence pulses. Unwanted coherence-transfer pathways that contribute to the signal are caused by pulse imperfections, and phase cycling can be used to reduce their effect by selecting only the desired coherence-transfer pathways. This was demonstrated for the CSA-amplified PASS experiment in Section 4.5.

The recoupling sequences act on transverse magnetization, which corresponds to single-quantum coherences. The pulses applied during the 2DCSA recoupling sequence are all π-pulses, which only change the sign of the coherence order, and in the SUPER pulse sequence only 2π-pulses are used, which leave the coherence order unchanged. Thus, the desired coherence order is always ± 1 during the 2DCSA and SUPER recoupling sequences. The desired coherence-transfer pathways are shown for the six π-pulse 2DCSA and SUPER pulse-sequence units in Figure 5.7 on the following page. The States method[58] of quadrature detection is used for both 2DCSA and SUPER. This requires that symmetric coherence-transfer pathways are selected by the phase cycle during the t_1 period; that is, if the $(+p)$-quantum coherence order is selected, then the $(-p)$-order must also be selected. The symmetric coherence-transfer pathways are shown in red and blue in Figure 5.7.

Cogwheel phase cycling offers the possibility of selecting only the desired coherence-transfer pathways, even when many pulses are applied. The analysis is the same as that used for the CSA-amplified PASS experiment. The pathway signature is defined as

$$\sum_{q=1}^{n-1} \Delta\nu_{q,q+1} p_{q,q+1} - \nu_n p_{n,\mathrm{rec}}, \tag{5.19}$$

where $p_{q,q+1}$ is the coherence order between the qth and $(q+1)^{\mathrm{th}}$ pulse and $\Delta\nu_{q,q+1}$ is the difference in the winding numbers of the same pair of pulses. The pathway signature of
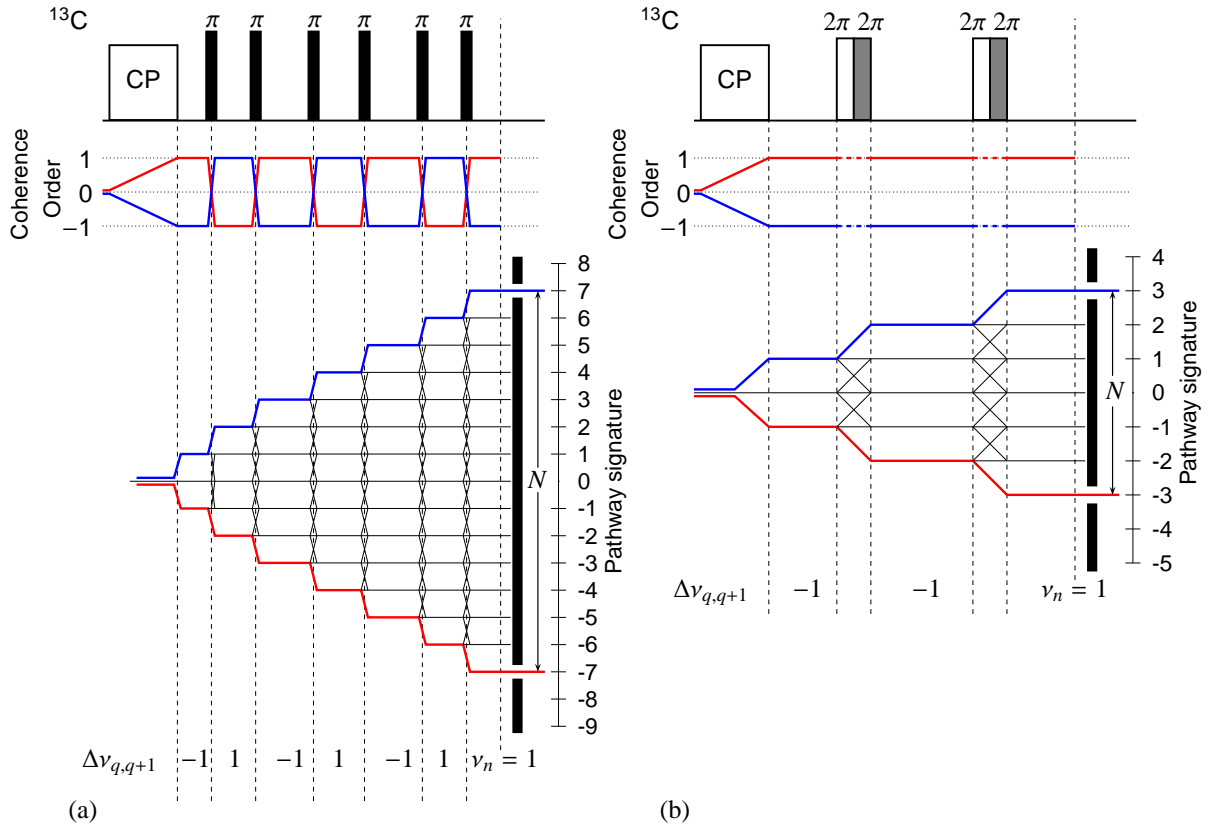
Figure 5.7: Desired coherence-transfer pathways and cogwheel splitting diagrams for one pulse-sequence unit of the (a) six π-pulse 2DCSA and (b) SUPER pulse sequences. The red and blue lines in the cogwheel splitting diagram correspond to the pathway signatures of the red and blue coherence-transfer pathways. Further details are given in the main text.

the desired coherence-transfer pathways must be (*i*) different from the pathway signatures associated with any undesired coherence-transfer pathway, and (*ii*) not differ by a multiple of N (the total number of steps in the phase cycle) from any undesired pathway signature.

These conditions are best visualised using a cogwheel splitting diagram. These are shown in the lower part of Figure 5.7 for one pulse-sequence unit of 2DCSA and SUPER, where the build up of the pathway signature is plotted underneath the pulse sequence for all possible coherence-transfer pathways. For the phase cycle to select only the desired coherence-transfer pathways, the values of $\Delta \nu_{q,q+1}$ must be chosen so that the desired pathway signatures are unique. If the desired coherence-transfer pathway $\boldsymbol{p}^0$ is the blue pathway and $\boldsymbol{p}^{0\prime}$ is the red pathway plotted in Figure 5.7, this condition is fulfilled by choosing $\Delta \nu_{q,q+1} = p^0_{q,q+1} = -p^{0\prime}_{q,q+1}$ and $\nu_n = -p^0_{n,\mathrm{rec}} = p^{0\prime}_{n,\mathrm{rec}} = +1$, as shown in the splitting diagrams. Only the pathway signatures that pass through the barrier on the right hand side of the splitting diagram are selected. The spacing between holes in the barrier is the number of steps in the phase cycle, while the position of the gaps is determined by the receiver phase. Thus, to select both the red and blue pathways in Figure 5.7, the number of steps in the phase cycle must be 14 for 2DCSA and 6 for SUPER, which is double the magnitude of their pathway signatures. For a greater number of 2DCSA and SUPER pulse-sequence units, the cogwheel splitting diagrams have the same form as in Figure 5.7, and although the range of pathway signature values is greater, the red and blue pathways always lie at the extreme values.

A complication arises when using cogwheel phase cycling in conjunction with the States method for 2DCSA and SUPER, due to the need to select symmetric coherence-transfer pathways. In both experiments, the number of pulses used in the recoupling sequence is increased as the t_1 period is incremented. Selecting both symmetric pathways then requires increasing the number of steps in the phase cycle with each t_1 increment, this is illustrated schematically in Figure 5.8 on the next page. Recording all steps in the phase cycles means each t_1 increment is acquired with a different number of scans. This can be corrected by appropriate weighting of the two-dimensional dataset, but this is rather inconvenient to implement experimentally and during data processing.

The solution to this difficulty is to use the echo anti-echo method of quadrature detection, described in in Section 2.2.1, following the method proposed by Bachmann *et al.*[60] In one experiment a π-pulse is applied just prior to recording the FID to give the echo signal. The π-pulse is removed in a second experiment to record an anti-echo signal, as illustrated in Figure 5.9 on the following page. Using this method the symmetric coherence-transfer pathways are not simultaneously selected during the t_1 period. Instead, the blue pathway
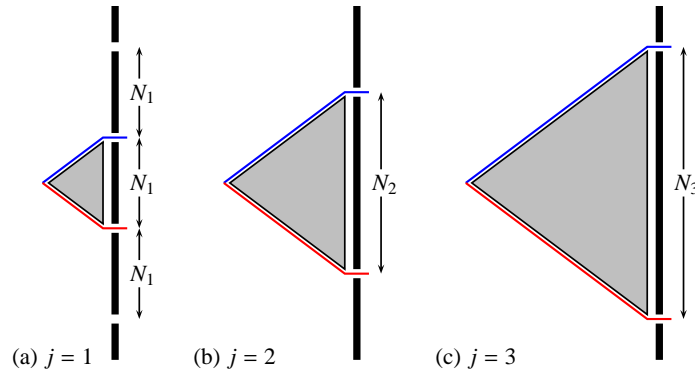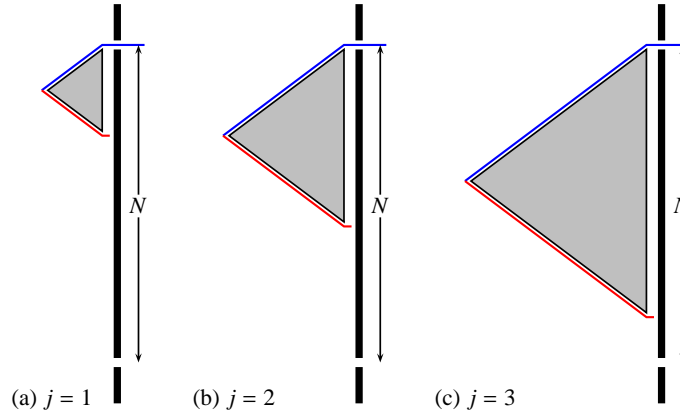
Figure 5.8: Schematic cogwheel splitting diagrams for 2DCSA or SUPER recoupling sequences with (a) $j = 1$, (b) $j = 2$ and (c) $j = 3$, where j is the number of pulse-sequence units. The build up of pathway signatures is represented by the grey triangle, with the desired red and blue pathway signatures shown along its edge. N_1, N_2 and N_3 are the number of steps needed in the phase cycle when using the States[58] method of quadrature detection.

in Figure 5.7 is selected to give the anti-echo signal and the red pathway the echo signal (the additional π-pulse converts the $(+1)$-quantum coherence at the end of the recoupling sequence to a (-1)-quantum coherence that can be detected). This means that the number of steps in the phase cycle is only restricted to being *greater* that twice the pathway signature of the desired coherence-transfer pathway. Thus, the same number of phase cycle steps can used for all t_1 increments, while still selecting only one coherence-transfer pathway; this is illustrated schematically in Figure 5.10 on the next page. In the echo anti-echo case, the number of steps in the phase cycle must be large enough to select only the desired coherence-transfer pathway for the recoupling sequence used for the largest t_1 value in the experiment.

It is worth commenting that the signal-to-noise ratio is $\sqrt{2}$ times greater when using the echo anti-echo detection method[60] than for the States method.[58] This corresponds to
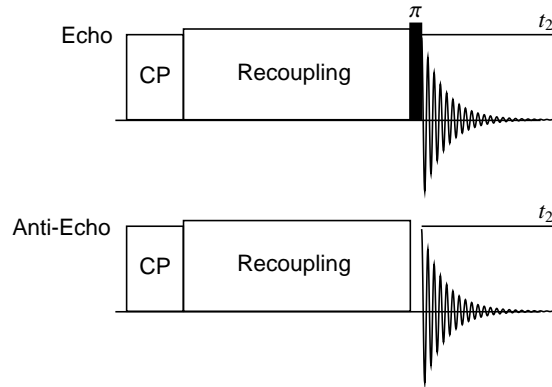
Figure 5.9: The echo anti-echo method of quadrature detection using the approach of Bachmann *et al.*[60] The 'Recoupling' block indicates either SUPER or 2DCSA pulse-sequence units.

(a) $j = 1$ (b) $j = 2$ (c) $j = 3$

Figure 5.10: Schematic cogwheel splitting diagrams for 2DCSA or SUPER recoupling sequences with (a) $j = 1$, (b) $j = 2$ and (c) $j = 3$, where j is the number of pulse-sequence units. The build up of pathway signatures is represented by the grey triangle, with the desired red and blue pathway signatures shown along its edge. The same number of steps N in the phase cycle is used in each case for the echo anti-echo method of detection.

halving the experiment time to achieve a specified signal-to-noise ratio, which may be especially useful for samples with low sensitivity.

Unfortunately, a new problem is introduced by this method, because of the π-pulse used to create the echo signal. Imperfections in this additional π-pulse cause the echo signal to have a lower intensity than the anti-echo signal. When processing the dataset, the echo ($S'_-(t_1, \omega_2)$) and anti-echo ($S'_+(t_1, \omega_2)$) signals are combined to form a new dataset, $S'_{E-AE}(t_1, \omega_2)$. Using the notation introduced in Section 2.2.1:

$$S'_{E-AE}(t_1, \omega_2) = aS'_+(t_1, \omega_2) + b[S'_-(t_1, \omega_2)]^*$$
$$= \exp(i\Omega_1 t)\exp(-t_1/T_{2,1})\{(a + b)\mathcal{A}_2 + (a - b)\mathcal{D}_2\}$$
$$S_{E-AE}(\omega_1, \omega_2) = \{\mathcal{A}_1^+ + i\mathcal{D}_1^+\}\{(a + b)\mathcal{A}_2 + (a - b)\mathcal{D}_2\}, \tag{5.20}$$

where a and b represent the relative weighting of the anti-echo and echo signals respectively. Unless the two signals have the same intensity ($a=b$), a dispersive component remains in the real part of the two-dimensional spectrum, causing an unwanted phase-twist contribution. To avoid this distortion, an alternative approach was developed. The method utilises a rotor-synchronised spin echo, shown in Figure 5.11 on the following page. For the anti-echo signal, the rotor synchronised echo has no effect on the resulting signal, other than to attenuate its intensity (due to π-pulse imperfections and transverse relaxation) so that its intensity is the same as the echo signals. Using this technique, no phase-twist contributions have been observed in the two-dimensional lineshapes.

As discussed in Section 4.3.1, to remove quadrature artefacts from the spectrum, the
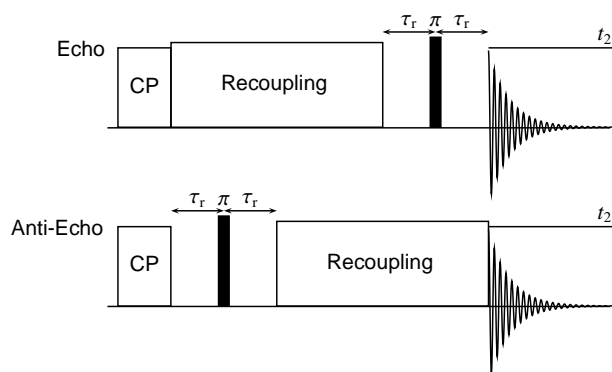
Figure 5.11:   Rotor-synchronised echo method used in this work to record echo and anti-echo signals. The 'Recoupling' block represents either the 2DCSA or SUPER pulse sequence.

winding number labelled ν_{rec} must actually be applied as a post-digitizer phase shift ϕ_{dig}, rather than as a receiver phase shift ϕ_{rec}. This was not possible for the spectrometers used in this work and instead the ν_{rec} was applied at the receiver. The number of steps in the phase cycles was chosen to be even (by adding an additional step) so that the ^1H $\pi/2$-pulse used before CP could be alternated in phase between $+x$ and $-x$ on alternate scans an even number of times, the post-digitizer phase being adjusted to account for this. This selects only carbon signals generated by CP and also removes the DC-offset caused by non-ideal behaviour of the quadrature receiver.

The winding numbers for the six π-pulse 2DCSA sequence are shown in Figure 5.12. For the SUPER experiment, the pulse length error compensation of the 4π-pulse is retained by adjusting their phases as $2\pi_\phi 2\pi_{180+\phi}$ blocks, where ϕ is varied during phase cycling. The winding numbers for the SUPER experiments are shown in Figure 5.13. Cogwheel phase-cycled experiments are indicated by the suffix (COG).

The number of steps required in the phase cycle depends on the number of pulses used in the last t_1 increment. The total number of steps, N, required in the SUPER(COG) experiment is $N = 4j_{max} + 6$, where j_{max} is the maximum number of pulse-sequence units used in the experiment. Thus, to record 32 t_1 points, 134 phase-cycle steps are required for the SUPER(COG) experiment, which is roughly double that needed for the conventional implementation of SUPER that uses a 64 steps.

The six π-pulse 2DCSA(COG) sequence needs $N = 12j_{max} + 6$ steps in its phase cycle, and the four π-pulse sequence $N = 8j_{max} + 6$ steps. Therefore, with 32 t_1 values recorded the four π-pulse version uses 262 phase-cycle steps and the six π-pulse sequence 390 steps. These are phase cycles are rather long, but for many samples this many acquisitions may be needed to achieve a good signal-to-noise ratio in any case.
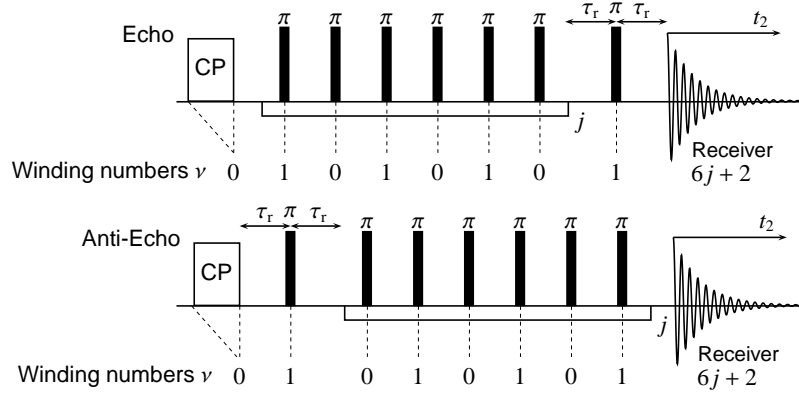
Figure 5.12: Winding numbers required for the six π-pulse 2DCSA(COG) sequence. The total number of steps in the cogwheel phase cycle is $N = 12j_{max} + 6$, where j_{max} is the maximum number of pulse-sequence units used in the experiment.
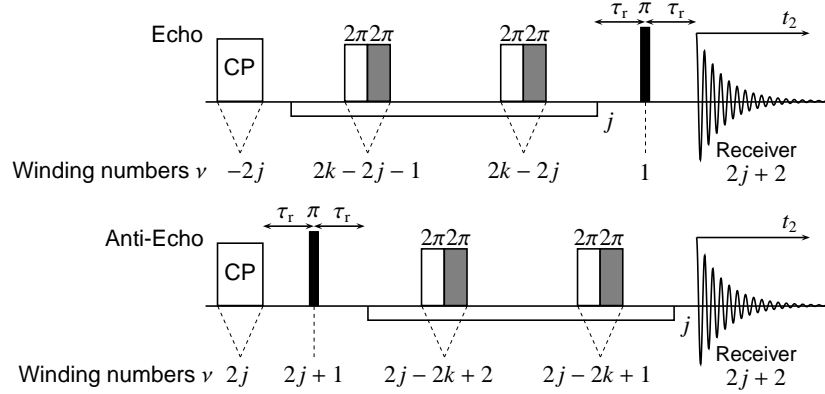

Figure 5.13: Winding numbers for the SUPER(COG) pulse sequence. The total number of steps in the phase cycle is $N = 4j_{max} + 6$, where j_{max} is the maximum number of pulse-sequence units used in the experiment. The grey pulses have a 180° phase shift from the adjacent white pulse. The number of pulse-sequence units used in the sequence is j, indexed by k: $k = 1$ for the first unit in the sequence and $k = j$ for the last.

(a) $j < j_{\max}/2$ (b) $j = j_{\max}/2$ (c) $j > j_{\max}/2$ (d) $j = j_{\max}$
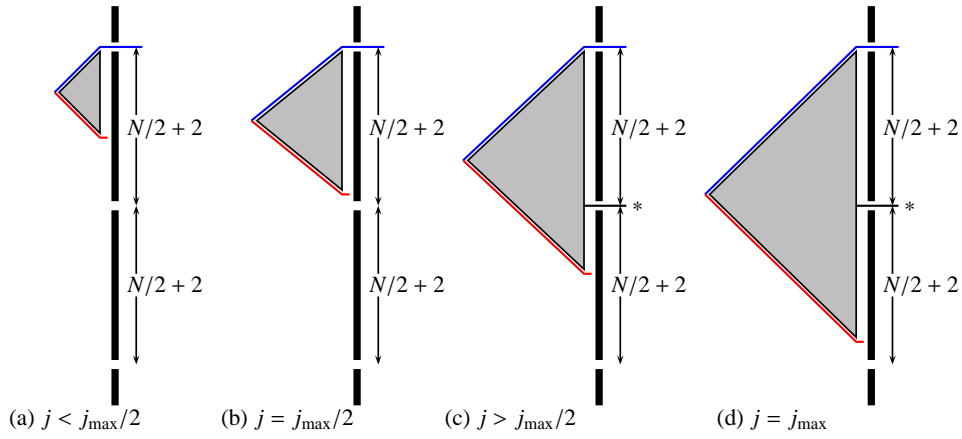
Figure 5.14: Schematic cogwheel splitting diagrams where the number of steps in the phase cycle has been reduced from $N = 12 j_{\max} + 6$ (needed to select exclusively the desired pathway signature) to $N/2 + 2$. (a), (b) For $j \leq j_{\max}/2$ only the desired pathway signature is selected. (c), (d) For $j_{\max}/2 < j \leq j_{\max}$ only one unwanted pathway signature is selected, marked by the asterisk.

For the 2DCSA(COG) experiments, it was found that the number of steps in the phase cycle could be halved from the $N = 12 j_{\max} + 6$ requirement without introducing noticeable effects in the spectra. Consideration of the cogwheel splitting diagram shows that this reduction in the number of steps in the phase cycle causes unwanted pathway signatures to be selected in addition to the desired pathway signature. For a full phase cycle of $N = 12 j_{\max} + 6$ steps, reducing the number of steps in the cycle to $N/2 - 4$ for odd $j_{\max}$, or $N/2 + 2$ for even $j_{\max}$, results in a phase cycle that still selects only the desired coherence-transfer pathway for the first half of the t_1 increments of the experiment, as shown in Figure 5.14(a),(b); thereafter, one unwanted pathway signature is selected for the rest of the t_1 increments (Figure 5.14(c)(d)). This does not appear to affect the recorded spectra, probably because the early t_1 points are the most important for defining the major features of the powder pattern, and the unwanted pathway signature selected during the later t_1 increments represents a relatively small fraction of the total unwanted coherence-transfer pathways.

5.3.1   Multiplex phase cycling

A multiplex phase cycling approach[66] can be implemented for the 2DCSA(COG) and SUPER(COG) experiments. For example, the schemes shown in Figure 5.15 could be used to extract the echo and anti-echo signals from a single two-dimensional dataset. When using the multiplex phase cycling method, the minimum experiment time is half that needed when not using this technique. However, in addition to the data storage
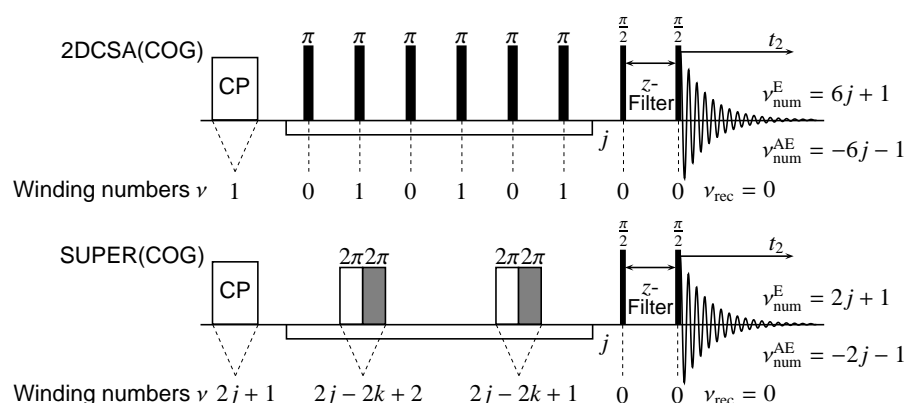
Figure 5.15: The multiplex phase cycling scheme for (a) 2DCSA(COG) and (b) SUPER(COG). In (a) the total number of steps in the cogwheel phase cycle is $N = 12j_{max} + 4$ and in (b) $N = 4j_{max} + 4$, where j_{max} is the maximum number of pulse-sequence units used in the experiment. In each case, ν_{num}^{E} and ν_{num}^{AE} are the winding numbers for the numerical phase shifts needed to extract the echo and anti-echo signals respectively. During the z-filter the ^{1}H decoupling is turned off.

and processing complications of the multiplex phase cycling approach, there is the further disadvantage that the signal-to-noise ratio will be half that achieved using the cogwheel phase cycling schemes in Figures 5.12 and 5.13 (for the same experiment time). Consequently, multiplex phase cycling will only be useful in cases where the signal-to-noise ratio is favourable and is not a limiting factor for the experiment time.

5.3.2   Experimental examples

Figure 5.16 compares the results for α-glycine from using the conventional and cogwheel phase-cycled version of the 2DCSA and SUPER experiments. In these cross-sections, the isotropic shift is chosen to appear at 0 Hz, which is the convention used for all cross-sections shown in this chapter. In Figure 5.16, best-fit simulated lineshapes are overlaid in red, and the best fit parameters are given in the caption. These simulations were performed using the SIMPSON program,[39] with a calculated static powder pattern fitted to the experimental cross-section using the Simplex method to minimise the root mean square deviation between the two lineshapes. Exponential line broadening of *lb* Hz was applied to the FID before Fourier transformation, and the fitting procedure optimised the values of δ_{aniso}, η_{CS}, *lb* and an intensity weighting. The simulated and cogwheel phase cycled experimental results fit very well, and demonstrate that the the distorted lineshapes and artefacts that occur for the original versions of 2DCSA and SUPER are avoided. The fitted parameters are consistent with those obtained from static powder sample measurements on the same sample, which gave $\delta_{aniso} = -71$ ppm, $\eta_{CS} = 0.91$.
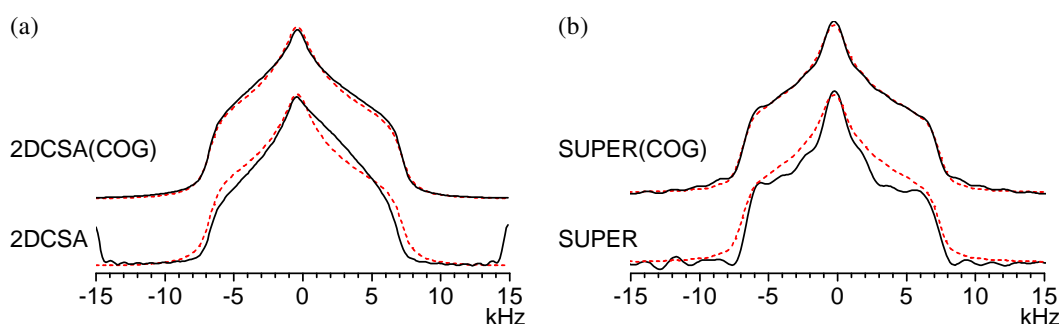
Figure 5.16: Comparison of the conventional and cogwheel phase-cycled versions of the (a) 2DCSA and (b) SUPER experiment for ^{13}C. The sample used in (a) was ^{13}C-1-α-glycine, and in (b) natural abundance α-glycine. In both experiments, 32 t_1 values were used, except for SUPER(COG), where only 20 increments were collected. The dashed red lines show simulated static lineshapes using the parameters (a) $\delta_{\mathrm{aniso}} = -72$ ppm, $\eta_{\mathrm{CS}} = 0.90$, $lb = 1280$ Hz and (b) $\delta_{\mathrm{aniso}} = -73$ ppm, $\eta_{\mathrm{CS}} = 0.91$, $lb = 1080$ Hz.

As a second example, the 2DCSA(COG) and SUPER(COG) ^{13}C spectra were recorded for fumaric acid monoethyl ester. The labelling scheme for the ^{13}C sites is shown in Figure 5.17. The SUPER(COG) and 2DCSA(COG) cross-sections for sites (b-f) are shown in Figures 5.18 and 5.19 on page 135, with best fit lineshapes (calculated by the same procedure used for glycine) overlaid on the experimental results. The best fit
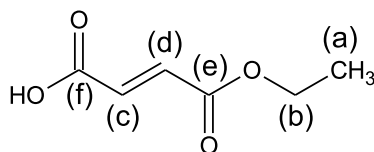
Figure 5.17: Fumaric acid monoethyl ester and the labelling scheme used in this chapter, based on solution-state NMR chemical shift assignments.[212]

parameters are summarised in Table 5.1, where the results obtained using CSA-amplified PASS experiment with a scaling factor of 10.4 are also shown for comparison. Error estimates were made by adjusting the best fit parameters until a noticeable change in the lineshape was seen. The fitted parameters from the three experiments are consistent with each other, within the estimated uncertainties, with the largest difference occurring for sites (c) and (d).

The experimental and simulated lineshapes fit well, and the edges and singularities in the powder lineshapes coincide with the simulations in all cases. Comparing the 2DCSA(COG) and SUPER(COG) results, the line broadening required for the optimum fitted lineshapes in the SUPER(COG) results is systematically smaller than for the 2DCSA(COG) cross-sections. Both sets of results compare favourably with previously literature examples of 2DCSA and SUPER; for example, compare the results in Figure 5.18 with Figures 6 and 8 of reference [190]. It is clear that the longer phase

	Site	2DCSA(COG)	SUPER(COG)	CSA-amplified PASS
	δ_{aniso} / ppm	-44±4	- 41±4	- 41±2
(b)	η_{CS}	0.69±0.1	0.70±0.1	0.73±0.07
	lb / Hz	2600	2400	
	δ_{aniso} / ppm	103±4	103±4	97±4
(c)	η_{CS}	0.71±0.05	0.70±0.05	0.71±0.05
	lb / Hz	1620	1600	
	δ_{aniso} / ppm	106±4	107±4	103±4
(d)	η_{CS}	0.73±0.05	0.71±0.05	0.69±0.05
	lb / Hz	1696	1500	
	δ_{aniso} / ppm	88±2	89±3	86±3
(e)	η_{CS}	0.24±0.03	0.23±0.03	0.25±0.04
	lb / Hz	920	570	
	δ_{aniso} / ppm	70±3	69±3	67±3
(f)	η_{CS}	1.0±0.03	1.0±0.03	1.0±0.05
	lb / Hz	1250	1180	

Table 5.1: Summary of fitted parameters for sites (b-f) of fumaric acid monoethyl ester for the SUPER(COG) and 2DCSA(COG) results in Figures 5.18 and 5.19. CSA-amplified PASS results using a scaling factor of 10.2, which were shown in Figure 4.10 on page 97, are also given.

cycle needed in the 2DCSA(COG) and SUPER(COG) experiments is greatly outweighed by the advantage of recording undistorted lineshapes.

Since the number of steps in the phase cycle for the SUPER(COG) experiment is typically only around double that of the conventional version, it seems reasonable to suggest that SUPER(COG) should be used routinely, unless the spin-lattice relaxation time of the samples makes the required number of acquisitions per t_1 increment impractical. In the following section, it is shown that further improvements can be made to the results obtained using the 2DCSA(COG).

5.4   Improved implementations of the 2DCSA experiment

The 2DCSA(COG) experiment is a significant improvement over the original implementation of the 2DCSA experiment, but there are still two limitations. First, the phase cycle involved is rather long, and second, the powder pattern lineshapes appear highly broadened compared with ideal static lineshapes.

In addition to transverse relaxation occuring during the t_1 period, the overly broad lineshapes result from two sources. First, the effects of pulse imperfections reduce the signal intensity as the number of pulse-sequence units in the recoupling sequence is
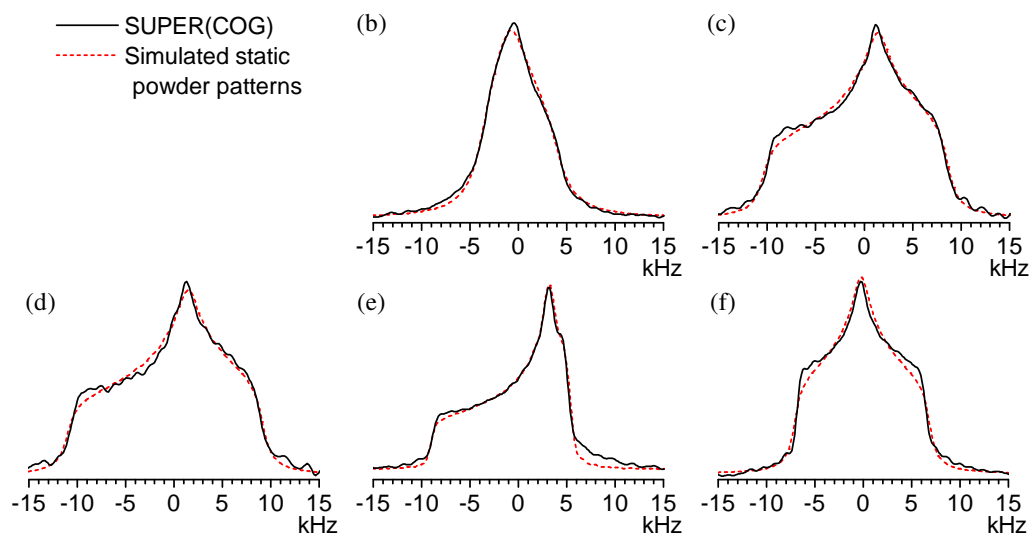
Figure 5.18: Cross-sections taken from the SUPER(COG) experimental ^{13}C spectrum of fumaric acid monoethyl ester. Best fit simulated static powder pattern lineshapes are overlaid in red. Further details are given in the main text.
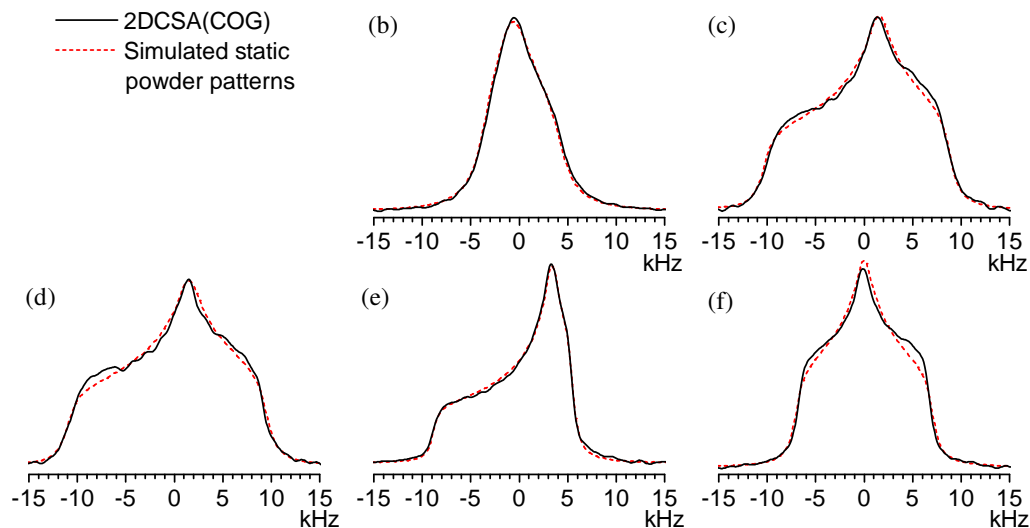

Figure 5.19: Cross-sections taken from the 2DCSA(COG) experimental ^{13}C spectrum of fumaric acid monoethyl ester. Best fit simulated static powder pattern lineshapes are overlaid in red. Further details are given in the main text.

increased. Second, the ^{13}C–^{1}H dipolar interaction is recoupled when both ^{1}H and ^{13}C are irradiated during the π-pulses (as will be discussed in Section 5.6.1), and causes dephasing of the signal and a loss of signal intensity. Both processes cause an exponential decay of the t_1 signal as a function of the number of pulse-sequence units, which manifests itself as a broadening of the powder pattern lineshape. The observed signal s_{obs} can be related to the ideal signal s_{ideal} (which does not decay due to relaxation or pulse imperfections) by

$$s_{\text{obs}}(j, t_2) = s_{\text{ideal}}(j, t_2) \exp(-j\lambda_{\text{decay}}) \exp(-t_2/T_2), \tag{5.21}$$

where the signal has been written as a function of the number of pulse-sequence units in the recoupling sequence (j), rather than of t_1, and λ_{decay} is a decay constant which characterises the signal loss during a pulse-sequence unit.

In principle, one could multiply the recorded FID by a rising exponential weighting function to counteract the exponential decay factor $\exp(-j\lambda_{\text{decay}})$ in Equation (5.21). In practice, this leads to rather poor results because the exponential function amplifies the noise in the signal. In addition, the effects of pulse imperfections are greater for the later t_1 points, and are magnified by the weighting function, which usually leads to distorted as well as noisy spectra.

The results of the 2DCSA experiment can be substantially improved by performing the experiment in a somewhat different method to the conventional implementation. First, it is noted that with evolution under the average Hamiltonian in Equation (5.4), the propagator $\hat{U}(t_1)$ of the rotating-frame density operators is

$$\hat{U}(jl\tau_{\text{r}}) = \exp\left\{-i\left(\xi\omega_{\text{iso}} + \chi[C_1'(\Omega_{\text{PR}}) + C_2'(\Omega_{\text{PR}})]\right) jl\tau_{\text{r}}\hat{I}_z\right\}, \tag{5.22}$$

where j is the number of pulse-sequence units with duration $l\tau_{\text{r}}$ and $t_1 = jl\tau_{\text{r}}$. Therefore, the phase acquired by the single-quantum coherences during the recoupling sequence is

$$\phi(jl\tau_{\text{r}}; \Omega_{\text{PR}}) = \left(\xi\omega_{\text{iso}} + \chi[C_1'(\Omega_{\text{PR}}) + C_2'(\Omega_{\text{PR}})]\right) jl\tau_{\text{r}}. \tag{5.23}$$

Usually the t_1 period is incremented by increasing the number of pulse-sequence units (increasing j) in the recoupling sequence. If, however, the isotropic scaling factor (ξ) is chosen to be zero (using the six π-pulse recoupling sequence), then the same effect may be achieved by changing (i) *either j or* the anisotropic scaling factor χ, or (ii) *both j and χ*. Variation of the anisotropic scaling factor (χ) is achieved by changing the pulse timings used in the recoupling sequence. This is where the utility of calculating the pulse timings

for specific values of χ becomes evident.

Under the condition $\xi = 0$, an effective t_1 time, which takes into account the scaling effect of the recoupling sequence, can be defined to be

$$t_1^{\text{eff}} = jl\tau_{\text{r}}\chi. \tag{5.24}$$

Fourier transformation of the signal from the indirect dimension with respect to t_1^{eff} gives powder patterns that are the same as one-dimensional static spectra using the usual time variable (assuming $\omega_{\text{iso}} = 0$).

5.4.1 Constant-time implementation

If, in Equation (5.23), j is kept constant and equal to j_{total}, then the experiment becomes a constant-time experiment (CT-2DCSA), in the sense that the t_1 evolution period is fixed throughout the experiment. This has the advantage that the observed t_1 signal is the same as the ideal signal, except for an overall weighting factor determined by the signal decay during the recoupling sequence

$$s_{\text{obs}}(t_1^{\text{eff}}, t_2) = s_{\text{ideal}}(t_1^{\text{eff}}, t_2) \exp(-j_{\text{total}}\lambda_{\text{decay}}) \exp(-t_2/T_2), \tag{5.25}$$

where the signal has now been written as a function of the effective t_1 time. The penalty is that the signal-to-noise ratio of the recorded spectrum may be significantly reduced by the $\exp(-j_{\text{total}}\lambda_{\text{decay}})$ weighting factor.

The spectral width (SW) in the indirect dimension (which takes into account the scaling effect of the recoupling sequence) and the anisotropic scaling factor $\chi(k)$ of the kth increment of t_1^{eff} in the constant-time experiment are related by

$$t_1^{\text{eff}}(k) = \frac{k-1}{SW} = j_{\text{total}}l\chi(k)\tau_{\text{r}} \quad 1 \le k \le k_{\text{max}}, \tag{5.26}$$

where k_{max} is the total number of (complex) points recorded in the indirectly-observed dimension.

If the maximum possible anisotropic scaling factor for the chosen value of l is χ_{max} (with isotropic scaling factor $\xi = 0$), then the required value of j_{total} is calculated from

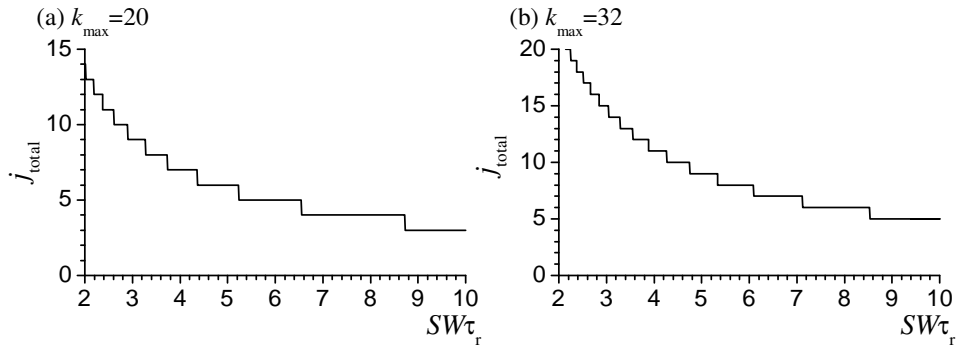$$j_{\text{total}} = \text{Ceil}\left(\frac{k_{\text{max}} - 1}{SW\chi_{\text{max}}l\tau_{\text{r}}}\right). \tag{5.27}$$

Figure 5.20: Variation of the total number of pulse-sequence units required (j_{total}) with the ratio of the spectral width to spinning frequency ($SW\tau_r$) for the constant-time implementation of the 2DCSA experiment, for (a) $k_{max} = 20$ and (b) $k_{max} = 32$.

Ceil(x) is a function that rounds x up to the nearest integer. Equation (5.27) shows that the greater the value of $\chi_{max}l$, the smaller the total number of pulse-sequence units (j_{total}) needed, and hence, fewer π-pulses are used in the recoupling sequence. For this reason, it is advantageous to use the pulse-sequence unit over three rotor periods ($l = 3$, $\chi_{max} = 0.242$) rather than that lasting one rotor period ($l = 1$, $\chi_{max} = 0.395$).

Combining Equations (5.26) and (5.27), the anisotropic scaling factor required for the kth point in the indirectly observed dimension is determined by

$$\chi(k) = \frac{1}{\text{Ceil}\left(\frac{k_{max}-1}{SW\chi_{max}l\tau_r}\right)} \cdot \frac{k-1}{SWl\tau_r}. \tag{5.28}$$

For the quasi-static spectrum of a powder sample, recorded such that the powder pattern covers at least half the F_1 spectral width, 32 (complex) t_1 data points is usually sufficient to define the lineshape, and often just 20 points can be used. Figure 5.20 illustrates the dependence of j_{total} on the ratio of the spectral width to spinning frequency ($SW\tau_r$) for recording 20 and 32 points in the indirectly observed dimension ($l = 3$, $\chi_{max} = 0.242$).

A cross-section taken through the isotropic peak in the F_2 dimension of the experiment does not contain an equal contribution from all crystallites in the powder sample if spinning sidebands are present in the F_2 dimension. This causes the cross-section lineshape to deviate from an ideal static powder pattern. The ideal lineshape can be extracted by calculating the projection onto the F_1 axis, but the signal-to-noise ratio of this projection is lower than that of the cross-section.[221] To minimise this effect, and to optimise the signal-to-noise ratio, the spinning frequency should be chosen to give only low order spinning sidebands in the F_2 dimension. For this purpose, it is sufficient to use spinning frequencies greater than $|\omega_0\Delta_{CS}/2|$, where Δ_{CS} is the chemical shielding

anisotropy parameter of the powder pattern being measured.

In addition, the spectral width needs to be roughly three times the value of $|\omega_0 \Delta_{CS}|$. This ensures that the spectrum contains the powder pattern without aliasing and with the baseline visible. This requirement, combined with the spinning frequency restraint, means that the ratio of the spectral width to the spinning frequency should be $SW\tau_r \lesssim 6$.

For 32 t_1^{eff} data points, there is a relatively narrow, but useful, practical range with $SW\tau_r \approx 6$ that corresponds to using between six and ten pulse-sequence units (see Figure 5.20). When recording 20 data points, fewer pulse-sequence units are required, which is experimentally favourable because pulse imperfections have less effect. In a 9.4 T magnetic field, sp^2 carbons (which have relatively large δ_{aniso}) require spinning frequencies around 5 kHz to provide a suitable spectral width in F_1, whilst avoiding many spinning sidebands in the F_2 dimension. For sp^3 sites, slower spinning ($\approx$ 2.5 kHz) is preferable. These spinning conditions for CT-2DCSA are similar to those that must be used with the SUPER experiment.[190]

5.4.2 Optimised implementation of 2DCSA

If *both j and* χ_{max} are varied during the experiment, then the 2DCSA experiment can be optimised such that the minimum possible number of π-pulses is used for each value of t_1^{eff}; this experiment is referred to as OPT-2DCSA. This implementation minimises the signal decay caused by pulse imperfections and ^{13}C–^{1}H dipolar coupling, and benefits from the optimum signal-to-noise ratio possible.

The number of pulse-sequence units $j(k)$ and the anisotropic scaling factor $\chi(k)$ required for the kth increment of t_1^{eff} are

$$j(k) = \text{Ceil}\left(\frac{k-1}{SW\chi_{\text{max}}l\tau_r}\right) \tag{5.29}$$

$$\chi(k) = \frac{1}{\text{Ceil}\left(\frac{k-1}{SW\chi_{\text{max}}l\tau_r}\right)} \cdot \frac{k-1}{SWl\tau_r}. \tag{5.30}$$

The maximum number of pulse-sequence units, which occurs for the last t_1^{eff} increment of the experiment, is the same j_{total} as for the constant-time experiment with the same F_1 spectral width and spinning frequency.

Increasing the number of pulse-sequence units applied in the recoupling sequence in a
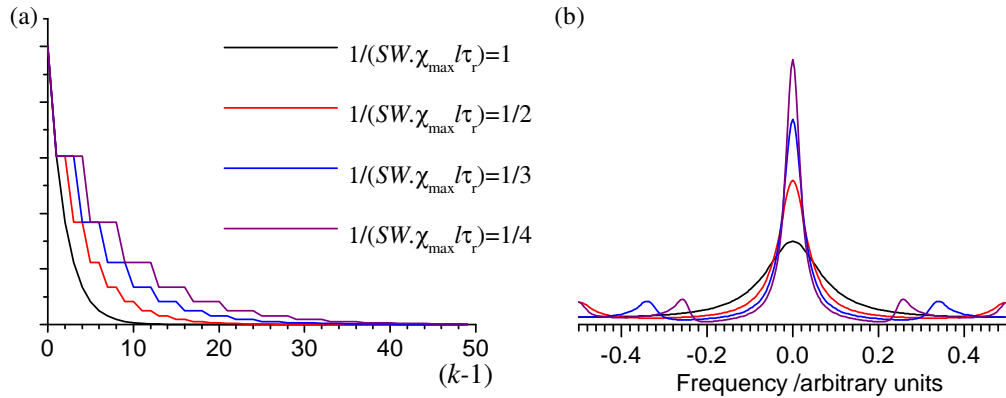
Figure 5.21: (a) Stepped-exponential decay functions $\exp\{-j(k)l\tau_r\lambda_{decay}\}$, where λ_{decay} is a decay constant that describes the signal attenuation with increasing numbers of pulse-sequence units and $j(k) = \text{Ceil}((k - 1)/(SW\chi_{max}l\tau_r))$. Four values of $(SW\chi_{max}l\tau_r)^{-1}$ are illustrated. (b) Fourier transforms of the functions in (a). The same decay constant λ_{decay} was used for all functions.

non-linear manner causes a non-exponential ('stepped exponential') decay of the signal as a function of $t_1^{eff}(k)$. Because the lineshape in the frequency domain is determined by the Fourier transform of the function describing the decay of the signal, a stepped exponential decay causes a non-Lorentzian lineshape (for individual crystallites). To illustrate this effect, three decay function are shown in Figure 5.21, each with the form $\exp\{-j(k)l\tau_r\lambda_{decay}\}$, where $j(k)$ is defined by Equation (5.29). The Fourier transforms of the stepped exponential functions have much narrower linewidths than the Fourier transform of the exponential decay. However, there are small ridges in the baseline of the Fourier transforms of stepped exponential decays.

The experimental spectra correspond to the ideal powder pattern lineshape convoluted with the Fourier transform of the stepped-exponential function (Section 1.8.4).[21] This means that the OPT-2DCSA method could introduce new artefacts into the spectrum. However, these artefacts will be small, except if very rapid signal decay occurs, in which case it is unlikely that useful results will be obtained by multiple π-pulse recoupling experiments in any case. Consistent with this argument, no artefacts have been found in experimental spectra recorded using this approach.

5.4.3 Experimental implementation

As in Section 5.3, cogwheel phase cycling was used in both the CT-2DCSA and OPT-2DCSA experiments; this is indicated by the suffix '(COG)'. Because the maximum number of pulse-sequence units used in these experiments is much smaller than for
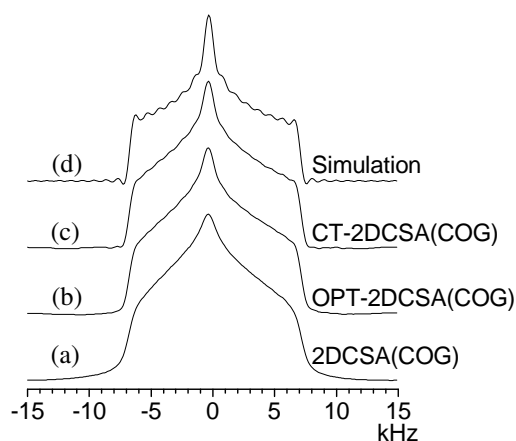
Figure 5.22: (a) 2DCSA(COG), (b) OPT-2DCSA(COG), (c) CT-2DCSA(COG) experimental results and (d) SIMPSON simulation for carbonyl ^{13}C site in ^{13}C-1-α-glycine. The plots show the cross-section taken through the carbonyl peak of the F_2 dimension. 32 complex data points were collected in the indirect dimension. In all cases $\omega_{\mathrm{r}}/2\pi = 5$ kHz and $SW = 30$ kHz and for (b) and (c) $j_{\mathrm{total}} = 8$. Simulated powder pattern used the parameters $\delta_{\mathrm{aniso}} = -71$ ppm and $\eta_{\mathrm{CS}} = 0.91$, which were determined from static sample powder pattern measurements.

2DCSA(COG), the number of steps in the phase cycle is usually around 100. The pulse timings and number of pulse-sequence units required for each increment of t_1^{eff} were calculated using a MuPAD[210] procedure, detailed in Appendix B, which automatically produced a file that was formatted to be read by the spectrometer when executing the experiment. This experimental procedure removes the need for several versions of the pulse program. An alternative procedure would use polynomial fits to the pulse timings as a function of χ, and use these formulae to calculate the required pulse timings within the pulse program.

Stable spinning is necessary for both these experiments. Standard commercial spinning hardware routinely stabilises the spinning frequency to within ±2 Hz, which was found to be sufficient for these experiments.

5.4.4 Experimental demonstration

As an initial demonstration of these experiments, a comparison of the spectra obtained by the OPT-2DCSA(COG) and CT-2DCSA(COG) experiments was made using ^{13}C-1-α-glycine, and Figure 5.22 show the cross-sections taken through the F_2 isotropic peak of the carbonyl site, together with a simulated static powder pattern (parameters were determined from a static spectrum). The correct form of the powder pattern was obtained using each method and each gives values of δ_{aniso} within ±1 ppm of each other.
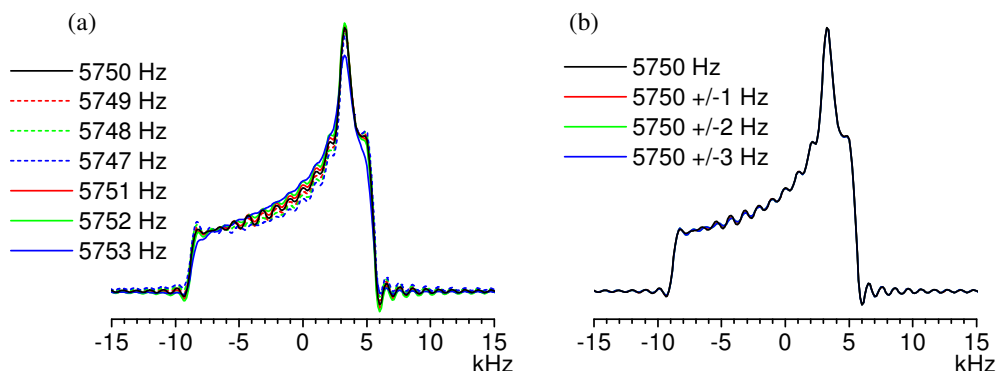
Figure 5.23: The effect of spinning frequency errors. (a) Simulated lineshapes for the CT-2DCSA experiment for a nominal MAS frequency of 5750 Hz used to calculate the pulse times, but a range of actual spinning frequencies. (b) The lineshapes resulting from averaging the lineshapes in (a) for MAS frequency errors up to ± 1 Hz, ± 2 Hz and ± 3 Hz. The simulation parameters used were $j_{total} = 8$, $SW = 32$ kHz, $-\omega_0 \Delta_{CS}/2\pi = -8.8$ kHz and $\eta_{CS} = 0.25$. Ideal π-pulses were assumed in the simulations.

This confirms that both experiments can be performed in practice.

The CT-2DCSA(COG) and OPT-2DCSA(COG) methods give improved sharpness at the edges and peak in the powder pattern lineshape, compared with 2DCSA(COG) for the carbonyl ^{13}C site in glycine. The difference in the results of the CT-2DCSA(COG) and OPT-2DCSA(COG) experiments is rather small, probably because the ^{13}C–^{1}H dipolar coupling is quite small for the carbonyl carbon in glycine.

The CT-2DCSA experiment involves relatively small changes in the pulse timings on consecutive t_1^{eff} increments, typically of the order of 100th of a rotor period. For this reason, sensitivity to instability of the MAS may be expected. This effect was investigated using numerical simulations of the CT-2DCSA experiment with $j_{total} = 8$ and an F_1 spectral width of $SW = 32$ kHz. A nominal MAS frequency of $\omega_r/2\pi = 5750$ Hz was used to calculate the pulse timings used in the pulse sequence, and the F_1 lineshape when the actual spinning frequency deviated from this value was calculated. The resulting lineshapes are presented in Figure 5.23(a), and show some variation in the lineshape due to MAS frequency errors. Figure 5.23(b) shows the lineshapes resulting from averaging the FIDs for errors of $(0, \pm 1)$ Hz, $(0, \pm 1, \pm 2)$ Hz and $(0, \pm 1, \pm 3)$ Hz in the MAS frequency. The four lineshapes in Figure 5.23(b) are nearly identical and indicate that, provided the MAS is stabilised to within ± 3 Hz of the nominal spinning frequency, the effect of MAS instability will be negligible.

Fumaric acid monoethyl ester was used to test these experiments with a more complex sample, and the results are summarised in Figure 5.24 on page 144. For all six

Site	OPT-2DCSA	CT-2DCSA		Site	OPT-2DCSA	CT-2DCSA
(a)	14±1 ppm	14.0±1 ppm		(a)	0.35±0.05	0.34±0.05
(b)	-42±2 ppm	-43±2 ppm		(b)	0.72±0.03	0.73±0.03
(c)	100±2 ppm	99±2 ppm		(c)	0.73±0.03	0.71±0.03
(d)	105±2 ppm	105±2 ppm		(d)	0.71±0.03	0.71±0.03
(e)	88±2 ppm	88±2 ppm		(e)	0.24±0.03	0.24±0.03
(f)	69±2 ppm	-68±2 ppm		(f)	1.00±0.03	1.00±0.03

(a) δ_{aniso} values.   (b) η_{CS} values.

Table 5.2: Comparison of the best fit δ_{aniso} and η_{CS} values for the six ^{13}C sites of fumaric acid monoethyl ester from the results in Figures 5.24 using CT-2DCSA and OPT-2DCSA. Error estimates are based on adjusting the best fit parameters until visible deviation of the simulated lineshape from the experimental result is seen.

^{13}C sites in this molecule there is a clear advantage in using the modified versions 2DCSA. The improvement upon the 2DCSA(COG) experiment is especially noticeable in Figure 5.24(b), which corresponds to the CH$_2$ site that suffers particularly seriously from the effect of ^{13}C–^{1}H dipolar coupling, and is very broad in both the SUPER(COG) and 2DCSA(COG) experiments. A lower signal-to-noise ratio is evident for the constant-time implementation, but compensating for this is the very well-defined powder patterns that are obtained. There are no obvious baseline artefacts present in the results obtained using the OPT-2DCSA(COG) experiment, despite the stepped exponential decay of the signal, and the powder pattern lineshapes compare favourably with those obtained using 2DCSA(COG).

Simulated powder patterns were calculated using SIMPSON,[39] based on a static sample model, and the number of simulated data points and the spectral width was the same as recorded experimentally. Linebroadening was not used for any of the spectra shown, and small truncation artefacts can be seen in the cross-sections, although these do not obscure the edges of the powder patterns. The simulated lineshapes shown in Figure 5.24 are lineshapes fitted to the CT-2DCSA(COG) results (optimising δ_{aniso} and η_{CS}). Fitting was performed using the Simplex method implemented in the SIMPSON program and the best fit parameters are shown in Table 5.2. The fitted CSA parameters are consistent with those determined using the CSA-amplified PASS experiment in Section 4.4, to within 2 ppm and 0.05 for the values of δ_{aniso} and η_{CS} respectively.

There is, however, a slight deviation of the experimental lineshapes from the simulated static patterns for the sites with large δ_{aniso} values. This arises because the contribution to the isotropic peak in the directly observed dimension is not the same for all crystallites. This effect is shown for site (e) in Figure 5.25(a) on page 145, where the cross-section
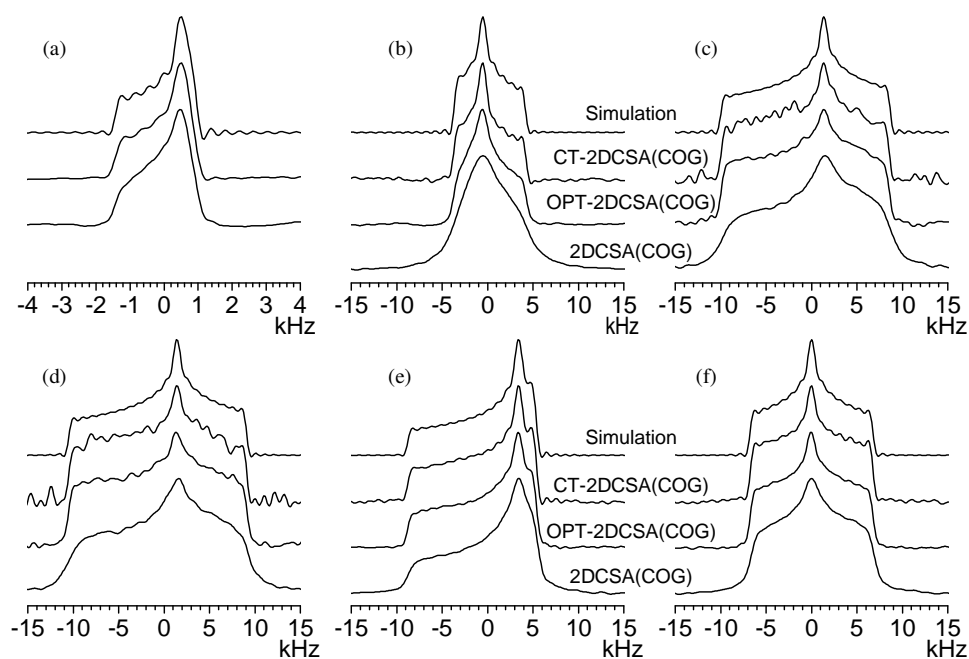
Figure 5.24: F_1 cross-sections of the six carbon sites of fumaric acid monoethyl ester for the 2DCSA(COG), OPT-2DCSA(COG) and CT-2DCSA(COG) experiments, and the corresponding simulated static powder patterns. The labelling scheme for the ^{13}C sites was given in Figure 5.17. For site (a) the spinning frequency used was 2350 Hz with a spectral width of 13 kHz in the indirectly observed dimension. For sites (b)-(f) the spinning frequency used was 5750 Hz with a spectral width of 32 kHz. In both cases, $j_{total} = 8$. For the 2DCSA(COG) experiment a 206 step phase cycle was used, selecting at most one unwanted pathway signature.
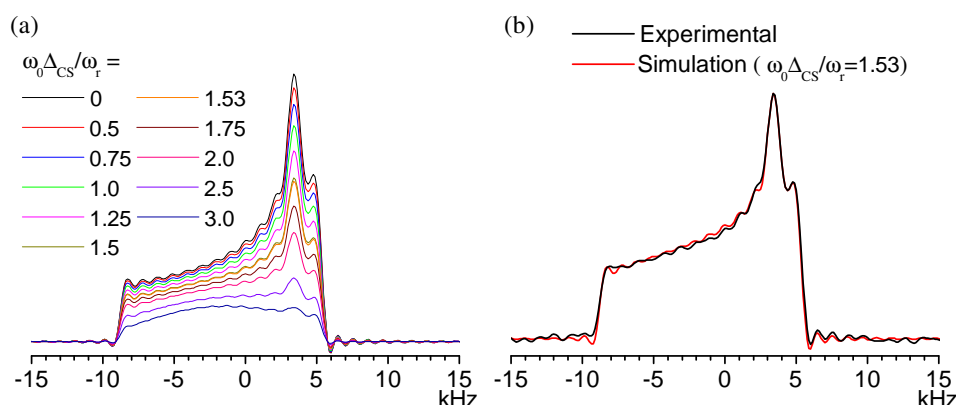
Figure 5.25: (a) Simulated cross-sections taken through the isotropic peak in the F_2 dimension of the CT-2DCSA(COG) spectrum for a range of spinning frequencies, using $-\omega_0\Delta_{CS}/2\pi = -8.8$ kHz and $\eta_{CS} = 0.25$, for site (e) of fumaric acid monoethyl ester. (b) Comparison of the experimental and simulated cross-section for site (e) of fumaric acid monoethyl ester at 5750 Hz MAS.

through the F_2 isotropic peak was calculated for a range of spinning frequencies using the FORTRAN-77 program described at the end of this chapter. The edges and peak of the powder pattern remain well defined, even though the overall lineshape is affected as the spinning frequency is reduced. The experimental cross-section for site (e) in fumaric acid monoethyl ester fits precisely with the calculated F_2 isotropic peak cross-section for the experimental spinning frequency used, shown in Figure 5.25(b), further emphasising the stability and robustness of the experiment. As mentioned previously, the projection onto the F_1 axis could be calculated, and would have the usual static powder pattern lineshape but a lower signal-to-noise ratio than the cross-section.

Further experimental examples are shown in Figure 5.26 on the next page. The cross-section for hexamethyl benzene in Figure 5.26(a) shows truncation artefacts when using CT-2DCSA(COG) because of the small asymmetry and limited number of t_1 data points. These artefacts can, of course, be removed by apodization. More than 32 data points were not recorded using the CT-2DCSA(COG) experiment because the π-pulse sequence becomes very long and may be unstable. Fifty t_1 data points were recorded using OPT-2DCSA(COG) and in this case the truncation artefacts do not appear. Figure 5.26(b) shows the ^{13}C carbonyl site of L-histidine monohydrochloride monohydrate, and Figure 5.26(c) gives an example of measuring powder patterns with relatively small δ_{aniso} values for the two CH_3 sites of the dipeptide Ala-Ala.
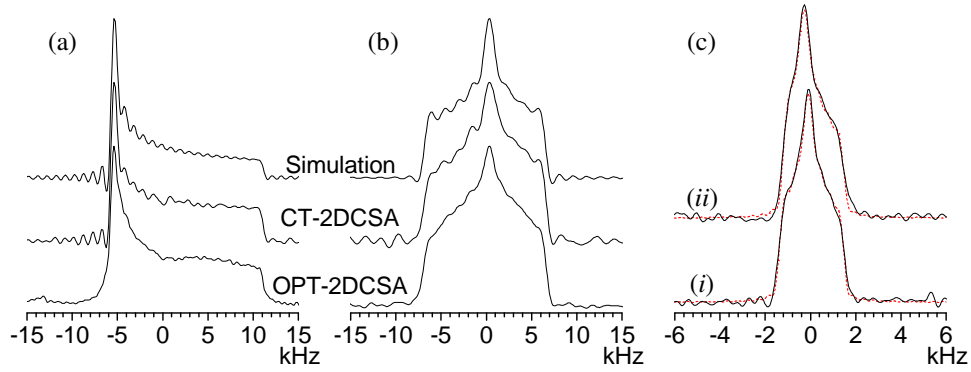
Figure 5.26: Experimental results for (a) the sp^2 site in hexamethyl benzene and simulated powder pattern using $\delta_{\text{aniso}} = -111$ ppm, $\eta_{\text{CS}} = 0$[170] and (b) the carbonyl carbon of histidine monohydrochloride monohydrate $\delta_{\text{ansio}} = 68$ ppm, $\eta_{\text{CS}} = 0.9$, both recorded at a spinning frequency of 5750 Hz, $SW = 32$ kHz and $j_{\text{total}} = 8$. (c) Powder patterns for the two CH$_3$ ^{13}C sites of Ala-Ala at (*i*) 18 ppm and (*ii*) 19 ppm, recorded using CT-2DCSA(COG) with $\omega_{\text{r}} = 3150$ Hz, $SW = 14$ kHz and $j_{\text{total}} = 10$. The red lines show simulated best fits with (*i*) $\delta_{\text{aniso}} = -14.8$ ppm, $\eta_{\text{CS}} = 0.86$ and (*ii*) $\delta_{\text{aniso}} = -14.9$ ppm, $\eta_{\text{CS}} = 0.63$.

5.5 Inclusion of spinning sideband suppression

In 2DCSA and SUPER spectra, if the spinning frequency does not significantly exceed $|\omega_0 \Delta_{\text{CS}}|$ for all nuclei in the sample, spinning sidebands are present in the F_2 dimension of the spectrum. Spinning sidebands may overlap with the isotropic peak of another nuclear environment, so it may be desirable to suppress them. This can be achieved using the *To*tal *S*uppression of *S*pinning *S*idebands (TOSS) method.[200, 220]

In its usual form, TOSS is a technique that, in effect, removes spinning sidebands from a one-dimensional spectrum. This is useful for simplifying MAS spectra containing many spinning sidebands. An example is shown in Figure 5.27(a).

A series of rotor-synchronised π-pulses, typically four or five, are applied prior to detection of the NMR signal, Figure 5.27(b). The experiment is therefore very similar to 2D-PASS and the analysis of the experiment follows the same lines detailed in Section 4.2. The propagator of the density operator is factored into two parts, $\hat{U} = \hat{U}_{\text{RF}}\hat{U}^*$. A five π-pulse sequence is assumed here, so the RF propagator at the end of the TOSS sequence is $\hat{U}_{\text{RF}}(\tau_{\text{seq}}) = \exp(-\text{i}5\pi\hat{I}_x)$. In contrast to the 2D-PASS experiment, the π-pulse timings are chosen so that the interaction-frame first-order average Hamiltonian is[220]

$$\frac{1}{\tau_{\text{seq}}} \int_0^{\tau_{\text{seq}}} \hat{\mathcal{H}}_{\text{CS}}^*(t')\text{d}t' = -\frac{1}{\tau_{\text{seq}}}\Phi(\tau_{\text{seq}}; \Omega_{\text{PR}})\hat{I}_z \,, \tag{5.31}$$

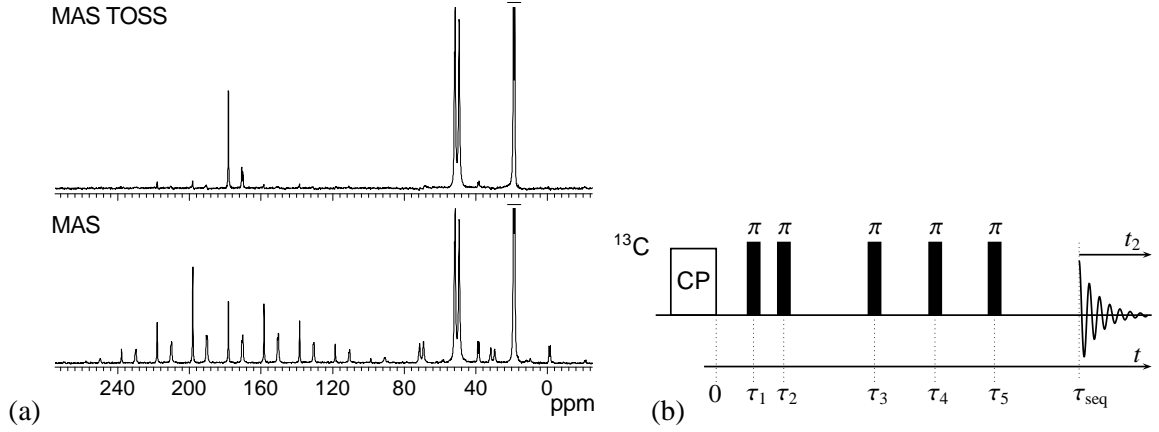where $\Phi(\tau_{\text{seq}}; \Omega_{\text{PR}})$ was defined in Equation (4.8) on page 79. If this condition is fulfilled,

Figure 5.27: (a) Example of ^{13}C NMR spectra recorded with, and without, the TOSS sequence prior to signal detection. The sample was Ala-Ala, using a MAS spinning frequency of 2000 Hz. The small distortions in the baseline of the TOSS spectrum where spinning sidebands 'should' occur are caused by pulse imperfections. (b) The 5-pulse TOSS sequence with initial CP step, showing only the sequence on the observed channel.

the propagator of the rotating-frame density operator over the TOSS sequence is

$$\hat{U}_{\text{TOSS}}(\tau_{\text{seq}}) = \exp\left[-\text{i}5\pi\hat{I}_x\right]\exp\left[\text{i}\Phi(\tau_{\text{seq}};\Omega_{\text{PR}})\hat{I}_z\right]. \tag{5.32}$$

For an initial rotating-frame density operator (after CP) $\hat{\rho}(0) = \frac{1}{2}\left(\hat{I}_+ + \hat{I}_-\right)$, the measured signal is proportional to $\overline{\langle\hat{I}_+\rangle}$ and is calculated by

$$s(\tau_{\text{seq}}, t_2; \Omega_{\text{PR}}) = \text{Tr}\left[\hat{U}_{\text{MAS}}(t_2 + \tau_{\text{seq}}, \tau_{\text{seq}})\hat{U}_{\text{TOSS}}(\tau_{\text{seq}})\hat{\rho}(0)\hat{U}_{\text{TOSS}}^{-1}(\tau_{\text{seq}})\hat{U}_{\text{MAS}}^{-1}(t_2 + \tau_{\text{seq}}, \tau_{\text{seq}})\hat{I}_+\right],$$
$$\tag{5.33}$$

where proportionality constants have been omitted for convenience, and $\hat{U}_{\text{MAS}}(t_2 + \tau_{\text{seq}}, \tau_{\text{seq}})$ is the propagator describing time-evolution of the rotating-frame density operator during MAS, which from Equation (4.10) on page 79 is

$$\hat{U}_{\text{MAS}}(t_2 + \tau_{\text{seq}}, \tau_{\text{seq}}) = \exp\left\{-\text{i}\left(\omega_{\text{iso}}t_2 + \Phi(t_2 + \tau_{\text{seq}};\Omega_{\text{PR}}) - \Phi(\tau_{\text{seq}};\Omega_{\text{PR}})\right)\hat{I}_z\right\}. \tag{5.34}$$

So the detected signal after TOSS is

$$s(\tau_{\text{seq}}, t_2; \Omega_{\text{PR}}) = \frac{1}{2}\overbrace{e^{\text{i}\Phi(\tau_{\text{seq}};\Omega_{\text{PR}})}}^{\text{TOSS}}\overbrace{e^{\text{i}\omega_{\text{iso}}t_2}e^{-\text{i}\Phi(\tau_{\text{seq}};\Omega_{\text{PR}})}e^{\text{i}\Phi(t_2;\Omega_{\text{PR}})}}^{t_2 \text{ MAS}} \tag{5.35}$$

$$= \frac{1}{2}e^{\text{i}\omega_{\text{iso}}t_2}e^{\text{i}\Phi(t_2;\Omega_{\text{PR}})}$$

$$= \frac{1}{2}e^{\text{i}\omega_{\text{iso}}t_2}\sum_{k=-\infty}^{+\infty}F_k e^{\text{i}k\gamma}e^{\text{i}k\omega_{\text{r}}t_2}. \tag{5.36}$$

In Equation (5.35), the origin of different terms is indicated by the braces, and the Fourier

expansion of the $e^{i\Phi(t_2;\Omega_{PR})}$ function has been used to obtain Equation (5.36), as defined in Equation (4.13) on page 80. The Euler angles $\Omega_{PR} = \{\alpha, \beta, \gamma\}$ relate the chemical shift PAF to the rotor frame (the PR subscripts of α, β, γ have been dropped for convenience). For a powder sample with a uniform distribution of crystallites over all possible γ values for each (α, β) pair, it is appropriate to integrate $s(\tau_{seq}, t_2; \Omega_{PR})$ with respect to γ over its range 0 to 2π, leading to the 'γ-averaged' signal

$$\overline{s(\tau_{seq}, t_2; \alpha, \beta)} = \frac{1}{2\pi} \int_0^{2\pi} s(\tau_{seq}, t_2; \alpha, \beta) d\gamma = \frac{1}{2} F_0 e^{i\omega_{iso}t_2}. \tag{5.37}$$

Therefore the spinning sidebands from crystallites with different γ orientations sum to zero and only the isotropic peak remains in the spectrum. This justifies the choice for the form of the first-order average Hamiltonian in Equation (5.31).

Turning now to consider the signal resulting from an experiment where 2DCSA or SUPER recoupling is followed by the TOSS sequence, the signal (assuming here that $\xi = 0$) is described by

$$s(t_1, \tau_{seq}, t_2; \Omega_{PR}) = \frac{1}{2} \overbrace{e^{-i(C_1'(\Omega_{PR}) + C_2'(\Omega_{PR}))\chi t_1}}^{\text{2DCSA}} \overbrace{e^{i\Phi(t_1 + \tau_{seq}; \Omega_{PR})}}^{\text{TOSS}} \overbrace{e^{-i\Phi(t_1 + \tau_{seq}; \Omega_{PR})} e^{i\omega_{iso}t_2} e^{i\Phi(t_1 + \tau_{seq} + t_2; \Omega_{PR})}}^{t_2 \text{ MAS}}$$

$$= \frac{1}{2} e^{-i(C_1'(\Omega_{PR}) + C_2'(\Omega_{PR}))\chi t_1} e^{i\Phi(t_1 + \tau_{seq} + t_2; \Omega_{PR})} e^{i\omega_{iso}t_2}$$

$$= \frac{1}{2} e^{-i(C_1'(\Omega_{PR}) + C_2'(\Omega_{PR}))\chi t_1} e^{i\omega_{iso}t_2} \sum_k F_k e^{ik(\omega_r(t_1 + \tau_{seq}) + \gamma)} e^{ik\omega_r t_2}. \tag{5.38}$$

The $e^{-i(C_1'(\Omega_{PR}) + C_2'(\Omega_{PR}))\chi t_1}$ factor depends upon γ, and so integration of the signal $s(t_1, \tau_{seq}, t_2; \Omega_{PR})$ with respect to the γ crystallite orientation, as used to obtain Equation (5.37), does not lead to the removal of spinning sidebands in the F_2 dimension. Instead, an alternative method must be used.

The method proposed by Schmidt-Rohr[222] introduces a z-filter of duration Δ between the recoupling and TOSS sequences. The experiment is performed N_{TOSS} times, with the z-filter time Δ incremented according to

$$\Delta(n) = \Delta_0 + \frac{n2\pi}{\omega_r N_{TOSS}} \qquad n = 0, 1, \ldots, N_{TOSS} - 1, \tag{5.39}$$

where Δ_0 is the minimum time period Δ. This is shown below to suppress spinning sidebands with order less than N_{TOSS}. Using this approach, amplitude-modulated datasets are recorded and (assuming cosine modulation) the signal in Equation (5.38) is rewritten

to include the *z*-filter

$$
\begin{aligned}
s(t_1, \tau_{\text{seq}}, n, t_2; \Omega_{\text{PR}}) = {} & \frac{1}{2} \overbrace{\cos\left((C_1'(\Omega_{\text{PR}}) + C_2'(\Omega_{\text{PR}}))\chi t_1\right)}^{\text{2DCSA}} \\
& \times \overbrace{e^{i\Phi(t_1+\Delta+\tau_{\text{seq}};\Omega_{\text{PR}})}}^{\text{TOSS}} \overbrace{e^{-i\Phi(t_1+\Delta+\tau_{\text{seq}};\Omega_{\text{PR}})} e^{i\omega_{\text{iso}}t_2} e^{i\Phi(t_1+\Delta+\tau_{\text{seq}}+t_2;\Omega_{\text{PR}})}}^{t_2 \text{ MAS}} \\
= {} & \frac{1}{2} \cos\left((C_1'(\Omega_{\text{PR}}) + C_2'(\Omega_{\text{PR}}))\chi t_1\right) e^{i\omega_{\text{iso}}t_2} e^{i\Phi(t_1+\Delta+\tau_{\text{seq}}+t_2;\Omega_{\text{PR}})} \\
= {} & \frac{1}{2} \cos\left([C_1'(\Omega_{\text{PR}}) + C_2'(\Omega_{\text{PR}})]\chi t_1\right) e^{i\omega_{\text{iso}}t_2} \\
& \times \sum_k F_k \exp\left\{ik\left(\omega_{\text{r}}(t_1 + \tau_{\text{seq}} + \Delta_0) + \gamma + \frac{n2\pi}{N_{\text{TOSS}}}\right)\right\} \exp\left[ik\omega_{\text{r}}t_2\right].
\end{aligned}
$$

(5.40)

The signals from the N_{TOSS} experiments are summed, so it is necessary to evaluate

$$
\overline{s(t_1, \tau_{\text{seq}}, n, t_2; \Omega_{\text{PR}})} = \sum_{n=0}^{N_{\text{TOSS}}-1} s(t_1, \tau_{\text{seq}}, n, t_2; \Omega_{\text{PR}}).
$$

(5.41)

The only part of $s(t_1, \tau_{\text{seq}}, n, t_2; \Omega_{\text{PR}})$ that depends on n is the $\exp(i2\pi nk/N_{\text{TOSS}})$ factor in the second line of Equation (5.40). Therefore, it is useful to evaluate the follwing summation:

$$
\sum_{n=0}^{N_{\text{TOSS}}-1} \exp\left\{ik\frac{n2\pi}{N_{\text{TOSS}}}\right\} = \sum_{n=0}^{N_{\text{TOSS}}-1} \left\{e^{i2\pi k/N_{\text{TOSS}}}\right\}^n = \frac{1 - \left\{e^{i2\pi k/N_{\text{TOSS}}}\right\}^{N_{\text{TOSS}}}}{1 - e^{i2\pi k/N_{\text{TOSS}}}} = N_{\text{TOSS}}\delta_{k,ZN_{\text{TOSS}}},
$$

(5.42)

were Z is any integer and the Dirac delta function $\delta_{k,ZN_{\text{TOSS}}}$ is equal to one if $k = N_{\text{TOSS}}Z$ and otherwise is zero. Using this result, the summation in Equation (5.41) is

$$
\begin{aligned}
\overline{s(t_1, \tau_{\text{seq}}, n, t_2; \Omega_{\text{PR}})} = {} & \frac{1}{2}N_{\text{TOSS}} \cos\left([C_1'(\Omega_{\text{PR}}) + C_2'(\Omega_{\text{PR}})]\chi t_1\right) e^{i\omega_{\text{iso}}t_2} \\
& \times \sum_k \delta_{k,ZN_{\text{TOSS}}} F_k \exp\left\{ik\left(\omega_{\text{r}}(t_1 + \tau_{\text{seq}} + \Delta_0) + \gamma\right)\right\} \exp\left[ik\omega_{\text{r}}t_2\right].
\end{aligned}
$$

(5.43)

The delta function in the second line of Equation (5.43) causes suppression of spinning sidebands in the F_2 dimension, except for those of order $k = ZN_{\text{TOSS}}$, where Z is any integer number.

This approach to F_2 spinning sideband suppression is easily included in the conventional implementation of 2DCSA and TOSS, as both require amplitude modulated signals

for the States method.[58] This is not the case for the echo anti-echo method used for 2DCSA(COG) and SUPER(COG), so the $\sqrt{2}$ signal-to-noise advantage would have to be surrendered and the t_1 data points would need to be weighted during data processing if the Schmidt-Rohr method were used. Instead, an alternative solution for F_2 sideband suppression is presented here.

Rather than incrementing the duration of a z-filter, the duration of the TOSS sequence (τ_{seq}) is incremented according to the condition

$$\tau_{\text{seq}}(n) = \tau_{\text{seq},0} + \frac{n2\pi}{\omega_{\text{r}}N_{\text{TOSS}}} \qquad n = 0, 1, \ldots, N-1, \tag{5.44}$$

where $\tau_{\text{seq},0}$ is the shortest TOSS sequence used. For exactly the same reason as described for the Schmidt-Rohr method of sideband suppression, this approach suppresses spinning sidebands up the $N_{\text{TOSS}}^{\text{th}}$ order. In using this approach, it must be assumed that transverse relaxation is negligible over one rotor period. This is usually acceptable for most organic solids when using high-power ^{1}H decoupling, and if it is not, then it is unlikely that useful results would be obtained by a two-dimensional recoupling experiment in any case.

The pulse timings in the TOSS sequence are determined using the method demonstrated by Antzutkin and co-workers,[220] which was outlined in Section 4.2.1 for calculating the pulse times for the CSA-amplified PASS experiment. It may be shown that the pulse times in the TOSS sequence must satisfy the conditions:[200, 220]

$$0 = 2\sum_{q=1}^{5}(-1)^{q-1}\cos(m\omega_{\text{r}}\tau_q) - 1 \tag{5.45}$$

$$0 = 2\sum_{q=1}^{5}(-1)^{q-1}\sin(m\omega_{\text{r}}\tau_q) \tag{5.46}$$

$$0 = 2\sum_{q=1}^{5}(-1)^{q-1}\tau_q - \tau_{\text{seq}}, \tag{5.47}$$

with $m = 1$ and $m = 2$. These non-linear simultaneous equations were solved numerically[220] for a range of τ_{seq} values using MuPAD,[210] and pulse timings are plotted in Figure 5.28 on the next page. A convenient ranges of well-spaced pulse timings exists for $0.8 \leq \tau_{\text{seq}}/\tau_{\text{r}} \leq 1.55$ and $2.5 \leq \tau_{\text{seq}}/\tau_{\text{r}} \leq 4$, which can be used to implement the incremented TOSS sequence method of F_2 spinning sideband suppression.

This spinning sideband suppression technique is demonstrated here using the SUPER(COG) experiment for α-glycine. Suppression of the first-order spinning sidebands was per-
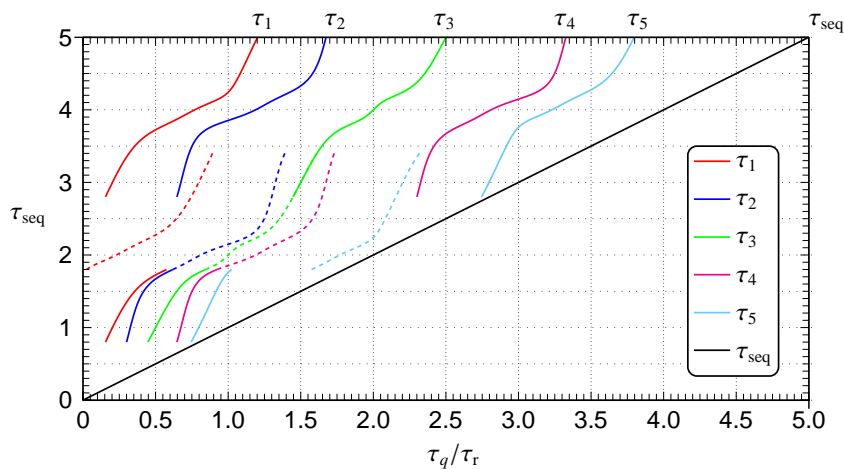
Figure 5.28: A series of pulse timings, τ_q ($q = 1 - 5$), for TOSS sequences as a function of the total sequence length τ_{seq}. Three bands of results are plotted; to differentiate these bands over regions of overlap, the second band is plotted as dashed lines.
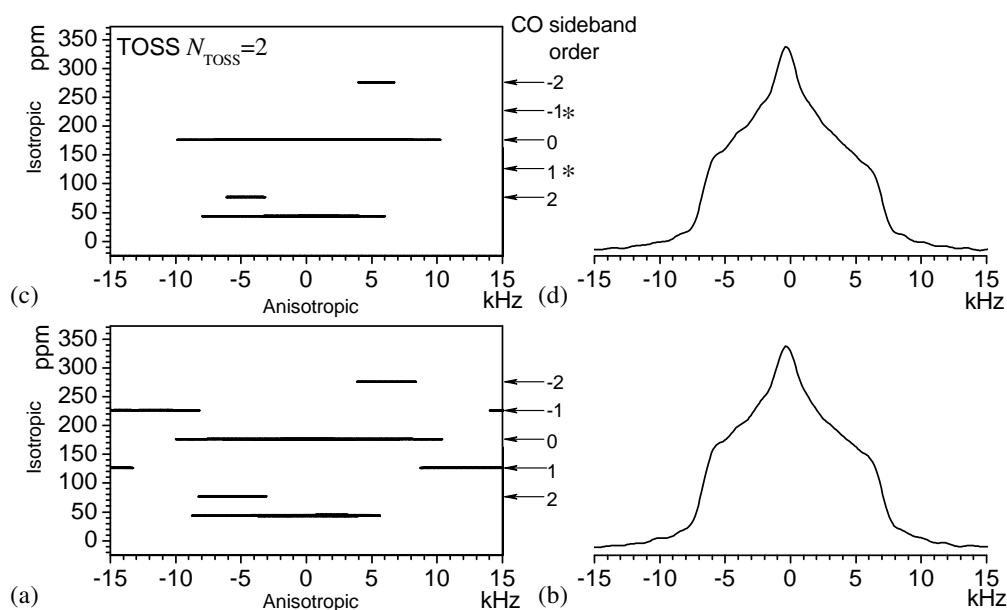

Figure 5.29: SUPER(COG) ^{13}C spectra of α-glycine performed (a) with and (c) without sideband suppression. In (c), only the first-order spinning sidebands in the F_2 dimension were suppressed using $N_{\text{TOSS}} = 2$. The position of the carbonyl spinning sidebands are shown on the right of the spectra, with the suppressed sidebands indicated by asterisks. (b) and (d) show the cross-section taken through the carbonyl F_2 isotropic peak at 176.4 ppm of the spectra in (a) and (c) respectively.

formed with $N_{\mathrm{TOSS}} = 2$ ($\tau_{\mathrm{seq}}/\tau_{\mathrm{r}} = 2.8, 3.3$ for TOSS), and the results are presented in Figure 5.29. No distortions are seen in the cross-section extracted from the two-dimensional spectrum, and the advantages from using the echo anti-echo method have been retained. As for the Schmidt-Rohr method of F_2 spinning sideband suppression, the incremented TOSS sequence approach can be used in any two-dimensional experiment.

Cogwheel phase cycling was adjusted to account for the additional π-pulses used in the TOSS sequence for the experimental results shown in Figure 5.29. For both the Schmidt-Rohr method of sideband suppression and the incremented TOSS version, the phase cycle must be completed for each increment of the z-filter/TOSS sequence, causing an N_{TOSS}-fold increase in the minimum duration of the total experiment.

5.6 Comparing 2DCSA and SUPER experiments

The results using SUPER(COG) and 2DCSA(COG), presented in Section 5.3, showed the line broadening seen in the experimental powder patterns to be smaller for the SUPER(COG) experiment. This difference arise from two sources. First, the phase modulation of the pulses in the SUPER(COG) experiment compensates for pulse length imperfections, whereas no such effect is possible for the π-pulses used in the 2DCSA(COG) experiment (unless composite pulses are used). Second, the ^{13}C–^{1}H recoupling effect that occurs when both the ^{1}H and ^{13}C channels are irradiated simultaneously during the recoupling sequence is quite different. This recoupling effect causes dephasing of the magnetization and hence a loss of signal intensity, and is investigated in the following section.

5.6.1 ^{13}C-^{1}H dipolar coupling during multiple pulse recoupling sequences

The effect on the ^{13}C–^{1}H dipolar coupling during multiple-pulse sequences is concisely treated using an average Hamiltonian approach, proposed by Ishii and co-workers.[189] A similar analysis was used to evaluate the average dipolar Hamiltonian during CP in Section 2.1.2.

When ^{1}H decoupling is used, and a pulse is applied to the ^{13}C channel, the rotating-frame
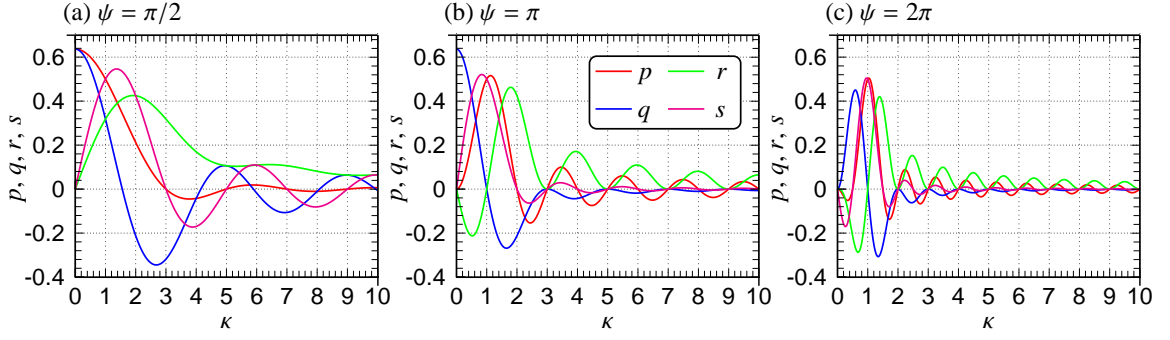
Figure 5.30: Coefficients of Equation (5.49) as functions of the ratio κ of the S-spin to I-spin RF field strength ratio.

Hamiltonian (including only the heteronuclear dipolar coupling internal interaction) is

$$\hat{\mathcal{H}} = b_{IS}(3\cos^2\theta_D - 1)\hat{I}_z\hat{S}_z + \omega_1^I\hat{I}_x + \omega_1^S\hat{S}_x, \tag{5.48}$$

where S is the abundant spin (typically ^{1}H) and I is the rare spin (for example ^{13}C or ^{15}N) and ω_1^S and ω_1^I are their associated RF field strengths. The dipolar coupling constant b_{IS} and θ_D were defined in Section 1.11. Transforming into the interaction frame of the (dominant) $\omega_1^I\hat{I}_x + \omega_1^S\hat{S}_x$ part of this Hamiltonian, the interaction-frame Hamiltonian is

$$
\begin{aligned}
\hat{\mathcal{H}}^* &= \exp\left\{i(\omega_1^I\hat{I}_x + \omega_1^S\hat{S}_x)\right\} b_{IS}(3\cos^2\theta_D - 1)\hat{I}_z\hat{S}_z \exp\left\{-i(\omega_1^I\hat{I}_x + \omega_1^S\hat{S}_x)\right\} \\
&= b_{IS}(3\cos^2\theta_D - 1)\left(\hat{I}_z\cos(\omega_1^I t) + \hat{I}_y\sin(\omega_1^I t)\right)\left(\hat{S}_z\cos(\omega_1^S t) + \hat{S}_y\sin(\omega_1^S t)\right), \tag{5.49}
\end{aligned}
$$

which only contains the heteronuclear-dipolar coupling term. The first-order average Hamiltonian, evaluated in this frame over the duration (τ_p) of the pulse applied to the S nuclei, takes the form[189]

$$\overline{\hat{\mathcal{H}}^{*(1)}} = b_{IS}(3\cos^2\theta_D - 1)\left(p\hat{S}_z\hat{I}_z + q\hat{S}_z\hat{I}_y + r\hat{S}_y\hat{I}_z + s\hat{S}_y\hat{I}_y\right). \tag{5.50}$$

The p, q, r and s coefficients are given by

$$p = \frac{1}{2}\left\{\frac{\sin((1+\kappa)\psi_I)}{(1+\kappa)\psi_I} + \frac{\sin((1-\kappa)\psi_I)}{(1-\kappa)\psi_I}\right\} \tag{5.51}$$

$$q = -\frac{1}{2}\left\{\frac{\cos((1+\kappa)\psi_I) - 1}{(1+\kappa)\psi_I} + \frac{\cos((1-\kappa)\psi_I) - 1}{(1-\kappa)\psi_I}\right\} \tag{5.52}$$

$$r = -\frac{1}{2}\left\{\frac{\cos((1+\kappa)\psi_I) - 1}{(1+\kappa)\psi_I} - \frac{\cos((1-\kappa)\psi_I) - 1}{(1-\kappa)\psi_I}\right\} \tag{5.53}$$

$$s = \frac{1}{2}\left\{\frac{\sin((1-\kappa)\psi_I)}{(1-\kappa)\psi_I} - \frac{\sin((1+\kappa)\psi_I)}{(1+\kappa)\psi_I}\right\}, \tag{5.54}$$

with $\kappa = \omega_1^S/\omega_1^I$ and $\psi_I = \omega_1^I \tau_p$, the latter of which corresponds to the rotation angle caused by the pulse on the I nuclei. The values of the four coefficients p, q, r and s are plotted in Figure 5.30 for a $\pi/2$-, π- and 2π-pulse on the I nuclei. The coefficients are non-zero except for $\kappa = (2Z + 1)$ for π-pulses and $\kappa = 1 + Z$ for 2π-pulses, where Z is a positive integer. Heteronuclear dipolar coupling is recoupled unless all coefficients are zero. This requires that $\kappa = 3$ for a π-pulse applied to the I spin, or $\kappa = 2$ for a 2π-pulse applied to the I spin.

The SUPER experiment uses 2π-pulses rather than the π-pulses used in 2DCSA, so it requires $\kappa = 2$ rather than $\kappa = 3$ in order to decouple the ^{1}H nuclei. That is, SUPER requires a decoupling RF field strength of double that used for the 2π-pulses, whereas 2DCSA needs a decoupling RF field strength of three times the π-pulse RF field strength. Clearly it is easier to achieve this for the SUPER experiment than for 2DCSA.

A series of experiments were performed to assess the extent to which recoupling of the ^{13}C–^{1}H heteronuclear dipolar interaction influences the signal intensity in SUPER and 2DCSA experiments. Eight pulse-sequence units were used in the recoupling sequence before signal detection. For the 2DCSA pulse-sequence unit, the isotropic and anisotropic scaling factors were zero. For the SUPER pulse-sequence units, the pairs of $2\pi_x 2\pi_{-x}$-pulses were centred about $0.25\tau_r$ and $0.75\tau_r$, with a π-pulse inserted between the fourth and fifth pulse-sequence units so that the magnetization from different crystallites was refocused at the start of the signal detection. Cogwheel phase cycling was used in all experiments.

For both the SUPER and 2DCSA pulse sequences, two series of experiments were performed. First, the ^{13}C RF field strength was set to 35 kHz and the ^{1}H decoupling RF field strength varied from 45 kHz up to 110 kHz. Second, the ^{1}H decoupling RF field strength was set to 100 kHz and the ^{13}C RF field strength increased from 35 kHz to 90 kHz. The sample used was α-glycine, and the ^{13}C signal intensities of the CH_2 and carbonyl sites were measured. The results for the 2DCSA and SUPER pulse sequences are in Figures 5.31 and 5.32, respectively.

The most striking feature in these results is the greater signal intensity resulting from the SUPER pulse-sequence under all RF field-strength regimes investigated. The SUPER experiment benefits from both 2π-pulses which have a less demanding decoupling RF field strength requirement, and also the self-compensation for pulse length errors achieved by the $2\pi_x 2\pi_{-x}$-pulses. Both lead to lower signal losses than are seen in the 2DCSA experiment.
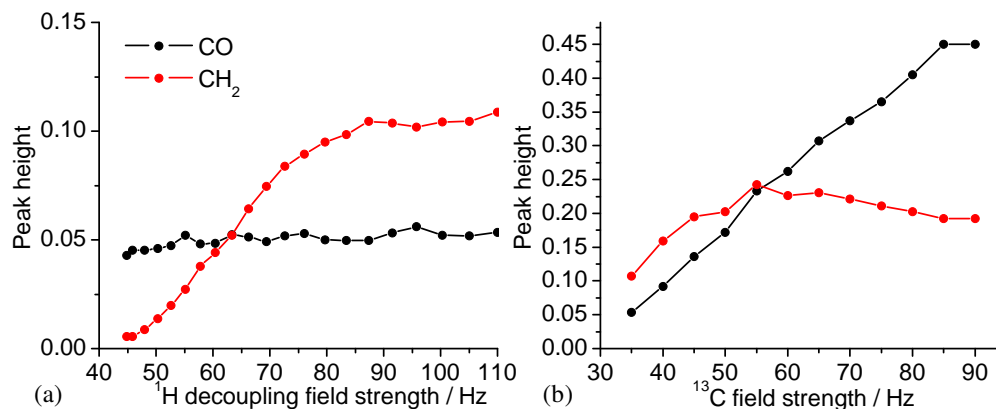
Figure 5.31: Peak heights of the CH_2 and carbonyl ^{13}C signals from α-glycine following 8 (six π-pulse) 2DCSA pulse-sequence units with $\chi = \xi = 0$. (a) The carbon RF field strength was $\omega_1^C/2\pi = 35$ kHz. (b) The proton RF field strength was $\omega_1^H/2\pi = 100$ kHz. Peak heights are normalised to those obtained from a one-dimensional spectrum, which correspond to the peak heights for perfect refocussing of the signals.
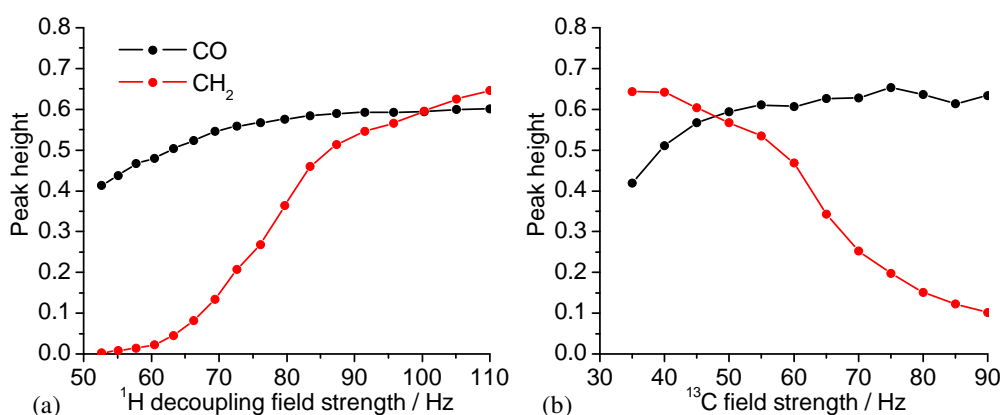

Figure 5.32: Peak heights of the CH_2 and carbonyl ^{13}C signals from α-glycine following 8 SUPER pulse-sequence units. (a) The carbon RF field strength was $\omega_1^C/2\pi = 35$ kHz. (b) The proton RF field strength was $\omega_1^H/2\pi = 100$ kHz. Peak heights are normalised to those obtained from a one-dimensional spectrum, which correspond to the peak heights for perfect refocussing of the signals.

Figure 5.31(a) shows that the glycine carbonyl ^{13}C signal intensity is little affected by the proton decoupling RF field strength used in the 2DCSA experiment, which is expected because this ^{13}C site is not directly-bonded to hydrogen. By contrast, the CH$_2$ has a very strong dependence on the ^{1}H RF field strength. The effect of changing the ^{13}C RF field strength is very different, and the signal intensities of both sites are strongly affected (Figure 5.31(b)). There is an increase in the peak intensity of both the carbonyl and CH$_2$ site with the ^{13}C RF field strength up to 60 kHz; thereafter, only the carbonyl peak intensity increases with the ^{13}C RF field strength. Because the carbonyl site was shown to be little affected by the ^{1}H RF field strength, the most likely cause of this variation is pulse imperfections and finite pulse length effects. The predicted ^{13}C–^{1}H dipolar recoupling suggests that the CH$_2$ signal intensity should decrease as the ratio between the ^{1}H and ^{13}C RF field strengths is reduced, therefore the initial increase is attributed to a reduction in the effects of pulse imperfections. This suggests that hard pulses should always be used for 2DCSA, regardless of the ^{13}C–^{1}H dipolar coupling during the pulses.

These results confirm the prediction that the SUPER experiment experiences less serious ^{13}C–^{1}H dipolar recoupling effects than the 2DCSA experiment. Therefore the SUPER(COG) experiment should be used in preference to 2DCSA(COG), unless the MAS frequency required is too high to be used with SUPER(COG). However, it is worth noting that under the typical experimental conditions used in SUPER(COG) experiments, $\omega_r/2\pi = 5$ kHz and $\chi' = 0.155$, a ^{13}C RF field strength of ≈ 60 kHz is required. Comparing the signal intensities from the SUPER experiment under these conditions with those of the 2DCSA experiment using a ^{13}C RF field strength of ≈ 85 kHz and ^{1}H RF field strength of 100 kHz in both cases, the carbonyl signal is only about 30% greater than for the 2DCSA experiment, whilst the CH$_2$ signal is roughly double. Assuming exponential decay of the signal intensity $s(j)$ as the number of pulse-sequence units j is increased

$$s(j) = s_0 \exp(-j\lambda_{\text{decay}}), \tag{5.55}$$

where s_0 is the signal intensity in a one-dimensional spectrum, the decay constants of the SUPER and 2DCSA experiments under the above conditions are for the CH$_2$ ^{13}C site $\lambda_{\text{decay}}^{\text{2DCSA}} \approx 2\lambda_{\text{decay}}^{\text{SUPER}}$, and for the carbonyl ^{13}C site $\lambda_{\text{decay}}^{\text{2DCSA}} \approx 1.6\lambda_{\text{decay}}^{\text{SUPER}}$. This point is returned to in the next section.
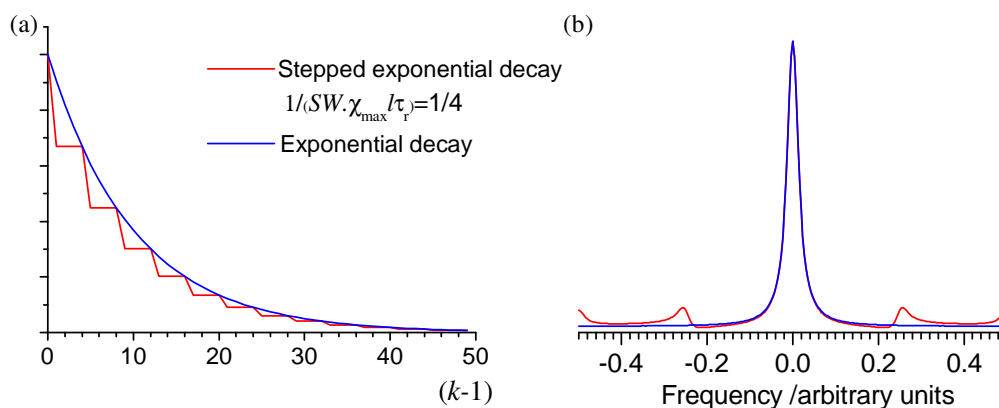
Figure 5.33: (a) A stepped-exponential decay of the form $\exp\{-j(k)\lambda_{\text{decay}}\}$, where $j(k) = \text{Ceil}((k-1)/(SW\chi_{\text{max}}l\tau_{\text{r}}))$ and $(SW\chi_{\text{max}}l\tau_{\text{r}})^{-1} = 1/4$, and an exponential decay of the form $\exp\{-(k-1)\lambda_{\text{decay}}/4\}$. (b) The corresponding Fourier transforms of the functions plotted in (a); the lineshapes have been scaled to have the same maximum height.

5.6.2 Comparison of CT-2DCSA, OPT-2DCSA and SUPER

Comparing the CT-2DCSA(COG) and SUPER(COG) experiments, CT-2DCSA(COG) will always give a lower signal-to-noise ratio than SUPER(COG), because of the less favourable ^{13}C–^{1}H recoupling of the π-pulses. However, the CT-2DCSA(COG) experiment has the advantage of giving the ideal static lineshape in the F_1 domain, because the signal in the indirectly observed dimension does not decay as t_1^{eff} is increased during the experiment. For this reason, if a sufficient signal-to-noise ratio can be ensured, CT-2DCSA is the method of choice for obtaining undistorted powder pattern lineshapes. This is especially valuable if two powder patterns have the same isotropic chemical shift, because separating them requires excellent resolution of the lineshape.

It was concluded in the previous section that SUPER(COG) should be used in preference to 2DCSA(COG). This, however, does not immediately mean the SUPER(COG) should also be used instead of OPT-2DCSA(COG). This is because the number of pulse-sequence units in the recoupling sequence is not increased linearly with t_1^{eff} for OPT-2DCSA(COG). This causes a stepped exponential decay of the t_1^{eff} signals.

When performing the OPT-2DCSA(COG) experiment under with the same spinning spinning frequency and F_1 spectral width as SUPER(COG), for 32 data points in the indirectly observed dimension the number of pulse-sequence units is $j_{\text{max}} \approx 8$. So there is approximately a four-fold reduction in the number of pulse-sequence units used in the recoupling sequence of OPT-2DCSA(COG) compared with SUPER(COG). This means that $(SW\chi_{\text{max}}m\tau_{\text{r}})^{-1} \approx 1/4$, and the stepped-exponential decay of the t_1 signal has the

form shown by the red line in Figure 5.33(a). The blue line overlaid in Figure 5.33(a) is an exponential decay function with a decay constant equal to one-fourth of that used for the stepped exponential. Comparison of their corresponding Fourier transforms show their frequency domain linewidths to be approximately equal.

This observation means that the larger signal decay measured for 2DCSA pulse-sequence unit does not necessarily cause a larger line broadening of the powder patterns from the OPT-2DCSA(COG) experiment, compared with those from using SUPER(COG). If $\lambda_{\text{decay}}^{\text{2DCSA}}$ and $\lambda_{\text{decay}}^{\text{SUPER}}$ describe the decay constants for the two experiments, the OPT-2DCSA spectra will show a smaller line broadening effect than SUPER, provided $\lambda_{\text{decay}}^{\text{2DCSA}} \lesssim 4\lambda_{\text{decay}}^{\text{SUPER}}$. This condition is often fulfilled, even for CH_2 carbon sites.

For example, in Section 5.6.1, the decay constants of the SUPER and 2DCSA experiments were determined for the CH_3 and carbonyl ^{13}C sites of glycine. Using a ^{13}C RF field strength of 60 kHz for SUPER and 85 kHz for 2DCSA and ^1H decoupling RF field strength of 100 kHz, the decay constants are $\lambda_{\text{decay}}^{\text{2DCSA}} \approx 2\lambda_{\text{decay}}^{\text{SUPER}}$ for the CH_2 ^{13}C site, and $\lambda_{\text{decay}}^{\text{2DCSA}} \approx 1.6\lambda_{\text{decay}}^{\text{SUPER}}$ for the carbonyl ^{13}C site. Thus, for both sites the condition that $\lambda_{\text{decay}}^{\text{2DCSA}} \lesssim 4\lambda_{\text{decay}}^{\text{SUPER}}$ is fulfilled. Further support for this analysis is shown by the fumaric acid monoethyl ester spectra shown in Figure 5.34, where the results from SUPER(COG) and OPT-2DCSA(COG) are compared. Less broadened ^{13}C powder pattern lineshapes are seen in the OPT-2DCSA(COG) results for fumaric acid monoethyl ester, compared with the SUPER(COG) measurements. The advantage of OPT-2DCSA is emphasised by results for the methylene ^{13}C site, Figure 5.34(b), which shows significantly less line broadening in the OPT-2DCSA experiment than the SUPER results.

The optimum choice between OPT-2DCSA(COG) and SUPER(COG) in terms of line broadening effects will be sample dependent, but provided cogwheel phase cycling is implemented, both experiments give undistorted powder pattern lineshapes.

5.7   Summary

Cogwheel phase cycling has been shown to improve the robustness of both Tycko's 2DCSA experiment and the SUPER experiment, so that both give reliable and undistorted quasi-static powder patterns. The constant-time implementation of the 2DCSA experiment (CT-2DCSA(COG)) was shown to give the optimum lineshapes for the powder patterns, while the optimised version (OPT-2DCSA(COG)) maximises the signal-to-noise ratio for 2DCSA.
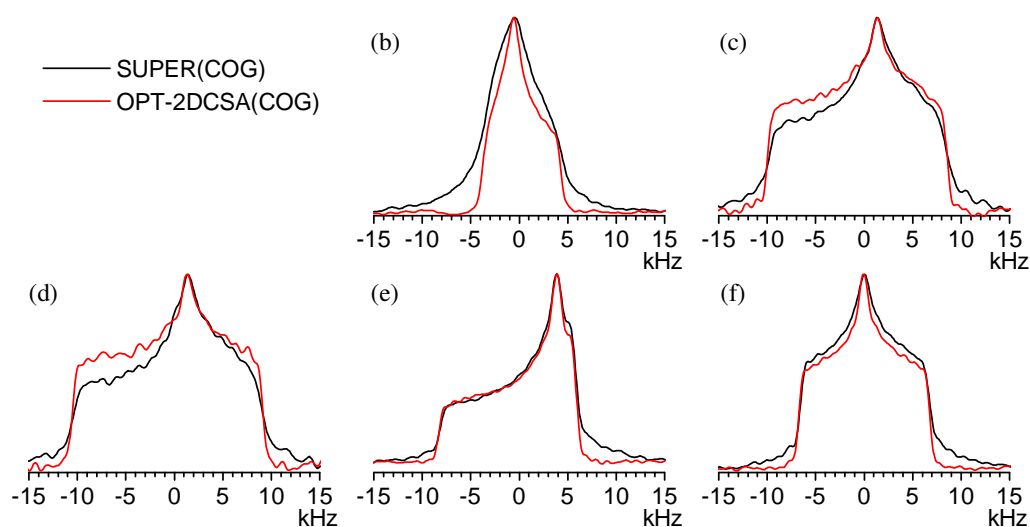
Figure 5.34: F_1 cross-sections from the OPT-2DCSA(COG) and SUPER(COG) ^{13}C spectra of fumaric acid monoethyl ester. Experimental details were given in Figures 5.18 and 5.24, and the labelling scheme for sites (b-f) is in Figure 5.17. The spectra are scaled to have the same maximum height.

All new versions of the experiments developed in this chapter are no more complicated, or time-consuming, to set up than the original implementations and may prove useful for laboratories that do not posses slow spinning or variable-angle spinning hardware for other methods used to measure the chemical shift tensor.

In addition to the experimental results presented in this chapter, these new methods have been applied to a variety of materials, including organic samples such as ^{13}C NMR of paracetamol[223] and inorganic solids such as ^{119}Sn NMR of pyrochlore samples ($Y_2Sn_2O_7$ and $Y_2Ti_{0.4}Sn_{1.6}O_7$) and ^{31}P NMR of AlPO-15.

5.8 Experimental details

All experiments were implemented on a Bruker Avance spectrometer operating at 100.56 MHz for ^{13}C using a 4 mm zirconia rotors and standard spinning hardware that stabilised spinning to within ±2 Hz. Unless otherwise specified in figure captions, TPPM[52] or SPINAL-64[54] ^{1}H decoupling was used with an RF field strength of ∼ 100 kHz, ^{13}C RF field strengths for the π-pulses were ∼ 80 kHz and cross polarization[47] was used with a ramped spin-lock field[50] applied to the ^{1}H channel.

All samples were obtained from Sigma-Aldrich and used without further purification and rotors were packed without restricting the sample volume to the central region.

5.9   Simulation methods

Numerical simulation were performed using the SIMPSON package.[39] To calculate the CSA powder pattern lineshapes, a static powder sample model was used rather than simulation of the complete recoupling pulse sequence, except for the simulations in Figure 5.25. No weighting functions were applied to the calculated FID prior to Fourier transformation, unless otherwise stated. Powder averaging was performed using at least 2000 crystallites, and typically many more were used (up to 28656) following either the REPULSION[72] or ZCW[73] schemes, and in all simulations convergence of the powder averaging was checked as described in Section 2.4 on page 56.

Where the cross-section through the F_2 isotropic peak was calculated, complete simulation of the two-dimensional experiment using SIMPSON is rather time consuming. Instead, a different strategy was adopted. The signal in the two-dimensional experiment is

$$s(t_1, t_2; \Omega_{PR}) \propto \mathrm{e}^{\mathrm{i}(C_1'(\Omega_{PR})+C_2'(\Omega_{PR}))\chi t_1} \mathrm{e}^{-\mathrm{i}\Phi(t_1;\Omega_{PR})} \mathrm{e}^{\mathrm{i}\Phi(t_1+t_2;\Omega_{PR})} \tag{5.56}$$

$$\propto \mathrm{e}^{\mathrm{i}(C_1'(\Omega_{PR})+C_2'(\Omega_{PR}))\chi t_1} \mathrm{e}^{-\mathrm{i}\Phi(0;\Omega_{PR})} \mathrm{e}^{\mathrm{i}\Phi(t_2;\Omega_{PR})}, \tag{5.57}$$

where the knowledge that t_1 is a multiple of rotor periods and the periodicity of $\Phi(t, \Omega_{PR})$ has been used. Using the Fourier expansion of $\exp(\mathrm{i}\Phi(t, \Omega_{PR}))$, as defined in Equation (4.13), the signal is written as

$$s(t_1, t_2; \Omega_{PR}) \propto \mathrm{e}^{\mathrm{i}(C_1'(\Omega_{PR})+C_2'(\Omega_{PR}))\chi t_1} \mathrm{e}^{-\mathrm{i}\Phi(0;\Omega_{PR})} \sum_{k=-\infty}^{+\infty} F_k(\alpha, \beta) \mathrm{e}^{\mathrm{i}k\gamma} \mathrm{e}^{\mathrm{i}k\omega_r t}. \tag{5.58}$$

Thus, the cross-section taken through the isotropic peak in the F_2 dimension is the Fourier transform of:

$$s'(t_1; \Omega_{PR}) \propto \mathrm{e}^{\mathrm{i}(C_1'(\Omega_{PR})+C_2'(\Omega_{PR}))\chi t_1} \mathrm{e}^{-\mathrm{i}\Phi(0;\Omega_{PR})} F_0(\alpha, \beta). \tag{5.59}$$

If the TOSS sequence is also used, then the $\mathrm{e}^{-\mathrm{i}\Phi(0;\Omega_{PR})}$ factor is omitted.

A FORTRAN-77 program was written to calculate the cross-section signal using Equation (5.59), and to perform the appropriate powder averaging. The powder average must be performed over all three Euler angles $\Omega_{PR} = \{\alpha, \beta, \gamma\}$. This is in contrast to static sample simulations, where the crystallite Euler angles relate the principal axis frame to the laboratory frame, and only the α and β angles are involved in the powder average. For convenience, the FORTRAN program is written to produce an output file that is compatible with SIMPSON. The FORTRAN routine can be called, and the output file

read, using standard TCL commands within the SIMPSON input script. This allows all the processing and optimization operations of the SIMPSON package to be utilised. Despite the additional angle dependence in the powder averaging scheme and additional calculation steps involved, the FORTRAN program takes no longer than double the time required by SIMPSON to simulate a static sample, and both are relatively quick, taking only a few seconds.

6

Methods using ^{14}N in solid-state NMR

Despite the high natural abundance of ^{14}N and its ubiquitous presence in biological and pharmaceutical molecules, few studies can be found in the literature that have used this nucleus. This is because ^{14}N is a nucleus with spin-1 and often experiences a large quadrupole coupling with $C_Q/2\pi$ of a few megahertz. This makes direct observation of an ^{14}N signal very difficult for powder samples, and there are few examples of directly observed ^{14}N spectra for samples with large quadrupole couplings. The most successful experiments have been performed by Jakobsen and co-workers,[224] but even in their work the largest quadrupole coupling constants were $C_Q/2\pi \approx 1.2$ MHz.

A ^{14}N nucleus may also affect a spin-1/2 nucleus if there is significant dipolar coupling between the two. Sometimes this effect can be exploited to extract useful information about the nuclear spin interactions present in the spin system, while in other cases the coupling causes an unwanted splitting of peaks in the MAS spectrum, and a reduced signal-to-noise ratio.

In this chapter, a method for removing the splitting and broadening seen in the MAS spectra of ^{13}C nuclei that are dipolar-coupled to ^{14}N spins is demonstrated. This ^{14}N decoupling technique is combined with the CT-2DCSA experiment, developed in Chapter 5, to provide an improved method for determining the relative orientation of the ^{13}C chemical shift tensor and dipolar coupling tensor PAFs in ^{13}C–^{14}N spin pairs. In the final section, a new experiment is proposed for investigating the orientation of the ^{14}N quadrupole tensor PAF with respect to the ^{13}C chemical shift tensor PAF in dipolar-coupled ^{13}C–^{14}N spin pairs.

6.1   Decoupling of ^{14}N in ^{13}C MAS NMR

In solid-state ^{13}C MAS NMR spectra, the asymmetric splitting observed for signals arising from carbon nuclei in ^{13}C-^{14}N spin pairs has been well documented.[225–229] An example is shown in Figure 6.1 on the next page.
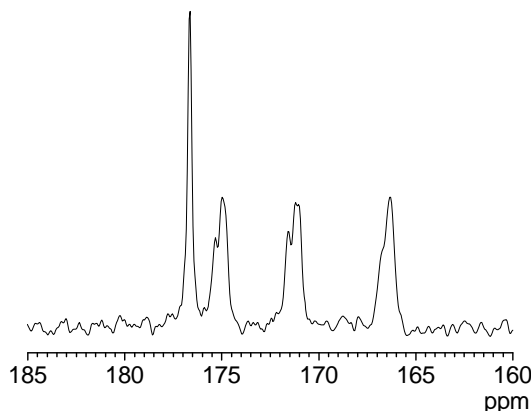
Figure 6.1: The carbonyl region in the ^{13}C MAS spectrum of the short peptide Gly-Pro-Gly-Gly, illustrating the asymmetric splitting and broadening of the peaks caused by a directly bonded ^{14}N nucleus for three amide sites and the non-split signal of the carboxylate ^{13}C site at 176 ppm. The static field strength was 9.4 T.

The effect of a quadrupolar nucleus on an observed dipolar-coupled spin-1/2 nucleus was first reported by VanderHart and Gutowsky[225] for static samples. For the MAS case, various theoretical approaches to analyse this effect have been reported, including a perturbation treatment[230] and an analytical density operator approach.[231] The average Hamiltonian approach is outlined here.[232] The (non-truncated) laboratory-frame Hamiltonian for a ^{13}C–^{14}N spin pair is

$$\hat{\mathcal{H}}_{\text{lab}} = \hat{\mathcal{H}}_Z^C + \hat{\mathcal{H}}_Z^N + \hat{\mathcal{H}}_{CS}^{\text{full,C}} + \hat{\mathcal{H}}_{IS}^{\text{full,CN}} + \hat{\mathcal{H}}_Q^{\text{full,N}}, \tag{6.1}$$

where $\hat{\mathcal{H}}_Z^C$ and $\hat{\mathcal{H}}_Z^N$ are the ^{13}C and ^{14}N Zeeman Hamiltonians, $\hat{\mathcal{H}}_{CS}^{\text{full,C}}$ is the ^{13}C chemical shielding Hamiltonian, $\hat{\mathcal{H}}_{IS}^{\text{full,CN}}$ is the ^{13}C–^{14}N dipolar coupling Hamiltonian, and $\hat{\mathcal{H}}_Q^{\text{full,N}}$ is the ^{14}N quadrupolar coupling Hamiltonian; the superscript 'full' indicates that these are the non-truncated Hamiltonians that were defined in Table 1.1 on page 25. The strategy described in Sections 1.3.1 and 1.9.1 is used to truncate the Hamiltonian in Equation (6.1). First, transformation from the laboratory frame into the interaction frame of the Zeeman Hamiltonian ($\hat{\mathcal{H}}_Z^C + \hat{\mathcal{H}}_Z^N$) is performed using the propagator $\hat{U}_0(t) = \exp\left[-\mathrm{i}\left(\omega_0^N \hat{S}_z + \omega_0^C \hat{I}_z\right)t\right]$, where ^{14}N is the S spin and ^{13}C the I spin with Larmor frequencies ω_0^N and ω_0^C respectively. This interaction frame corresponds to viewing both the I and S spins in their respective rotating frames. The first-order and second-order average Hamiltonians of the interaction-frame Hamiltonian are then calculated. The

interaction-frame Hamiltonian is

$$\tilde{\tilde{\mathcal{H}}}(t) = \exp\left\{i\left(\omega_0^N \hat{S}_z + \omega_0^C \hat{I}_z\right)t\right\}\left(\hat{\mathcal{H}}_{CS}^{full,C} + \hat{\mathcal{H}}_{IS}^{full,CN} + \hat{\mathcal{H}}_Q^{full,N}\right)\exp\left\{-i\left(\omega_0^N \hat{S}_z + \omega_0^C \hat{I}_z\right)t\right\}.$$

(6.2)

The interaction-frame Hamiltonian $\tilde{\tilde{\mathcal{H}}}(t)$ is periodic, such that $\tilde{\tilde{\mathcal{H}}}(t) = \tilde{\tilde{\mathcal{H}}}(t + t_c)$, with the period t_c corresponding to the time at which the rotating frames of both the I and S spins coincide with the laboratory frame, and the average Hamiltonian is evaluated over the duration t_c. The first-order average Hamiltonian of the interaction-frame Hamiltonian in Equation (6.2) contains the truncated ^{13}C chemical shielding, heteronuclear dipolar coupling and (first-order) ^{14}N quadrupolar coupling Hamiltonians, which were defined in Equations (1.78), (1.91) and (1.94) respectively:

$$\overline{\tilde{\tilde{\mathcal{H}}}^{(1)}} = \hat{\mathcal{H}}_{CS}^C + \hat{\mathcal{H}}_{IS} + \hat{\mathcal{H}}_Q.$$

(6.3)

The quadrupolar coupling interaction may be sufficiently large that it is necessary to calculate the second-order average Hamiltonian, which is defined by

$$\overline{\tilde{\tilde{\mathcal{H}}}^{(2)}} = \frac{-i}{2t_c}\int_0^{t_c}dt\int_0^{t'}dt'\left[\tilde{\tilde{\mathcal{H}}}(t),\tilde{\tilde{\mathcal{H}}}(t')\right],$$

(6.4)

The dipolar and chemical shielding interactions are sufficiently small that commutators of these two terms with themselves, or with each other, can be ignored. This leaves the 'cross-term' from the commutator involving the ^{14}N quadrupole coupling and the dipolar coupling Hamiltonian, and the term with the commutator of the quadrupolar coupling Hamiltonian with itself.* The contribution to the second-order average Hamiltonian from the commutator of the quadrupolar Hamiltonian with itself gives the second-order quadrupolar Hamiltonian defined in Equation (1.95); this term does not affect the ^{13}C spectrum obtained from a CP MAS experiment and can be ignored in the present case. Evaluating Equation (6.4) (see Appendix C), it may be shown that the cross-term between the dipolar and quadrupolar coupling term is given by

$$\overline{\tilde{\tilde{\mathcal{H}}}^{(2)}} = -\frac{1}{\omega_0^N}\frac{eQ}{2S(2S-1)\hbar}(D_{xz}^{lab}V_{xz}^{lab} + D_{yz}^{lab}V_{yz}^{lab})\hat{I}_z(3\hat{S}_z^2 - \hat{S}\cdot\hat{S}),$$

(6.5)

where D_{ij}^{lab} and V_{ij}^{lab} are components of the dipolar and quadrupolar interaction tensors expressed in the laboratory frame. Truncation of the Magnus expansion at the second-

---

*If the ^{14}N chemical shielding is included, this also leads to a cross-term with the quadrupole Hamiltonian,[233] but this has no effect on a ^{13}C spectrum recorded in a CP MAS experiment and is ignored here.

order average Hamiltonian is valid provided that the quadrupolar coupling constant C_Q is sufficiently small with respect to the ^{14}N Larmor frequency; this requires that $C_Q/\omega_0^N \lesssim 0.4$,[232] which is the case for most ^{13}C–^{14}N spin pairs in organic solids at intermediate static field strength. Note that the magnitude of the cross-term scales inversely with the Larmor frequency of the quadrupolar nucleus.

For rotating samples, the components of the dipolar and quadrupolar coupling tensors, expressed in the laboratory frame, are constantly changing. The details are not given here (see Appendix C), but it is found that the evolution of the spin system due to the dipolar-quadrupolar cross-term Hamiltonian does not average to zero over one rotor period, and the evolution that occurs depends on the crystallite orientation. This is in contrast to evolution of the spin system due to anisotropic component of the chemical shift and dipolar coupling interactions, which does average to zero. In the fast-MAS limit, the dipolar coupling and CSA interactions are averaged to zero, and the only remaining terms in the rotating-frame Hamiltonian (neglecting the ^{14}N first- and second-order quadrupolar Hamiltonian, as these do not affect the ^{13}C spectrum) are from the isotropic shift and the dipolar-quadrupolar cross-term

$$\hat{\mathcal{H}} = \omega_{\text{iso}}\hat{I}_z + \overline{\tilde{\hat{\mathcal{H}}}_{\text{MAS}}^{(2)}}, \tag{6.6}$$

where $\omega_{\text{iso}}\hat{I}_z$ is the isotropic chemical shift Hamiltonian for ^{13}C and $\overline{\tilde{\hat{\mathcal{H}}}_{\text{MAS}}^{(2)}}$ is the second-order dipolar-quadrupolar cross-term Hamiltonian averaged over one rotor period to give the effective Hamiltonian in the fast-MAS limit. Using a Zeeman product basis (Section 1.4 on page 13), there are six eigenstates of the Zeeman Hamiltonian ($\hat{\mathcal{H}}_Z^C + \hat{\mathcal{H}}_Z^N$), which are denoted $|m_N, m_C\rangle$ with $m_N = +1, 0, -1$ and $m_C = +\frac{1}{2}, -\frac{1}{2}$, where m_N and m_C are the eigenvalues of $\hat{S}_z$ for ^{14}N and $\hat{I}_z$ for ^{13}C respectively. The Zeeman states are also eigenfunctions of the rotating-frame Hamiltonian in Equation (6.6). In the fast-MAS limit, the energies $E(m_N, m_C)$ of the eigenstates (as viewed in the rotating frame) are calculated from

$$E(m_N, m_C) = \langle m_N, m_C | \omega_{\text{iso}}\hat{I}_z + \overline{\tilde{\hat{\mathcal{H}}}_{\text{MAS}}^{(2)}} | m_N, m_C \rangle. \tag{6.7}$$

In Equation (6.7) there is a factor of $\langle m_N, m_C | 3\hat{S}_z^2 - \hat{S} \cdot \hat{S} | m_N, m_C \rangle$ arising from the $\overline{\tilde{\hat{\mathcal{H}}}_{\text{MAS}}^{(2)}}$ term. It is equal to 1, −2 and 1 for $m_N = -1, 0, +1$ respectively, and so the ^{13}C single-quantum transitions between the $|m_N, \frac{1}{2}\rangle$ and $|m_N, -\frac{1}{2}\rangle$ states with $m_N = +1$ and −1 have the same energy. A coherence between two eigenstates of a spin system evolves over time to acquire a phase, which corresponds to a rotation of the coherence in the complex plane at a frequency equal to the energy difference between the two eigenstates (Section 1.3).
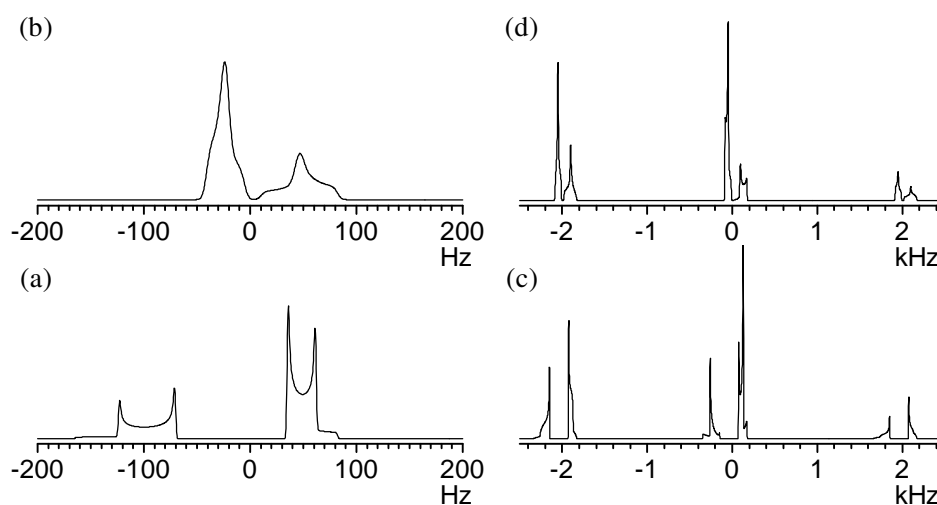
Figure 6.2: Simulated ^{13}C NMR spectra of ^{13}C-^{14}N spin pairs. (a),(b) MAS 10 kHz $\delta_{\text{aniso}} = 0$, $b_{ij}/2\pi = -12$ kHz, $C_Q/2\pi = 1$ MHz, $\eta_Q = 0$, $\omega_0^{\text{N}}/2\pi = 7.29$ MHz: (a) dipolar and quadrupolar PAF both coincident; (b) dipolar PAF related to the quadrupolar PAF by Euler angles $\{0, 90, 0\}$. (c),(d) MAS 2 kHz (central 3 spinning sidebands shown), $-\Delta\omega_{\text{CS}}/2\pi = 6$ kHz, $b_{ij}/2\pi = -12$ kHz, $C_Q/2\pi = 4$ MHz, $\eta_Q = 0$, $\omega_0^{\text{N}}/2\pi = 14.47$ MHz: (c) dipolar, chemical shift and quadrupolar PAFs all coincident; (d) dipolar PAF related to the chemical shift and quadrupolar PAFs by Euler angles $\{0, 90, 0\}$. Exponential line broadening of 6 Hz was applied to the FID to give spectrum (b) and the other three spectra used line broadening of 3 Hz. Powder averaging used 2000 crystallites following the REPULSION scheme.[72]

Thus, the detected (-1)-quantum coherence between the $|m_{\text{N}}, \frac{1}{2}\rangle \longrightarrow |m_{\text{N}}, -\frac{1}{2}\rangle$ states is phase modulated at the same frequency for $m_{\text{N}} = +1$ and -1, but at a different frequency for the ^{13}C (-1)-quantum coherence with $m_{\text{N}} = 0$. consequently, the ^{13}C peak in the fast-MAS spectrum is split into a 2:1 asymmetric doublet. The magnitude of this splitting depends on the crystallite orientation, and therefore a powder sample gives a characteristic powder pattern lineshape.

The lineshapes seen for the ^{13}C isotropic peak and spinning sidebands reflect the relative orientations of the quadrupolar, chemical shielding and dipolar coupling tensor PAFs. For example, simulated lineshapes for ^{13}C–^{14}N spin pairs are presented in Figure 6.2; these were calculated using a purpose-written FORTRAN-77 routine.[†] In principle, at least, these lineshapes can be analysed to determine the relative orientation of the three interaction tensors and their magnitude.[227,229,232] In practice, however, because the splitting in the lineshape scales inversely with the static field strength, at intermediate field strengths (≈ 9.4 T) the lineshape tends to become too narrow for detailed analysis. In addition, the lineshapes are usually significantly broadened by ^{13}C–^{1}H dipolar coupling and detailed features are not resolved (for example, see Figure 6.1). Simulation of the

[†]Simulations included the effect of the ^{13}C chemical shift, ^{13}C–^{14}N dipolar coupling and the second-order dipolar-quadrupolar cross-term Hamiltonians.

experimental lineshape is further complicated by the need to include differential line broadening of the two components in the asymmetric doublet,[232,234] and by the strong interdependence of the fitted dipolar coupling constant b_{IS} and quadrupolar coupling constant C_Q.[166]

Despite being too narrow for detailed analysis, the linewidth of signals from the carbon nuclei in ^{13}C–^{14}N spin pairs are still significantly greater than those of isolated ^{13}C spins, and are typically of the order of 100 Hz when recorded in a static field strength of 9.4 T. This can contribute to lower resolution and much reduced peak heights in the spectra of molecules containing carbon nuclei in near proximity to ^{14}N. For instance, the peak heights of the amide carbon signals in Figure 6.1 are roughly half that of the carboxylate carbon signal. For these reasons it may be helpful to be able to decouple this residual dipolar coupling. A new method for performing this is described in the following sections. First, it is necessary to discuss the effects of RF irradiation upon ^{14}N, in order to understand how decoupling can be achieved.

6.1.1 Radio-frequency irradiation of ^{14}N nuclei

The behaviour of ^{14}N nuclei under RF irradiation is governed by the quadrupolar coupling as well as by the amplitude of the RF field. The magnitude of the quadrupolar coupling experienced by a nucleus depends upon the orientation of the crystallite with respect to the static field, and both single-quantum transitions of ^{14}N are affected by the quadrupolar coupling to first order. The quadrupole coupling constant $C_Q/2\pi$ is often of the order of a 1 MHz or more, while the current NMR probes can only withstand ^{14}N RF field strengths up to $\omega_1^N/2\pi \approx 50$ kHz. Thus, in most samples, the vast majority of crystallites are oriented such that their constituent ^{14}N nuclei have single-quantum transition frequencies that are far away from the RF frequency (compared to the RF field strength), and most ^{14}N nuclei in a static powder sample are little affected by the irradiation.

Nonetheless, under sample spinning conditions the RF irradiation at the Larmor frequency *can* have a significant effect upon the ^{14}N nuclei in a powder sample. During RF irradiation, the rotating-frame Hamiltonian governing an isolated ^{14}N spin system is

$$\hat{\mathcal{H}} = \omega_{\text{iso}}\hat{S}_z + \omega_1^N\hat{S}_x + \frac{\omega_Q}{3}\left(3\hat{S}_z^2 - \hat{S}\cdot\hat{S}\right), \tag{6.8}$$

where the first term in Equation (6.8) is the chemical shift Hamiltonian with isotropic shift ω_{iso}^N and the anisotropic terms of the chemical shift are omitted. The second term
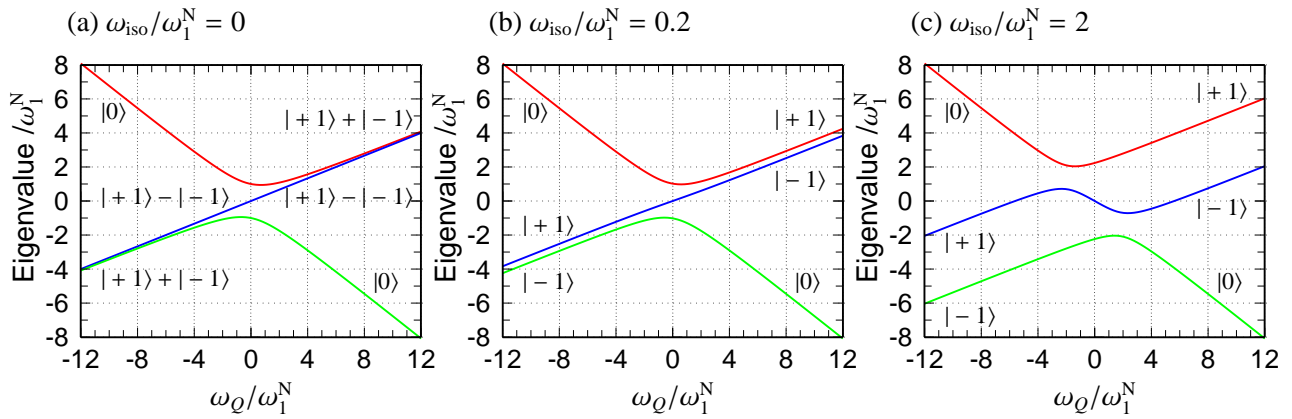
Figure 6.3: Eigenvalues of the Hamiltonian in Equation (6.8) as a function of ω_Q/ω_1^N, for three values of ω_{iso}/ω_1^N. The eigenfunctions in the limits of large $|\omega_Q|$ are shown in each case, although normalisation factors have been omitted.

in Equation (6.8) is the RF Hamiltonian, with RF field amplitude ω_1^N, and the last term is the first-order quadrupole coupling Hamiltonian with ω_Q defined as in Equation (1.97) on page 35. The second-order quadrupolar coupling Hamiltonian has been omitted for simplicity, as its effect is small and does not change the final conclusions. The eigenstates of $\hat{\mathcal{H}}$ can be determined numerically by diagonalizing the matrix representation of the Hamiltonian given in Equation (6.8). In the Zeeman basis (ordered $|+1\rangle$, $|0\rangle$, $|-1\rangle$) the matrix representation of the Hamiltonian in Equation (6.8) is

$$\mathcal{H} = \begin{pmatrix} \omega_Q/3 + \omega_{iso} & 2^{-1/2}\omega_1^N & 0 \\ 2^{-1/2}\omega_1^N & -2\omega_Q/3 & 2^{-1/2}\omega_1^N \\ 0 & 2^{-1/2}\omega_1^N & \omega_Q/3 - \omega_{iso} \end{pmatrix}. \tag{6.9}$$

The eigenvalues of $\hat{\mathcal{H}}$ are plotted as a function of ω_Q/ω_1^N for three offset values, $\omega_{iso}/\omega_1^N = 0, 0.2$, and 2, in Figure 6.3. When $\omega_{iso} = 0$, shown in Figure 6.3(a), in the limit of large values of $|\omega_Q|$, the eigenstates are $|0\rangle$, $2^{-1/2}(|+1\rangle + |-1\rangle)$ and $2^{-1/2}(|+1\rangle - |-1\rangle)$. It may be shown that for $\omega_{iso} = 0$, irradiation of ^{14}N nuclei generates double-quantum coherences if $\omega_Q \gg \omega_1^N$.[235] When $\omega_Q \approx 0$, the eigenstates are described as a linear combinations of all three of the Zeeman functions.

In contrast, for non-zero ω_{iso} values (Figure 6.3(b,c)), in the limit of large values of $|\omega_Q|$, the eigenstates are essentially the Zeeman functions $|+1\rangle$, $|0\rangle$ and $|-1\rangle$. However, in the region where $\omega_Q \approx \pm\omega_{iso}$, the eigenfunctions of $\hat{\mathcal{H}}$ are linear combinations of all three of the Zeeman functions. In the following, it is assumed that ^{14}N RF irradiation is applied with small ω_{iso}/ω_1^N (but not $\omega_{iso}/\omega_1^N = 0$), so that essentially only a single avoided crossing at $\omega_{iso} \approx 0$ is seen, as in Figure 6.3(b) .

Prior to the RF field being switched on, the populations of the ^{14}N Zeeman states are determined by the Boltzmann distribution. When the RF radiation is turned on, the eigenstates of the system are suddenly changed, as shown in Figure 6.3. The populations of the Zeeman states before the RF irradiation determine the populations of each new eigenstate, according to the relative contribution of the Zeeman states to each of the new eigenstates.

Because the sample is rotating, ω_Q is constantly changing. If $|\omega_Q|$ for a nucleus is initially large compared to ω_1^N, and then undergoes a sign change (a 'zero-crossing') before finally returning to a large value, the state of the spin system may change if RF radiation is applied during the zero-crossing. The final state of the spin system depends on how rapidly the zero-crossing occurred, and two limits can be identified: sudden passage and adiabatic passage.

Under sudden passage conditions, the Hamiltonian changes rapidly through the zero-crossing, and a spin in a particular eigenstate $|m_N\rangle$ prior to the zero-crossing remains in the same eigenstate after the crossing; the spin system is unaffected by the zero-crossing and the populations of the eigenstates (and any coherences) are unchanged. In the adiabatic limit, the Hamiltonian changes infinitely slowly, and each eigenstate of the Hamiltonian prior to the zero-crossing transforms into the eigenstate of the Hamiltonian after the zero-crossing that is connected to it by continuity, which means the transformation of each eigenstate to the one connected to it by the same coloured line during the zero-crossing in Figure 6.3.[10] For example, if ω_Q is initially large and negative and undergoes an adiabatic zero-crossing during RF irradiation, the change in eigenstates is $|+1\rangle \longrightarrow |-1\rangle$, $|-1\rangle \longrightarrow |0\rangle$ and $|0\rangle \longrightarrow |+1\rangle$ (for $\omega_{iso} > 0$). For a spin system initially at thermal equilibrium, the effect of an adiabatic zero-crossing during RF irradiation can be interpreted as an adiabatic transfer of populations between Zeeman states.

The condition for the adiabatic limit requires that the duration Δt of the zero-crossing and the smallest energy difference ΔE between the eigenstates must fulfil[10, 236]

$$\alpha = \Delta t \Delta E \gg 1, \tag{6.10}$$

where α is dubbed the adiabatic parameter. Vega has defined a working definition of the adiabaticity parameter for quadrupolar nuclei under spinning conditions and RF irradiation as[236]

$$\alpha = \frac{\left(\omega_1^N\right)^2}{2\omega_Q^{PAF}\omega_r}, \tag{6.11}$$

where ω_r is the spinning frequency and $\omega_Q^{PAF} = 3\pi C_Q/(2I(2I-1))$ is the quadrupolar splitting parameter defined on page 35. Equation (6.11) is based on $\Delta E = \omega_1^N$, and an estimate of the duration for ω_Q changing from ω_1^N to $-\omega_1^N$ to be $\omega_1^N/2\omega_Q^{PAF}\omega_r$. The value of α gives an approximate measure of the degree to which a zero-crossing is adiabatic, but the precise nature of a zero-crossing depends on the crystallite orientation, and near-adiabatic behaviour has been found even for $\alpha \approx 0.4$.[236–238]

Between the sudden and adiabatic limits, in the intermediate regime, partial conversion of the eigenstates to those connected by continuity during the ω_Q zero-crossing, and partial conversion to other wavefunctions that may not be eigenstates of the Hamiltonian in Equation (6.8) occurs.[236,237] For a spin system initially at thermal equilibrium, this causes partial transfer of populations between the Zeeman states and conversion of the initial Zeeman state populations to a variety of coherences. Owing to the large quadrupolar coupling often experienced by ^{14}N nuclei and the relatively low RF field strengths that can be used experimentally, for many experiments involving ^{14}N the ω_Q zero-crossings will occur in the intermediate regime. For example, with the typical experimental parameters $\omega_1^N/2\pi = 20$ kHz, $\omega_r/2\pi = 5$ kHz and $\omega_Q^{PAF}/2\pi = 2$ MHz, the adiabaticity parameter is $\alpha = 0.02$, which is an order of magnitude smaller than that needed to give adiabatic behaviour.

Over one revolution of a powder sample about the magic angle, ω_Q for each crystallite undergoes either two or four zero-crossings. The fraction of crystallites that have undergone zero-crossings as a function of sample rotation can be determined[239] and is plotted in Figure 6.4 on the following page for three values of the quadrupole asymmetry parameter (η_Q). There is little difference between the three plots in Figure 6.4 for the initial portion of the rotor period, with a maximum in the number of single zero-crossings occurring at about one-third of a rotor period. This feature is discussed later.

6.1.2 Pulsed decoupling of residual ^{13}C–^{14}N coupling in MAS NMR

For a ^{13}C–^{14}N spin pair, the rotating-frame Hamiltonian including only terms that affect the evolution of the ^{13}C nuclei (under MAS) can be written as

$$\hat{\mathcal{H}}(t) = \omega(t; \Omega_{PR}^{CS})\hat{I}_z + \omega_D(t; \Omega_{PR}^{IS})\hat{I}_z\hat{S}_z + \omega^{(2)}(t; \Omega_{PR}^{(2)})(3\hat{S}_z^2 - \hat{S}\cdot\hat{S}), \qquad (6.12)$$

where the first term is the chemical shift interaction, the second is the heteronuclear dipolar coupling Hamiltonian and the third is the dipolar-quadrupolar cross-term interaction.
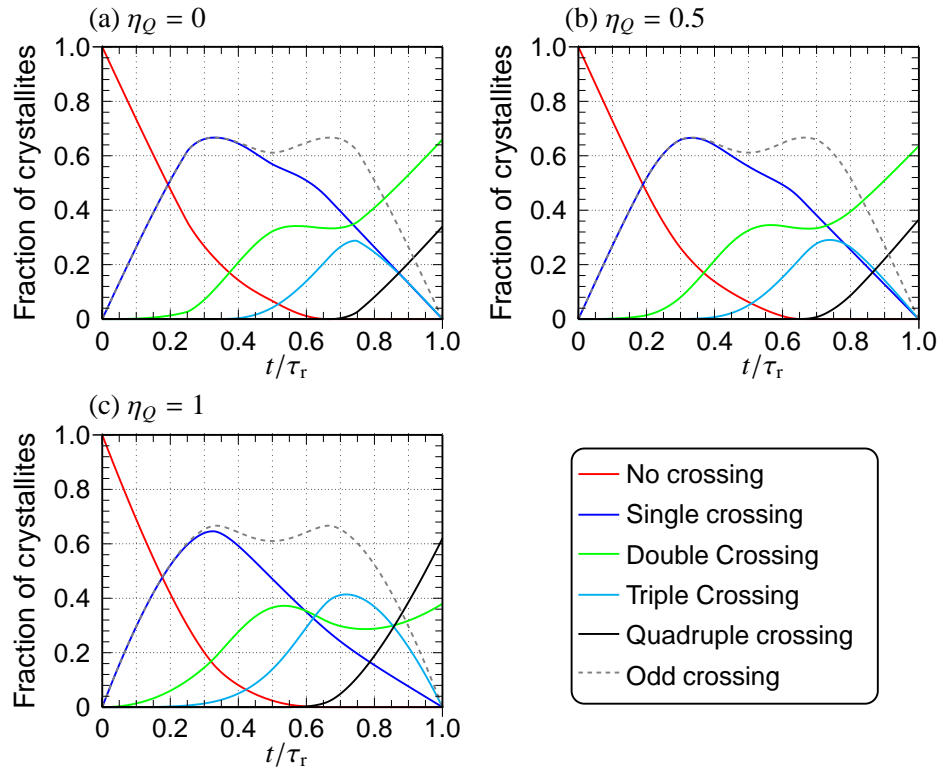
Figure 6.4: The fraction of crystallites that have undergone no zero-crossings, one, two, three and four zero-crossings and an odd number of zero-crossings, as a function of the sample rotation angle. This is shown for three values of η_Q. Averaging over the crystallite orientations was performed using 200 values for α_{PR} and γ_{PR} in uniform steps between $0°$ and $360°$, and 100 values for β_{PR} distributed uniformly between $0°$ and $180°$.

The $\omega(t, \Omega^{\text{CS}}_{\text{PR}})$ factor describes the time dependence of the chemical shift Hamiltonian due to MAS (as defined in Equation (2.8)), and similarly the $\omega_{\text{D}}(t; \Omega^{IS}_{\text{PR}})$ and $\omega^{(2)}(t; \Omega^{(2)}_{\text{PR}})$ factors account for the orientation dependence under MAS of the heteronuclear dipolar coupling and the second-order dipolar-quadrupolar cross-term Hamiltonian respectively.

The ^{13}C (-1)-quantum coherences are phase-modulated at a (time-dependent) frequency $\omega_{\text{tot}}(t; m_{\text{N}})$ equal to the energy difference between the two states $|m_{\text{N}}, -\frac{1}{2}\rangle$ and $|m_{\text{N}}, \frac{1}{2}\rangle$ involved (Section 1.3); for the three ^{13}C (-1)-quantum coherences, these frequencies are

$$m_{\text{N}} = +1 \qquad \omega_{\text{tot}}(t; 1) = \omega(t; \Omega^{\text{CS}}_{\text{PR}}) + \omega_{\text{D}}(t; \Omega^{IS}_{\text{PR}}) + \omega^{(2)}(t; \Omega^{(2)}_{\text{PR}}) \qquad (6.13)$$

$$m_{\text{N}} = 0 \qquad \omega_{\text{tot}}(t; 0) = \omega(t; \Omega^{\text{CS}}_{\text{PR}}) - 2\omega^{(2)}(t; \Omega^{(2)}_{\text{PR}}) \qquad (6.14)$$

$$m_{\text{N}} = -1 \qquad \omega_{\text{tot}}(t; -1) = \omega(t; \Omega^{\text{CS}}_{\text{PR}}) - \omega_{\text{D}}(t; \Omega^{IS}_{\text{PR}}) + \omega^{(2)}(t; \Omega^{(2)}_{\text{PR}}), \qquad (6.15)$$

and the phase $\phi(t; m_{\text{N}})$ of each single-quantum coherence at a time t is given by the integral

$$\phi(t; m_{\text{N}}) = \int_0^t \omega_{\text{tot}}(t'; m_{\text{N}}) \mathrm{d}t'. \qquad (6.16)$$

If a transfer of populations between the ^{14}N Zeeman states occurs, the ^{13}C (-1)-quantum coherences are affected. For example, if the populations of the $m_{\text{N}} = 1$ and $m_{\text{N}} = 0$ ^{14}N Zeeman states are exchanged, the coherences between the $|1, -\frac{1}{2}\rangle$ and $|1, \frac{1}{2}\rangle$ states are converted to coherences between the $|0, -\frac{1}{2}\rangle$ and $|0, \frac{1}{2}\rangle$ states, and vice versa. If this transfer of populations occurs at time t_{a}, the overall phase of the coherence between the $|0, -\frac{1}{2}\rangle$ and $|0, \frac{1}{2}\rangle$ states at a time $t > t_{\text{a}}$ is

$$\phi(t; 0) = \int_0^{t_{\text{a}}} \omega_{\text{tot}}(t'; +1) \mathrm{d}t' + \int_{t_{\text{a}}}^t \omega_{\text{tot}}(t'; 0) \mathrm{d}t'. \qquad (6.17)$$

To decouple the second-order dipolar-quadrupolar cross-term Hamiltonian, the populations of the ^{14}N Zeeman states must be transferred between the ^{14}N Zeeman states sufficiently rapidly that the contribution to the phase acquired by each coherence due to the second-order cross-term averages to zero over a short time period. However, the phase acquired by ^{13}C (-1)-quantum coherences due to evolution under the dipolar coupling term in Equation (6.12) is also affected by changes in the ^{14}N Zeeman state populations, and interferes with the MAS averaging that usually occurs for this term. Consequently it is not obvious that decoupling of ^{14}N should be possible. Nonetheless, this is investigated in the following sections.

The only previous study of ^{14}N decoupling in the literature used the technique of overtone

irradiation.[240] If the quadrupole coupling constant is large, it is possible to directly excite and detect coherences between the ^{14}N $|+1\rangle$ and $|-1\rangle$ Zeeman states in a single quantum process by using overtone RF irradiation at double the ^{14}N Larmor frequency.[241] Overtone decoupling was developed to average the (first-order) dipolar coupling that causes a splitting of the peaks in the ^{13}C NMR spectra of static single crystal samples. Irradiation at the overtone frequency causes transitions between the $|+1\rangle$ and $|-1\rangle$ Zeeman states of ^{14}N. For sufficiently rapid transitions between the two states, the net phase acquired by the detected (-1)-quantum coherences between $|m_N, -\frac{1}{2}\rangle$ and $|m_N, \frac{1}{2}\rangle$ states for $m = +1$ and $m = -1$ is equal to the average of the phases acquired by each coherence in the absence of overtone irradiation. This averages to zero the contribution to the phase acquired by the (-1)-quantum coherence due to the (first-order) dipolar coupling, but not the contribution due to the second-order dipolar-quadrupolar cross-term Hamiltonian. For this reason, overtone irradiation is not a strategy for decoupling the residual dipolar splitting seen in MAS spectra.

It is also noted that a self-decoupling mechanism has been proposed in the literature for ^{13}C–^{14}N spin pairs.[229, 230] The self-decoupling mechanism relies on rapid spin-lattice relaxation of the ^{14}N spin, which means that the nuclei frequently change between the different spin states due to relaxation rather than RF irradiation. This rapid change causes the collapse of the residual spitting of the ^{13}C signal from a ^{13}C–^{14}N spin pair. However, few examples of this effect exist.

The problem of removing the residual splitting in ^{13}C-^{14}N spin pairs is similar to that investigated by Delevoye *et al.* for removing J-coupling between ^{31}P and ^{27}Al nuclei in ^{31}P MAS NMR.[242] In their study, they investigated using continuous RF irradiation to decouple the spin pairs, and found low ^{27}Al RF field strengths for the continuous irradiation to give optimum performance.

Under MAS conditions, the occurrence of two or four zero-crossings of ω_Q over a rotor period, for all ^{14}N nuclei in a powder sample, can allow the RF irradiation to affect all ^{14}N nuclei in the sample. Provided zero-crossings during RF irradiation occur in the intermediate or adiabatic-passage regimes, changes in the populations of all three ^{14}N Zeeman states are expected. This introduces the possibility of averaging the effect of the dipolar-quadrupolar cross-term Hamiltonian on the ^{13}C nuclei under MAS.

The approach investigated here involves applying pulses of length τ_p to the ^{14}N nuclei at a rate of ω_{pulse}, illustrated in Figure 6.5 on the next page, during the acquisition of the ^{13}C FID. Decoupling of ^{1}H nuclei by the usual methods (Section 2.1.3) is also used during
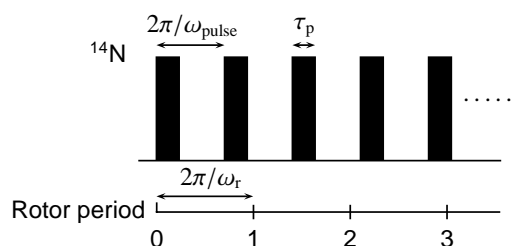
Figure 6.5: Decoupling sequence used for ^{14}N. The duration of the pulses applied to the ^{14}N channel is τ_p, with the rate of pulsing being ω_{pulse} (the pulses start at time points spaced at intervals of $2\pi/\omega_{\mathrm{pulse}}$). ω_r is the spinning frequency.

acquisition.

The motivation for using a train of pulses here, rather than continuous irradiation, was two-fold. First, it is desirable not to irradiate both the ^{1}H and ^{14}N channels of the probe simultaneously for long periods, as this can risk damaging or degrading the probe. Secondly, the magic-angle spinning averaging process (for the first-order dipolar coupling interaction) and zero-crossings of ω_Q during RF irradiation (that are needed to average the residual dipolar splitting) occur on the same time scale. For this reason, significant interference between the two processes is expected. Indeed, this is found experimentally, and it was hoped that by investigating a train of pulses it would be possible to minimise the interference of the two processes by adjusting the timing and duration of pulses used.

The usual techniques for analysing heteronuclear decoupling schemes,[55,56] such as average Hamiltonian theory, cannot readily accommodate the (approximately) adiabatic population transfer process that occurs during ^{14}N irradiation. Further, the complicated time dependence of the RF irradiation, sample rotation and zero-crossings is difficult to treat analytically. For these reasons a detailed theoretical treatment of the ^{14}N decoupling process is not attempted here. Instead, in the following sections, experimental results are presented to illustrate the observed properties of ^{14}N decoupling, and computer simulations are used to investigate the decoupling effect.

6.1.3 Experimental methods

Experiments were performed on a Bruker Avance spectrometer operating at 100.69 MHz for ^{13}C. A commercial Bruker triple resonance probe was used with 4mm zirconia rotors and standard spinning hardware that stabilised the spinning frequency (ω_r) to within ± 2 Hz. SPINAL-64 ^{1}H decoupling[54] was applied with an RF field strength of $\approx$80-90 kHz. The ^{14}N RF field strength was calibrated using the signal from solid ammonium chloride,

and the ^{14}N offset frequency was set to -50 kHz relative to the ^{14}N signal from an aqueous solution of glycine. During signal acquisition, to decouple ^{14}N from the ^{13}C nuclei, pulses of length τ_p and RF field strength ω_1^N were applied to the ^{14}N channel at a rate of ω_{pulse} as detailed in Figure 6.5. The pulses used in the decoupling sequence were alternated in phase following the XY-16 cycle: $(x, y, x, y, y, x, y, x, -x, -y, -x, -y, -y, -x, -y, -x)$,[213] except where stated. All samples were obtained from Sigma-Aldrich and used without further purification.

6.1.4   Experimental results

Figure 6.6 illustrates the typical results that were obtained with pulsed ^{14}N decoupling for the ^{13}C NMR spectra of the peptides Ala-Ala and Gly-Pro-Gly-Gly. The increase in peak heights and reduction in linewidths is dramatic in both cases: for the Gly-Pro-Gly-Gly sample, the enhancement of peak heights of the ^{14}N coupled ^{13}C nuclei is between 80% and 100%. This represents up to a four-fold reduction in the experiment time to achieve a specified signal-to-noise ratio.

Comparison of the spectra recorded with and without ^{14}N irradiation shows a small (uniform) frequency shift of the peaks in the ^{14}N decoupled spectra. The origin of this frequency shift is the Bloch-Siegert effect,[14, 18] caused by the second-order average Hamiltonian of the RF Hamiltonian $\overline{\tilde{\mathcal{H}}}_{BS}^{(2)} = \omega_0^C \left[(\omega_1^N)^2 / \left(\omega_{ref}^2 - (\omega_0^C)^2 \right) \right] \hat{I}_z$ introduced in Section 1.5.2, where ω_{ref} is the RF frequency. The Bloch-Siegert shift is significant in this instance due to the relatively small difference between the frequency of the ^{14}N irradiation ($\omega_{ref} \approx \omega_0^N$) and the ^{13}C Larmor frequency. To ensure accurate chemical shift measurements, a spectrum of a reference sample should be recorded using the same decoupling parameters used in the experiments.

There are three experimental parameters for the ^{14}N decoupling scheme used: the pulse length τ_p, the pulse rate ω_{pulse}, and the ^{14}N RF field strength ω_1^N. In addition, the decoupling efficiency depends on the sample spinning frequency ω_r. The decoupling was found to be independent of the ^{14}N offset frequency, at least within a range of ±100 kHz from the aqueous glycine ^{14}N resonance, and so in contrast to ^{1}H decoupling, careful optimisation of the ^{14}N offset frequency is not necessary.

In this section, experiments to investigate the characteristics of the decoupling effect are presented. The trends in the decoupling efficiency with the experimental parameters were measured by comparison of the peak heights in spectra acquired with and without
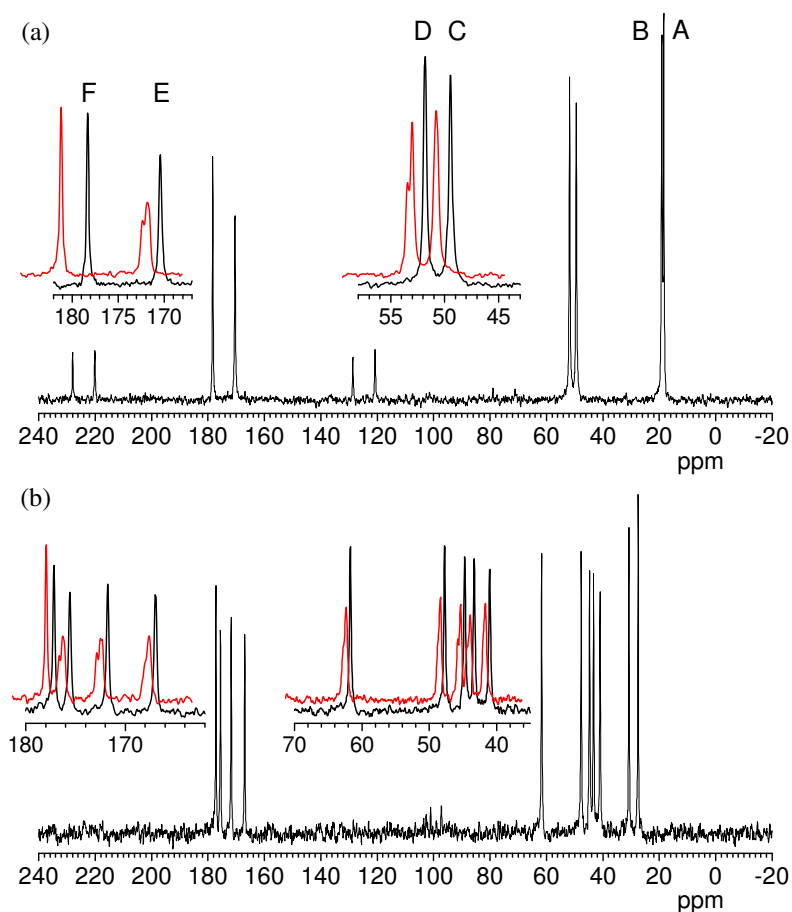
Figure 6.6: (a) The ^{13}C NMR spectra of Ala-Ala recorded with ^{14}N decoupling. Expansions of sites C, D, E and F are shown with the non-decoupled spectra overlaid (and offset for clarity) in red. Decoupling parameters: $\omega_1^N/2\pi = 17$ kHz, $\omega_r/2\pi = 5.0$ kHz, $\omega_{pulse}/2\pi = 5.5$ kHz, $\tau_p = 55$ ms. (b) The ^{13}C NMR spectrum of the peptide Gly-Pro-Gly-Gly. Expansions show the non-decoupled spectra superimposed (and offset for clarity) in red. Decoupling parameters: $\omega_1^N/2\pi = 24$ kHz, $\omega_r = 7.5$ kHz, $\omega_{pulse}/2\pi = 7.0$ kHz, $\tau_p = 60$ ms. The static field strength was 9.4 T.
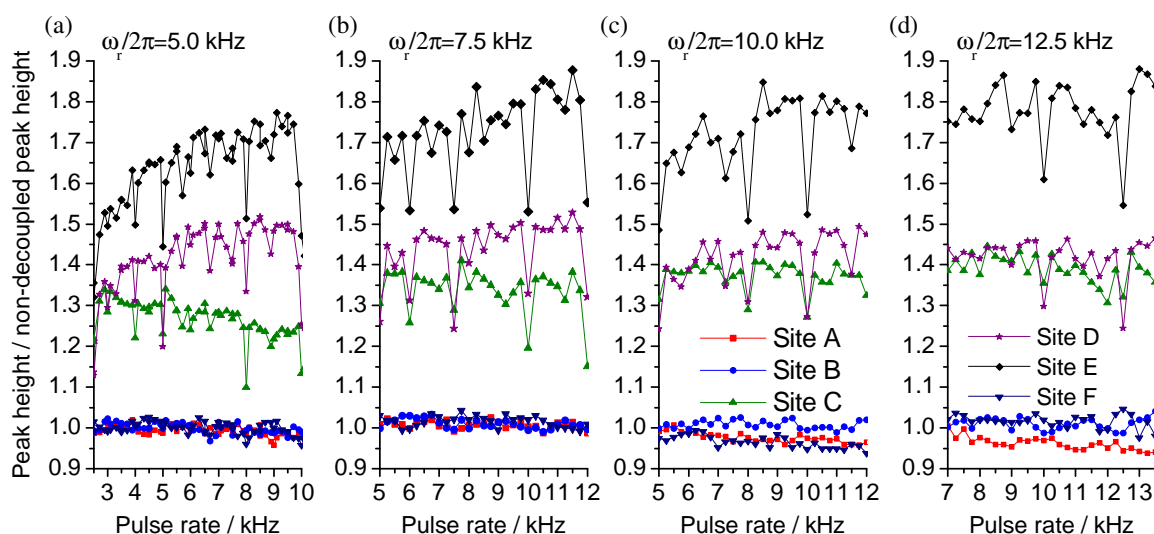
Figure 6.7: Effect of the rate of pulsing ω_{pulse} in the ^{14}N decoupling sequence for the six ^{13}C signals of Ala-Ala at site A: 18 ppm, B: 19 ppm, C: 49 ppm, D: 51.5 ppm, E: 170.5 ppm, F: 178 ppm. In each case the ^{14}N RF field strength $\omega_1^N/2\pi$ was 17 kHz and the pulse length $\tau_p = 40\,\mu$s. Magic-angle spinning frequencies ω_r used are shown in the figure. The static field strength was 9.4 T.

^{14}N decoupling, for the six ^{13}C sites in the dipeptide Ala-Ala. These are labelled in Figure 6.6(a): site A at 18 ppm, site B at 19 ppm, site C at 49 ppm, site D at 51.5 ppm, site E at 170.5 ppm and site F at 178 ppm. Sites C, D and E are all directly bonded to ^{14}N nuclei, although site C shows only a slight broadening due to residual dipolar coupling to ^{14}N, whereas the splitting is clearly resolved for sites D and E. Sites A, B and F are two bonds away from the nearest ^{14}N nucleus and show no splitting due to residual dipolar coupling.

Experimentally, the ^{14}N decoupling efficiency has a complex dependence on the rate of pulsing ω_{pulse}, which is shown in Figure 6.7. For the sites that are bonded to ^{14}N, effective decoupling is achieved over a wide range of pulse rates. The enhancement of the peak heights ranges from 30% to 77%, where the greatest enhacement occurs for the site E due to the large splitting seen in the non-decoupled spectrum for this site. There are, however, specific pulse rates at which inferior decoupling is achieved, and these occur at all the spinning frequencies investigated. Experimentally, choosing ω_{pulse} to be slightly greater, or lower, than the sample spinning frequency avoids the inferior decoupling performance seen when the pulse rate and spinning frequency are equal. Other pulse rate values ω_{pulse} giving poor decoupling tend to lie far away from $\omega_{\text{pulse}} \approx \omega_r$. Sites A, B and F, which are not bonded to ^{14}N, are unaffected by the ^{14}N decoupling, as expected.

The experiments at 5 kHz MAS in Figure 6.7(a) were repeated using a lower ^{14}N RF field strength of 13 kHz, and also using longer ^{14}N pulses; the results are shown in Figure 6.8.
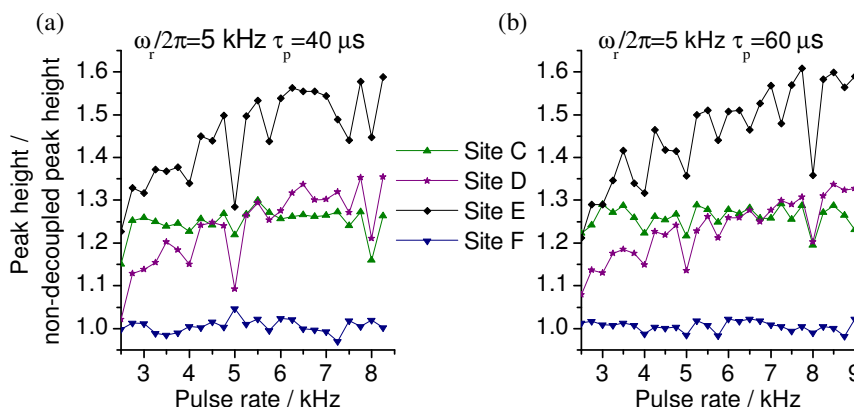
Figure 6.8: Effect of the rate of pulsing ω_{pulse} in the ^{14}N decoupling sequence for the six ^{13}C signals of Ala-Ala at site C: 49 ppm, D: 51.5 ppm, E: 170.5 ppm, F: 178 ppm. In both cases the MAS frequency was 5 kHz and the ^{14}N RF field strength $\omega_1^{\mathrm{N}}/2\pi$ was 13 kHz. In (a) the pulse length was $\tau_{\mathrm{p}} = 40\,\mu$s and (b) the pulse length was pulse length $\tau_{\mathrm{p}} = 60\,\mu$s. The static field strength was 9.4 T.

With both the lower RF field strength and longer pulses in the decoupling sequence, the same variation of the peak heights with ω_{pulse} was observed as in Figure 6.7(a), although the increase in the peak heights from decoupling is reduced with the lower ^{14}N RF field used. This indicates that the strategy of setting the pulse rate ω_{pulse} to slightly greater than the spinning frequency ω_{r} can generally be applied to avoid poor decoupling performance.

For decoupling of the residual dipolar coupling to occur, the ^{14}N nuclei must be affected by the RF irradiation, and the discussion in Section 6.1.1 showed that this only occurs when ω_Q is in the region $\omega_Q \approx 0$ during RF irradiation. The ω_Q zero-crossings that occur within the sample are coordinated with the rotor orientation during MAS, with each crystal orientation undergoing ω_Q zero-crossings at the same point in each rotor period. The orientation of the rotor during the first 40 ^{14}N pulses of different decoupling sequences is plotted for 5 kHz MAS in Figures 6.9, and 7.5 kHz MAS in Figure 6.10, with the pulse durations shown being those used in Figure 6.7. If $\omega_{\mathrm{pulse}} = \omega_{\mathrm{r}}$ (Figures 6.9(b) and 6.10(b)), it is clear that the same set of crystallites undergo zero-crossings during each ^{14}N pulse, as the rotor orientation is the same during each pulse. At 5 kHz MAS, a 40 μs pulse occupies 20% of a rotor period, and Figure 6.4 on page 171 shows that nearly 50% of crystallites contain ^{14}N nuclei that do not undergo zero-crossings during the pulse and are therefore largely unaffected by the ^{14}N RF irradiation. This is likely, at least in part, to give the observed decrease in decoupling performance. With $\omega_{\mathrm{pulse}} \neq \omega_{\mathrm{r}}$, in general a different set of crystallites undergo a zero-crossing during each pulse, leading (over a

period of time) to RF irradiation affecting all ^{14}N nuclei in the powder sample.

There remain other values of ω_{pulse} that also give relatively poor decoupling performance; however, it is not obvious from consideration of the coordination of pulses with the rotor orientation why inferior decoupling performance is observed in these cases.

Figure 6.11 on page 182 shows the experimental results for the effect of the ^{14}N decoupling RF field strength on the peak heights. It is found that for $\omega_{\text{r}}/2\pi = \omega_{\text{pulse}}/2\pi = 5$ kHz, the peak intensities of sites A, B and F decrease significantly as the ^{14}N RF field strength is increased, even though these sites are not directly bonded to nitrogen. Site F is relatively remote from the ^{14}N spins and its strongest ^{13}C–^{14}N dipolar coupling is $b_{\text{CN}}/2\pi = -\gamma_C \gamma_N \mu_0 \hbar/2\pi (r_{\text{CN}}^3 4\pi) = -150$ Hz, based on the reported crystal structure,[243] so one would hope not to see any effect from the decoupling sequence on this signal. The decrease in signal intensity for these sites with increasing ^{14}N RF field strength suggests that *recoupling* of the first-order ^{13}C–^{14}N dipolar coupling is occurring. The possibility of an effect unrelated to ^{14}N was excluded by repeating the experiment using hexamethyl benzene and adamantane (which obviously do not contain nitrogen). For these samples, only a very small decrease in peak heights of $< 3\%$ was observed when applying the decoupling pulses at the highest ^{14}N RF field strength of 25 kHz. This may be due to RF field inhomogeneity, causing broadening through variation in the Bloch-Siegert shift across the sample volume, or from a spectrometer effect caused by the high-power pulsing used.

As noted earlier, the contribution to the phase acquired by the ^{13}C single-quantum coherences due to dipolar coupling is also affected by population transfers between the ^{14}N Zeeman states, and this interferes with MAS averaging of this interaction. For sites C, D and E (which are directly bonded to nitrogen and clearly affected by the second-order dipolar-quadrupolar cross-term), their peak heights initially increase with the ^{14}N RF field strength, with effective decoupling of ^{14}N achieved, but their signal intensities reach a maximum. This is presumably the result of a compromise between decoupling the residual dipolar coupling, and recoupling the first-order dipolar interaction between the ^{13}C and ^{14}N nuclei.

Fortunately, when using ω_{pulse} offset from ω_{r}, quite different experimental results are obtained. Sites A, B and F are only slightly affected by the decoupling pulses, even at the highest RF field strengths, and the other sites also experience improved decoupling at all RF field strengths, which is the desired behaviour. This origin of this effect is not understood.
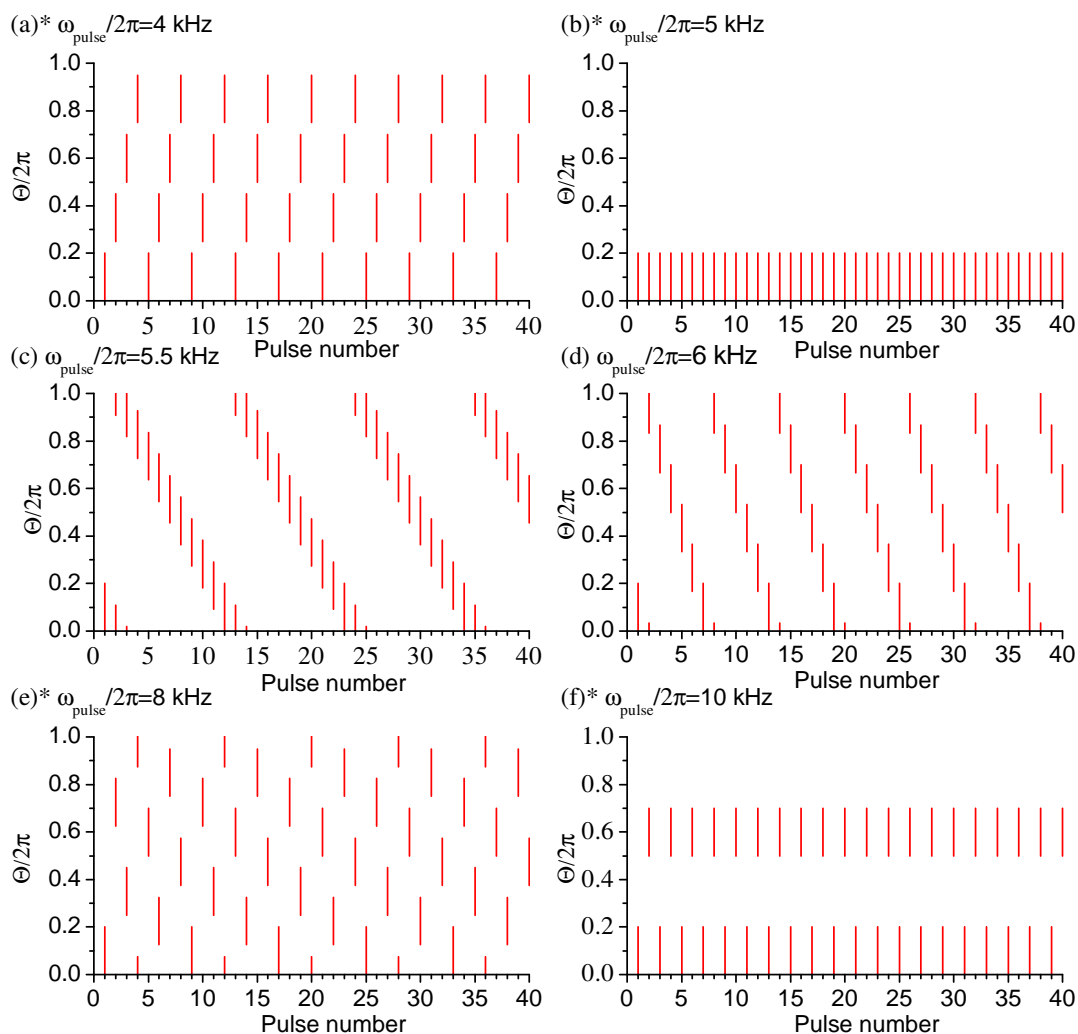
Figure 6.9: Coordination of pulses in the ^{14}N decoupling sequence with sample orientation using a spinning frequency of 5 kHz and pulse length of 40 μs. The rotor orientation is specified by the rotation angle (Θ) of the rotor about its rotation axis, where $\Theta=0$ at the start of the first pulse. The red lines indicate the rotor orientation reached during each pulse. The value of ω_{pulse} is indicated above each plot, and an asterisk indicates values at which poor ^{14}N decoupling occurred.
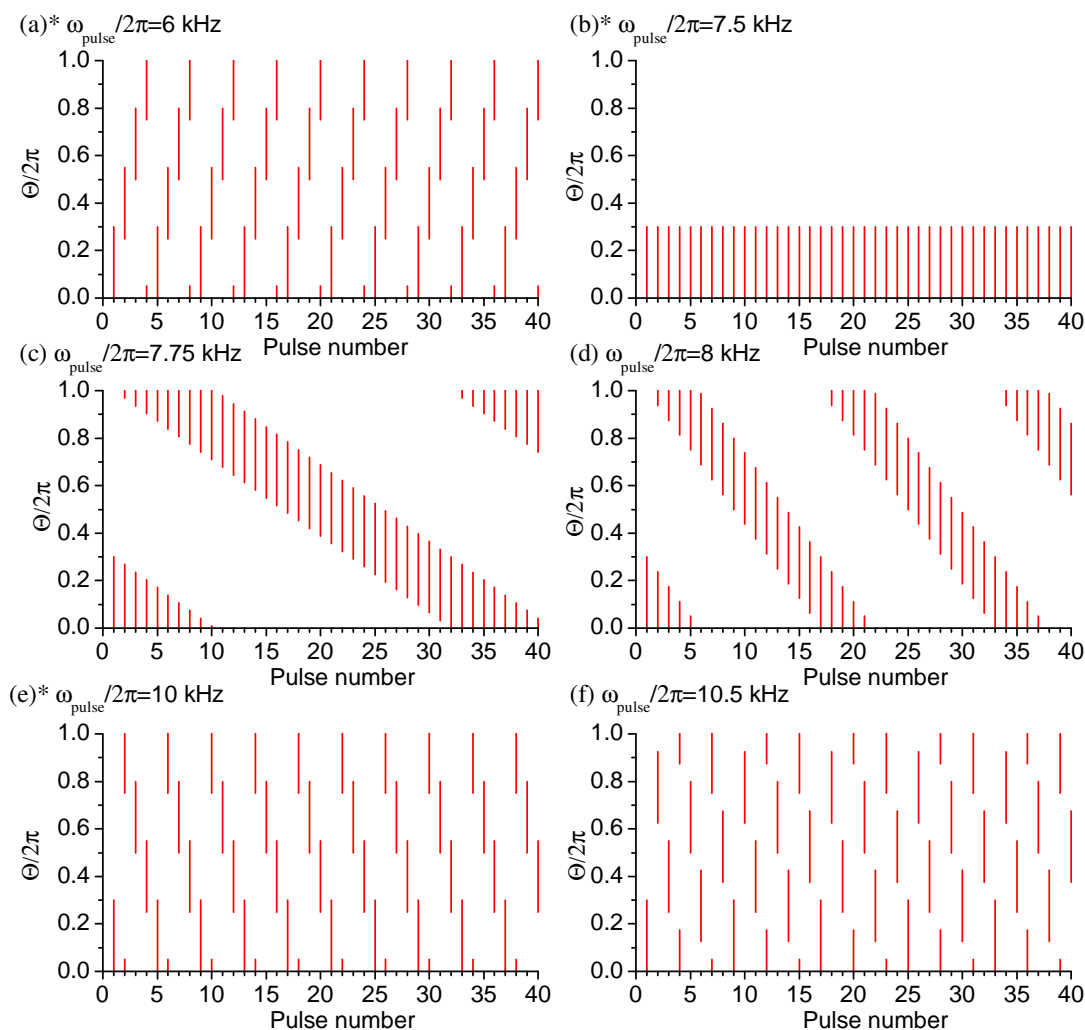
Figure 6.10: Coordination of pulses in the ^{14}N decoupling sequence with sample orientation using a spinning frequency of 7.5 kHz and pulse length of 40 μs. The rotor orientation is specified by the rotation angle (Θ) of the rotor about its rotation axis, where $\Theta=0$ at the start of the first pulse. The red lines indicate the rotor orientation reached during each pulse. The value of ω_{pulse} is indicated above each plot, and an asterisk indicates values at which poor ^{14}N decoupling occurred.
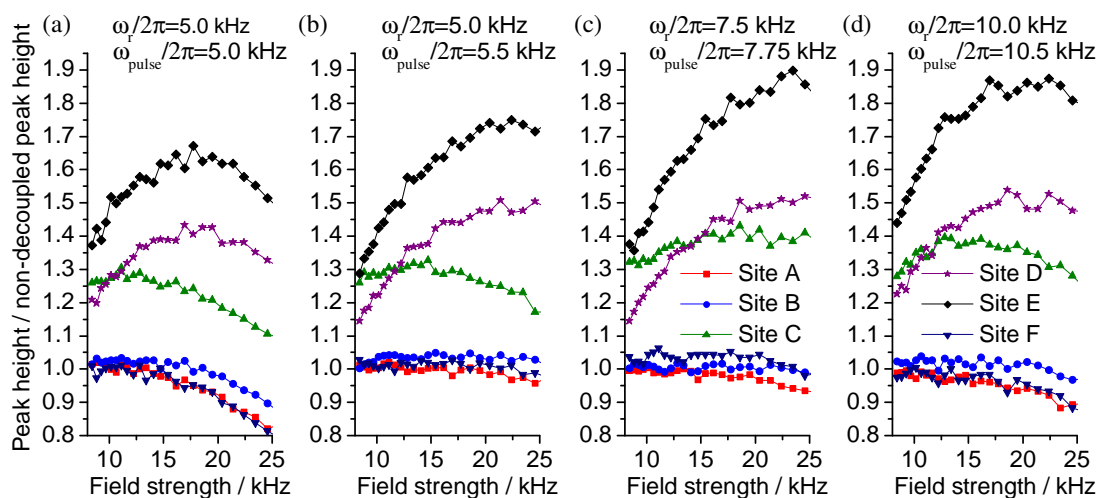
Figure 6.11: Effect of the decoupling RF field strength ω_1^N on the ^{14}N decoupling for the six ^{13}C signals of Ala-Ala at site A: 18 ppm, B: 19 ppm, C: 49 ppm, D: 51.5 ppm, E: 170.5 ppm, F: 178 ppm. In each case the pulse length τ_p used in the decoupling sequence was 40 μs, and the spinning frequency (ω_r) and rate of pulsing (ω_{pulse}) used are shown in the figure. The static field strength was 9.4 T.

The influence of the pulse length was also analysed experimentally and the results are shown in Figure 6.12. The advantage of using a pulse rate that is incommensurate with the spinning frequency is again clearly evident in Figure 6.12(a-d), where a significant gain in decoupling efficiency is achieved by offsetting ω_r and ω_{pulse}. There is an optimum pulse length for decoupling at lower spinning rates, while at higher spinning frequencies, the enhancement in peak height appears to plateau with increasing RF pulse lengths. This suggests that there is no advantage in using ^{14}N pulses that exceed half a rotor period, which is beneficial as it reduces the time for which pulses are simultaneously applied to two channels of the probe.

6.1.5 Computer simulation methods

Accurate numerical evaluation of the Liouville–von Neumann equation, described in Section 2.4 on page 56, for ^{14}N decoupling in ^{13}C-^{14}N spin pairs is hampered by the need to use very short time steps over which the Hamiltonian can be treated as constant. This is necessary because the quadrupole interaction is large and changes rapidly under MAS. In addition, each time step requires the matrix representation of the Hamiltonian to be diagonalised. The time required to perform diagonalisation of an n-dimensional square matrix scales approximately as n^3,[244] so this takes roughly 27 times longer for a (6×6) matrix, required for the ^{13}C–^{14}N spin-system, than for a (2×2) matrix used in isolated

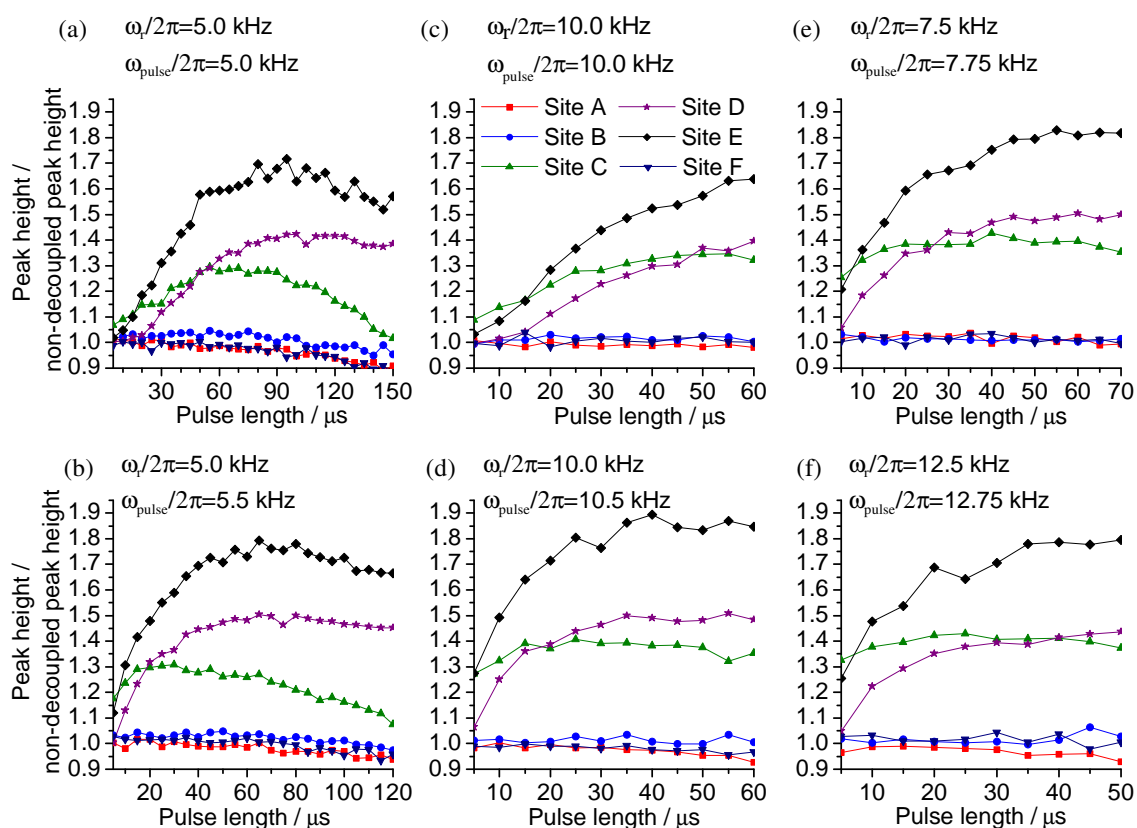Figure 6.12: Dependence of peak height on the pulse length used in the ^{14}N decoupling sequence for the six resonances of Ala-Ala at sites A: 18 ppm, B: 19 ppm, C: 49 ppm, D: 51.5 ppm, E: 170.5 ppm, F: 178 ppm. The RF fields strength ω_1^N was 17 kHz in each case and the spinning frequency (ω_r) and rate of pulsing (ω_{pulse}) are shown in the figure. The static field strength was 9.4 T.

spin-1/2 simulations. Both of these factors contribute to make this approach to numerical simulations prohibitively time consuming in the present case.

For these reasons, an approximate method to simulate the effects of ^{14}N irradiation was used. Instead of propagating the full matrix representation of the density operator throughout the detection period, only the evolution of the detected ^{13}C (-1)-quantum coherences is calculated. These correspond to coherences between the $|m_N, -\frac{1}{2}\rangle$ and $|m_N, \frac{1}{2}\rangle$ states for $m_N = +1, 0, -1$. The simulations include the effects of the ^{13}C chemical shift Hamiltonian, ^{13}C–^{14}N (first-order) dipolar coupling Hamiltonian and the dipolar-quadrupolar second-order cross-term Hamiltonian. To model the effect of the ^{14}N RF pulses, four approximations are made:

- The ^{14}N RF irradiation only affects nuclei during zero-crossings of ω_Q.

- The ^{14}N irradiation only causes a population transfer during zero-crossings (it is assumed no ^{14}N coherences are generated).

- Population transfer occurs instantaneously at the zero-crossing and occurs between Zeeman states connected by continuity during the zero-crossings.

- The efficiency of the population transfer is specified by a single parameter, and is the same for all crystallites.

Consequently, the simulations only investigate the contribution of adiabatic population transfer caused by zero-crossings during RF irradiation to the decoupling of the ^{13}C–^{14}N spin pairs.

Using this approach, the time step over which the Hamiltonian can be treated as constant is longer than when performing a full numerical evaluation of the Liouville–von Neumann equation. This is because the evolution of the ^{14}N spin under the quadrupolar coupling interaction is not calculated, and it is only necessary to identify the times during each rotor period that zero-crossings of ω_Q occur.

A FORTRAN-77 program was written to perform these simulations. Typically, the simulations divided the rotor period into 200 steps, and between these points the Hamiltonian was approximated to be constant. In addition, 678 REPULSION[72] (α, β) crystallite orientations and 100 γ values were used in the powder averaging process. With these parameters, each simulation required about two minutes of calculation time on Pentium 4 2.0 MHz desktop computer.
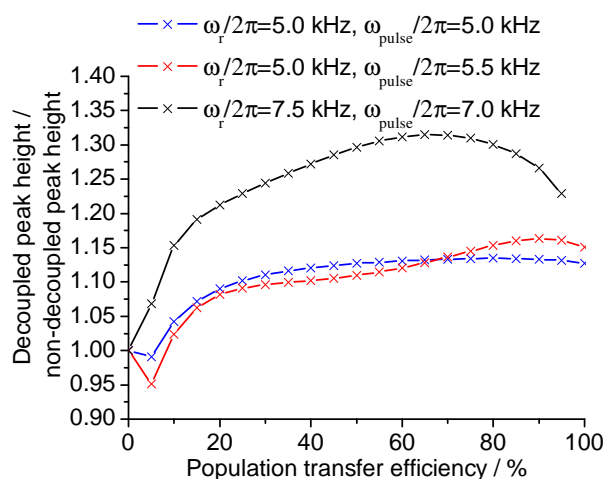
Figure 6.13: Calculated effect of the population transfer efficiency used in the ^{14}N decoupling simulations. The pulse length in the simulations was $40\,\mu$s. Compare with Figure 6.11.

6.1.6 Computer simulation results

Simulation results shown here assumed that the dipolar coupling principal z-axis was perpendicular to the z-axis of the chemical shift and quadrupolar coupling tensor PAFs, as this gave a splitting in the calculated lineshape similar to that seen experimentally. The chemical shift and quadrupolar coupling PAFs had the same orientation. Other simulation parameters were $-\omega_0^C \Delta_{CS} = 7.7$ kHz, $\eta_{CS} = 0.96$, $C_Q/2\pi = 3.5$ MHz, $\eta_Q = 0$, $b_{IS}/2\pi = -850$ Hz, and $\omega_0^N = 29.16$ MHz (9.4 T static field). Exponential line broadening of 40 Hz was applied to the simulated FIDs before Fourier transformation. Further details are given in figure captions.

In Figure 6.13, the effect of the population transfer efficiency used in the simulations is shown. Increasing the ^{14}N population transfer efficiency used in the computer simulations of ^{14}N decoupling parallels the effect of increasing the adiabaticity parameter due to an increased ^{14}N RF field strength. A significant increase in the peak-height is predicted even for relatively low population transfer efficiencies ($\approx 20\%$), confirming that the adiabatic population transfer model can lead to a decoupling effect. In contrast to the experimental results, however, no significant advantage in using a rate of pulsing slightly offset from the spinning frequency was calculated.

Figure 6.14 illustrates simulation results investigating the effect of varying the rate of pulsing on decoupling efficiency. The simulations predict very different behaviour than measured experimentally. In the experimental results for the Ala-Ala sample, a decoupling effect was observed for a wide range of pulse rates, with only very specific
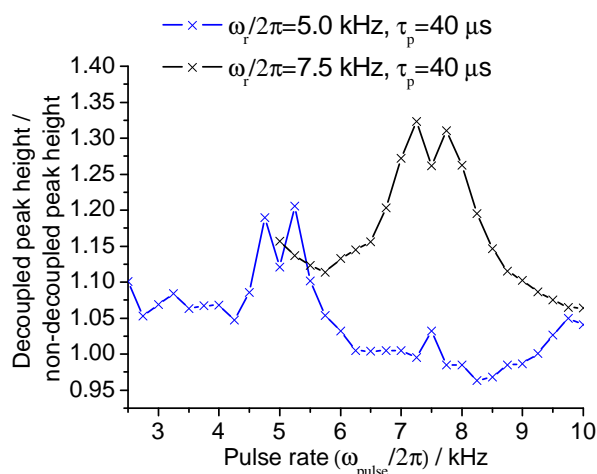
Figure 6.14: Simulation results for the effect of the rate of pulsing ω_{pulse} in the ^{14}N decoupling sequence. The pulse length in the simulations was 40 μs and the population transfer efficiency was 40 %. Compare with Figure 6.7 and Figure 6.8.
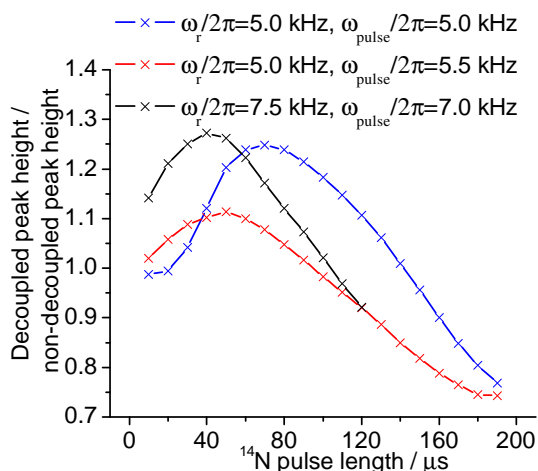
Figure 6.15: Simulation results for the effect of the ^{14}N decoupling pulse length τ_p. The population transfer efficiency used in the simulations was 40%. Compare with Figure 6.12

frequencies at which reduced performance was measured. In contrast, the simulations predicts effective decoupling is only obtained when the rate of pulsing is similar to the spinning frequency. It is worth commenting that the calculated lineshapes, despite only showing a modest increase in peak height, show no splitting due to the residual dipolar coupling, giving a single peak at the isotropic frequency.

Finally, the calculated effect of the ^{14}N pulse lengths, shown in Figure 6.15, follows a similar trend to the experimental results in Figure 6.12. A maximum in the peak height was calculated to occur at approximately one third of a rotor period, and thereafter a decrease in peak height occurs with increasing pulse lengths. The decrease in peak heights as the pulse length is increased is much more rapid in the calculated results than for the
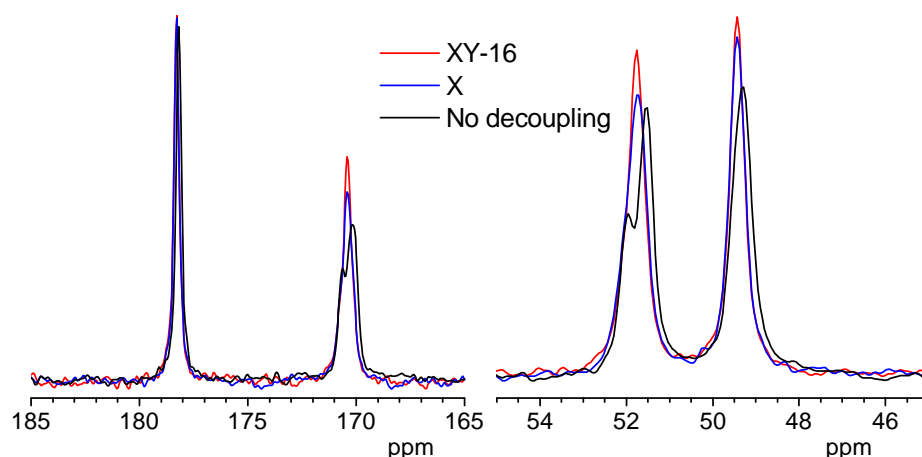
Figure 6.16: Expansions from the ^{13}C NMR spectra of Ala-Ala recorded without ^{14}N decoupling (black), with decoupling using RF pulses with the same phase (*x*-pulses) (blue) and with decoupling RF pulses alternating in phase following the XY-16 sequence.[213] Experimental parameters: $\omega_{pulse}/2\pi$=5 kHz, $\omega_r/2\pi$=5 kHz, τ_p=40 μs, $\omega_1^N/2\pi$=27 kHz. The static field strength was 9.4 T.

experimental observations, and offsetting the rate of pulsing and the spinning frequency was again not calculated to give improved decoupling.

6.1.7 Discussion and conclusion

Although the population transfer model for the zero-crossings during ^{14}N decoupling predicts an increase in peak heights and removal of the residual splitting in the ^{13}C peaks, it fails to reproduce the major trends in the experimental results. In particular, the variation in decoupling efficiency with the rate of pulsing is calculated to be very different than measured experimentally. This indicates that there is an additional mechanism causing the decoupling effect. Further evidence for a more complicated mechanism contributing to the decoupling effect comes from experiments comparing ^{13}C spectra recorded using ^{14}N RF pulses all with the same phase and with alternated phases, following the XY-16 scheme,[213] shown in Figure 6.16. If the only effect of the RF irradiation were a transfer of populations between the ^{14}N Zeeman states, a dependence on the RF phase would not be expected, since the coherence order change is zero.

It has not been possible in the present study to identify why a dependence on the ^{14}N phase is seen in the ^{13}C spectrum. However, some pertinent considerations may be noted. Away from the region where $\omega_Q \approx 0$, the ^{14}N RF irradiation has no effect on the ^{14}N spins, unless $\omega_{iso} = 0$, in which case excitation of double-quantum coherences may occur. However,

this method of double-quantum excitation is unlikely to be significant in the present case, as the excitation efficiency is generally rather low and is sensitive to the $\omega_{iso} = 0$ condition.[235] Moreover, double-quantum excitation only affects the ^{14}N $|+1\rangle$ and $|-1\rangle$ Zeeman states, and so is not expected to average the second-order dipolar-quadrupolar cross-term, for the same reason as overtone decoupling fails. The ^{14}N decoupling effect must therefore result from changes in the spin system occurring during the periods around ω_Q zero-crossings when RF irradiation is on. The dependence of the ^{13}C signal on the phase of the RF field suggests that ^{14}N coherences are generated by RF irradiation, and that these are important in the decoupling effect, but it is not immediately clear how this is achieved.

A more thorough computational study requires numerical evaluation of the Liouville–von Neumann equation, possibly making use of a high-performance computing facility. These simulations would calculate the evolution of the ^{14}N spin system during the zero-crossings, and consequently provide a full description of the spin system. Analysis of the density operator during zero-crossings may give some insight into the evolution of the spin system that is occurring during RF irradiation. Alternatively, it may become possible to use of the recent SPINEVOLUTION simulation program developed by the Griffin group.[71] SPINEVOLUTION does not rely on matrix diagonalisation procedures and has been shown to achieve considerable time savings compared with other NMR simulation programs for calculations involving multiple spin systems. However, the current version of the program (SPINEVOLUTION 2.9) does not allow simulations involving the quadrupolar interactions or the dipolar-quadrupolar cross-term Hamiltonian, but this may soon be implemented.

Experimentally, ^{14}N decoupling is found to be effective over a relatively wide range of parameter values, although experimental optimization is necessary to achieve the best results. From the experimental study presented here, it is clear that it is important to offset the rate of pulsing in the decoupling sequence slightly from the sample spinning frequency, and for the range of spinning frequencies investigated, near optimum performance of the decoupling scheme can be achieved over a reasonably broad range of pulse lengths around $\tau_p \approx \tau_r/3$. With the current probe limitations, the decoupling RF field strength is unlikely to be chosen to be too high; therefore, in setting up the decoupling sequence, one needs only to place the irradiation frequency close to the ^{14}N resonances and to optimise the pulse lengths and pule rate to achieve effective decoupling of the residual splitting in ^{13}C–^{14}N spin pairs.

Although the experimental characteristics of the ^{14}N decoupling of the residual splitting

in ^{13}C MAS spectra have been identified, a complete theoretical description of the mechanism that brings about the decoupling effect has not possible in the present study. The calculation results presented here demonstrate that the observed decoupling effect cannot be completely accounted for by population transfers between the ^{14}N Zeeman states alone and further work is needed to understand the origin of the observed experimental behaviour.

6.1.8 Further work: applications of ^{14}N decoupling

The advantage in terms of linewidth and peak height from decoupling the residual dipolar splitting in ^{13}C–^{14}N spin pairs is clearly demonstrated by the results in Figure 6.6. This technique is, of course, only useful in the cases where the residual dipolar splitting is the dominant contribution to the linewidth. This is often the case, though, for microcrystalline samples. Since peptides and many pharmaceutical samples contain nitrogen, ^{14}N decoupling may frequently prove useful in their study. In addition, if a sample requires a long recycle delay between acquisitions, which often occurs for crystalline samples, the reduction in the number of scans to achieve a specific signal-to-noise ratio is useful.

The gain in the signal-to-noise ratio is especially advantageous when performing two-dimensional experiments, such as recoupling experiments to record the ^{13}C chemical shift anisotropy of ^{14}N-coupled sites. It may also find useful application in the ^{13}C–^{14}N heteronuclear multiple-quantum correlation experiments that have very recently been developed in the groups of Gan[245] and Bodenhausen,[246] where signal-to-noise is at an extreme premium if using natural ^{13}C isotopic abundance samples. These experiments are performed at much higher spinning frequencies (~30 kHz) than could be investigated in the present work, owing to hardware limitations. Further analysis of the decoupling effects at the higher spinning frequencies and RF field strengths achievable with a 2.5 mm rotor probe is needed. Since the adiabaticity parameter is proportional to $(\omega_1^N)^2/\omega_r$, it is reasonable to suppose that effective decoupling could be achieved with the higher RF field strengths possible with a 2.5 mm probe, despite the higher spinning frequency.

The removal of the splitting in the directly-observed dimension also simplifies the complicated lineshapes that are otherwise observed in two-dimensional spectra.[166,247] For example, in a two-dimensional chemical shift powder pattern recoupling experiment for a ^{14}N coupled ^{13}C nucleus, if the splitting in the F_2 dimension is removed, the powder

patterns can be analysed from a cross-section taken through the isotropic peak in the F_2 dimension. Without decoupling of ^{14}N, either the full two-dimensional lineshape must be fitted to extract the parameters of interest, or the projection onto the F_1 dimension must be calculated. Fitting a two-dimensional lineshape is computationally demanding, and the calculation depends upon many different variables, while a projection suffers from a lower signal-to-noise ratio than a cross-section.[221] This is illustrated in the next section.

Another interesting possible application is the multiple-quantum magic-angle spinning (MQMAS) experiment.[87,248] MQMAS is a two-dimensional experiment that uses an echo pulse sequence to refocus evolution caused by the second-order quadrupole Hamiltonian during the t_1 period, which is not averaged to zero by MAS alone. By using appropriate data processing, a high-resolution dimension separates the second-order quadrupole powder patterns in the two-dimensional spectrum. If an observed nucleus is coupled to ^{14}N, then its peak in the high-resolution dimension is broadened due to the second-order dipolar-quadrupolar cross-term Hamiltonian, which significantly reduces the resolution of different peaks in the spectrum.[249] Using ^{14}N decoupling may reduce this effect to some extent, and merits further investigation.‡ This situation is slightly different to the ^{13}C–^{14}N spin pair case because there are two dipolar-quadrupolar cross-terms in the Hamiltonian, since both nuclei in the spin pair are quadrupolar.

Tentative measurements of using the pulsed decoupling scheme for ^{27}Al–^{31}P spin systems have also been performed on a sample of AlPO-15.§ While continuous irradiation, as proposed by Delevoye and co-workers,[242] tended to reduce the signal intensity, the pulsed decoupling method gave a modest increase in peak heights by about 10%, along with a concomitant reduction in the linewidths, shown in Figure 6.17. This suggests that the findings of the present study may be transferred to other spin pairs, and this may be a fruitful line of investigation. This particular application is quite different from the ^{13}C–^{14}N spin pair case because ^{27}Al is a spin-3/2 nucleus with the central transition unaffected by the quadrupole coupling to first-order. This means that the central transition will be affected throughout RF irradiation of the sample, in addition to effects brought about by ω_Q zero-crossings during RF irradiation.
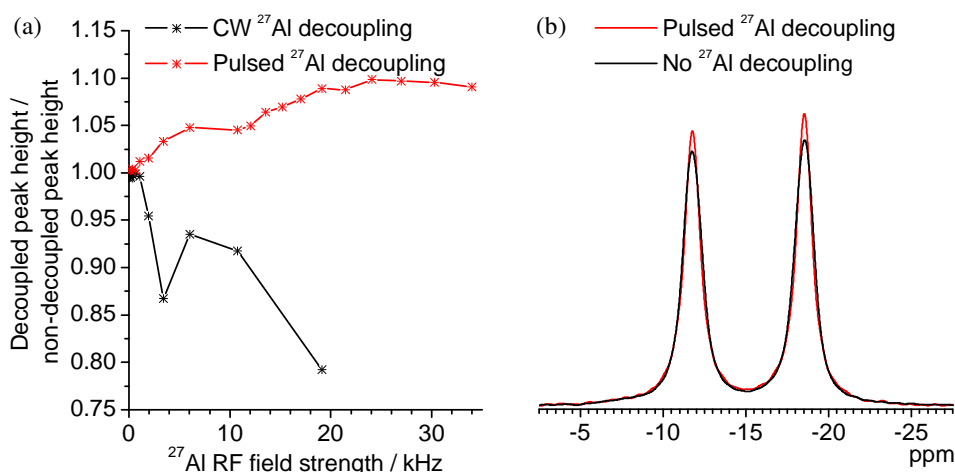
Figure 6.17: (a) Peak height of the ^{31}P signal of AlPO-15 at -13 ppm using continuous wave (CW) and pulsed decoupling. The spinning frequency was 6.15 kHz and the ^{27}Al decoupling pulse rate was 5 kHz with pulse lengths of 45 μs. TPPM ^{1}H decoupling was used with an RF field strength of ~80 kHz. (b) Comparison of decoupled and non-decoupled ^{31}P NMR spectra of AlPO-15.

6.2 Dipolar - CSA tensor correlation for ^{13}C–^{14}N spin pairs

The relative orientation of a chemical shift tensor PAF and dipolar coupling tensor PAF can provide useful information about the orientation of the chemical shift tensor in the molecular frame, since the dipolar coupling tensor is known to have its principal z-axis oriented along the internuclear vector between the coupled spins.

The simplest method to determine the relative orientation of the chemical shift and dipolar coupling tensor PAFs is to record the static spectrum of a powder sample (assuming resolution of different ^{13}C sites is possible). For ^{13}C–^{14}N spin pairs, the ^{13}C powder pattern is more complicated than for an isolated ^{13}C spin, as illustrated in Figure 6.18(a), and can loosely be described as a modulation of the CSA powder pattern due to the dipolar coupling. As stated earlier, there are six eigenstates of the rotating-frame Hamiltonian for a dipolar coupled ^{13}C–^{14}N spin pair: $|m_N, m_C\rangle$ with $m_N = +1, 0, -1$ and $m_C = +\frac{1}{2}, -\frac{1}{2}$, and three ^{13}C single-quantum transitions between the $|m_N, \frac{1}{2}\rangle$ and $|m_N, -\frac{1}{2}\rangle$ states with $m_N = +1, 0, -1$. For a static sample, each ^{13}C single-quantum transition has a different frequency: $\omega + D_{zz}^{\text{lab}}$, ω and $\omega - D_{zz}^{\text{lab}}$ for $m_N = +1, 0, -1$ respectively, where ω is due to the ^{13}C chemical shift Hamiltonian and D_{zz}^{lab} is the zz component of the dipolar coupling tensor expressed in the laboratory frame. The effect of the second-order dipolar-quadrupolar cross-term has been ignored here because it is significantly smaller in magnitude than the first-order dipolar coupling interaction and has only a slight effect on the observed powder pattern. The observed powder pattern lineshape can be considered to be constructed from three superimposed powder patterns corresponding to the ^{13}C single-quantum transitions
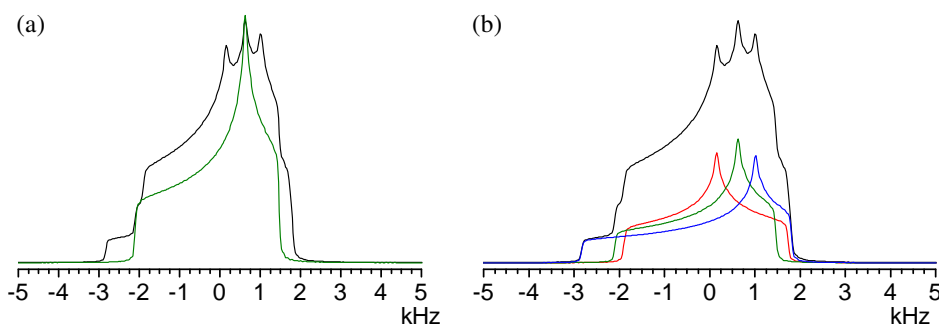
Figure 6.18: (a) Isolated (green) and ^{13}C–^{14}N dipolar-coupled ^{13}C static powder patterns (black). (b) ^{13}C–^{14}N dipolar coupled (black) ^{13}C static powder pattern, and constituent components with $m_N = +1, 0, -1$ (red,green,blue). Simulations used $-\omega_0^C \Delta_{CS}/2\pi = -2100$ Hz, $\eta_{CS} = 0.4$, and $b_{ij}/2\pi = -650$ Hz.

with $m_N = -1, 0, +1$, as shown in Figure 6.18(b).

The precise static lineshape depends on the relative orientations of the CSA and dipolar coupling interactions, as well as their principal values, and analysis of the powder pattern can extract this information. This technique was first identified by Kaplan *et al.* for ^{13}C-^{15}N and ^{13}C–^{14}N spin pairs.[162]

The relative orientation of the ^{13}C chemical shift tensor PAF and the ^{13}C–^{14}N dipolar coupling tensor PAF can be specified using a set of Euler angles. The dipolar coupling tensor is axially symmetric ($D_{xx}^{PAF} = D_{yy}^{PAF}$), and therefore only two Euler angles are needed to specify the (physically distinguishable) relative orientations of the two axis frames. Here, the Euler angles $\Omega_{DC} = \{0, \beta_{DC}, \gamma_{DC}\}$ are chosen to relate the dipolar tensor PAF to the chemical shift tensor PAF. The principal axis frame z-axis of the dipolar coupling tensor is aligned along the internuclear vector, so the two angles can also be visualised as polar angles describing the orientation of the internuclear axis within the principal axis frame of the ^{13}C CSA tensor: colatitude β_{DC} and longitude $180 - \gamma_{DC}$.

There have been numerous applications of lineshape analysis of this type, with particular interest focused on model peptide samples.[163,250–252] In each of these studies, the limitation upon resolution when recording static spectra required isotopic enrichment of the particular ^{13}C site of interest in the molecule. This is not a generally applicable approach.

Previous studies have recognised that the dipolar coupling to a ^{14}N nucleus may need to be included in the calculation of the ^{13}C spinning sideband intensities.[253] In practice, the effect is rather small, except at very slow spinning frequencies, and can often be neglected. In studies where it has been included, the dipolar coupling tensor orientation was not

determined from the experimental data, presumably because the effect of the dipolar tensor PAF orientation on the spinning sideband intensities was too small to reliably obtain this information. Instead, the orientation from quantum-mechanical calculation results or literature values were used.[164, 254] Thus it appears that MAS spectra are not a practical approach to obtaining the tensor orientations for ^{13}C–^{14}N spin pairs.

The obvious solution to the limitation of overlapping static powder patterns in one-dimensional spectra is to use a two-dimensional experiment that recouples quasi-static powder patterns of the ^{13}C sites in one dimension, and separates them by a high resolution dimension. This is possible, in principle, using any experiment that recouples the chemical shift anisotropy. The chemical shift Hamiltonian is linear in the $\hat{I}_z$ operator, which is the spin part of the Hamiltonian affected by ^{13}C multiple pulse recoupling. The dipolar coupling Hamiltonian is also linear in the $\hat{I}_z$ operator; thus, it too must be recoupled and is subject to the same scaling as the ^{13}C chemical shift interaction in any CSA recoupling scheme.

Three studies using this approach have been reported for ^{13}C–^{14}N spin pairs. The first study by the group of Grant[166] used the FIREMAT[198] experiment. As discussed previously, this experiment requires specialist probe hardware for slow sample spinning which is unavailable in most laboratories. Moreover, the analysis of the spectrum required fitting two-dimensional lineshapes, including the residual dipolar spitting in the F_2 dimension. This is computationally demanding and is not convenient for most NMR laboratories. The second study, recently reported by Wi and co-workers,[167] recorded quasi-static powder patterns with the SUPER[190] experiment. Reasonable agreement between their experimental tensor orientations and quantum-mechanical calculations was reported for the C_α carbon sites of short peptides, with an average difference between calculated and experimental values of ±14°. This good agreement is perhaps rather surprising, as the modulation of the CSA powder pattern by the dipolar coupling appeared to be rather poorly resolved in their experimental results. A different approach by Nielsen and co-workers[255] used the rotary-resonance condition, with RF irradiation of the ^{13}C nuclei to recouple both the ^{13}C CSA and dipolar coupling to ^{14}N. This experiment was demonstrated for alanine and glycine, but sensitivity to the rotary-resonance condition and RF inhomogeneity was reported, and consequently the experiment requires a variation of less than 7.5% in the RF field strength across the sample volume.

In the experiments presented here, the CT-2DCSA experiment, described in Section 5.4.2, was investigated. The CT-2DCSA method was expected to be the preferred choice to resolve dipolar modulated powder patterns since, except for a scaling in the intensity and

experimental instabilities, the cross-sections through the F_1 dimension are the same as ideal static spectra and give the optimum definition of the powder pattern lineshape. In addition, irradiation of the ^{14}N nuclei during the t_2 period was performed to remove the residual dipolar splittings in the F_2 dimension. There are two advantages from using ^{14}N decoupling. First, the signal-to-noise ratio for the ^{14}N coupled spins is increased. Second, a cross-section through the isotropic peak can be analysed, rather than a projection calculated over the full F_2 peak width, which gives a further signal-to-noise ratio benefit.

To demonstrate this experiment, both the C$_\alpha$ and amide carbon sites of the dipeptide Ala-Ala were investigated. These represent two quite different cases: for the C$_\alpha$ site, $|b_{ij}/(\omega_0 \Delta_{CS})| \sim 1/3$, whereas for the amide nitrogen $|b_{ij}/(\omega_0 \Delta_{CS})| \sim 1/10$ in a static field of 9.4 T, where b_{ij} is the ^{13}C–^{14}N dipolar coupling constant and Δ_{CS} is the chemical shielding anisotropy parameter.

6.2.1 Data analysis

Analysis of the experimental results was performed by fitting simulated lineshapes to the experimental cross-sections using the SIMPSON program[39] to minimise the root mean square deviation (RMSD) between the two lineshapes. The ^{13}C–^{14}N bond length shows only a small variation between samples, and was not included as a variable in the fitting procedure. For the C$_\alpha$ carbons $b_{ij}/2\pi = -700$ Hz was used (bond length of 1.47 Å), and for the amide ^{13}C site, $b_{ij}/2\pi = -900$ Hz (bond length of 1.34 Å) was used, based on averaged literature values.[256] Contrary to the comments of Wi *et al.*, it was found that when fitting the simulated lineshape to the experimental results for the C$_\alpha$ sites, optimisation of the chemical shift anisotropy parameters (δ_{aniso} and η_{CS}) could not be performed independently of the polar angles describing the dipolar tensor orientation. If this approach was used, the fitted lineshapes tended to be from local minima of the RMSD in the parameter space, rather than the global minimum of the RMSD. Optimisation of a fitted lineshape by variation of five different parameters (δ_{aniso}, η_{CS}, β_{DC}, γ_{DC} and a weighting factor) tends to be unstable, so the following procedure was used.

In the first step, the physically distinguishable range ($0° - 90°$) of the two polar angles describing the relative orientations of the dipolar and chemical shift PAFs was sampled at intervals of 5°. For each of the 361 combinations of the polar angles, the RMSD between the experimental and simulated lineshape was minimised by optimising δ_{aniso}, η_{CS} and a intensity scaling factor. This process can be fully automated when using SIMPSON, and

only a single input file is required. The simulations used a static sample model, rather than simulating the CT-2DCSA recoupling sequence.

The polar angles and CSA parameters that gave the minimum RMSD between the experimental and simulated lineshapes in the first fitting step were used as starting values for a second fitting procedure. The polar angles and weighting factor were optimised (keeping δ_{aniso}, η_{CS} fixed), then δ_{aniso}, η_{CS} and weighting factor were optimised again (with the new polar angles fixed); this cycle was repeated until no further reduction in the RMSD was achieved. For this second step of the fitting procedure, the effect of a finite spinning frequency on the cross-section through the F_2 isotropic peak was taken into account in the simulations by using a purpose-written FORTRAN-77 program (following a similar method to that described in Section 5.9, but including the additional dipolar-coupling interaction), together with the minimisation and processing routines of the SIMPSON package.[39]

This fitting approach is substantially more computationally demanding than that used by Wi *et al.*, but avoids spurious results. Despite this, the complete fitting process required less than 24 hours of computer time using an Intel Pentium 4 2.0 GHz desktop computer.

For the amide ^{13}C site, the effect of dipolar coupling on the CSA lineshape is much smaller than for the C_α sites due to the larger δ_{aniso} for this site, and only the second step in the above fitting procedure for the C_α sites was needed.

6.2.2   Results and discussion

Experimental F_1 cross-sections for the amide ^{13}C and C_α sites were recorded in separate experiments so that the optimum experimental parameters could be used in each case. The F_1 spectral widths were 14 kHz and 30 kHz for the C_α and amide ^{13}C sites respectively, and in both experiments 32 complex t_1 data points were acquired.

Plots of the RMSD between the simulated and experimental lineshapes are shown in Figure 6.19 for the two C_α sites in Ala-Ala (sites C and D as labelled in Figure 6.6) giving signals at 49 ppm and 51.5 ppm respectively. The RMSD calculated by SIMPSON is given by

$$\text{RMSD} = 10^3 \frac{\sum_i \left(A_i^{\text{re}} - B_i^{\text{re}} \right)^2}{\sum_i \left(A_i^{\text{re}} + B_i^{\text{re}} \right)^2}, \tag{6.18}$$

where A_i^{re} and B_i^{re} are the real parts of the ith data point of the experimental and simulated lineshapes respectively. The RMSD values plotted in Figure 6.6 are normalised to the minimum value achieved in the fitting procedure.

For both C_α sites of Ala-Ala, an unambiguous minimum in the RMSD was obtained, and the tensor orientations are quite different for the two sites. The best fit parameters are shown in Table 6.1. The error estimates in the fitted parameters are based on adjusting the parameters until the deviation of simulated line shape from the experimental lineshape exceeded the noise level in the spectrum. The best fit simulated lineshapes from the second minimisation procedure are overlaid on the experimental results in Figure 6.20. Comparison of the experimental and best fit simulated lineshapes provides convincing evidence of the success in both the experimental and fitting methodology used here.

For the amide carbon site, the modulation of the CSA powder pattern in the experimental lineshape occurs mainly at the edge of the lineshape. Although the dipolar modulation of the amide ^{13}C CSA powder pattern lineshape appears rather small, it is reproducible and simulations show a clear dependence on the β_{DC} and γ_{DC} angles. The best fit simulated lineshape of the amide site is overlaid on the experimental result in Figure 6.21 on page 198, and best fit parameters are also shown in Table 6.1. The β_{DC} and γ_{DC} angles are determined with less certainty than for the C_α sites, owing to the relatively smaller modulation of the CSA powder pattern lineshape. Nonetheless, the chemical shift parameters and β_{DC} and γ_{DC} angles determined from the two-dimensional experiment are consistent with the results of Hartzell *et al.*, who performed a one-dimensional experiment using a static sample of ^{13}C, ^{15}N labelled Ala-Ala[163] and reported values of $\delta_{\text{aniso}} = 75$ ppm and $\eta_{\text{CS}} = 0.97, \beta_{\text{DC}} = 90.2°$ and $\gamma_{\text{DC}} = 39.5°$ for the carbonyl site.

Use of the CT-2DCSA experiment is critical for obtaining undistorted powder pattern lineshapes and for resolving the modulation of ideal CSA powder pattern due to the dipolar coupling interaction. For example, the relatively small modulation of the amide ^{13}C CSA powder pattern lineshape, due to dipolar coupling to ^{14}N, would almost certainly not be resolved if using the SUPER, OPT-2DCSA or 2DCSA experiments described in Chapter 5. Even for the C_α sites, where the modulation of the lineshape by the dipolar coupling interaction is much more pronounced than from the amide ^{13}C site, the details in the lineshape are easily obscured by line broadening effects or distortions in the lineshape caused by experimental imperfections, both of which hinder accurate fitting of the experimental data.

The principal disadvantage and limitation of using the CT-2DCSA experiment is the loss

	Site C: C_α, 49 ppm	Site D: C_α, 51.5 ppm	Site E: amide, 170.5 ppm
δ_{aniso}	-23 ± 1 ppm	-19 ± 1 ppm	77 ± 2 ppm
η_{CS}	0.35 ± 0.04	0.19 ± 0.04	0.96 ± 0.04
β_{DC}	$24° \pm 10°$	$61° \pm 5°$	$83 \pm 15°$
γ_{DC}	$72° \pm 10°$	$68° \pm 10°$	28 ± 20

Table 6.1: Best fit parameters from numerical fitting of the experimental lineshapes for the ^{14}N coupled ^{13}C sites in Ala-Ala.
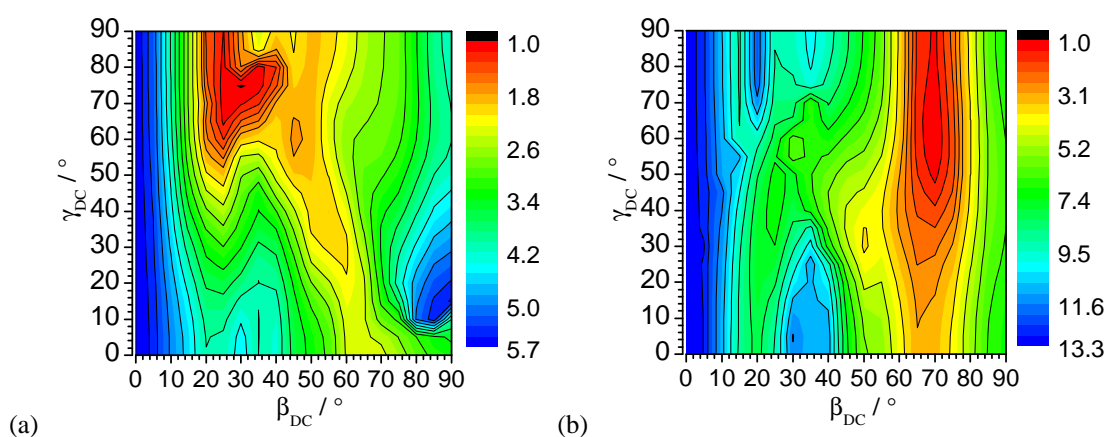
Figure 6.19: Root mean square deviation between the experimental and simulated lineshapes, optimised with respect to δ_{aniso} and η_{CS} for each β_{DC}, γ_{DC} combination. The root mean square deviation is normalised to the overall minimum value achieved. (a) C_α carbon at 49 ppm (site C) and (b) C_α carbon at 51.5 ppm (site D)
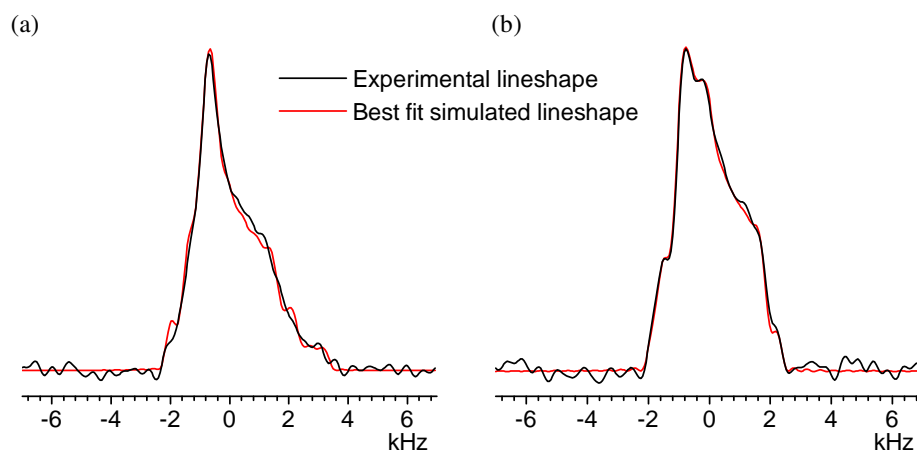
Figure 6.20: Experimental cross-sections from the anisotropic dimension of the CT-2DCSA spectrum and the best fit simulations overlaid in red for (a) C_α carbon at 49 ppm (site C), best fit parameters $\delta_{aniso} = -23$ ppm, $\eta_{CS} = 0.35$, $\beta_{DC} = 24°$, $\gamma_{DC} = 72°$ and (b) C_α carbon at 51.5 ppm (site D), best fit parameters $\delta_{aniso} = -19$ ppm, $\eta_{CS} = 0.19$, $\beta_{DC} = 68°$, $\gamma_{DC} = 58°$.
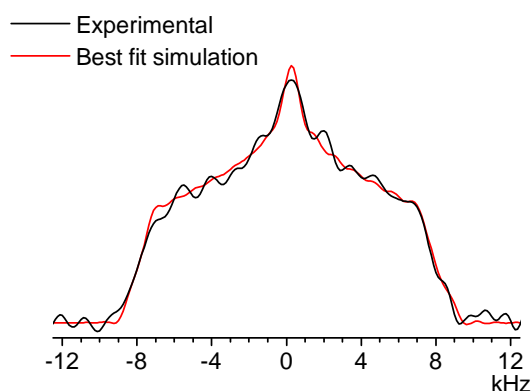
Figure 6.21: Experimental CT-2DCSA cross-section from the anisotropic dimension of the CT-2DCSA spectrum for the amide ^{13}C site of Ala-Ala. Overlaid in red is the best fit simulation. Best fit parameters $\delta_{\mathrm{aniso}} = 77 \pm 2$ ppm, $\eta_{\mathrm{CS}} = 0.96 \pm 0.04$, $\beta_{\mathrm{DC}} = 83 \pm 20$, $\gamma_{\mathrm{DC}} = 28 \pm 15$. F_1 spectral width was 30 kHz, 32 complex t_1 points were recorded and the spinning frequency was 5 kHz.

of signal intensity caused by the many π-pulses in the recoupling sequence, as discussed in Chapter 5. This may be particularly problematic for samples with an intrinsically low sensitivity. It should be noted, though, that the signal-to-noise ratio can always be improved by repeating the experiment, whereas there is no simple solution to determine unresolved features in a lineshape recorded by another method.

6.2.3   Experimental

All experiments in were performed using the same hardware described in Section 6.1.3. In the CT-2DCSA experiments, 10 pulse-sequence units were used with spinning frequencies of 3.15 kHz and 5 kHz for the C$_\alpha$ and amide sites respectively. ^{13}C π-pulse lengths were 7 μs, while ^{1}H decoupling used the SPINAL-64[54] method with an RF field strength of ~95 kHz. The ^{14}N decoupling used a RF field strength of 17 kHz, experiments using 3.15 kHz and 5 kHz MAS respectively used pulse lengths of 50 μs and 40 μs, and pulse rates of 3.5 kHz and 5.5 kHz.

6.3   CSA - quadrupolar tensor correlation for ^{13}C–^{14}N spin pairs

In this section, a new experiment to correlate the orientation of a ^{13}C chemical shift tensor and a ^{14}N quadrupole tensor is outlined. Although not discussed at length in Chapter 3, measurement of the quadrupole tensor can provide structural information in a similar

manner to the chemical shift interaction. This is because the electric field gradient at the nucleus depends of the electron density about the nucleus. The methods to measure the quadrupole tensor are very different to the chemical shift,[87] but both rely on numerical quantum mechanical calculations, or established empirical trends, for interpretation of measured tensor in terms of the structure.

As discussed earlier, ^{14}N is spin-1 and often experiences a quadrupole coupling constant of a few megahertz, which makes direct excitation and measurement of ^{14}N spectrum extremely difficult, although spectra have been reported for up to $C_Q/2\pi \approx 1.2$ MHz.[224] One possible strategy to obtain information about an ^{14}N nucleus is to use a nearby coupled spin-1/2 nucleus to 'probe' the quadrupole interaction. An approach to do this has very recently been developed by the groups of Gan[245] and Bodenhausen,[246] whereby the residual dipolar coupling is used to correlate the evolution of either ^{14}N single-quantum or double-quantum coherences during the t_1 period with the isotropic shift of the coupled ^{13}C nucleus. From this, the quadrupole coupling constant can be determined from the lineshape in the indirectly observed dimension of the spectrum. This interesting strategy has yielded good results for ^{13}C isotopically enriched samples, but at present the excitation efficiency for generating ^{14}N coherences is very low, and obtaining a useful signal-to-noise ratio with natural abundance ^{13}C samples is challenging.

The experiment that is pursued in this section is illustrated in Figure 6.22. The first part of the experiment can be thought of a filter applied before a CSA recoupling experiment. This filter can be identified as the REAPDOR¶ experiment.[257] The second part is the CT-2DCSA experiment described in Section 5.4.1 on page 137. The aim of the filter is to reduce the signal intensity selectively from a set of crystallite orientations, so that a modulation of the CSA powder pattern lineshape is observed in the spectrum from the CT-2DCSA part of the experiment. As shown in the following analysis and simulations, the modulation of the ^{13}C powder pattern depends on the relative orientations of the ^{14}N quadrupole, ^{13}C–^{14}N dipolar and ^{13}C chemical shift interaction tensors.

The REAPDOR filter consists of a period of heteronuclear dipolar recoupling, using the REDOR$^{\|}$ dipolar recoupling sequence,[98] followed by a ^{14}N pulse and a second period of dipolar recoupling. To evaluate the effect of the filter sequence, average Hamiltonian theory can be employed. In the first instance, the effect of the ^{14}N pulse is ignored. The

---

¶Rotational-Echo, Adiabatic-Passage DOuble-Resonance
$^{\|}$Rotational-Echo DOuble Resonance
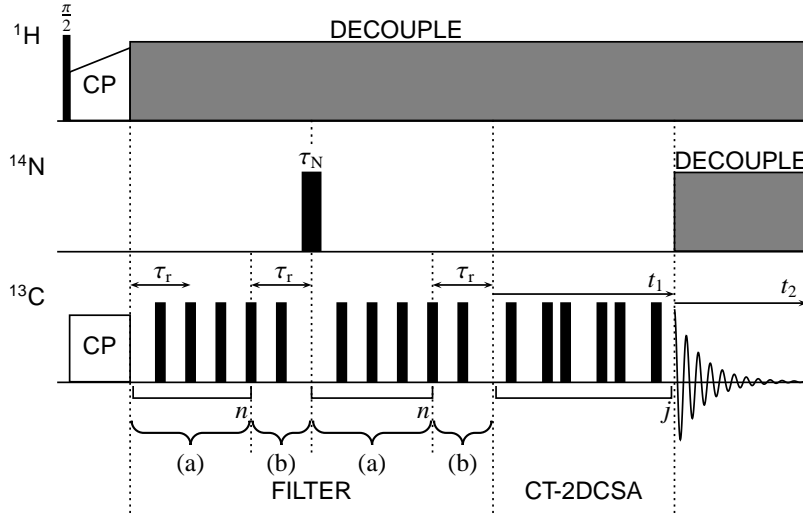
Figure 6.22: Proposed filtered CT-2DCSA experiment. Solid blocks are π-pulses, unless otherwise indicated. During the filter period, the sets of grouped π-pulses on the ^{13}C channel occur n times. Further details are given in the main text.

heteronuclear dipolar coupling Hamiltonian can be written as

$$\hat{\mathcal{H}}_{IS}(t) = \omega_{\mathrm{D}}(t; \Omega_{\mathrm{PL}})\hat{I}_z\hat{S}_z, \tag{6.19}$$

where ^{13}C is the I spin, ^{14}N is the S spin and $\omega_{\mathrm{D}}(t; \Omega_{\mathrm{PL}})$ describes the time dependence of the dipolar coupling interaction owing to MAS. It has a similar form to that of the chemical shift interaction introduced in Equation (2.8) on page 39, and is

$$\omega_{\mathrm{D}}(t; \Omega_{\mathrm{PR}}) = 2b_{IS}\left[-\frac{1}{\sqrt{2}}\sin(2\beta_{RL})\cos(\omega_{\mathrm{r}}t + \gamma_{RL}) + \frac{1}{2}\sin^2(\beta_{PR})\cos(2\omega_{\mathrm{r}}t + 2\gamma_{RL})\right]. \tag{6.20}$$

The propagator $\hat{U}(\tau_{\mathrm{filt}})$ of the rotating-frame density operator over the filter sequence can be divided into two parts: (a) the set of four π-pulses repeated n times in the sequence that are grouped and labelled '(a)' in Figure 6.22 ($\hat{U}_{\mathrm{a}}$); and (b) the following rotor period consisting of a single π-pulse ($\hat{U}_{\mathrm{b}}$), labelled '(b)' in Figure 6.22. The second half of the filter sequence is the same as the first half, so the propagator over the complete filter sequence is $\hat{U}(\tau_{\mathrm{filt}}) = \hat{U}_{\mathrm{b}}\left(\hat{U}_{\mathrm{a}}\right)^n \hat{U}_{\mathrm{b}}\left(\hat{U}_{\mathrm{a}}\right)^n$.

Using the same approach as in Section 4.2, $\hat{U}_{\mathrm{a}}$ is factored into two parts: $\hat{U}_{\mathrm{a}} = \hat{U}_{\mathrm{RF,a}}\hat{U}_{\mathrm{a}}^*$, $\hat{U}_{\mathrm{RF,a}}$ is the propagator due to the RF Hamiltonian while $\hat{U}_{\mathrm{a}}^*$ is due to the interaction-frame Hamiltonian. The interaction-frame Hamiltonian is calculated using

$$\hat{\mathcal{H}}_{IS}^*(t) = \hat{U}_{\mathrm{RF,a}}^{-1}(t)\hat{\mathcal{H}}_{IS}(t)\hat{U}_{\mathrm{RF,a}}(t). \tag{6.21}$$

The pulses are approximated to be infinitely short, and assumed to be x-pulses, so that after the qth pulse at τ_q the RF propagator is

$$\hat{U}_{\text{RF,a}}(t) = \exp\left\{-\text{i}q\pi\hat{I}_x\right\}, \qquad \tau_q < t < \tau_{q+1}, \tag{6.22}$$

and since the first part of the filter sequence consists of four π-pulses, $U_{\text{RF,a}} = \exp(-\text{i}4\pi\hat{I}_x)$. Including only the heteronuclear dipolar interaction, the interaction-frame first-order average Hamiltonian for section (a) of the filter sequence is

$$\overline{\mathcal{H}}_{\text{a}}^{(1)} = \frac{1}{2\tau_{\text{r}}}\hat{I}_z\hat{S}_z\left\{\int_0^{\frac{\tau_{\text{r}}}{2}}\omega_D(t';\Omega_{PR})\text{d}t' - \int_{\frac{\tau_{\text{r}}}{2}}^{\tau_{\text{r}}}\omega_D(t';\Omega_{PR})\text{d}t'\right.$$

$$\left. + \int_{\tau_{\text{r}}}^{\frac{3\tau_{\text{r}}}{2}}\omega_D(t';\Omega_{PR})\text{d}t' - \int_{3\frac{\tau_{\text{r}}}{2}}^{2\tau_{\text{r}}}\omega_D(t';\Omega_{PR})\text{d}t'\right\}$$

$$= \frac{\overline{D}}{\tau_{\text{r}}}\hat{I}_z\hat{S}_z, \tag{6.23}$$

$$\overline{D} = \int_0^{\frac{\tau_{\text{r}}}{2}}\omega_D(t';\Omega_{PR})\text{d}t' - \int_{\frac{\tau_{\text{r}}}{2}}^{\tau_{\text{r}}}\omega_D(t';\Omega_{PR})\text{d}t' \tag{6.24}$$

Similarly for part (b), $\hat{U}_{\text{b}} = \hat{U}_{\text{RF,b}}\hat{U}_{\text{b}}^*$, and $U_{\text{RF,b}} = \exp(-\text{i}\pi\hat{I}_x)$ with the interaction-frame first-order average Hamiltonian

$$\overline{\mathcal{H}}_{\text{b}}^{(1)} = \frac{\overline{D}}{\tau_{\text{r}}}\hat{I}_z\hat{S}_z \tag{6.25}$$

Combining these results, and approximating $\hat{U}_{\text{a}}^* = \exp\left(-\text{i}2\overline{\mathcal{H}}_{\text{a}}^{(1)}\tau_{\text{r}}\right)$ and $\hat{U}_{\text{b}}^* = \exp\left(-\text{i}\overline{\mathcal{H}}_{\text{b}}^{(1)}\tau_{\text{r}}\right)$, the rotating-frame propagator over the complete filter (in the absence of the ^{14}N pulse) is

$$\hat{U}(\tau_{\text{filt}}) = \hat{U}_{\text{b}}\hat{U}_{\text{a}}\hat{U}_{\text{b}}\hat{U}_{\text{a}}$$

$$= \text{e}^{-\text{i}\pi\hat{I}_x}\text{e}^{-\text{i}(\overline{D}\hat{I}_z\hat{S}_z)}\left(\text{e}^{-\text{i}4\pi\hat{I}_x}\text{e}^{-\text{i}(2\overline{D}\hat{I}_z\hat{S}_z)}\right)^n\text{e}^{-\text{i}\pi\hat{I}_x}\text{e}^{-\text{i}(\overline{D}\hat{I}_z\hat{S}_z)}\left(\text{e}^{-\text{i}4\pi\hat{I}_x}\text{e}^{-\text{i}(2\overline{D}\hat{I}_z\hat{S}_z)}\right)^n$$

$$= \text{e}^{-\text{i}\pi\hat{I}_x}\text{e}^{-\text{i}(\overline{D}\hat{I}_z\hat{S}_z)}\text{e}^{-\text{i}4n\pi\hat{I}_x}\text{e}^{-\text{i}(2n\overline{D}\hat{I}_z\hat{S}_z)}\text{e}^{-\text{i}\pi\hat{I}_x}\text{e}^{-\text{i}(\overline{D}\hat{I}_z\hat{S}_z)}\text{e}^{-\text{i}4n\pi\hat{I}_x}\text{e}^{-\text{i}(2n\overline{D}\hat{I}_z\hat{S}_z)}$$

$$= \text{e}^{-\text{i}(4n+1)\pi\hat{I}_x}\text{e}^{-\text{i}((1+2n)\overline{D}\hat{I}_z\hat{S}_z)}\text{e}^{-\text{i}(4n+1)\pi\hat{I}_x}\text{e}^{-\text{i}((1+2n)\overline{D}\hat{I}_z\hat{S}_z)}$$

$$= \text{e}^{-\text{i}(8n+2)\pi\hat{I}_x}\text{e}^{+\text{i}((1+2n)\overline{D}\hat{I}_z\hat{S}_z)}\text{e}^{-\text{i}\pi\hat{I}_x}\text{e}^{-\text{i}((1+2n)\overline{D}\hat{I}_z\hat{S}_z)}$$

$$= \text{e}^{-\text{i}(8n+2)\pi\hat{I}_x}, \tag{6.26}$$

where the relations $\text{e}^{-\text{i}\pi\hat{I}_x}\text{e}^{+\text{i}\pi\hat{I}_x} = \hat{\mathbf{1}}$ and $\text{e}^{+\text{i}\pi\hat{I}_x}\text{e}^{-\text{i}(\overline{D}\hat{I}_z\hat{S}_z)}\text{e}^{-\text{i}\pi\hat{I}_x} = \text{e}^{+\text{i}(\overline{D}\hat{I}_z\hat{S}_z)}$ have been used repeatedly. Equation 6.26 shows that evolution due to the heteronuclear dipolar coupling during the first half of the filter sequence is reversed (refocused) during the second half in the absence of a ^{14}N pulse. It may easily be shown that the pulse sequence also refocuses

the chemical shift evolution at the end of the pulse sequence. Thus, there is no change in the initial density operator following CP, where $\hat{\rho}(0) = \frac{1}{2}\left(\hat{I}_+ + \hat{I}_-\right) + \hat{S}_z$.

If an ^{14}N pulse is introduced at the mid-point of the filter sequence, then a quite different result is found. The ^{14}N pulse causes an adiabatic transfer of populations between the ^{14}N Zeeman states, which also causes a change in the ^{13}C single-quantum coherence evolution frequency, as described in Section 6.1.1. If this occurs, then the second half of the filter sequence will not refocus the evolution of each single-quantum coherence that occurred during the first half of the sequence.

Figure 6.4 showed that if the ^{14}N pulse is less than a third of a rotor period long, only a fraction of the crystallites in a powder sample contain ^{14}N nuclei that undergo an ω_Q zero-crossing. The ^{13}C nuclei dipolar coupled to those ^{14}N nuclei that do undergo a zero-crossing make a smaller contribution to the CSA powder pattern, because of the lack of refocusing described above. Those that do not will evolve as if the RF pulse was not used and their signals are refocussed at the end of the filter. This causes a modulation of the ideal CSA powder pattern lineshape, compared with the powder pattern recorded without the ^{14}N pulse during the filter sequence. The lineshape is characteristic of the orientation of the quadrupolar, dipolar and chemical shift tensor PAF orientations. This occurs because the relative orientation of the chemical shift tensor and quadrupolar tensor determines the frequency at which crystallites that undergo a zero-crossing appear in the quasi-static CSA powder patterns, while the dipolar coupling tensor orientation influences the value of $\overline{D}$ for each crystallite. However, precise prediction of the lineshapes generated by the pulse sequence in Figure 6.22 requires numerical simulations.

The quasi-static powder pattern lineshapes, obtained from the filtered CT-2DCSA experiment, depend on many parameters: for the ^{13}C chemical shift, δ_{aniso} and η_{CS}; for the dipolar coupling, b_{IS} and the orientation of the dipolar coupling tensor PAF with respect to the chemical shift tensor PAF Ω_{DC}; for the ^{14}N quadrupolar coupling, C_Q and η_Q and the orientation of the quadrupolar coupling tensor PAF with respect to the ^{13}C chemical shift tensor PAF Ω_{QC}; and for the ^{14}N pulse, the pulse duration (τ_{N}), the offset frequency ($\omega_{\text{iso}}^{\text{N}}$) and RF field strength (ω_1^{N}); and finally, the spinning frequency (ω_{r}) and the number of π-pulses used in the filter sequence. Fortunately, some of these parameters are known (ω_{r}, τ_{N}, number of π-pulses) or can be determined from the experiment described in Section 6.2 (^{13}C δ_{aniso}, η_{CS}, b_{IS}, Ω_{DC}). However, the ^{14}N quadrupolar coupling constants C_Q, η_Q, the ^{14}N offset frequency $\omega_{\text{iso}}^{\text{N}}$ and the Euler angles Ω_{QC} are unknown, and the aim is to determine these parameters from the quasi-static powder pattern experimental lineshape. In addition, inhomogeneity of the ^{14}N RF field across the sample volume

introduces a further complication.

Initial numerical simulations using representative parameters for peptide samples indicate that the main effect of the filter sequence is to cause a general reduction in intensity of the entire quasi-static powder pattern, rather than a significant change in the lineshape, at achievable ^{14}N RF field strengths (< 50 kHz). For the quadrupole tensor orientation, the quasi-static powder pattern lineshape is found to be sensitive mainly to the β_{QC} Euler angle, Figure 6.23. However, it only becomes possible to differentiate the effect of the quadrupolar tensor orientation on the quasi-static lineshape if high ^{14}N RF field strengths ($\omega_1^N > 40$ kHz) are used in the simulations, which also causes a significant loss of signal intensity, compared with a reference spectrum without an ^{14}N pulse used in the filter sequence.

Example simulated quasi-static lineshapes illustrating the effect of the offset frequency ω_{iso}^N, and the quadrupole coupling paramters C_Q and η_Q, are shown in Figure 6.24 and 6.25 respectively. In each case, an ^{14}N RF field strength in excess of 40 kHz is needed to obtain a quasi-static lineshape that shows a significant dependence on the simulation parameters and could, in principal, be used to determine the unknown quadrupolar parameters.

A high signal-to-noise ratio is expected to be required in order to determine the desired parameters (C_Q, η_Q, ω_{iso} and β_{QC}) by fitting the experimental lineshape. In order to see a change in the lineshape (rather than just a loss of intensity), high ^{14}N RF field strengths are required in the filter sequence, which also cause a significant loss of signal. In addition, the many π-pulses involved in the recoupling sequence also causes a signal loss, due to pulse imperfections and ^{13}C–^{14}N dipolar coupling. Both these factors will make it challenging to obtain spectra that have a useful signal-to-noise ratio and an experimental lineshape that can be fitted unambiguously by a simulated lineshape to determine the unknown quadrupolar tensor PAF orientation and parameters. This is illustrated by the preliminary experimental results shown in Figure 6.26 on page 206 for the amide ^{13}C site in Ala-Ala, where the signal-to-noise ratio is too low for detailed features of the static lineshape to be resolved in the ^{14}N dephased quasi-static lineshape, even after three days of experiment time. Comparison of the ^{14}N dephased lineshape with the reference spectrum indicates a slight change in lineshape, similar to that seen in the simulations shown in Figures 6.23-6.25 for an ^{14}N RF field strength $\omega_1^N = 30 - 40$ kHz. However, a detailed fitting of the experimental ^{14}N dephased lineshape has not been possible.

The available NMR probe used in the present study was limited to ^{14}N RF field strengths up to 35 kHz, and so it was not possible to use the filtered CT-2DCSA experiment as a

strategy to determine useful information about an ^{14}N nucleus via a dipolar coupled ^{13}C spin. Further work is required to investigate the potential of this experiment if higher ^{14}N RF field strengths can be used in the filter sequence to obtain a greater change in the ^{14}N dephased quasi-static powder pattern lineshape.

6.3.1   Simulation and experimental methods

Simulations were performed using the SIMPSON program.[39] The complete recoupling sequence was simulated using ideal π-pulses for the ^{13}C nuclei. A total of 18 π-pulses were used in the recoupling sequence and the duration of the ^{14}N pulse in filter sequence was $\tau_N = 62.5\,\mu$s, corresponding to $\tau_r/4$ at the spinning frequency used $\omega_r/2\pi = 4000$ kHz. The dipolar coupling constant was $b_{IS}/2\pi = -850$ Hz and the CSA parameters and dipolar tensor orientation (Ω_{DC}) were based on those for the amide ^{13}C site in Ala-Ala: $-\omega_0\Delta_{CS}/2\pi = 7.7$ kHz, $\eta_{CS} = 0.95$, $\Omega_{DC} = \{0, 90, 39.5\}$. The quadrupolar coupling parameters were $C_Q/2\pi = 3$ MHz, $\eta_Q = 0.25$, $\alpha_{QC} = 0$, $\gamma_{QC} = 0$, and the ^{14}N offset frequency was $\omega_{iso}^N/2\pi = 0$ kHz, unless otherwise stated. Powder averaging used 2000 (α,β) orientations following the REPULSION scheme,[72] and the maximum time step over which the Hamiltonian was treated as constant was 1 μs.

The experimental results were recorded using the same spectrometer hardware described in Section 6.1.3. In the filter sequence, 18 π-pulses were used with a ^{14}N pulse of duration $\tau_N = 62.5\,\mu$s, corresponding to $\tau_r/4$ at the spinning frequency used $\omega_r/2\pi = 4000$ kHz, and RF field strength of $\omega_1^N/2\pi = 35$ kHz. The CT-2DCSA sequence involved six pulse-sequence units and 32 complex t_1 data points were recorded. Cross polarization[44] used a ramped ^{1}H spin-lock field[50] and ^{1}H decoupling by the SPINAL-64[54] method was used with an RF field strength of ≈ 80 kHz.

6.4   Summary

A new method for removing the residual splitting seen in the MAS spectra of ^{13}C sites that are coupled to ^{14}N has been demonstrated. This ^{14}N decoupling method is simple to implement experimentally, and effective decoupling is achieved over a wide range of ^{14}N RF field strengths, pulse lengths and pulse rates. Decoupling of ^{14}N gives a significant improvement in the signal-to-noise ratio for ^{13}C sites where the residual
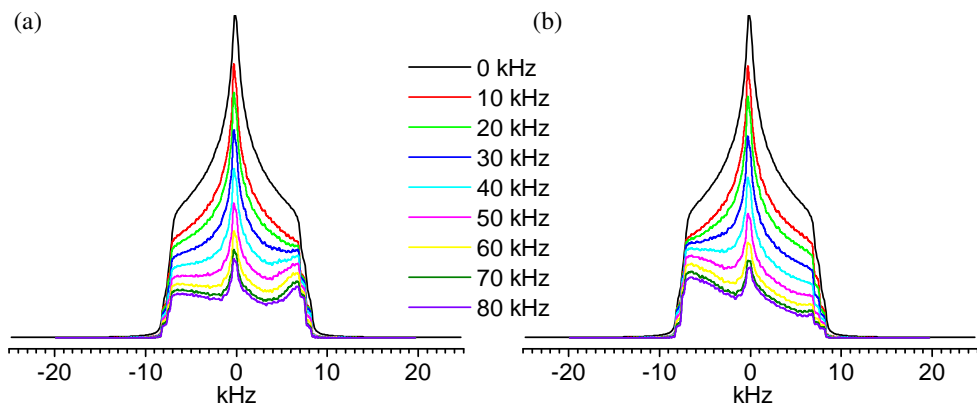
Figure 6.23: Simulations of the filtered CT-2DCSA experiment for a range of ^{14}N RF field strengths. (a) $\beta_{QC} = 0$ and (b) $\beta_{QC} = 90$. Other parameters are detailed in Section 6.3.1.
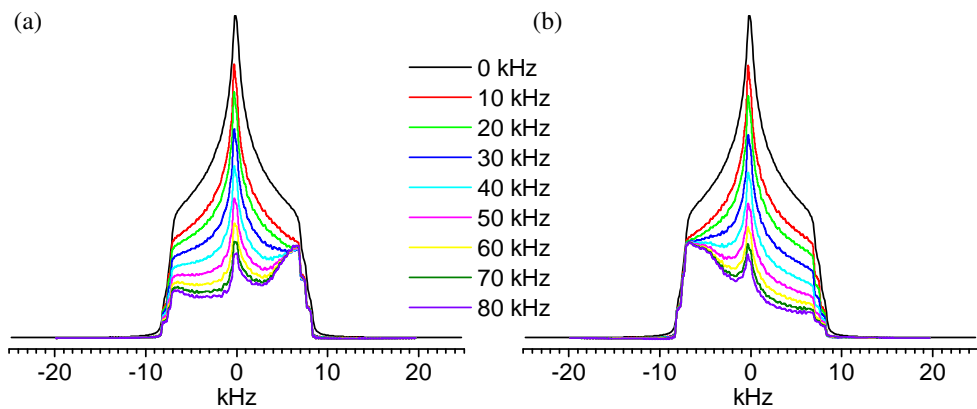
Figure 6.24: Simulations of the filtered CT-2DCSA experiment for an offset frequency of $\omega_{iso}^{N}/2\pi = 50$ kHz and (a) $\beta_{QC} = 0$ (compare with Figure 6.23(a)) and (b) $\beta_{QC} = 90$ (compare with Figure 6.23(b)) using a range of ^{14}N RF field strengths. Other parameters are detailed in Section 6.3.1.
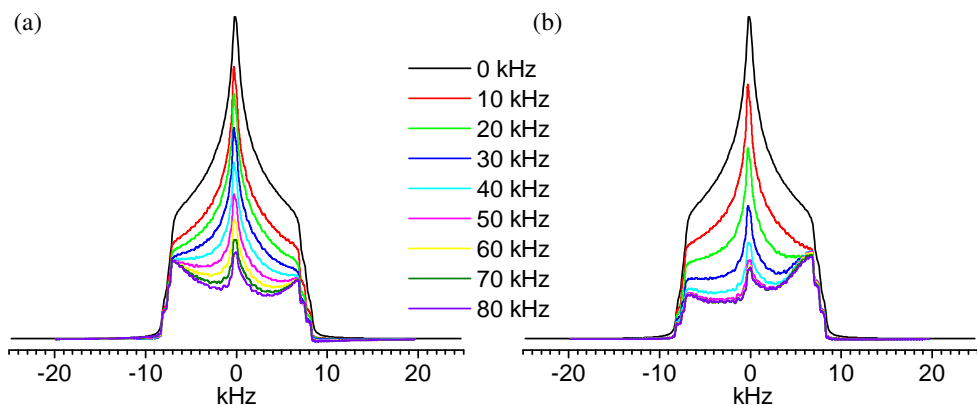
Figure 6.25: Simulations of the filtered CT-2DCSA experiment for (a) $\eta_Q = 1$ and $C_Q = 3$ MHz, and (b) $\eta_Q = 0.25$ and $C_Q = 1$ MHz, using a range of ^{14}N RF field strengths and $\beta_{QC} = 0$ in both cases (compare with Figure 6.23(a)). Other parameters are detailed in Section 6.3.1.
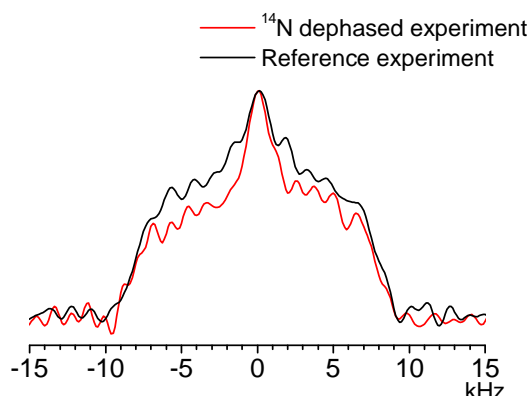
Figure 6.26: Experimental cross-sections for the amide ^{13}C site of Ala-Ala using the filtered CT-2DCSA pulse sequence in Figure 6.22. The filter used 18 π-pulses, and a ^{14}N pulse of duration $\tau_N = 0.25\tau_r$ and RF field strength $\omega_1^N/2\pi = 35$ kHz. A reference spectrum, recorded without ^{13}C–^{14}N dipolar dephasing, is shown for comparison. The two lineshapes are scaled to have the same maximum height.

dipolar-quadrupolar cross-term splitting is the dominant contribution to the linewidth, and simplifies the lineshapes that are obtained in two-dimensional experiments.

The use of ^{14}N decoupling in conjunction with the CT-2DCSA experiment was shown to allow measurement of dipolar modulated CSA powder patterns, from which the orientation of the internuclear axis between ^{13}C–^{14}N spin pairs in the ^{13}C chemical shift PAF could be determined. The use of ^{14}N decoupling allows cross-sections from the two-dimensional spectrum to be analysed, rather than requiring projections over the F_2 peak to be calculated, and increases the signal-to-noise ratio of the spectra.

Finally, a new experiment has been proposed to obtain information about the ^{14}N quadrupolar interaction in ^{13}C–^{14}N dipolar-coupled spin pairs, by measurement of ^{13}C signal. Simulations and experimental results show that the experiment requires higher ^{14}N RF field strengths than could be investigated experimentally in the present study, due to hardware limitations, and further work is needed to assess the potential of this approach.

7 | References

1. A. Abragam, *Principles of Nuclear Magnetism*, International series of monographs on physics, Oxford University Press, Oxford, 1961.

2. M. Mehring, *Principles of High Resolution NMR in Solids*, Springer-Verlag, Berlin, New York, 1983.

3. M. Goldman, *Quantum Description of High-Resolution NMR in Liquids*, International Series of Monographs of Chemistry, Oxford University Press, Oxford, 1988.

4. C. P. Slichter, *Principles of Magnetic Resonance*, Springer-Verlag, Berlin-Heidelberg, 3 ed., 1989.

5. K. Schmidt-Rohr and H. W. Spiess, *Multidimensional Solid-State NMR and Polymers*, Academic Press, London, San Diego, 1994.

6. M. Mehring and V. A. Weberruß, *Object-Oriented Magnetic Resonance*, Academic Press, San Diego, California, 2001.

7. M. H. Levitt, *Spin Dynamics*, John Wiley & Sons, Ltd, Chichester, 2001.

8. M. J. Duer, *Solid-State NMR Spectroscopy*, Blackwell Science, Oxford, 2004.

9. J. Keeler, *Understanding NMR Spectroscopy*, John Wiley & Sons Ltd, Chichester, 2005.

10. A. Messiah, *Quantum Mechanics*, Elsevier Science, Amsterdam, 1961.

11. P. W. Atkins and R. S. Friedman, *Molecular Quantum Mechanics*, Oxford University Press, Oxford, 3 ed., 1997.

12. J. C. Hoch and A. S. Stern, *NMR Data Processing*, Wiley-Liss, Inc., New York, 1996.

13. M. M. Maricq and J. S. Waugh, *J. Chem. Phys.*, 1979, **70**, 3300–3316.

14. U. Haeberlen, *High Resolution NMR in Solids*, Adv. Magn. Reson., Supplement 1, Academic Press, New York, 1976.

15. M. M. Maricq, *Phys. Rev. B*, 1988, **25**, 6622–6632.

16. U. Haeberlen and J. S. Waugh, *Phys. Rev.*, 1968, **175**, 2–10.

17. M. H. Levitt, *J. Magn. Reson.*, 1997, **126**, 164–182.

18. F. Bloch and A. Siegert, *Phys. Rev.*, 1940, **57**, 522–527.

19. N. Bloembergen, E. M. Purcell, and R. V. Pound, *Phys. Rev.*, 1948, **73**, 679–712.

20. R. R. Ernst and W. A. Anderson, *Rev. Sci. Instr.*, 1966, **37**, 93–102.

21. R. N. Bracewell, *The Fourier Transform and Its Applications*, McGraw-Hill, Singapore, 2000.

22. D. Moskau, *Concepts Magn. Reson.*, 2002, **15**, 164–176.

23. J. C. Lindon and A. G. Ferrige, *Prog. Nucl. Magn. Reson. Spec.*, 1980, **14**, 27–66.

24. R. R. Ernst, *Adv. Magn. Reson.*, 1966, **2**, 1–135.

25. W. G. Proctor and F. C. Yu, *Phys. Rev.*, 1950, **77**, 717.

26. N. F. Ramsey, *Phys. Rev.*, 1950, **78**, 699–703.

27. R. Schneiher, *J. Chem. Phys.*, 1968, **48**, 4905–4909.

28. R. G. Griffin, J. D. Ellett, M. Mehring, J. G. Bullitt, and J. S. Waugh, *J. Chem. Phys.*, 1972, **57**, 2147–2155.

29. M. N. Burnett and C. K. Johnson ORTEP-III: Oak Ridge thermal ellipsoid plot program for crystal structure illustrations Technical Report ORNL-6895, Oak Ridge National Laboratory, 1996.

30. R. Radeglia, *Solid State Nucl. Magn. Reson.*, 1995, **4**, 317–321.

31. N. Bloembergen and T. J. Rowland, *Acta. Met.*, 1953, **1**, 731–746.

32. P. G. Jönsson and A. Kvick, *Acta. Cryst. B*, 1972, **28**, 1827–1833.

33. J. Mason, *Solid State Nucl. Magn. Reson.*, 1993, **2**, 285–288.

34. J. Herzfeld and A. E. Berger, *J. Chem. Phys.*, 1980, **73**, 6021–6030.

35. E. R. Andrew and R. Bersohn, *J. Chem. Phys.*, 1950, **18**, 159–161.

36. J. H. Van Vleck, *Phys. Rev.*, 1948, **74**, 1168–1183.

37. S. N. Stuart, *J. Magn. Reson. Series A*, 1993, **101**, 327–328.

38. M. Goldman, P. J. Grandinetti, A. Llor, Z. Olejniczak, and J. R. Sachleben, *J. Chem. Phys*, 1992, **97**, 8947–8960.

39. M. Bak, J. Rasmussen, and N. Nielsen, *J. Magn. Reson.*, 2000, **147**, 296–330.

40. I. J. Lowe, *Phys. Rev. Lett.*, 1959, **2**, 285–287.

41. E. R. Andrew, A. Bradbury, and R. G. Eades, *Nature*, 1958, **182**, 1659.

42. A. Samoson, J. Past, I. Heinmaa, T. Tuherm, T. Anupõld, A. Reinhold, R. Stern, M. Ernst, B. Meier, Z. Gan, and M. Carravetta In *Abstr. 45 ENC, Asilomer*, 2004.

43. M. H. Levitt, *J. Magn. Reson.*, 1988, **82**, 427–433.

44. A. Pines, M. G. Gibby, and J. S. Waugh, *J. Chem. Phys.*, 1972, **56**, 1776–1777.

45. A. Pines, M. G. Gibby, and J. S. Waugh, *Chem. Phys. Lett*, 1972, **15**, 373–376.

46. S. Hartmann and E. Hahn, *Phys. Rev.*, 1962, **128**, 2042–2053.

47. A. Pines, M. G. Gibby, and J. S. Waugh, *J. Chem. Phys.*, 1973, **59**, 569–590.

48. E. O. Stejskal, J. Schaefer, and J. S. Waugh, *J. Magn. Reson.*, 1977, **28**, 105–112.

49. D. Marks and S. Vega, *J. Magn. Reson. Series A*, 1996, **118**, 157–172.

50. G. Metz, X. Wu, and S. O. Smith, *J. Magn. Reson. Series A*, 1994, **110**, 219–227.

51. T. M. Barbara and E. H. Williams, *J. Magn. Reson.*, 1992, **99**, 439–442.

52. A. E. Bennett, C. Rienstra, M. Auger, K. V. Lakshmi, and R. Griffin, *J. Chem. Phys.*, 1995, **103**, 6951–6958.

53. B. Fung, A. K. Khitrin, and K. Ermolaev, *J. Magn. Reson.*, 2000, **142**, 97–101.

54. T. Braunoger, P. Wormald, and P. Hodgkinson, *Monatsh. Chem.*, 2002, **133**, 1549–1574.

55. M. Ernst, *J. Magn. Reson.*, 2003, **162**, 1–34.

56. P. Hodgkinson, *Prog. Nucl. Magn. Reson. Spect.*, 2005, **46**, 197–222.

57. J. Keeler and D. Neuhaus, *J. Magn. Reson.*, 1985, **63**, 454–472.

58. D. J. States, R. A. Haberkorn, and D. J. Ruben, *J. Magn. Reson.*, 1982, **48**, 286–292.

59. D. Marion and K. Wuthruch, *Biochem Biophys. Res. Commun.*, 1983, **113**, 967–974.

60. P. Bachmann, W. P. Aue, L. Müller, and R. R. Ernst, *J. Magn. Reson.*, 1977, **28**, 29–39.

61. G. Bodenhausen, H. Kogler, and R. R. Ernst, *J. Magn. Reson.*, 1984, **58**, 370–388.

62. M. H. Levitt, P. K. Madhu, and C. E. Hughes, *J. Magn. Reson.*, 2002, **155**, 300–306.

63. G. Zuckerstätter and N. Müller, *J. Magn. Reson.*, 2006, **181**, 244–253.

64. A. Jerschow and R. Kumar, *J. Magn. Reson.*, 2003, **160**, 59–64.

65. C. E. Hughes, M. Carravetta, and M. H. Levitt, *J. Magn. Reson.*, 2004, **167**, 259–265.

66. N. Ivchenko, C. E. Hughes, and M. H. Levitt, *J. Magn. Reson.*, 2003, **160**, 52–58.

67. P. Hodgkinson and L. Emsley, *Prog. Nucl. Magn. Reson. Spec.*, 2000, **36**, 201–239.

68. M. Edén, *Concepts Magn. Reson. A*, 2003, **17**, 117–154.

69. M. Edén, *Concepts Magn. Reson. A*, 2003, **18**, 1–23.

70. M. Edén, *Concepts Magn. Reson. A*, 2003, **18**, 24–55.

71. M. Veshtort and R. G. Griffin, *J. Magn. Reson.*, 206, **178**, 248–283.

72. M. Bak and N. Chr. Nielsen, *J. Magn. Reson.*, 1997, **125**, 132–139.

73. V. B. Cheng, H. H. Suzukawa, and M. Wolfsberg, *J. Chem. Phys.*, 1973, **59**, 3992–3999.

74. M. Edén and M. H. Levitt, *J. Magn. Reson.*, 1998, **132**, 220–239.

75. B. Stevensson and M. Edén, *J. Magn. Reson.*, 2006, **181**, 162–176.

76. D. Reichert, *Annual Rev. NMR Spect.*, 2005, **55**, 159–203.

77. D. A. Middleton, X. Peng, D. Saunders, K. Shankland, W. I. David, and A. J. Markvardsen, *Chem. Comm.*, 2002, pp. 1976–1977.

78. J. Dutour, N. Guillou, C. H. F. Taulelle, C. Mellot-Draznieks, and G. Féret, *Solid State Sci.*, 2004, **6**, 1059–1067.

79. D. H. Brouwer, P. E. Kristiansen, C. A. Fife, and M. H. Levitt, *J. Am. Chem. Soc.*, 2005, **542**, 542–543.

80. D. H. Brouwer, R. J. Darton, R. E. Morris, and M. H. Levitt, *J. Am. Chem. Soc.*, 2005, **127**, 10365–10370.

81. J. F. Collin, T. Batalle, S. E. Ashbrook, N. Audebrand, L. Le Pollès, J. Y. Pivan, and E. Le Fur, *Inorg. Chem.*, 2006, **45**, 6034–6040.

82. O. N. Antzutkin, *Solid-State NMR Spectroscopy: Principles and Applications*, Blackwell Science, Oxford, 2002; chapter 7, pp. 280–390.

83. V. J. McBrierty and K. J. Packer, *Nuclear Magnetic Resonance in Solid Polymers*, Cambridge University Press, Cambridge, 1993.

84. R. J. Kirkpatrick, K. A. Smith, S. Schramm, G. Turner, and W. H. Yang, *Annu. Rev. Earth Planet. Sci.*, 1985, **13**, 29–47.

85. J. Klinowski, *Anal. Chim. Acta*, 1993, **283**, 929–965.

86. H. Eckert, *Prog. Nucl. Magn. Reson.*, 1992, **24**, 159–293.

87. S. E. Ashbrook and M. J. Duer, *Concepts Magn. Reson. A*, 2006, **28**, 183–248.

88. J. Cavanagh, W. J. Fairbrother, A. G. Palmer, and N. J. Skelton, *Protein NMR Spectroscopy: Principles and Practice*, Academic Press, San Diego, 1996.

89. ed. J. Mason, *Multinuclear NMR*, Plenum Press, New York, 1987.

90. S. Spera and A. Bax, *J. Am. Chem. Soc.*, 1991, **113**, 5490–5492.

91. A. C. de Dios, J. G. Pearson, and E. Oldfield, *Science*, 1993, **260**, 1491–1496.

92. R. K. Harris, P. Y. Ghi, H. Puschmann, D. C. Apperley, U. J. Griesser, R. B. Hammond, C. Ma, K. J. Roberts, G. J. Pearce, J. R. Yates, and C. J. Pickard, *Org. Process Res. Dev.*, 2005, **9**, 902–910.

93. I. J. King, F. Fayon, D. Massiot, R. K. Harris, and J. S. O. Evans, *Chem. Comm.*, 2001, pp. 1766–1767.

94. D. C. Apperley, A. H. Forster, R. K. H. R. Fournier 1, P. Hodgkinson, R. W. Lancaster, and T. Rades, *Magn. Reson. Chem.*, 2005, **43**, 881–892.

95. M. Edén and M. H. Levitt, *J. Chem. Phys.*, 1999, **111**, 1511–1519.

96. M. Carravetta, M. Edén, X. Zhao, A. Brinkmann, and M. H. Levitt, *Chem. Phys. Lett.*, 2000, **321**, 205–215.

97. M. H. Levitt in *Encyclopedia of Nuclear Magnetic Resonance*, Vol. 9; John Wiley & Sons, Ltd, Chichester, 2002; pp. 165–196.

98. T. Gullion and J. Schaefer, *J. Magn. Reson.*, 1989, **81**, 196–200.

99. Y. Pan, T. Gullion, and J. Schaefer, *J. Magn. Reson.*, 1990, **90**, 330–340.

100. J. R. Garbow and T. Gullion, *J. Magn. Reson.*, 1991, **94**, 442–445.

101. T. G. Oas, R. G. Griffin, and M. H. Levitt, *J. Chem. Phys.*, 1988, **89**, 692–695.

102. M. Bjerring and N. Chr. Nielsen, *Chem. Phys. Lett.*, 2003, **370**, 496–503.

103. J. C. Chan and H. Echert, *J. Chem. Phys.*, 2001, **115**, 6095–6105.

104. X. Zhao, M. Edén, and M. H. Levitt, *Chem. Phys. Lett.*, 2001, **342**, 353–361.

105. M. H. Levitt, D. P. Raleigh, F. Creuzet, and R. G. Griffin, *J. Chem. Phys.*, 1990, **92**, 6347–6364.

106. A. E. Bennett, J. H. Ok, and R. G. Griffin, *J. Chem. Phys.*, 1992, **96**, 8624–8627.

107. W. Sommer, J. Gottwald, D. E. Demco, and H. W. Spiess, *J. Magn. Reson. Series A*, 1995, **113**, 131–134.

108. Y. K. Lee, N. D. Kurur, M. Helmle, O. G. Johannessen, N. C. Nielsen, and M. H. Letvitt, *Chem. Phys. Lett*, 1995, **242**, 304–309.

109. S. Dusold and A. Sebald, *Annual Rev. NMR Spect.*, 2000, **41**, 185–264.

110. Y. Todokoro, I. Yumen, K. Fukushima, S. Kang, J. Park, T. Kohno, K. Wakamatsu, H. Akutsu, and T. Fujiwara, *Biophys. J.*, 2006, **91**, 1368–1379.

111. C. Jäeger, N. S. Groom, E. A. Bowe, A. Horner, M. E. Davies, R. C. Murray, and M. J. Duer, *Chem. Mater.*, 2005, **17**, 3059–3061.

112. C. Brown, R. Achey, R. Fu, T. Gedris, and A. E. Stiegman, *J. Am. Chem. Soc.*, 2005, **127**, 11590–11591.

113. T. Gullion and C. H. Pennington, *Chem. Phys. Lett.*, 1998, **290**, 88–93.

114. G. Goobes, V. Raghumathan, E. A. Louie, J. M. Gibson, G. L. Olsen, and G. P. Drobny, *Solid State Nucl. Magn. Reson.*, 2006, **29**, 242–250.

115. C. A. Michal and L. W. Jelinski, *J. Am. Chem. Soc.*, 1997, **119**, 9059–9060.

116. C. P. Jaroniec, J. C. Lansing, B. A. Tounge, M. Belenky, J. Herzfeld, and R. G. Griffin, *J. Am. Chem. Soc.*, 2001, **123**, 1292–1293.

117. C. P. Jaroniec, B. A. Tounge, J. Herzfeld, and R. G. Griffin, *J. Am. Chem. Soc.*, 2001, **123**, 3507–3519.

118. C. P. Jaroniec, C. Filip, and R. G. Griffin, *J. Am. Chem. Soc.*, 2002, **124**, 10728–10742.

119. C. P. Jaroniec, C. E. MacPhee, V. S. Bajaj, M. T. McMahon, C. M. Dobson, and R. G. Griffin, *Proc. Natl. Acad. Sci. U.S.A.*, 2004, **101**, 711–716.

120. L. Sonnenberg, S. Luca, and M. Baldus, *J. Magn. Reson.*, 2004, **166**, 100–110.

121. J. Schmedt auf der Günne, *J. Magn. Reson.*, 2006, **180**, 186–196.

122. B. Elena and L. Emsley, *J. Am. Chem. Soc.*, 2005, **127**, 9140–9146.

123. B. Elena, G. Pintacuda, N. Mifsud, and L. Emsley, *J. Am. Chem. Soc.*, 2006, **128**, 9555–9560.

124. H. Heise, W. Hoyer, S. Becker, O. C. Andronesi, D. Riedel, and M. Baldus, *Proc. Natl. Acad. Sci. U.S.A.*, 2005, **102**, 15871–15876.

125. G. Cornilescu, F. Delaglio, and A. Bax, *J. Biomol. NMR.*, 1999, **13**, 289–302.

126. W. S. Veeman, *Prog. Nucl. Magn. Reson. Spec.*, 1984, **16**, 193–235.

127. J. Smith, E. MacNamara, D. Raftery, T. Borchardt, and S. Byrn, *J. Am. Chem. Soc.*, 1998, **120**, 11710–11713.

128. E. A. Christopher, R. K. Harris, and R. A. Fletton, *Solid State Nucl. Magn. Reson.*, 1992, **1**, 93–101.

129. J. R. Smith, W. Xu, and D. Raftery, *J. Phys. Chem. B*, 2006, **110**, 7766–7776.

130. J. D. Mao and K. Schmidt-Rohr, *Solid State Nucl. Magn. Reson.*, 2004, **26**, 36–45.

131. A. C. de Dios and E. Oldfield, *Solid State Nucl. Magn. Reson.*, 1996, **6**, 101–125.

132. D. Sitkoff and D. A. Case, *Prog. Nucl. Magn. Reson. Spect.*, 1998, **32**, 165–190.

133. U. Sternberg, R. Witter, and A. Ulrich, *Annual Rev. NMR Spect.*, 2004, **52**, 53–104.

134. A. M. Orendt, J. C. Facelli, and D. M. Grant, *Chem. Phys. Lett.*, 1999, **302**, 499–504.

135. G. Wu, K. Yamada, S. Dong, and H. Grondey, *J. Am. Chem. Soc.*, 2000, **122**, 4215–4216.

136. M. Strohmeier, D. Stueber, and D. M. Grant, *J. Phys. Chem. A*, 2003, **107**, 7629–7642.

137. M. Strohmeier and D. M. Grant, *J. Am. Chem. Soc.*, 2004, **126**, 966–977.

138. M. D. Segall, P. J. D. Lindan, M. J. Probert, C. J. Pickard, P. J. Hasnip, S. J. Clark, and M. C. Payne, *J. Phys. Condens. Matter*, 2002, **14**, 2717–2744.

139. C. J. Pickard and F. Mauri, *Phys. Rev. B*, 2001, **63**, 245101.

140. J. R. Yates, S. E. Dobbins, C. J. Pickard, F. Mauri, P. Y. Ghic, and R. K. Harris, *Phys. Chem. Chem. Phys.*, 2005, **7**, 1402–1407.

141. C. Gervais, R. Dupree, K. J. Pike, C. Bonhomme, M. Profeta, C. J. Pickard, and F. Mauri, *J. Phys. Chem. A*, 2005, **109**, 6960–6969.

142. R. K. Harris, P. Y. Ghi, R. B. Hammond, C. Y. Ma, K. J. Roberts, J. R. Yates, and C. J. Pickard, *Magn. Reson. Chem.*, 2006, **44**, 325–333.

143. F. Koch, W. Prieß, R. Witter, and U. Sternberg, *Macromol. Chem. Phys.*, 2000, **201**, 1930–1939.

144. S. Rossano, F. Mauri, C. J. Pickard, and I. Farnan, *J. Phys. Chem. B*, 2005, **109**, 7245–7250.

145. R. Witter, U. Sternberg, and A. S. Ulrich, *J. Am. Chem. Soc.*, 2006, **128**, 2236–2243.

146. R. K. Harris, *Analyst*, 2006, **131**, 351–373.

147. N. Tjandra and A. Bax, *J. Am. Chem. Soc.*, 1997, **119**, 9576–9577.

148. R. H. Havlin, H. Le, D. D. Laws, A. C. deDios, and E. Oldfield, *J. Am. Chem. Soc.*, 1997, **119**, 11951–11958.

149. H. Sun, L. K. Sanders, and E. Oldfield, *J. Am. Chem. Soc.*, 2002, **124**, 5486–5495.

150. M. Hong, *J. Am. Chem. Soc.*, 2000, **122**, 3762–3770.

151. E. Y. Chekmenev, R. Z. Xu, M. S. Mashuta, and R. J. Wittebort, *J. Am. Chem. Soc.*, 2002, **124**, 11894–11899.

152. J. Birn, A. Poon, Y. Mao, and A. Ramamoorthy, *J. Am. Chem. Soc.*, 2004, **126**, 8529–8534.

153. R. Witter, S. Hesse, and U. Sternberg, *J. Magn. Reson.*, 2003, **161**, 35–42.

154. S. Hesse and C. Jäeger, *Cellulose*, 2005, **12**, 5–14.

155. R. Witter, U. Sternberg, S. Hesse, T. Kondo, F. Koch, and A. S. Ulrich, *Macromolecules*, 2006, **39**, 6125–6132.

156. J. K. Harper, D. H. Barich, E. M. Heider, and D. M. Grant, *Cryst. Growth. & Design*, 2005, **5**, 1737–1742.

157. J. K. Harper, D. M. Grant, Y. Zhang, P. L. Lee, and R. Von Dreele, *J. Am. Chem. Soc.*, 2006, **128**, 1547–1552.

158. S. Olejniczak and M. J. Potrzebowski, *Org. Biomol. Chem.*, 2004, **2**, 2315–2322.

159. C. E. Hughes, S. Olejniczak, J. Helinski, W. Ciesielski, M. Repisky, O. C. Andronesi, M. J. Potrzebowski, and M. Baldus, *J. Phys. Chem. B*, 2005, **109**, 23175–23182.

160. M. Linder, A. Höhener, and R. R. Ernst, *J. Chem. Phys.*, 1980, **73**, 4959–4970.

161. Y. Wei, D. Lee, and A. Ramamoorthy, *Chem. Phys. Lett.*, 2000, **324**, 20–24.

162. S. Kaplan, A. Pines, R. G. Griffin, and J. S. Waugh, *Chem. Phys. Lett.*, 1974, **25**, 78–79.

163. C. J. Hartzell, M. Whitfield, T. G. Oas, and G. P. Drobny, *J. Am. Chem. Soc.*, 1987, **109**, 5966–5969.

164. Y. Wei, D. Lee, and A. Ramamoorthy, *J. Am. Chem. Soc.*, 2001, **123**, 6118–6126.

165. Y. Wei, D. Lee, A. E. McDermott, and A. Ramamoorthy, *J. Magn. Reson.*, 2002, **158**, 23–35.

166. M. Strohmeier, D. W. Alderman, and D. Grant, *J. Magn. Reson.*, 2002, **155**, 263–177.

167. S. Wi, H. Sun, E. Oldfield, and M. Hong, *J. Am. Chem. Soc.*, 2005, **127**, 6451–6458.

168. F. J. Blanco and R. Tycko, *J. Magn. Reson.*, 2001, **149**, 131–138.

169. M. Hong, J. D. Gross, C. M. Rienstra, R. G. Griffin, K. K. Kumashiro, and K. Schmidt-Rohr, *J. Magn. Reson.*, 1997, **129**, 85–92.

170. S. Pausak, J. Tegenfeldt, and J. S. Waugh, *J. Chem. Phys.*, 1974, **61**, 1338–1344.

171. T. Vosegaard, E. Hald, V. Langer, H. J. Skov, P. Daugaard, H. Bildœ, and H. J. Hakobsen, *J. Magn. Reson.*, 1998, **135**, 126–132.

172. S. C. Shekar, A. Ramamoorthy, and R. J. Witterbort, *J. Magn. Reson.*, 2002, **155**, 257–262.

173. H. J. M. De Groot, S. O. Smith, A. C. Kolbert, J. M. L. Courtin, C. Winkel, J. Lugtenburg, and R. G. Griffin, *J. Magn. Reson.*, 1991, **91**, 30–38.

174. N. J. Clayden, C. M. Dobson, L. Lian, and D. J. Smith, *J. Magn. Reson.*, 1986, **69**, 476–487.

175. O. N. Antzutkin, Y. K. Lee, and M. H. Levitt, *J. Magn. Reson.*, 1998, **135**, 144–155.

176. P. Hodgkinson and L. Emsley, *J. Phys. Chem.*, 1997, **107**, 4808–4816.

177. G. E. Maciel, N. M. Szeverenyi, and M. Sardashti, *J. Magn. Reson.*, 1985, **64**, 365–374.

178. J. R. Sachleben and L. Frydman, *Solid State Nucl. Magn. Reson.*, 1997, **7**, 301–311.

179. R. C. Zeigler, R. A. Wind, and G. E. Maciel, *J. Magn. Reson.*, 1988, **79**, 299–306.

180. A. C. Kolbert, D. P. Raleigh, M. H. Levitt, and R. G. Griffin, *J. Phys. Chem.*, 1989, **90**, 679–689.

181. A. Bax, N. M. Szeverenyi, and G. E. Maciel, *J. Magn. Reson*, 1983, **55**, 494–497.

182. A. Bax, N. M. Szeverenyi, and G. E. Maciel, *J. Magn. Reson*, 1983, **52**, 147–152.

183. T. Mizuno, K. Takegoshi, and T. Terao, *J. Magn. Reson.*, 2004, **171**, 15–19.

184. L. Frydman, G. Chingas, Y. Lee, P. Grandinetti, M. Eastman, G. Barrall, and A. Pines, *J. Chem. Phys.*, 1992, **97**, 4800–4808.

185. M. A. Alla, E. I. Kundla, and E. T. Lippmaa, *JETP Lett.*, 1978, **27**, 194–197.

186. Y. Yarim-Agaev, P. N. Tutunjian, and J. S. Waugh, *J. Magn. Reson.*, 1982, **47**, 51–60.

187. A. Bax, N. M. Szeverenyi, and G. E. Maciel, *J. Magn. Reson.*, 1983, **51**, 400–408.

188. R. Tycko, G. Dabbagh, and P. A. Mirau, *J. Magn. Reson.*, 1989, **85**, 265–274.

189. Y. Ishii, J. Ashida, and T. Terao, *Chem. Phys. Lett.*, 1995, **246**, 439–445.

190. S. Liu, J. Mao, and K. Schmidt-Rohr, *J. Magn. Reson.*, 2002, **155**, 15–28.

191. M. Hong, D. Isailovic, R. A. McMillan, and V. P. Conticello, *Biopolymers*, 2003, **70**, 158–168.

192. R. Y. Dong, J. Zhang, and K. Fodor-Csorba, *Chem. Phys. Lett.*, 2006, **417**, 475–479.

193. Y. Ishii and T. Terao, *J. Chem. Phys.*, 1998, **109**, 1366–1374.

194. Z. Gan, *J. Am. Chem. Soc.*, 1992, **114**, 8307–8310.

195. J. Z. Hu, A. M. Orendt, D. W. Alderman, R. J. Pugmire, C. H. Ye, and D. M. Grant, *Solid State Nucl. Magn. Reson.*, 1994, **3**, 181–197.

196. J. Z. Hu, W. Wang, F. Liu, M. S. Solum, D. W. Alderman, R. J. Pugmire, and D. M. Grant, *J. Magn. Reson*, 1995, **113**, 210–222.

197. J. Z. Hu, D. W. Alderman, C. Ye, R. J. Pugmire, C. H. Ye, and D. M. Grant, *J. Magn. Reson. Series A*, 1993, **105**, 82–87.

198. D. W. Alderman, G. McGeorge, J. Z. Hu, R. J. Pugmuire, and D. M. Grant, *Mol. Phys.*, 1998, **95**, 1113–1126.

199. G. McGeorge, D. W. Alderman, and D. M. Grant, *J. Magn. Reson.*, 1999, **137**, 138–143.

200. W. T. Dixon, *J. Chem. Phys.*, 1982, **77**, 1800–1809.

201. S. De Lacroix, J. J. Titman, A. Hagemeyer, and H. Spiess, *J. Magn. Reson.*, 1992, **97**, 435–443.

202. O. N. Antzutkin, S. C. Shekar, and M. H. Levitt, *J. Magn. Reson.*, 1995, **115**, 7–19.

203. C. Crockford, H. Geen, and J. J. Titman, *Chem. Phys. Lett.*, 2001, **344**, 367–373.

204. L. Shao, C. Crockford, H. Geen, G. Grasso, and J. J. Titman, *J. Magn. Reson.*, 2004, **167**, 75–86.

205. T. Gullion, *J. Magn. Reson.*, 1989, **85**, 614–619.

206. M. Strohmeier and D. M. Grant, *J. Magn. Reson.*, 2004, **168**, 296–307.

207. G. McGeorge, J. Z. Hu, C. L. Mayne, D. W. Alderman, R. J. Pugmire, and D. M. Grant, *J. Magn. Reson.*, 1997, **129**, 134–144.

208. B. Eléna, S. Hediger, and L. Emsley, *J. Magn. Reson.*, 2003, **160**, 40–46.

209. C. Crockford *New methodologies in solid-state NMR* PhD thesis, University of Nottingham, 2002.

210. SciFace Software GmbH & Co.KG, *Mupad Computer Algebra System*, 2005.

211. D. Reichert and G. Hempel, *Concepts Magn. Reson. A*, 2002, **14**, 130–139.

212. H. Fritz and H. Sauter, *J. Magn. Reson.*, 1975, **18**, 527–544.

213. T. Gullion, D. B. Baker, and M. S. Conradi, *J. Magn. Reson.*, 1990, **89**, 479–484.

214. T. Gullion and J. Schaefer, *J. Magn. Reson.*, 1991, **92**, 439–442.

215. L. Shao, C. Crockford, and J. J. Titman, *J. Magn. Reson.*, 2006, **178**, 155–161.

216. E. Vinogradov, P. K. Madhu, and S. Vega, *Top. Curr. Chem.*, 2005, **246**, 33–90.

217. D. P. Raleigh, M. H. Levitt, and R. G. Griffin, *Chem. Phys. Lett.*, 1988, **146**, 71–76.

218. S. R. Kiihne, A. F. L. Creemers, J. Lugtenburg, and H. J. M. De Groot, *J. Magn. Reson.*, 2005, **172**, 1–8.

219. A. E. Bennett, C. M. Rienstra, J. M. Griffiths, W. Zhen, P. T. Lansbury, and R. G. Griffin, *J. Chem. Phys.*, 1998, **108**, 9463–9479.

220. O. Antzutkin, Z. Song, X. Feng, and M. Levitt, *J. Chem. Phys.*, 1994, **100**, 130–140.

221. K. Nagayama, P. Bachmann, K. Wüthrich, and R. R. Ernst, *J. Magn. Reson.*, 1969, **31**, 133–148.

222. E. R. deAzevedo, W. G. Hu, T. J. Bonagamba, and K. Schmidt-Rohr, *J. Chem. Phys.*, 2000, **112**, 8988–9001.

223. R. S. Stein *Structural studies using solid-state NMR* PhD thesis, University of Cambridge, 2006.

224. T. Giavani, H. Bildsøe, J. Skibsted, and H. J. Jakobsen, *J. Magn. Reson.*, 2004, **166**, 262–272.

225. D. L. VanderHart and H. S. Gutowsky, *J. Am. Chem. Soc.*, 1967, **89**, 5056–5057.

226. J. G. Hexem, M. H. Frey, and S. J. Opella, *J. Chem. Phys.*, 1982, **77**, 3847–3856.

227. A. Naito, S. Ganapathy, and C. A. McDowell, *J. Magn. Reson.*, 1982, **48**, 367–381.

228. A. C. Olivieri, L. Frydman, and L. E. Diaz, *J. Magn. Reson.*, 1987, **75**, 50–62.

229. R. K. Harris and A. C. Olivieri, *Prog. Nucl. Magn. Reson.*, 1992, **24**, 435–456.

230. A. C. Olivieri, *J. Magn. Reson.*, 1989, **81**, 201–205.

231. S. Ding and C. A. McDowell, *J. Chem. Phys.*, 1997, **107**, 7762–7772.

232. Z. Gan and D. M. Grant, *J. Magn. Reson.*, 1990, **90**, 522–534.

233. S. Wi, S. E. Ashbrook, S. Wimperis, and L. Frydman, *J. Chem. Phys.*, 2003, **118**, 3131–3140.

234. K. Takegoshi, A. Naito, and C. A. McDowell, *Magn. Reson. Chem.*, 1986, **24**, 544.

235. S. Vega, *J. Chem. Phys.*, 1978, **68**, 5518–5527.

236. A. J. Vega, *J. Magn. Reson.*, 1992, **96**, 50–68.

237. C. P. Grey, W. S. Veeman, and A. J. Vega, *J. Chem. Phys.*, 1993, **98**, 7711–7724.

238. E. Hughes, T. Gullion, A. Goldbourt, S. Vega, and A. Vega, *J. Magn. Reson.*, 2002, **156**, 230–241.

239. Y. Ba, H. Kao, C. P. Grey, L. Chopin, and T. Gullion, *J. Magn. Reson.*, 1998, **133**, 104–114.

240. K. V. Ramanathan and S. J. Opella, *J. Magn. Reson.*, 1988, **78**, 367–370.

241. R. Tycko and S. J. Opella, *J. Chem. Phys.*, 1987, **86**, 1761–1774.

242. L. Delevoye, C. Fernandez, C. M. Morais, J. Amoureux, V. Montouillout, and J. Rocha, *Solid State Nucl. Magn. Reson.*, 2002, **22**, 501–512.

243. R. J. Fletterick, C. Tsai, and R. E. Hughes, *J. Phys. Chem.*, 1971, **75**, 918–922.

244. W. H. Press, S. A. Teukolsky, W. T. Vetterling, and B. P. Flannery, *Numerical Recipes*, Cambridge University Press, Cambridge, 2 ed., 1992.

245. Z. Gan, *J. Am. Chem. Soc.*, 2006, **128**, 6040–6041.

246. S. Cavadini, A. Lupulescu, S. Antonijevic, and G. Bodenhausen, *J. Am. Chem. Soc.*, 2006, **128**, 7706–7707.

247. C. P. Grey, A. P. Eijkelenboom, and W. S. Veeman, *Solid State Nucl. Magn. Reson.*, 1995, **4**, 113–120.

248. L. Frydman and J. S. Harwood, *J. Am. Chem. Soc.*, 1995, **117**, 5367–5368.

249. S. Wi and L. Frydman, *J. Chem. Phys.*, 2000, **112**, 3248–3261.

250. T. Oas, C. J. Hartzell, T. J. McMahon, G. P. Drobny, and F. W. Dahiquist, *J. Am. Chem. Soc.*, 1987, **109**, 5956–5962.

251. F. Saparovic, K. Hayamizu, R. Smith, and B. A. Cornell, *Chem. Phys. Lett.*, 1991, **181**, 157–162.

252. T. Asakura, Y. Yamazaki, K. W. Seng, and M. Demura, *J. Mol. Struct.*, 1998, **446**, 179–190.

253. R. Tycko and D. P. Weliky, *J. Chem. Phys.*, 1996, **105**, 7915–7930.

254. J. Heller, D. D. Laws, M. Tomaselli, D. S. King, D. E. Wemmer, A. Pines, R. H. Havlin, and E. Oldfield, *J. Am. Chem. Soc.*, 1997, **119**, 7827–7831.

255. L. Odgaard, M. Bak, H. J. Jakobsen, and N. Chr. Nielsen, *J. Magn. Reson.*, 2001, **148**, 298–308.

256. ed. D. R. Lide, *CRC Handbook of Chemistry and Physics*, CRC Press, Boca Raton, 84 ed., 2003.

257. T. Gullion, *Chem. Phys. Lett.*, 1995, **246**, 325–330.

258. M. E. Rose, *Elementary Theory of Angular Momentum*, Dover Publications, New York, 1995.

259. S. Ganapathy, S. Schramm, and E. Oldfield, *J. Chem. Phys.*, 1982, **77**, 4360–4365.

A
Quantum Mechanical Notation

A.1   Wavefunctions and Operators

The quantum mechanical description of an isolated system of nuclei, often referred to as a (nuclear) spin system, is given by a wavefunction, denoted here by Ψ. It is usual in NMR to factor the wavefunction into a spatial wavefunction, that depends only upon the positions of the the nuclei in the spin system, and a nuclear spin wavefunction that describes the spin states: $|\Psi\rangle = |\psi_{\text{spin}}\rangle|\psi_{\text{spatial}}\rangle$. In most cases, for NMR, only the nuclear spin wavefunction of the system needs to be considered, hereafter is is assumed that wavefunctions refer only to the spin wavefunction.

The value of an observable represented by the operator $\hat{Q}$ averaged over multiple measurements (the expectation value) is calculated from the wavefunction describing the spin system by

$$\langle\hat{Q}\rangle = \frac{\langle\psi|\hat{Q}|\psi\rangle}{\langle\psi|\psi\rangle}, \tag{A.1}$$

where Dirac notation has been employed for convenience. In the case that the wavefunction satisfies

$$\hat{Q}|\psi\rangle = q|\psi\rangle, \tag{A.2}$$

where q is a constant, the wavefunction is termed an eigenfunction (or eigenstate) of the operator $\hat{Q}$, and q is its eigenvalue.

Over time, the wavefunction of a system evolves according to the Schrödinger equation (in both bra and ket form):

$$\frac{\partial|\psi(t)\rangle}{\partial t} = -\frac{\mathrm{i}}{\hbar}\hat{\mathcal{H}}(t)|\psi(t)\rangle \qquad\qquad \frac{\partial\langle\psi(t)|}{\partial t} = \frac{\mathrm{i}}{\hbar}\langle\psi(t)|\hat{\mathcal{H}}(t), \tag{A.3}$$

where $\hat{\mathcal{H}}(t)$ is the quantum mechanical operator for the energy of the system, referred to as the Hamiltonian. In the case that the Hamiltonian is time-independent, there are

solutions to the time-dependent Schrödinger equation of the form

$$|\psi(t)\rangle = |\psi'\rangle \exp(-iEt/\hbar), \tag{A.4}$$

where $|\psi'\rangle$ is also time-independent and satisfies the time-independent Schrördinger equation

$$\hat{\mathcal{H}}|\psi'\rangle = E|\psi'\rangle, \tag{A.5}$$

with E corresponding to the energy of the state represented by $|\psi'\rangle$.

By redefining the Hamiltonian as $\hat{\mathcal{H}}/\hbar \rightarrow \hat{\mathcal{H}}$ (and $E/\hbar \rightarrow E$), the factor of $1/\hbar$ disappears from Equation (A.3) and the exponential factor in Equation (A.5), with the consequence that energies are specified in angular frequency units.

A.2   Angular Momentum Operators

The Cartesian components of the angular momentum operator, $\hat{\boldsymbol{J}}$, are defined as

$$\hat{J}_x = -i\hbar\left(y\frac{\partial}{\partial z} - z\frac{\partial}{\partial y}\right) \tag{A.6}$$

$$\hat{J}_y = -i\hbar\left(z\frac{\partial}{\partial x} - x\frac{\partial}{\partial z}\right) \tag{A.7}$$

$$\hat{J}_z = -i\hbar\left(x\frac{\partial}{\partial y} - y\frac{\partial}{\partial x}\right). \tag{A.8}$$

An equivalent definition for the component parallel to a unit vector $\boldsymbol{n}$, in terms of the angle of rotation, φ, about this direction, is

$$\hat{J}_{\boldsymbol{n}} = -i\hbar\frac{\partial}{\partial\varphi}. \tag{A.9}$$

The factor of $\hbar$ included in the right hand side of Equation (A.6) gives the angular momentum in the usual SI units. Hereafter, the quantity $\hbar$ will be omitted from the right hand side, with the effect that angular momentum is given in units of $\hbar$. These three Cartesian components of the angular momentum may be shown to obey the commutation relations

$$\left[\hat{J}_x, \hat{J}_y\right] = i\hat{J}_z, \quad \left[\hat{J}_y, \hat{J}_z\right] = i\hat{J}_x, \quad \left[\hat{J}_z, \hat{J}_x\right] = i\hat{J}_y. \tag{A.10}$$

So each Cartesian component commutes with the square of the total angular momentum, $\hat{J}^2 = \hat{J}_x^2 + \hat{J}_y^2 + \hat{J}_z^2$. Consequently, wavefunctions may be found that are eigenfunctions of both $\hat{J}^2$ and one (arbitrary) Cartesian component $\hat{J}_\alpha$ ($\alpha = x, y, z$). However, as the individual Cartesian components of the angular momentum do not commute, these eigenfunctions will not be eigenfunctions of either of the other two Cartesian components. It is usual to consider eigenfunctions of $\hat{J}^2$ and $\hat{J}_z$.

The eigenfunctions of the $\hat{J}^2$ and $\hat{J}_z$ are the spherical harmonics that are characterised by two quantum numbers: J and m_J, which must both be integers. If the eigenvalue of $\hat{J}^2$ is $J(J+1)$ and that of $\hat{J}_z$ is m_J, then the commutation relations require that $m = -J, -J+1, \ldots, J-1, J$; it follows that there are $2J+1$ eigenstates of $\hat{J}_z$ and $\hat{J}^2$ for a specified value of J. Two linear combinations of the $\hat{J}_x$ and $\hat{J}_y$ operators prove useful:

$$\hat{J}_+ = \left(\hat{J}_x + i\hat{J}_y\right) \qquad \hat{J}_- = \left(\hat{J}_x - i\hat{J}_y\right). \tag{A.11}$$

The effect of these operators, called the raising and lowering operator respectively, is to inter-convert eigenfunctions with different m_J quantum numbers (within a scaling factor), leaving J unchanged. In summary,

$$\hat{J}^2|J, m_J\rangle = J(J+1)|J, m_J\rangle \tag{A.12}$$

$$\hat{J}_z|J, m_J\rangle = m_J|J, m_J\rangle \tag{A.13}$$

$$\hat{J}_+|J, m_J\rangle = \sqrt{J(J+1) - m_J(m_J+1)}|J, m_J+1\rangle \tag{A.14}$$

$$\hat{J}_-|J, m_J\rangle = \sqrt{J(J+1) - m_J(m_J-1)}|J, m_J-1\rangle. \tag{A.15}$$

A.3   Rotation Operators

A rotation about a unit vector $\boldsymbol{n}$ is defined as positive for a clockwise rotation as viewed along the positive direction of $\boldsymbol{n}$. Rotations can be interpreted as *active* rotations: rotations of objects in a fixed coordinate frame; or *passive* rotations: a rotation of the coordinate system. The convention of Rose[258] is used here - the rotation operator $\hat{R}_{\boldsymbol{n}}(\theta)$ causes a positive rotation of a function in the defined axis frame, or equivalently a negative rotation to the axes.

An operator, $\hat{R}_{\boldsymbol{n}}(\alpha)$, that causes a positive rotation of infinitesimal angle α of the function upon which it acts about a vector $\boldsymbol{n}$ is related to the component of angular momentum
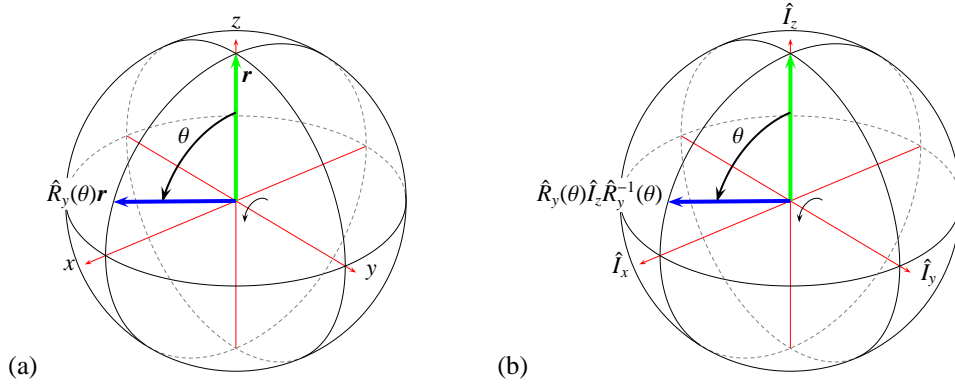
Figure A.1: (a) Rotation of a vector $\boldsymbol{r}$, initially along the z-axis, about the y-axis through an angle θ. (b) Rotation of the operator $\hat{I}_z$ about the y-axis through an angle θ.

operator along this same vector (Equation (A.9)) as

$$\hat{J}_n = \mathrm{i} \lim_{\alpha \to 0} \frac{\hat{R}_n(\alpha) - 1}{\alpha}. \tag{A.16}$$

For small α this gives $\hat{R}_n = 1 - \mathrm{i}\alpha\hat{J}_n + O(\alpha^2)$, and finite rotations can be achieved by sequence of infinitesimal rotations

$$\begin{aligned}
\hat{R}_{\boldsymbol{n}}(\theta) &= \lim_{k \to \infty} \left(1 - \mathrm{i}\frac{\theta}{k}\hat{J}_{\boldsymbol{n}}\right)^k \\
&= 1 - \mathrm{i}\theta\hat{J}_{\boldsymbol{n}} - \frac{1}{2!}\theta^2\hat{J}_{\boldsymbol{n}}^2 + \frac{\mathrm{i}}{3!}\theta^3\hat{J}_{\boldsymbol{n}}^3 \tag{A.17} \\
&= \exp\left[-\mathrm{i}\theta\hat{J}_{\boldsymbol{n}}\right] = \exp\left[\mathrm{i}\theta\hat{\boldsymbol{J}} \cdot \boldsymbol{n}\right], \tag{A.18}
\end{aligned}$$

where Equation (A.17) defines the meaning of the exponential of an operator. For example, $\hat{R}_y(\theta)\boldsymbol{r}$ rotates the vector $\boldsymbol{r}$ by an angle θ about the y-axis in Cartesian space. Rotation of a second rank tensor $\boldsymbol{\Lambda}$ about the y-axis is achieved by the operation

$$\boldsymbol{\Lambda}' = \hat{R}_y(\theta)\boldsymbol{\Lambda}\hat{R}_y^{-1}(\theta), \tag{A.19}$$

where $\hat{R}_y^{-1}(\theta) = \hat{R}_y(-\theta)$. Two further useful relationship exists if a set of three operators obey a cyclic commutation relation, that is

$$\left[\hat{A}, \hat{B}\right] = \mathrm{i}\kappa\hat{C}, \qquad \left[\hat{C}, \hat{A}\right] = \mathrm{i}\kappa\hat{B}, \qquad \left[\hat{B}, \hat{C}\right] = \mathrm{i}\kappa\hat{A}. \tag{A.20}$$

An example is the three Cartesian components of angular momentum (Equation (A.10)).

This cyclic property implies the relationships

$$\exp\left[-i\theta\hat{A}\right]\hat{B}\exp\left[+i\theta\hat{A}\right] = \hat{B}\cos\kappa\theta + \hat{C}\sin\kappa\theta \tag{A.21}$$

$$\exp\left[-i\theta\hat{A}\right]\exp\left[+i\hat{B}\right]\exp\left[+i\theta\hat{A}\right] = \exp\left[\hat{B}\cos\kappa\theta + \hat{C}\sin\kappa\theta\right]. \tag{A.22}$$

Considering the specific example of the angular momentum operators $\hat{J}_x$, $\hat{J}_y$ and $\hat{J}_z$, this gives

$$\exp\left[-i\theta\hat{J}_y\right]\hat{J}_z\exp\left[+i\theta\hat{J}_y\right] = \hat{J}_z\cos\theta + \hat{J}_x\sin\theta, \tag{A.23}$$

and its cyclic permutation. Equation (A.23) corresponds to a rotation of the operator $\hat{J}_z$ towards $\hat{J}_x$ about $\hat{J}_y$ by an angle θ. The effect of the rotation operator on a vector, and the rotation of an operator is illustrated in Figure A.1.

A.4   Euler Angles

Two Cartesian axis frames can be related to each other by a set of three Euler angles, shown in Figure A.2. Transformation from coordinate frame A to coordinate frame B is defined the the Euler angles $\Omega_{AB} = \{\alpha_{AB}, \beta_{AB}, \gamma_{AB}\}$ according to either of the equivalent definitions:

(i) Rotation of frame coincident with the A system by α_{AB} about original z_A-axis.	(i) Rotation of the frame coincident with the A system by γ_{AB} about the original z_A-axis
(ii) Rotation by β_{AB} about the new y'-axis.	(ii) Rotation by β_{AB} about the original y_A-axis
(iii) Rotation by γ_{AB} about the z_B-axis of the B frame to generate the coordinate frame B.	(iii) Rotation by α_{AB} about the original z_A-axis to generate the coordinate frame B

Since the definitions involve passive rotations, the rotation of a vector $\boldsymbol{r}_A$ defined in the original frame A into the frame defined by B is given by $\boldsymbol{r}_B = \hat{R}^{-1}(\alpha_{AB}, \beta_{AB}, \gamma_{AB})\boldsymbol{r}_A$, where the operator represents either of the following sequence of rotations:

$$\hat{R}^{-1}(\Omega_{AB}) = \hat{R}_{z_B}^{-1}(\gamma_{AB})\hat{R}_{y'}^{-1}(\beta_{AB})\hat{R}_{z_A}^{-1}(\alpha_{AB}) \tag{A.24}$$

$$\hat{R}^{-1}(\Omega_{AB}) = \hat{R}_{z_A}^{-1}(\alpha_{AB})\hat{R}_{y_A}^{-1}(\beta_{AB})\hat{R}_{z_A}^{-1}(\gamma_{AB}). \tag{A.25}$$
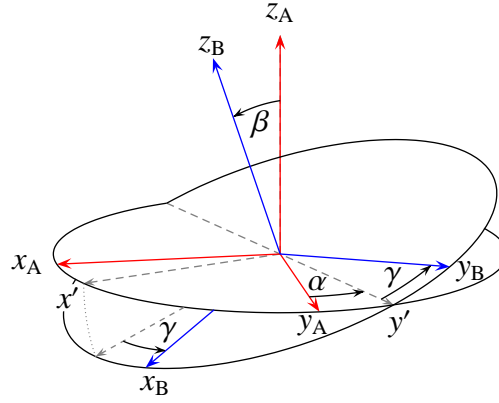
Figure A.2: Definition of the three Euler angles α, β, γ relating axis frame A to axis frame B.

Further, a second rank tensor $\mathbf{\Lambda}_B$ defined in axis system B is related to a second rank tensor $\mathbf{\Lambda}_A$ defined in axis system A by the rotation

$$\mathbf{\Lambda}_{\mathrm{B}} = \hat{R}^{-1}(\Omega_{\mathrm{AB}})\mathbf{\Lambda}_{\mathrm{A}}\hat{R}(\Omega_{\mathrm{AB}}). \tag{A.26}$$

The matrix representation of the rotation operators in Cartesian space are

$$R^{-1}(\Omega_{\mathrm{AB}}) = \begin{pmatrix} \begin{pmatrix} \cos\alpha\cos\beta\cos\gamma \\ -\sin\alpha\sin\gamma \end{pmatrix} & \begin{pmatrix} \sin\alpha\cos\beta\cos\gamma \\ +\cos\alpha\sin\gamma \end{pmatrix} & -\sin\beta\cos\gamma \\ \begin{pmatrix} -\cos\alpha\cos\beta\sin\gamma \\ -\sin\alpha\cos\gamma \end{pmatrix} & \begin{pmatrix} -\sin\alpha\cos\beta\sin\gamma \\ +\cos\alpha\cos\gamma \end{pmatrix} & \sin\beta\sin\gamma \\ \cos\alpha\sin\beta & \sin\alpha\sin\beta & \cos\beta \end{pmatrix}, \tag{A.27}$$

and $R(\Omega_{\mathrm{AB}}) = (R^{-1}(\Omega_{\mathrm{AB}}))^{\mathrm{T}}$.

A.5 Spin Angular Momentum

Nuclei possess an intrinsic angular momentum, called spin. The three Cartesian components of the spin angular momentum operator $\hat{\boldsymbol{I}}$ obey the same cyclic commutation relation as in Equation (A.10), and although the eigenfunctions of $\hat{I}^2$ and $\hat{I}_z$ cannot be written as spherical harmonics, they are characterised by two quantum numbers I and m and obey the analogous expressions Equation (A.13) to (A.15). In contrast to the quantum numbers J and m_J which must be integer numbers, the values of I and m are only restricted to being integer or half-integer. Since $\hat{I}_x$, $\hat{I}_y$ and $\hat{I}_z$ obey a cyclic commutation relation, the result expressed in Equation (A.21) and (A.22) can be applied to spin angular momentum.

B

MuPAD Procedures

MuPAD[210] is a computer algebra system that provides many numerical algorithms with a simple notebook oriented interface. The procedures used to calculate the pulse timings for the CSA-amplified PASS, CT-2DCSA and OPT-2DCSA experiments are detailed in the following sections, and are presented as should be typed into the notebook user interface of MuPAD.

B.1 Calculating pulse times for the CSA-amplified PASS experiment

The following procedure is used to calculate the pulse times used for the CSA-amplified PASS experiment, described in Section 4.2. The procedure is called by the command `csa_amp_pass(r,n,x,h,p)` where `r` is the duration of the pulse sequence unit in rotor periods, `n` is the number of pitch values to calculate and `x` is the required scaling factor. `h` determines the output format: if `h` =1, the pulse times, in units of rotor periods, are printed in a table format; for other values of `h` the pulse times are printed in a list form that can be copied to a BRUKER variable delay list for use in the pulse sequence. Finally, if `p` is set to be 1 then the pulse times are plotted as a function of the pitch.

- ```
  csa_amp_pass:=proc(r,n,x,h,p)

  begin

  if (h=1) then
    sol:=array(0..(n+1),0..5) else sol:=array(1..(n+1),1..5)
  end_if:

   thp:=array(0..n,1..5);

  /* set initial guess values for the solutions */
   solution:=[thp[(n/2),q]=q*r/6 $ q=1..5];

  /* cycle through all the pitch values Pi to 0 */
  ```

```
 for i from n/2 downto 0 do

/* set up nonlinear simulatneous equations*/
    fim:=2*sum(((-1)^q)*sin(m*thp[i,q]*2*PI), q=1..5)
               +((-1)^5)*((x-1)*sin(m*T)-x*sin(m*(T-theta)))=0;
    fre:=2*sum(((-1)^q)*cos(m*thp[i,q]*2*PI), q=1..5)
               +((-1)^5)*((x-1)*cos(m*T)-x*cos(m*(T-theta)))+1=0;
    tau:=T-2*sum((-1)^(5+q)*thp[i,q]*2*PI,q=1..5)=0;

    equations:={subs(fre, m=1, T=r*2*PI, theta=(i*2*(PI/n))),
                subs(fre, m=2, T=r*2*PI, theta=(i*2*(PI/n))),
                subs(fim, m=1, T=r*2*PI, theta=(i*2*(PI/n))),
                subs(fim, m=2, T=r*2*PI, theta=(i*2*(PI/n))),
                subs(tau, T=r*2*PI)};

/* solve the non-liear simultaneous equatuions */
    solution:=numeric::fsolve(equations,solution);

    if solution=FAIL then return("No sequence found - no solution") end_if;
    assign(solution);
/* set the initial guess for the next pitch value to the current solution */
    if (i > 0) then
       solution:=[thp[(i-1),q]=subs(thp[i,q],solution[q]) $ q=1..5]
    end_if;

  end_for:

 solution:=[thp[(n/2+1),q]=thp[n/2,q] $ q=1..5];

/* cycle through all the pitch values Pi to 2Pi */
   for i from (n/2+1) to n do

/* set up nonlinear simulatneous equations*/
    fim:=2*sum(((-1)^q)*sin(m*thp[i,q]*2*PI), q=1..5)
               +((-1)^5)*((x-1)*sin(m*T)-x*sin(m*(T-theta)))=0;
    fre:=2*sum(((-1)^q)*cos(m*thp[i,q]*2*PI), q=1..5)
               +((-1)^5)*((x-1)*cos(m*T)-x*cos(m*(T-theta)))+1=0;
    tau:=T-2*sum((-1)^(5+q)*thp[i,q]*2*PI,q=1..5)=0;

    equations:={subs(fre, m=1, T=r*2*PI, theta=(i*2*(PI/n))),
                subs(fre, m=2, T=r*2*PI, theta=(i*2*(PI/n))),
                subs(fim, m=1, T=r*2*PI, theta=(i*2*(PI/n))),
                subs(fim, m=2, T=r*2*PI, theta=(i*2*(PI/n))),
                subs(tau, T=r*2*PI)};
```

227

```
/* solve the non-liear simultaneous equatuions */
    solution:=numeric::fsolve(equations,solution);

    assign(solution);
    if (i < n) then
     solution:=[thp[(i+1),q]=subs(thp[i,q],solution[q]) $ q=1..5]
    end_if;

end_for:

/* check that the pulse timings lie in the correct range */
 if max(thp[i,j] $i=0..n $j=1..5)>r or min(thp[i,j] $i=0..16 $j=1..5)<0
  then return("No sequence found - times out of range")
 end_if;

/* format the output */

if (h=1) then
  sol[0,0]:="Theta";
  sol[0,1]:="t_1/t_r";
  sol[0,2]:="t_2/t_r";
  sol[0,3]:="t_3/t_r";
  sol[0,4]:="t_4/t_r";
  sol[0,5]:="t_5/t_r";

  for i from 1 to (n+1) do
   _assign(sol[i,0],((i-1)*2*(PI/n)));
   for j from 1 to 5 do
    _assign(sol[i,j],thp[(i-1),j]);
   end_for:
  end_for:
  output::tableForm(coerce(sol,DOM_LIST),Unquoted,Center,Column=6,
           Unique,Sort=FALSE);
end_if:

if _unequal(h,1) then
  for i from 1 to (n+1) do
   for j from 1 to 5 do
    _assign(sol[i,j],expr2text(thp[i-1,j])."s");
   end_for:
  end_for:
  output::tableForm(coerce(sol,DOM_LIST),Column=1,Sort=FALSE,Unquoted);
end_if:
```

228

```
if _equal(p,1) then
    dat1:=[([thp[i,1],((i)/n)] $i=0..n)];
    dat2:=[([thp[i,2],((i)/n)] $i=0..n)];
    dat3:=[([thp[i,3],((i)/n)] $i=0..n)];
    dat4:=[([thp[i,4],((i)/n)] $i=0..n)];
    dat5:=[([thp[i,5],((i)/n)] $i=0..n)];
    plot(plot::Listplot(dat1),plot::Listplot(dat2),
     plot::Listplot(dat3),plot::Listplot(dat4),plot::Listplot(dat5),
     Axes=Boxed,GridVisible=TRUE,ViewingBox=[0..r,0..1])
end_if:
```

Once the above text has been defined within the notebook, the pulse timings are calculated by typing, for example:

- `csa_amp_pass(4,32,3.4,1,1)`

to give the pulse timings for a pulse sequence unit of four rotor periods, scaling factor of $N_{unit} = 3.4$ and 32 values of the pitch. The pulse times would be printed as a table and also plotted.

B.2   Calculating pulse times for the CT-2DCSA experiment

The following MuPAD notebook calculates the required pulse timings for the CT-2DCSA experiment described in Section 5.4.1. The first input specifies the experimental parameters: desired F_1 spectral width, the sample spinning frequency, the number of t_1 data points to be acquired and the maximum value of the anisotropic scaling factor. The second input performs the calculation to determine the pulse timings and outputs the results as visual plot and table, followed by a list format that can be copied directly to a BRUKER variable delay list for use in the spectrometer pulse sequence.

- ```
  n:=3:           /* Duaration of the pulse sequence unit in rotor periods */
  DIGITS:=100:
  sw:=11200:      /* F1 Spectral width */
  wr:=2500:       /* Spinning frequency */
  nsteps:=32:     /* Number of t1 values in 2D experiment */
  Xmax:=0.24:     /* Maximum value of the anisotropic scaling factor */
  /* Calculate the total number of pulse sequence units required */
  nr:=ceil(nsteps*wr/(sw*n*Xmax));
  ```

```
/* Calculate the required anisotropic scaling factor for each t1eff value */
Xj:=[(i*wr/(n*nr*sw)) $i=0..nsteps]:
sol:=array(0..nsteps,1..2):
th[1]:=0:
th[2]:=1:
solution:=2:
```

- ```
  delete th[1]:
  delete th[2]:
  delete solution:

  /* set up  and solve the non-linear simulataneous eqns */
  csaeqna:=(sin(2*PI*th[1])-sin(2*PI*th[2])
            +sin((n*PI)/2-th[1]*2*PI+th[2]*2*PI)-PI*n*X/2):
  csaeqnb:=(sin(4*PI*th[1])-sin(4*PI*th[2])
            +sin((n*PI)-th[1]*4*PI+th[2]*4*PI)-PI*n*X):
  equations:={subs(csaeqna,X=Xj[1]),subs(csaeqnb,X=Xj[1])}:
  solution:=numeric::fsolve(equations,[th[1]=(0.6),th[2]=(1.1)],Random):
  assign(solution):
  sol[0,1]:=th[1]:
  sol[0,2]:=th[2]:

  for i from 1 to (nsteps-1) do
    delete th[1]:
    delete th[2]:
    delete solution:
    solution:=[th[j]=sol[i-1,j] $ j=1..2]:
    csaeqna:=(sin(2*PI*th[1])-sin(2*PI*th[2])
              +sin((n*PI/2)-th[1]*2*PI+th[2]*2*PI)-PI*n*X/2):
    csaeqnb:=(sin(4*PI*th[1])-sin(4*PI*th[2])
              +sin((n*PI)-th[1]*4*PI+th[2]*4*PI)-PI*n*X):
    equations:={subs(csaeqna,X=Xj[i+1]),subs(csaeqnb,X=Xj[i+1])}:
    solution:=numeric::fsolve(equations,solution,Random):
    assign(solution):
    sol[i,1]:=th[1]:
    sol[i,2]:=th[2]:
  end_for:

  vals3:= [(n/4) + sol[i,2] - sol[i,1] $ i=0..nsteps]:

  DIGITS:=10:

  /* Format the output */
  summary:=array(0..(nsteps+1),1..4):
  ```

```
summary2:=array(1..(nsteps+1),1..3):
summary[0,1]:="Scaling factor":
summary[0,2]:="t_1/t_r":
summary[0,3]:="t_2/t_r":
summary[0,4]:="t_3/t_r":

for i from 1 to (nsteps) do
  summary[i,1]:=float(Xj[i]):
  summary[i,2]:=sol[i-1,1]:
  summary[i,3]:=sol[i-1,2]:
  summary[i,4]:=vals3[i]:
  summary2[i,1]:=expr2text(sol[i-1,1])."s":
  summary2[i,2]:=expr2text(sol[i-1,2])."s":
  summary2[i,3]:=expr2text(vals3[i])."s":
end_for:

dat1:=[i $ i=0..(nsteps-1)]:
dat2:=[i $ i=0..(nsteps-1)]:
dat3:=[i $ i=0..(nsteps-1)]:

for i from 1 to nsteps do
  _assign(dat1[i],[summary[i,2],summary[i,1]]):
  _assign(dat2[i],[summary[i,3],summary[i,1]]):
  _assign(dat3[i],[summary[i,4],summary[i,1]]):
end_for:

plot(plot::Listplot(dat1,LineColor=RGB::Red,PointColor=RGB::Red),
  plot::Listplot(dat2,LineColor=RGB::Green,PointColor=RGB::Green),
  plot::Listplot(dat3,LineColor=RGB::Blue,PointColor=RGB::Blue),
  Axes=Boxed,AxesOrigin=[0,0],GridVisible=TRUE);

output::tableForm(coerce(summary,DOM_LIST),Unquoted,
                    Center,Column=4,Unique,Sort=FALSE);
output::tableForm(coerce(summary2,DOM_LIST),Unquoted,
                    Column=1,Unique,Sort=FALSE)
```

B.3   Calculating pulse times for the OPT-2DCSA experiment

The following MuPAD notebook calculates the required pulse timings for the OPT-2DCSA experiment described in Section 5.4.2.   The first input specifies the experimental

231

parameters: desired F_1 spectral width, the sample spinning frequency, the number of t_1 data points to be acquired and the maximum value of the anisotropic scaling factor. The second input performs the calculation to determine the pulse timings and outputs the results as visual plot and table, followed by the pulse timings and corresponding number of pulse sequence units in a list format that can be copied directly to a BRUKER variable delay list and variable counter list for use in the spectrometer pulse sequence.

```
• n:=3:            /* Duaration of the pulse sequence unit in rotor periods */
  DIGITS:=100:
  sw:=11200:    /* Spectral width */
  wr:=2500:     /* Spinning frequency */
  nsteps:=32:   /* Number of t1 values in 2D experiment */
  Xmax:=0.24:   /* Maximum value of the anisotropic scaling factor */


  /*Set up the array of pseudo t_1 variables*/
  S:=[float((k)/sw) $k=0..nsteps-1]:
  solution:=0:


  /*Calculate the number of 6 PI-pulse units for each t_1 increment*/
  U:=[ceil((wr*(j))/(Xmax*n*sw)) $j=0..(nsteps-1)]:
  U[1]:=1:
  /*Calculate the anistropic scaling factor required for each t_1 increment*/
  Xj:=[S[i+1]*wr/(U[i+1]*n) $i=0..nsteps]:
  /* Initialise some arrays */
  sol:=array(0..(nsteps-1),1..2):
  th[1]:=0:
  th[2]:=1:
  solution:=2:

• delete th[1]:
  delete th[2]:
  delete solution:

  /* set up  and solve the non-linear simulataneous eqns */
  csaeqna:=(sin(2*PI*th[1])-sin(2*PI*th[2])
           +sin((n*PI/2)-th[1]*2*PI+th[2]*2*PI)-PI*n*X/2):
  csaeqnb:=(sin(4*PI*th[1])-sin(4*PI*th[2])
           +sin((n*PI)-th[1]*4*PI+th[2]*4*PI)-PI*n*X):
  equations:={subs(csaeqna,X=Xj[1]),subs(csaeqnb,X=Xj[1])}:
  solution:=numeric::fsolve(equations,[th[1]=(0.3),th[2]=(0.6)],Random):
  assign(solution):
  sol[0,1]:=th[1]:
  sol[0,2]:=th[2]:
```

```
for i from 1 to (nsteps-1) do
  delete th[1]:
  delete th[2]:
  delete solution:
  solution:=[th[j]=sol[i-1,j] $ j=1..2]:
  csaeqna:=(sin(2*PI*th[1])-sin(2*PI*th[2])
           +sin((n*PI/2)-th[1]*2*PI+th[2]*2*PI)-PI*n*X/2):
  csaeqnb:=(sin(4*PI*th[1])-sin(4*PI*th[2])
           +sin((n*PI)-th[1]*4*PI+th[2]*4*PI)-PI*n*X):
  equations:={subs(csaeqna,X=Xj[i+1]),subs(csaeqnb,X=Xj[i+1])}:
  solution:=numeric::fsolve(equations,solution,Random):
  assign(solution):
  sol[i,1]:=float(th[1]):
  sol[i,2]:=float(th[2]):
end_for:


vals3:= [float((n/4) + sol[i,2] - sol[i,1]) $ i=0..nsteps]:

/* Format output */
summary:=array(0..(nsteps+1),1..5):
summary2:=array(1..(nsteps+1),1..3):
summary[0,1]:="Scaling factor":
summary[0,2]:="Number of units - 1":
summary[0,3]:="t_1/t_r":
summary[0,4]:="t_2/t_r":
summary[0,5]:="t_3/t_r":
DIGITS:=15:

for i from 1 to (nsteps) do
  summary[i,1]:=Xj[i]:
  summary[i,2]:=(U[i]-1):
  summary[i,3]:=sol[i-1,1]:
  summary[i,4]:=sol[i-1,2]:
  summary[i,5]:=vals3[i]:
  summary2[i,1]:=expr2text(sol[i-1,1])."s":
  summary2[i,2]:=expr2text(sol[i-1,2])."s":
  summary2[i,3]:=expr2text(vals3[i])."s":
end_for:


summary4:=array(1..(nsteps+1));

for i from 1 to (nsteps) do
```

```
    summary4[i]:=(U[i]-1);
end_for:

dat1:=[i $ i=0..nsteps]:
dat2:=[i $ i=0..nsteps]:
dat3:=[i $ i=0..nsteps]:

for i from 0 to nsteps do
  _assign(dat1[i+1],[summary[i+1,3],summary[i+1,1]]):
  _assign(dat2[i+1],[summary[i+1,4],summary[i+1,1]]):
  _assign(dat3[i+1],[summary[i+1,5],summary[i+1,1]]):
end_for:

plot(plot::Listplot(dat1,LineColor=RGB::Red,PointColor=RGB::Red),
     plot::Listplot(dat2,LineColor=RGB::Green,PointColor=RGB::Green),
     plot::Listplot(dat3,LineColor=RGB::Blue,PointColor=RGB::Blue),
     Axes=Boxed,AxesOrigin=[0,0],GridVisible=TRUE);

summary1:=coerce(summary,DOM_LIST):
summary3:=coerce(summary2,DOM_LIST):
summary5:=coerce(summary4,DOM_LIST):

output::tableForm(summary1,Unquoted,Center,Column=5,Unique,Sort=FALSE);
output::tableForm(summary5,Unquoted,Center,Column=1,Unique,Sort=FALSE);
output::tableForm(summary3,Unquoted,Column=1,Unique,Sort=FALSE)
```

C

Second-order dipolar-quadrupolar cross-term Hamiltonian

Calculation of the effect of a quadrupolar nucleus on a dipolar-coupled spin-1/2 nucleus is treated here using average Hamiltonian theory. The laboratory frame Hamiltonian is defined to be

$$\hat{\mathcal{H}}_{\text{lab}} = \hat{\mathcal{H}}_Z^C + \hat{\mathcal{H}}_Z^N + \hat{\mathcal{H}}_{\text{CS}}^{\text{full,C}} + \hat{\mathcal{H}}_{IS}^{\text{full,CN}} + \hat{\mathcal{H}}_Q^{\text{full,N}}, \tag{C.1}$$

where $\hat{\mathcal{H}}_Z^C$ and $\hat{\mathcal{H}}_Z^N$ are the ^{13}C and ^{14}N Zeeman Hamiltonians, $\hat{\mathcal{H}}_{\text{CS}}^{\text{full,C}}$ is the ^{13}C chemical shielding Hamiltonian, $\hat{\mathcal{H}}_{IS}^{\text{full,CN}}$ is the ^{13}C–^{14}N dipolar coupling Hamiltonian, and $\hat{\mathcal{H}}_Q^{\text{full,N}}$ is the ^{14}N quadrupole coupling Hamiltonian; the superscript 'full' indicates that these are the non-truncated Hamiltonians that were defined in Table 1.1 on page 25. The same strategy described in Sections 1.3.1 and 1.9.1 to truncate the Hamiltonian is used here. First, the Hamiltonian in the interaction frame of the Zeeman interaction ($\hat{\mathcal{H}}_Z^C + \hat{\mathcal{H}}_Z^N$) is calculated using the propagator $\hat{U}_0(t) = \exp\left[-\mathrm{i}\left(\omega_0^N \hat{S}_z + \omega_0^C \hat{I}_z\right)t\right]$, where ^{14}N is the S spin and ^{13}C the I spin, with Larmor frequencies ω_0^N and ω_0^C respectively. The interaction frame corresponds to viewing both the I and S spins in their respective rotating frames. The first-order and second-order average Hamiltonians of the interaction frame Hamiltonian are then calculated. The interaction frame Hamiltonian is

$$\tilde{\hat{\mathcal{H}}}(t) = \exp\left\{\mathrm{i}\left(\omega_0^N \hat{S}_z + \omega_0^C \hat{I}_z\right)t\right\}\left(\hat{\mathcal{H}}_{\text{CS}}^{\text{full,C}} + \hat{\mathcal{H}}_{IS}^{\text{full,CN}} + \hat{\mathcal{H}}_Q^{\text{full,N}}\right)\exp\left\{-\mathrm{i}\left(\omega_0^N \hat{S}_z + \omega_0^C \hat{I}_z\right)t\right\}. \tag{C.2}$$

The interaction-frame Hamiltonian $\tilde{\hat{\mathcal{H}}}(t)$ is periodic such that $\tilde{\hat{\mathcal{H}}}(t) = \tilde{\hat{\mathcal{H}}}(t + t_c)$, and the average Hamiltonian is evaluated over the duration t_c. The first-order average Hamiltonian will contain the truncated chemical shielding, dipolar coupling and quadrupolar coupling Hamiltonians.

The second-order average Hamiltonian is calculated from

$$\overline{\tilde{\hat{\mathcal{H}}}^{(2)}} = \frac{-\mathrm{i}}{2t_c} \int_0^{t_c} \mathrm{d}t \int_0^{t'} \mathrm{d}t' \left[\tilde{\hat{\mathcal{H}}}(t), \tilde{\hat{\mathcal{H}}}(t')\right]. \tag{C.3}$$

As discussed in Section 6.1, only the commutators between the dipolar and quadrupolar Hamiltonian need to be considered, thus

$$\overline{\tilde{\mathcal{H}}^{(2)}} = \frac{-\mathrm{i}}{2t_{\mathrm{c}}} \int_0^{t_{\mathrm{c}}} \mathrm{d}t \int_0^{t'} \mathrm{d}t' \left\{ \left[\tilde{\mathcal{H}}_Q^{\mathrm{full}}(t), \tilde{\mathcal{H}}_{IS}^{\mathrm{full}}(t') \right] + \left[\tilde{\mathcal{H}}_{IS}^{\mathrm{full}}(t), \tilde{\mathcal{H}}_Q^{\mathrm{full}}(t') \right] \right\}. \qquad (\mathrm{C.4})$$

The Hamiltonians for the dipolar and quadrupolar interactions can be written in the form:

$$\begin{aligned} \hat{\mathcal{H}}_{IS}^{\mathrm{full}} &= \frac{\sqrt{6}}{3} D_{2,0} \left[\hat{I}_z \hat{S}_z - \frac{1}{2} \left(\hat{I}_+ \hat{S}_- + \hat{I}_- \hat{S}_+ \right) \right] + \frac{1}{2} D_{2,-1} \left[\hat{I}_z \hat{S}_+ + \hat{I}_+ \hat{S}_z \right] \\ &\quad - \frac{1}{2} D_{2,+1} \left[\hat{I}_z \hat{S}_- + \hat{I}_- \hat{S}_z \right] + \frac{1}{2} D_{2,-2} \hat{I}_+ \hat{S}_+ + \frac{1}{2} D_{2,+2} \hat{I}_- \hat{S}_-, \qquad (\mathrm{C.5}) \end{aligned}$$

and

$$\begin{aligned} \hat{\mathcal{H}}_Q^{\mathrm{full}} &= \frac{eQ}{4S(2S-1)\hbar} \left(\frac{\sqrt{6}}{3} V_{2,0} \left[3\hat{S}_z^2 - \hat{S} \cdot \hat{S} \right] + V_{2,-1} \hat{S}_+ \left[2\hat{S}_z + 1 \right] - V_{2,+1} \hat{S}_- \left[2\hat{S}_z - 1 \right] \right. \\ &\quad \left. + V_{2,-2} \hat{S}_+^2 + V_{2,+2} \hat{S}_-^2 \right), \qquad (\mathrm{C.6}) \end{aligned}$$

where the $D_{2,q}$ and $V_{2,q}$ are components of the dipolar coupling and quadrupole coupling tensors written in spherical tensor form, and are chosen here to be defined in the laboratory frame of reference. The spherical tensors component $A_{k,q}$ of rank $k = 2$ and order q can be expressed as the components of a Cartesian second rank tensor by

$$A_{2,0} = \frac{\sqrt{6}}{2} A_{zz} \qquad A_{2+1} = -A_{xz} - \mathrm{i}A_{yz} \qquad A_{2,+2} = \frac{1}{2} \left(A_{xx} - A_{yy} \right) + \mathrm{i}A_{xy}$$

$$A_{2-1} = A_{xz} - \mathrm{i}A_{yz} \qquad A_{2,-2} = \frac{1}{2} \left(A_{xx} - A_{yy} \right) - \mathrm{i}A_{xy},$$

where the tensor A is either the dipolar or quadrupolar coupling tensor.

In the interaction frame, the dipolar and quadrupolar Hamiltonians are

$$\tilde{\tilde{\mathcal{H}}}_{IS}^{\text{full}}(t) = \frac{\sqrt{6}}{3} D_{2,0} \left[\hat{I}_z \hat{S}_z \right. \tag{C.7a}$$

$$\left. -\frac{1}{2} \left(\hat{I}_+ \hat{S}_- e^{i(\omega_0^I - \omega_0^S)t} + \hat{I}_- \hat{S}_+ e^{i(\omega_0^S - \omega_0^I)t} \right) \right] \tag{C.7b}$$

$$+ \frac{1}{2} D_{2,-1} \left[\hat{I}_z \hat{S}_+ e^{i\omega_0^S t} + \hat{I}_+ \hat{S}_z e^{i\omega_0^I t} \right] \tag{C.7c}$$

$$- \frac{1}{2} D_{2,+1} \left[\hat{I}_z \hat{S}_- e^{-i\omega_0^S t} + \hat{I}_- \hat{S}_z e^{-i\omega_0^I t} \right] \tag{C.7d}$$

$$+ \frac{1}{2} D_{2,-2} \hat{I}_+ \hat{S}_+ e^{i(\omega_0^I + \omega_0^S)t} + \frac{1}{2} D_{2,+2} \hat{I}_- \hat{S}_- e^{-i(\omega_0^I + \omega_0^S)t}, \tag{C.7e}$$

and

$$\tilde{\tilde{\mathcal{H}}}_Q^{\text{full}} = \frac{eQ}{4S(S-1)\hbar} \left(\frac{\sqrt{6}}{3} V_{2,0} \left[3\hat{S}_z^2 - \hat{S} \cdot \hat{S} \right] \right. \tag{C.8a}$$

$$+ V_{2,-1} \hat{S}_+ \left[2\hat{S}_z + 1 \right] e^{i\omega_0^S t} \tag{C.8b}$$

$$- V_{2,+1} \hat{S}_- \left[2\hat{S}_z - 1 \right] e^{-i\omega_0^S t} \tag{C.8c}$$

$$\left. + V_{2,-2} \hat{S}_+^2 e^{i2\omega_0^S t} + V_{2,+2} \hat{S}_-^2 e^{-i2\omega_0^S t} \right). \tag{C.8d}$$

The two integrals in Equation (C.4) only involve the products of the exponential factors between the different terms in Equations (C.7) and (C.8), and only commutators between different terms with non-zero integrals need to be evaluated. In addition, only commutators that, when evaluated, commute with the Zeeman Hamiltonian are included in the average Hamiltonian.[38] Consequently, it is only necessary to evaluate the commutator of the terms (C.7c) and (C.8c), and of (C.7d) and (C.8b).

For the commutator of the terms (C.7c) and (C.8c), one obtains

$$\int_0^{t_c} dt \int_0^t dt' \left[\frac{1}{2} D_{2,-1} \left(\hat{I}_z \hat{S}_+ e^{i\omega_0^S t} + \hat{I}_+ \hat{S}_z e^{i\omega_0^I t} \right), -V_{2,+1} \hat{S}_- \left(2\hat{S}_z - 1 \right) e^{-i\omega_0^S t'} \right]$$

$$= \int_0^{t_c} dt \frac{i}{\omega_0^S} \frac{D_{2,-1} V_{2,+1}}{2} \left[\left(\hat{I}_z \hat{S}_+ e^{i\omega_0^S t} + \hat{I}_+ \hat{S}_z e^{i(\omega_0^I) t} \right), \hat{S}_- \left(2\hat{S}_z - 1 \right) \right] \left(e^{-i\omega_0^S t} - 1 \right)$$

$$= \frac{i}{\omega_0^S} \frac{D_{2,-1} V_{2,+1}}{2} \left[\hat{I}_z \hat{S}_+, \hat{S}_- \left(2\hat{S}_z - 1 \right) \right]$$

$$= \frac{i}{\omega_0^S} \frac{D_{2,-1} V_{2,+1}}{2} \hat{I}_z \left(2\hat{S}_+ \hat{S}_- \hat{S}_z - \hat{S}_+ \hat{S}_- - 2\hat{S}_- \hat{S}_z \hat{S}_+ + \hat{S}_- \hat{S}_+ \right)$$

$$= \frac{i}{\omega_0^S} \frac{D_{2,-1} V_{2,+1}}{2} \hat{I}_z \left(2\hat{S}_+ \hat{S}_- \hat{S}_z - \hat{S}_+ \hat{S}_- - 2\hat{S}_- (\hat{S}_+ \hat{S}_z + \hat{S}_+) \right)$$

$$= \frac{i}{\omega_0^S} \frac{D_{2,-1} V_{2,+1}}{2} \hat{I}_z \left(2 \left[\hat{S}_+, \hat{S}_- \right] \hat{S}_z - \hat{S}_+ \hat{S}_- - \hat{S}_- \hat{S}_+ \right)$$

$$= \frac{i}{\omega_0^S} \frac{D_{2,-1} V_{2,+1}}{2} \hat{I}_z \left(4\hat{S}_z^2 - 2\hat{S} \cdot \hat{S} + 2\hat{S}_z^2 \right)$$

$$= \frac{i}{\omega_0^S} D_{2,-1} V_{2,+1} \hat{I}_z \left(3\hat{S}_z^2 - \hat{S} \cdot \hat{S} \right), \tag{C.9}$$

where the commutator $\left[\hat{S}_z, \hat{S}_+ \right] = \hat{S}_+$, and relations $\hat{S}_+ \hat{S}_- = \hat{S} \cdot \hat{S} - \hat{S}_z (\hat{S}_z - 1)$ and $\hat{S}_- \hat{S}_+ = \hat{S} \cdot \hat{S} - \hat{S}_z (\hat{S}_z + 1)$ have been used. Similarly, the commutator of the terms (C.7d) and (C.8b) is evaluated to give

$$\int_0^{t_c} dt \int_0^t dt' \left[-\frac{1}{2} D_{2,+1} \left(\hat{I}_z \hat{S}_- e^{-i\omega_0^S t} + \hat{I}_- \hat{S}_z e^{-i\omega_0^I t} \right), V_{2,-1} \hat{S}_+ \left(2\hat{S}_z + 1 \right) e^{+i\omega_0^S t'} \right]$$

$$= \frac{i}{\omega_0^S} D_{2,+1} V_{2,-1} \hat{I}_z \left(3\hat{S}_z^2 - \hat{S} \cdot \hat{S} \right). \tag{C.10}$$

Using the results in Equations (C.9) and (C.10), and the relationship

$$\int_0^{t_c} dt \int_0^t dt' \left[\tilde{\hat{\mathcal{H}}}_{IS}^{full}(t), \tilde{\hat{\mathcal{H}}}_Q^{full}(t') \right] = \int_0^{t_c} dt \int_0^t dt' \left[\tilde{\hat{\mathcal{H}}}_Q^{full}(t), \tilde{\hat{\mathcal{H}}}_{IS}^{full}(t') \right], \tag{C.11}$$

the second-order dipolar-quadrupolar cross-term Hamiltonian is given by

$$\overline{\tilde{\hat{\mathcal{H}}}^{(2)}} = \frac{-i}{2t_c} \int_0^{t_c} dt \left\{ \frac{2i}{\omega_0^S} \frac{eQ}{4S(S-1)\hbar} \left(D_{2,-1} V_{2,+1} + D_{2,+1} V_{2,-1} \right) \hat{I}_z \left(3\hat{S}_z^2 - \hat{S} \cdot \hat{S} \right) \right\}$$

$$= \frac{1}{\omega_0^S} \frac{eQ}{4S(S-1)\hbar} \left(D_{2,-1} V_{2,+1} + D_{2,+1} V_{2,-1} \right) \hat{I}_z \left(3\hat{S}_z^2 - \hat{S} \cdot \hat{S} \right) \tag{C.12}$$

$$= \frac{-1}{\omega_0^S} \frac{eQ}{2S(S-1)\hbar} \left(D_{xz} V_{xz} + D_{yz} V_{yz} \right) \hat{I}_z \left(3\hat{S}_z^2 - \hat{S} \cdot \hat{S} \right) \tag{C.13}$$

The product of the two spherical tensor components $A_{k,i}$ and $A'_{k,j}$, for example $D_{2,-1}V_{2,+1}$ in Equation (C.12), can be written as a linear combination of new set of spherical tensors of rank zero, two and four.[258] It may be shown that magic-angle spinning averages the terms in the Hamiltonian involving second-rank spherical tensors, but not those of zero- and fourth-rank.[259] Consequently the second-order dipolar-quadrupolar cross-term Hamiltonian is not fully averaged to zero by magic-angle spinning.